



Pauli, Peter (2020) *Lambda(1520) measurements at the GlueX experiment*.
PhD thesis.

<http://theses.gla.ac.uk/81591/>

Copyright and moral rights for this work are retained by the author

A copy can be downloaded for personal non-commercial research or study,
without prior permission or charge

This work cannot be reproduced or quoted extensively from without first
obtaining permission in writing from the author

The content must not be changed in any way or sold commercially in any
format or medium without the formal permission of the author

When referring to this work, full bibliographic details including the author,
title, awarding institution and date of the thesis must be given

Enlighten: Theses

<https://theses.gla.ac.uk/>
research-enlighten@glasgow.ac.uk

$\Lambda(1520)$ Measurements at the GlueX Experiment

Peter Pauli

Submitted in fulfilment of the requirements for the
Degree of Doctor of Philosophy

School of Physics and Astronomy
College of Science and Engineering
University of Glasgow



University
of Glasgow

August 2020

Abstract

This thesis presents the first measurements of the photon beam asymmetry Σ , spin-density matrix elements and differential cross-sections in $\Lambda(1520)$ photoproduction at photon beam energies between 8.2 GeV and 8.8 GeV. These measurements will help to constrain physics models, describing the production process of hadrons at high photon energies, as they are needed in the search for exotic mesons.

The data used in this analysis were recorded using the GlueX beamline and detector in Hall D of the Thomas Jefferson National Accelerator Facility (JLab) in Virginia, USA. JLab provides a 12 GeV electron beam which is converted to a linearly polarised photon beam on a thin diamond, via the coherent bremsstrahlung technique. The photon beam is incident on a liquid hydrogen target where it can produce various meson and baryon resonances such as the $\Lambda(1520)$. The GlueX detector setup surrounding the target is able to detect both charged and neutral final state particles resulting from the reaction. Careful analysis of their momentum and angular distributions allows the determination of the observables presented in this work.

For the extraction of physics observables the sPlot method was used together with unbinned extended maximum likelihood fitting and Markov Chain Monte Carlo methods. The effect of longitudinal phase space analyses was studied and resulted in a publication.

So far, previous measurements for this reaction have only been made at much lower or higher energies. This is the first measurement of this reaction in the energy range of GlueX. This work also provides the first measurement of polarised spin-density matrix elements for this reaction channel. These are critical steps towards GlueX's main goal, which is to establish and map out the spectrum of exotic hybrid mesons, an important milestone in our understanding of quantum chromo dynamics and the strong force.

Contents

| | |
|--|-------------|
| Abstract | i |
| Acknowledgements | xiii |
| Declaration | xiv |
| 1 Introduction | 1 |
| 2 $K^+\Lambda(1520)$ photoproduction formalism | 6 |
| 2.1 Spin-density matrix elements | 7 |
| 2.2 Differential cross-section | 17 |
| 2.3 Choice of binning variable | 18 |
| 3 Current experimental situation | 19 |
| 3.1 Previous measurements | 19 |
| 3.2 Status of theoretical description | 22 |
| 4 Experimental setup | 24 |
| 4.1 Continuous Electron Beam Accelerator Facility | 25 |
| 4.2 Linearly polarised photon beam | 26 |
| 4.3 Liquid hydrogen target | 33 |
| 4.4 The GlueX detector | 33 |
| 4.5 Event recording and trigger | 40 |
| 4.6 Detector simulation | 41 |
| 5 Data analysis and event selection | 43 |
| 5.1 Dataset | 43 |
| 5.2 Calibrations | 44 |
| 5.3 Event reconstruction | 49 |
| 5.4 Skimming and kinematic fitting | 50 |
| 5.5 General event selection | 52 |

| | | |
|----------|---|------------|
| 5.6 | Exclusive event selection | 54 |
| 6 | Observable extraction | 78 |
| 6.1 | Beam asymmetry | 78 |
| 6.2 | Spin-density matrix elements | 92 |
| 6.3 | Differential cross-section | 120 |
| 7 | Results and discussion | 123 |
| 7.1 | Beam asymmetry | 123 |
| 7.2 | Spin-density matrix elements | 124 |
| 7.3 | Interpretation of angular decay distributions | 124 |
| 7.4 | Differential cross-section | 127 |
| 7.5 | Conclusion | 129 |
| A | Derivation: Fit function for the fractional beam asymmetry | 131 |
| B | Additional plots from SDME extraction | 132 |
| C | Additional plots of systematic studies | 152 |
| C.1 | Event selection studies beam asymmetry | 152 |
| C.2 | Sideband studies spin-density matrix elements | 155 |
| C.3 | SDME result validation studies | 160 |
| C.4 | Event selection studies spin-density matrix elements | 180 |
| D | Numerical results | 196 |
| E | Longitudinal phase space analysis | 203 |

List of Tables

| | | |
|------|---|-----|
| 4.1 | Photon beam polarisation and orientation | 32 |
| 4.2 | Trigger conditions used in the Spring 2017 beam time | 41 |
| 4.3 | Summary of MC simulations produced for this work | 42 |
| 4.4 | Summary of GlueX specifications | 42 |
| 5.1 | Trigger summary | 45 |
| 5.2 | Cuts applied during skimming | 50 |
| 5.3 | PID timing cuts | 52 |
| 6.1 | All setups used to assess systematic uncertainties | 89 |
| 6.2 | Numerical results for systematic uncertainties on Σ | 91 |
| 6.3 | SDMEs used for signal generation | 101 |
| 6.4 | Summary of SDME validation studies | 112 |
| 6.5 | Sets of start parameters for SDME MCMC studies | 115 |
| 6.6 | Results for systematic uncertainties on the SDME extraction | 119 |
| D.1 | Final results for Σ extracted via an unbinned maximum likelihood fit | 196 |
| D.2 | Final results for ρ_{11}^0 | 197 |
| D.3 | Final results for ρ_{31}^0 | 197 |
| D.4 | Final results for ρ_{3-1}^0 | 197 |
| D.5 | Final results for ρ_{11}^1 | 198 |
| D.6 | Final results for ρ_{33}^1 | 198 |
| D.7 | Final results for ρ_{31}^1 | 198 |
| D.8 | Final results for ρ_{3-1}^1 | 199 |
| D.9 | Final results for ρ_{31}^2 | 199 |
| D.10 | Final results for ρ_{3-1}^2 | 199 |
| D.11 | Final results for $\Sigma = 2(\rho_{11}^1 + \rho_{33}^1)$ | 200 |
| D.12 | Final results for $\frac{2}{N} (N_0 ^2 + N_1 ^2)$ | 200 |
| D.13 | Final results for $\frac{2}{N} (U_0 ^2 + U_1 ^2)$ | 200 |
| D.14 | Final results for $\frac{2}{N} (N_{-1} ^2 + N_2 ^2)$ | 201 |
| D.15 | Final results for $\frac{2}{N} (U_{-1} ^2 + U_2 ^2)$ | 201 |

| | | |
|------|--|-----|
| D.16 | Final results for $\frac{2}{N} \operatorname{Re} (N_{-1}N_0^* - N_2N_1^*)$ | 201 |
| D.17 | Final results for $\frac{2}{N} \operatorname{Re} (U_{-1}U_0^* - U_2U_1^*)$ | 202 |
| D.18 | Final results for $\frac{2}{N} \operatorname{Re} (N_{-1}N_1^* + N_2N_0^*)$ | 202 |
| D.19 | Final results for $\frac{2}{N} \operatorname{Re} (U_{-1}U_1^* + U_2U_0^*)$ | 202 |

List of Figures

| | | |
|------|---|----|
| 1.1 | The standard model of particle physics | 2 |
| 1.2 | The running coupling constant α_s | 3 |
| 2.1 | Three production mechanisms for $\Lambda(1520)$ photoproduction | 6 |
| 2.2 | Definition of the Gottfried-Jackson frame | 9 |
| 2.3 | Definition of the helicity frame | 12 |
| 3.1 | Previous measurements from SLAC | 20 |
| 3.2 | Previous measurements from LAMP2 | 20 |
| 3.3 | Previous measurements from LEPS | 21 |
| 3.4 | Previous measurements from CLAS | 22 |
| 3.5 | Fits and model predictions by Yu and Kong | 23 |
| 4.1 | Overview of the GlueX experiment | 24 |
| 4.2 | Schematic view of CEBAF | 25 |
| 4.3 | Schematic view of the Hall D beam line | 26 |
| 4.4 | Diagram of the bremsstrahlung process | 27 |
| 4.5 | Calculated photon rate | 27 |
| 4.6 | Schematic view of the goniometer | 29 |
| 4.7 | Schematic view of the tagging system | 30 |
| 4.8 | Schematic view of the pair spectrometer | 31 |
| 4.9 | Photon beam polarisation and photon flux | 33 |
| 4.10 | Schematic view of the start counter detector | 34 |
| 4.11 | CDC during construction | 35 |
| 4.12 | CDC dE/dx spectrum | 36 |
| 4.13 | Various schematic views of the BCAL detector | 37 |
| 4.14 | Picture of the FCAL detector | 38 |
| 4.15 | Picture of the TOF wall | 39 |
| 4.16 | Lorentz factor of various particles plotted against particle momentum | 40 |
| 5.1 | Visualisation of analysis flow | 44 |

| | | |
|------|--|----|
| 5.2 | Example plots showing the effect of timing calibrations | 46 |
| 5.3 | Example plots showing the effect of BCAL gain calibrations | 48 |
| 5.4 | PID ΔT vs momentum plots | 53 |
| 5.5 | Vertex distributions | 55 |
| 5.6 | pK^- inv. mass fits for CL cut optimisation | 57 |
| 5.7 | FOM for CL cut optimisation | 58 |
| 5.8 | CL distributions before and after the event selection | 58 |
| 5.9 | Missing mass square distribution | 59 |
| 5.10 | Lab angle differences between the K^+ and the combined pK^- | 60 |
| 5.11 | Invariant mass of pK^- after all cuts | 61 |
| 5.12 | Dalitz plot of pK^-K^+ after all cuts | 61 |
| 5.13 | pK^- inv. mass after all cuts and additional cut against $\rho(770)$ meson | 62 |
| 5.14 | PID ΔT vs momentum plots after event selection | 64 |
| 5.15 | PID ΔT vs momentum plots after event selection for $-(t - t_{\min}) < 2 \text{ GeV}^2/c^2$ | 65 |
| 5.16 | Timing spectrum of pK^-K^+ events | 66 |
| 5.17 | sPlot fits for $-(t - t_{\min}) = 0 \text{ GeV}^2/c^2 - 0.3 \text{ GeV}^2/c^2$ | 68 |
| 5.18 | sPlot fits for $-(t - t_{\min}) = 0.3 \text{ GeV}^2/c^2 - 0.5 \text{ GeV}^2/c^2$ | 68 |
| 5.19 | sPlot fits for $-(t - t_{\min}) = 0.5 \text{ GeV}^2/c^2 - 0.7 \text{ GeV}^2/c^2$ | 69 |
| 5.20 | sPlot fits for $-(t - t_{\min}) = 0.7 \text{ GeV}^2/c^2 - 0.9 \text{ GeV}^2/c^2$ | 69 |
| 5.21 | sPlot fits for $-(t - t_{\min}) = 0.9 \text{ GeV}^2/c^2 - 1.1 \text{ GeV}^2/c^2$ | 70 |
| 5.22 | sPlot fits for $-(t - t_{\min}) = 1.1 \text{ GeV}^2/c^2 - 1.3 \text{ GeV}^2/c^2$ | 70 |
| 5.23 | sPlot fits for $-(t - t_{\min}) = 1.3 \text{ GeV}^2/c^2 - 1.6 \text{ GeV}^2/c^2$ | 71 |
| 5.24 | sPlot fits for $-(t - t_{\min}) = 1.6 \text{ GeV}^2/c^2 - 2.0 \text{ GeV}^2/c^2$ | 71 |
| 5.25 | Angular distribution of K^- in GJ frame with sig. and bkg. weights applied | 72 |
| 5.26 | Momentum transfer $-(t - t_{\min})$ and acceptance | 72 |
| 5.27 | PID ΔT vs momentum plots for bggen MC | 74 |
| 5.28 | PID ΔT vs momentum plots for bggen MC after event selection | 75 |
| 5.29 | Stacked histogram of bggen events after event selection | 76 |
| 5.30 | Amount of events of certain thrown topology that survive event selection | 76 |
| 5.31 | Stacked histogram of bggen events after event selection (full mass range) | 77 |
| 6.1 | K^+ ϕ -angle distributions with signal weights applied | 80 |
| 6.2 | Results for the beam asymmetry Σ | 81 |
| 6.3 | Pull distribution for Σ result validation with toy MC | 82 |
| 6.4 | Mean and width of pull distribution for Σ result validation | 83 |
| 6.5 | Results for the beam asymmetry Σ from an unbinned maximum likelihood fit | 84 |
| 6.6 | Comparison of Σ for binned and unbinned fits | 85 |
| 6.7 | Mean and width of pull distribution for Σ result validation for unbinned fits | 86 |
| 6.8 | Σ over the invariant mass range near the $\Lambda(1520)$ | 87 |

| | | |
|------|--|-----|
| 6.9 | K^+ ϕ -angle distributions with background weights applied | 88 |
| 6.10 | Systematic study inv. mass cut (setups 1-6) for Σ | 90 |
| 6.11 | Visualisation of Metropolis-Hastings MCMC algorithm | 94 |
| 6.12 | SDME timeline plot for $-(t - t_{\min}) = 0 \text{ GeV}^2/c^2 - 0.3 \text{ GeV}^2/c^2$ | 96 |
| 6.13 | SDME corner plot for $-(t - t_{\min}) = 0 \text{ GeV}^2/c^2 - 0.3 \text{ GeV}^2/c^2$ | 97 |
| 6.14 | Resulting fits from MCMC for $-(t - t_{\min}) = 0 \text{ GeV}^2/c^2 - 0.3 \text{ GeV}^2/c^2$ | 98 |
| 6.15 | SDME results in the Gottfried-Jackson frame | 98 |
| 6.16 | Results for Σ extracted via SDMEs compared to extraction via unbinned fit | 99 |
| 6.17 | χ^2/ndf distribution for all fits in SDME sideband study | 100 |
| 6.18 | Example sFit for thrown MC in SDME result validation study | 102 |
| 6.19 | Example SDME fits for thrown MC in result validation study | 102 |
| 6.20 | Validation results for thrown data ρ_{11}^0 | 103 |
| 6.21 | Validation results for thrown data ρ_{31}^0 | 103 |
| 6.22 | Validation results for thrown data ρ_{3-1}^0 | 104 |
| 6.23 | Validation results for thrown data ρ_{11}^1 | 104 |
| 6.24 | Validation results for thrown data ρ_{33}^1 | 104 |
| 6.25 | Validation results for thrown data ρ_{31}^1 | 105 |
| 6.26 | Validation results for thrown data ρ_{3-1}^1 | 105 |
| 6.27 | Validation results for thrown data ρ_{31}^2 | 105 |
| 6.28 | Validation results for thrown data ρ_{3-1}^2 | 106 |
| 6.29 | Comparison between real MC signal and signal extracted via sFit in thrown data | 107 |
| 6.30 | Example sFit for fully simulated MC in SDME result validation study | 108 |
| 6.31 | Example SDME fits for full MC simulation in SDME result validation study | 109 |
| 6.32 | Validation results for full simulation ρ_{11}^0 | 109 |
| 6.33 | Validation results for full simulation ρ_{31}^0 | 109 |
| 6.34 | Validation results for full simulation ρ_{3-1}^0 | 110 |
| 6.35 | Validation results for full simulation ρ_{11}^1 | 110 |
| 6.36 | Validation results for full simulation ρ_{33}^1 | 110 |
| 6.37 | Validation results for full simulation ρ_{31}^1 | 111 |
| 6.38 | Validation results for full simulation ρ_{3-1}^1 | 111 |
| 6.39 | Validation results for full simulation ρ_{31}^2 | 111 |
| 6.40 | Validation results for full simulation ρ_{3-1}^2 | 112 |
| 6.41 | Comparison between real MC sig. and sig. extracted via sFit for full simulation | 113 |
| 6.42 | Results for SDMEs for different start parameters of the MCMC | 116 |
| 6.43 | Barlow test results for start parameter studies for SDMEs | 117 |
| 6.44 | Differential cross-section for $\gamma p \rightarrow K^+ \Lambda(1520)$ | 122 |
| 7.1 | Final results for Σ extracted via an unbinned maximum likelihood fit | 124 |
| 7.2 | Final results for all SDMEs in eight bins of $-(t - t_{\min})$ | 125 |

| | | |
|------|--|-----|
| 7.3 | Final results for the beam asymmetry $\Sigma = 2(\rho_{11}^1 + \rho_{33}^1)$ | 126 |
| 7.4 | Natural and unnatural amplitudes as calculated from SDMEs | 128 |
| 7.5 | Differential cross-section results and comparison | 129 |
| B.1 | SDME timeline plot for $-(t - t_{\min}) = 0 \text{ GeV}^2/c^2 - 0.3 \text{ GeV}^2/c^2$ | 133 |
| B.2 | SDME corner plot for $-(t - t_{\min}) = 0 \text{ GeV}^2/c^2 - 0.3 \text{ GeV}^2/c^2$ | 134 |
| B.3 | SDME timeline plot for $-(t - t_{\min}) = 0.3 \text{ GeV}^2/c^2 - 0.5 \text{ GeV}^2/c^2$ | 135 |
| B.4 | SDME corner plot for $-(t - t_{\min}) = 0.3 \text{ GeV}^2/c^2 - 0.5 \text{ GeV}^2/c^2$ | 136 |
| B.5 | SDME timeline plot for $-(t - t_{\min}) = 0.5 \text{ GeV}^2/c^2 - 0.7 \text{ GeV}^2/c^2$ | 137 |
| B.6 | SDME corner plot for $-(t - t_{\min}) = 0.5 \text{ GeV}^2/c^2 - 0.7 \text{ GeV}^2/c^2$ | 138 |
| B.7 | SDME timeline plot for $-(t - t_{\min}) = 0.7 \text{ GeV}^2/c^2 - 0.9 \text{ GeV}^2/c^2$ | 139 |
| B.8 | SDME corner plot for $-(t - t_{\min}) = 0.7 \text{ GeV}^2/c^2 - 0.9 \text{ GeV}^2/c^2$ | 140 |
| B.9 | SDME timeline plot for $-(t - t_{\min}) = 0.9 \text{ GeV}^2/c^2 - 1.1 \text{ GeV}^2/c^2$ | 141 |
| B.10 | SDME corner plot for $-(t - t_{\min}) = 0.9 \text{ GeV}^2/c^2 - 1.1 \text{ GeV}^2/c^2$ | 142 |
| B.11 | SDME timeline plot for $-(t - t_{\min}) = 1.1 \text{ GeV}^2/c^2 - 1.3 \text{ GeV}^2/c^2$ | 143 |
| B.12 | SDME corner plot for $-(t - t_{\min}) = 1.1 \text{ GeV}^2/c^2 - 1.3 \text{ GeV}^2/c^2$ | 144 |
| B.13 | SDME timeline plot for $-(t - t_{\min}) = 1.3 \text{ GeV}^2/c^2 - 1.6 \text{ GeV}^2/c^2$ | 145 |
| B.14 | SDME corner plot for $-(t - t_{\min}) = 1.3 \text{ GeV}^2/c^2 - 1.6 \text{ GeV}^2/c^2$ | 146 |
| B.15 | SDME timeline plot for $-(t - t_{\min}) = 1.6 \text{ GeV}^2/c^2 - 2.0 \text{ GeV}^2/c^2$ | 147 |
| B.16 | SDME corner plot for $-(t - t_{\min}) = 1.6 \text{ GeV}^2/c^2 - 2.0 \text{ GeV}^2/c^2$ | 148 |
| B.17 | Resulting fits from MCMC for $-(t - t_{\min}) = 0 \text{ GeV}^2/c^2 - 0.3 \text{ GeV}^2/c^2$ | 149 |
| B.18 | Resulting fits from MCMC for $-(t - t_{\min}) = 0.3 \text{ GeV}^2/c^2 - 0.5 \text{ GeV}^2/c^2$ | 149 |
| B.19 | Resulting fits from MCMC for $-(t - t_{\min}) = 0.5 \text{ GeV}^2/c^2 - 0.7 \text{ GeV}^2/c^2$ | 149 |
| B.20 | Resulting fits from MCMC for $-(t - t_{\min}) = 0.7 \text{ GeV}^2/c^2 - 0.9 \text{ GeV}^2/c^2$ | 150 |
| B.21 | Resulting fits from MCMC for $-(t - t_{\min}) = 0.9 \text{ GeV}^2/c^2 - 1.1 \text{ GeV}^2/c^2$ | 150 |
| B.22 | Resulting fits from MCMC for $-(t - t_{\min}) = 1.1 \text{ GeV}^2/c^2 - 1.3 \text{ GeV}^2/c^2$ | 150 |
| B.23 | Resulting fits from MCMC for $-(t - t_{\min}) = 1.3 \text{ GeV}^2/c^2 - 1.6 \text{ GeV}^2/c^2$ | 151 |
| B.24 | Resulting fits from MCMC for $-(t - t_{\min}) = 1.6 \text{ GeV}^2/c^2 - 2.0 \text{ GeV}^2/c^2$ | 151 |
| C.1 | Systematic study CL cut (setups 7-10) for Σ | 152 |
| C.2 | Systematic study vertex cut (setups 11-14) for Σ | 153 |
| C.3 | Systematic study K^+ ΔT PID cut (setups 15-18) for Σ | 153 |
| C.4 | Systematic study K^- ΔT PID cut (setups 19-22) for Σ | 153 |
| C.5 | Systematic study p ΔT PID cut (setups 23-26) for Σ | 154 |
| C.6 | Systematic study background shape for Σ | 154 |
| C.7 | Systematic study polarisation plane offset for Σ | 154 |
| C.8 | SDME sideband study for pK^- inv. mass $1.46 \text{ GeV}/c^2 - 1.48 \text{ GeV}/c^2$ | 155 |
| C.9 | SDME sideband study for pK^- inv. mass $1.48 \text{ GeV}/c^2 - 1.50 \text{ GeV}/c^2$ | 156 |
| C.10 | SDME sideband study for pK^- inv. mass $1.50 \text{ GeV}/c^2 - 1.51 \text{ GeV}/c^2$ | 156 |

| | |
|---|-----|
| C.11 SDME sideband study for pK^- inv. mass $1.510\text{GeV}/c^2 - 1.515\text{GeV}/c^2$ | 157 |
| C.12 SDME sideband study for pK^- inv. mass $1.515\text{GeV}/c^2 - 1.520\text{GeV}/c^2$ | 157 |
| C.13 SDME sideband study for pK^- inv. mass $1.520\text{GeV}/c^2 - 1.525\text{GeV}/c^2$ | 158 |
| C.14 SDME sideband study for pK^- inv. mass $1.525\text{GeV}/c^2 - 1.530\text{GeV}/c^2$ | 158 |
| C.15 SDME sideband study for pK^- inv. mass $1.53\text{GeV}/c^2 - 1.54\text{GeV}/c^2$ | 159 |
| C.16 SDME sideband study for pK^- inv. mass $1.54\text{GeV}/c^2 - 1.56\text{GeV}/c^2$ | 159 |
| C.17 SDME sideband study for pK^- inv. mass $1.56\text{GeV}/c^2 - 1.58\text{GeV}/c^2$ | 160 |
| C.18 Example sFit for thrown MC with an artificial res. in SDME result valid. study | 161 |
| C.19 Example SDME fits for thrown MC with artificial res. in SDME result valid. study | 161 |
| C.20 Validation results for thrown data with artificial resolution ρ_{11}^0 | 162 |
| C.21 Validation results for thrown data with artificial resolution ρ_{31}^0 | 162 |
| C.22 Validation results for thrown data with artificial resolution ρ_{3-1}^0 | 162 |
| C.23 Validation results for thrown data with artificial resolution ρ_{11}^1 | 163 |
| C.24 Validation results for thrown data with artificial resolution ρ_{33}^1 | 163 |
| C.25 Validation results for thrown data with artificial resolution ρ_{31}^1 | 163 |
| C.26 Validation results for thrown data with artificial resolution ρ_{3-1}^1 | 164 |
| C.27 Validation results for thrown data with artificial resolution ρ_{31}^2 | 164 |
| C.28 Validation results for thrown data with artificial resolution ρ_{3-1}^2 | 164 |
| C.29 Comparison between real MC signal and signal extracted via sFit for thrown data with artificial resolution | 165 |
| C.30 Example sFit for thrown MC with an artificial acc. in SDME result valid. study | 166 |
| C.31 Example SDME fits for thrown MC with artificial acceptance in SDME result validation study | 167 |
| C.32 Validation for thrown data with artificial acceptance ρ_{11}^0 | 167 |
| C.33 Validation for thrown data with artificial acceptance ρ_{31}^0 | 167 |
| C.34 Validation for thrown data with artificial acceptance ρ_{3-1}^0 | 168 |
| C.35 Validation for thrown data with artificial acceptance ρ_{11}^1 | 168 |
| C.36 Validation for thrown data with artificial acceptance ρ_{33}^1 | 168 |
| C.37 Validation for thrown data with artificial acceptance ρ_{31}^1 | 169 |
| C.38 Validation for thrown data with artificial acceptance ρ_{3-1}^1 | 169 |
| C.39 Validation for thrown data with artificial acceptance ρ_{31}^2 | 169 |
| C.40 Validation for thrown data with artificial acceptance ρ_{3-1}^2 | 170 |
| C.41 Comparison between real MC signal and signal extracted via sFit for thrown data with artificial acceptance | 171 |
| C.42 Validation for full simulation without background ρ_{11}^0 | 172 |
| C.43 Validation for full simulation without background ρ_{31}^0 | 172 |
| C.44 Validation for full simulation without background ρ_{3-1}^0 | 173 |
| C.45 Validation for full simulation without background ρ_{11}^1 | 173 |

| | | |
|------|--|-----|
| C.46 | Validation for full simulation without background ρ_{33}^1 | 173 |
| C.47 | Validation for full simulation without background ρ_{31}^1 | 174 |
| C.48 | Validation for full simulation without background ρ_{3-1}^1 | 174 |
| C.49 | Validation for full simulation without background ρ_{31}^2 | 174 |
| C.50 | Validation for full simulation without background ρ_{3-1}^2 | 175 |
| C.51 | Validation for full simulation with small background and no sFit ρ_{11}^0 | 176 |
| C.52 | Validation for full simulation with small background and no sFit ρ_{31}^0 | 176 |
| C.53 | Validation for full simulation with small background and no sFit ρ_{3-1}^0 | 177 |
| C.54 | Validation for full simulation with small background and no sFit ρ_{11}^1 | 177 |
| C.55 | Validation for full simulation with small background and no sFit ρ_{33}^1 | 177 |
| C.56 | Validation for full simulation with small background and no sFit ρ_{31}^1 | 178 |
| C.57 | Validation for full simulation with small background and no sFit ρ_{3-1}^1 | 178 |
| C.58 | Validation for full simulation with small background and no sFit ρ_{31}^2 | 178 |
| C.59 | Validation for full simulation with small background and no sFit ρ_{3-1}^2 | 179 |
| C.60 | Results for SDMEs for the baseline setting and six variations (setups 1-6) . . . | 180 |
| C.61 | Barlow test results for invariant mass cut studies for SDMEs | 181 |
| C.62 | Results for SDMEs for the baseline setting and four variations (setups 7-10) . . | 182 |
| C.63 | Barlow test results for CL cut studies for SDMEs | 183 |
| C.64 | Results for SDMEs for the baseline setting and four variations (setups 11-14) . | 184 |
| C.65 | Barlow test results for vertex cut studies for SDMEs | 185 |
| C.66 | Results for SDMEs for the baseline setting and four variations (setups 15-18) . | 186 |
| C.67 | Barlow test results for K^+ PID cut studies for SDMEs | 187 |
| C.68 | Results for SDMEs for the baseline setting and four variations (setups 19-22) . | 188 |
| C.69 | Barlow test results for K^- PID cut studies for SDMEs | 189 |
| C.70 | Results for SDMEs for the baseline setting and four variations (setups 23-26) . | 190 |
| C.71 | Barlow test results for p PID cut studies for SDMEs | 191 |
| C.72 | Results for SDMEs for the baseline setting and three variations of bkg. shape . | 192 |
| C.73 | Barlow test results for background shape studies for SDMEs | 193 |
| C.74 | Results for SDMEs for the baseline setting and two variations of the polarisation plane angle | 194 |
| C.75 | Barlow test results for polarisation plane angle studies for SDMEs | 195 |
| E.1 | Van Hove plots for MC and real data | 204 |
| E.2 | Coordinate systems used to calculate the cut limits | 205 |
| E.3 | Coordinate system used to evaluate cut limits | 207 |
| E.4 | Van Hove plots for signal and background for all four tested scenarios | 208 |
| E.5 | Dalitz plots for all four discussed scenarios | 209 |
| E.6 | $\cos(\theta_{GJ})$ distribution for the K^- for all four studied scenarios | 210 |
| E.7 | Means and widths of the pull distributions for all spherical harmonic moments . | 212 |

E.8 Mean value and width of the four non-zero moments 213

Acknowledgements

Working towards a PhD is a long endeavour that requires help from many sides. I want to take this moment to thank the people and organisations that made this work possible.

First of all I would like to thank the Scottish Universities Physics Alliance and the School of Physics and Astronomy for funding my research. Without funding none of this would have been possible.

I would like to thank Dave Ireland for giving me the opportunity to conduct my research in the Nuclear and Hadron Physics group. I am very grateful to him and Ken Livingston for their supervision and guidance over the past years. They were always happy to help whenever I got stuck or needed some advice. I would also like to thank Derek Glazier and Bryan McKinnon for their continuous support throughout my PhD.

The whole Nuclear and Hadron Physics group deserves my thanks as they made my PhD a wonderful experience. I enjoyed coming to work every day.

I would also like to thank the GlueX collaboration, without which this work would not have been possible. Running such a big experiment is an outstanding team effort and everyone was always providing helpful comments and advice when needed.

I am also very thankful for the many discussions and helpful comments by Vincent Mathieu, who helped me enormously to make sense out of my results.

Last but not least I want to thank my girlfriend, my family and friends. There is a life outside research and they are always there for me when I need them.

Declaration

The work in this thesis is based on research carried out at the Nuclear and Hadron Physics Group, School of Physics & Astronomy, University of Glasgow, UK. No part of this thesis has been submitted elsewhere for any other degree or qualification and it is all my own work unless referenced to the contrary in the text.

©Peter Pauli 2020.

The copyright of this thesis rests with the author. No quotation from it is permitted without full acknowledgement.

Chapter 1

Introduction

This thesis describes the study of the reaction $\gamma p \rightarrow K^+ \Lambda(1520) \rightarrow K^+ K^- p$. Some of the first data taken with the GlueX experiment, located at Jefferson Laboratory, were analysed for this purpose. GlueX's main objective is the search for exotic hybrid mesons, which will aid our understanding of quark confinement. This work presents the first measurement of polarised spin-density matrix elements for the reaction and the first measurement of unpolarised spin-density matrix elements for the reaction in the photon beam energy range 8.2 GeV-8.8 GeV. It is one of several measurements carried out during the early stage of GlueX to study the various reaction mechanisms in this previously unexplored energy regime. It will also help in understanding the performance of the GlueX detector setup and photon beam line which is crucial to accomplish its main mission in the near future.

Quantum Chromo Dynamics (QCD) is the established quantum field theory describing the strong force within the Standard Model (SM) of particle physics. The strong force is, alongside gravity, electromagnetism and the weak force, one of four fundamental forces in nature. Like every force within the SM it is mediated by bosons (particles with integer spin). In the case of the strong force these bosons are called *gluons*. The other group of particles within the SM that are directly interacting through the strong force are called *quarks*. They are fermions (particles with half-integer spin) and come in three generations. The lightest quarks are called *up* and *down*. The up-quark carries an electric charge of $+2/3$ and the down-quark $-1/3$. The two heavier versions of the up- and down-quarks are called *charm* and *top*, also with charge $+2/3$, and *strange* and *bottom*, with charge $-1/3$, respectively. Due to their electric charge quarks can also interact electromagnetically, a force mediated through *photons*. Figure 1.1 visualises the complete SM. In addition to quarks and gluons it contains *leptons*, which do not interact through the strong force. These are also fermions and come in three generations as well. The *electron* and its two heavier partners, *muon* and *tau*, have electric charge -1 . The *neutrinos*, their almost massless counterparts, are chargeless and can therefore only interact through the weak force,

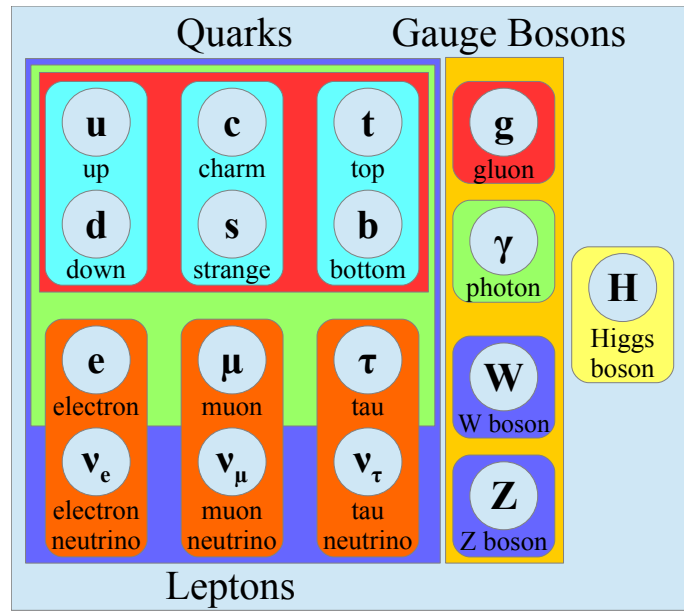


Figure 1.1: The standard model of particle physics. Taken from [1].

carried by the W^\pm and Z^0 boson. The last part of the SM is the *Higgs boson*. It can be seen as manifestation of the Higgs field, which plays an important role in mass generation of the fundamental particles in the SM.

Electromagnetic interactions are mediated by photons which couple to the electric charge. Therefore all electrically charged particles can interact electromagnetically. The counterpart of the electric charge in the strong force is called *colour charge*. Instead of positive and negative charge it comes in three colours (commonly *red*, *green* and *blue*) and three anti-colours (*anti-red*, *anti-green* and *anti-blue*). A crucial difference compared to electromagnetism is that gluons carry colour charge themselves. This means that they can self-interact which has very important consequences, as it directly affects the strong coupling constant α_s .

Two extremely important properties of QCD are *confinement* and *asymptotic freedom*. Confinement describes the empirical fact that all objects in nature are observed to be colour neutral. This means quarks, which carry a colour charge, are never observed on their own. This is related to the fact that the strong coupling constant α_s is large for large distances between the quarks (see Figure 1.2). If two quarks were to be pulled apart the energy in the binding of the two increases to a point where a new $q\bar{q}$ pair is created from the vacuum. Asymptotic freedom on the other hand describes the fact that at very small distances α_s becomes small, which means that the quarks appear almost free when really close to each other. It was discovered in 1973 by Gross, Politzer and Wilczek [3–6] and they were awarded the Nobel Prize in Physics for it in 2004. If probed at small distances (i.e. high energies) α_s is small enough to use perturbation theory to make calculations. The real world exists at much smaller energies where α_s is large. In this case perturbation theory cannot be applied and other ways have to be found to calculate

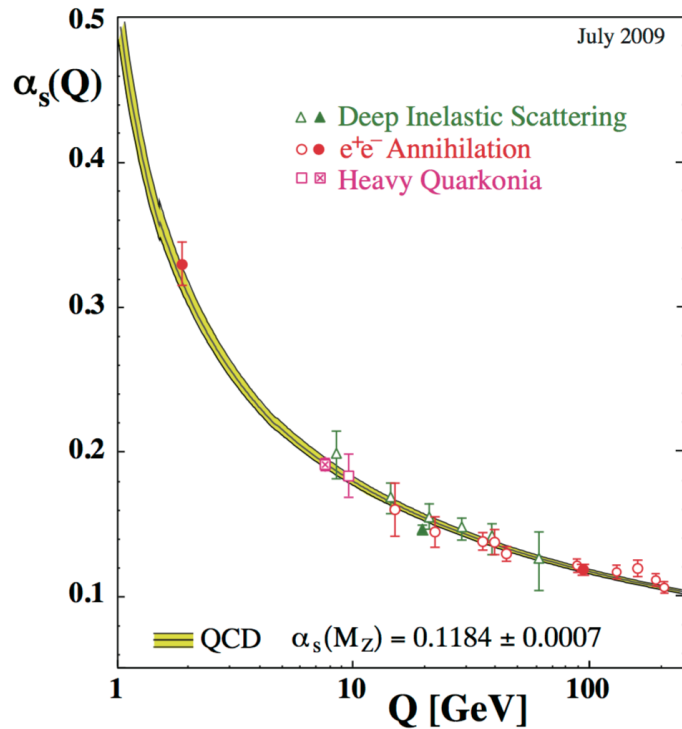


Figure 1.2: The running coupling constant α_s . Taken from [2].

properties arising from QCD. In general, these are model-dependent calculations not starting from first principles and need experimental input.

As stated before all objects in nature are observed to be colour neutral. Neutrality can be achieved by combining a colour with its anti-colour or by combining all three colours together. Therefore quarks and gluons always appear in bound states of two or more particles. Bound states consisting of an even number of quarks are called *mesons*, of an odd number of quarks *baryons*. The proton, which was discovered by Rutherford in 1919 (reprint [7]) has quark content *uud*. The neutron discovered by Chadwick in 1932 [8, 9] has quark content *udd*. These two baryons make up the atomic nucleus and together with electrons they constitute the vast majority of visible matter. With the advent of particle accelerators in the 1950s, many $q\bar{q}$, qqq and $\bar{q}\bar{q}\bar{q}$ states have been discovered. In the early 1960s Gell-Mann and Zweig proposed to use $SU(3)$ symmetry to organise mesons and baryons consisting of u, d and s quarks into multiplets [10–13] (the other quarks were not discovered at the time). Already when developing his quark model Gell-Mann realised that states like $qq\bar{q}\bar{q}$ (*tetraquarks*) or $qqq\bar{q}\bar{q}$ (*pentaquarks*) are allowed by QCD [12] even though they were not discovered at the time. Since the gluon carries a colour charge one could also imagine states that consist purely of gluons, so called *glueballs*, or states where the gluons do not just facilitate the binding of the quarks but also contribute to the overall quantum numbers of the bound state, e.g. by adding units of angular momentum. These states are called *hybrids*. States that are not simply two or three quark states are often referred to as exotic. So far, no definitive proof of such a state has been achieved, although they are a direct

consequence of QCD. Some evidence has been gathered, but definitively finding and identifying one of those states would be an important step towards establishing QCD as the theory of strong interaction.

So far, most evidence for non-conventional states comes from charmonium ($c\bar{c}$) and bottomonium ($b\bar{b}$) and B -meson decays. The first such candidate, the so called $X(3872)$, was discovered in 2003 by Belle [14]. Since then, many more states have been found in these decays that seem to have non- $q\bar{q}$ properties. For reviews of these states see Chapter 91 in the Particle Data Groups Review of Particle Physics [15], and [16–19]. What most of these states have in common is that they do not fit into the expected $c\bar{c}$ and $b\bar{b}$ mass spectra or that they are close to important decay thresholds. The latter could indicate some molecular structure. The $X(3872)$ for example lies less than 200 keV below the $D^0\bar{D}^{*0}$ threshold and is often identified with a bound state of these two mesons [20, 21]. A definitive proof for an exotic state is oftentimes not unambiguous. The exception to that is the discovery of a hybrid with quantum numbers not accessible to simple $q\bar{q}$ states. Usually mesons are classified by their J^{PC} quantum number. Normal mesons are two-body states ($q\bar{q}$) and as such their parity and charge conjugation quantum numbers have to follow certain rules (Chapter 15.2 [15]).

$$P = (-1)^{l+1} \quad (1.1)$$

$$C = (-1)^{l+s} \quad (1.2)$$

with s being the total spin of the quarks (0 or 1) and l being the orbital angular momentum between them. Therefore, only certain J^{PC} combinations are allowed, e.g. $J^{PC} = 0^{-+}$ for pseudoscalars and $J^{PC} = 1^{--}$ for vectors. The discovery of a state with quantum numbers that do not obey these criteria, e.g. a meson with $J^{PC} = 1^{-+}$, would be proof of an exotic nature. Therefore, these exotic quantum numbers are considered a *smoking gun*.

In recent years several observations of $J^{PC} = 1^{-+}$ states have been made (e.g. [22–26]) but more data is desirable to make a definitive statement about their nature. The GlueX experiment, on whose data this thesis is based, is dedicated to the search of exotic hybrid mesons. It was designed and built for this specific purpose and has as such certain distinct features that make it unique. Since exotic states are expected to decay to both neutral and charged final states, the GlueX detector is equipped to measure these final state particles with good energy and momentum resolution. This will enable the exclusive analysis of the same resonance decaying into multiple different final states. This would greatly increase confidence in a potential discovery. To produce the exotic states, GlueX uses a high energy linearly polarised photon beam. This has multiple advantages over experiments that have been carried out so far. The high energy means it is possible to produce the exotic meson in a t -channel process without intermediate baryon resonance. This will make the consecutive determination of its quantum numbers easier. In

contrast to e^+e^- annihilation, which can only produce $J^{PC} = 1^{--}$ resonances, photoproduction is capable of producing resonances with various different quantum numbers. This is critical in order to produce exotic mesons in large enough quantities to analyse them. The linear polarisation of the photon beam aids the identification of the exchange mechanism, a critical step in the analyses that will be carried out. To achieve a high energy photon beam, a high energy electron beam is necessary, which is available at Jefferson Laboratory in Virginia, USA.

One of the biggest problems in the search for exotic states is that they are subject to enormous backgrounds. Many known non-exotic mesons exist in the mass-range relevant for the exotic searches and the reaction channels are dominated by them. That makes a simple *bump hunt*, a search for peaks in an invariant mass spectrum, impossible. In addition, the determination of quantum numbers requires a partial wave analysis. That means the angular distribution of final state particles needs to be carefully analysed. In order to correctly perform the partial wave analysis and disentangle contributions from various resonance states, it is important to have an excellent understanding of the production processes involved. Therefore, a crucial first step in GlueX's scientific program is to establish the dominant production mechanisms in its energy range. This thesis works towards that goal. The $\Lambda(1520)$ is a baryon resonance with quark content uds which can decay into a proton and a K^- . It shows up strongly in many final states containing a proton and K^- , final states expected to contain exotic hybrids. Therefore, a good understanding of its production is desirable. So far, no data in the GlueX energy range exists which makes this work very important to constrain theoretical models.

The remainder of the thesis is structured as follows. Chapter 2 lays the theoretical foundation and introduces spin-density matrix elements, polarisation observables, and cross-sections. Chapter 3 contains a brief summary of the current data situation as well as the current status of the theoretical description of the reaction of interest. Chapter 4 contains a description of the GlueX experiment. It gives a summary of the accelerator and beam line and a detailed description of all detector systems relevant for this work. Chapter 5 describes the event selection. The extraction of the observables is reported in Chapter 6 in great detail. Finally, the results are discussed in Chapter 7. Appendices A to C contain additional information and plots regarding the observable extraction. Appendix D lists all numerical results and Appendix E contains a summary of a paper on longitudinal phase space analysis, which was written alongside this work.

Chapter 2

$K^+ \Lambda(1520)$ photoproduction formalism

In the following the theoretical framework describing the photoproduction of the $\Lambda(1520)$ together with a K^+ is laid out. The equations necessary to extract observables from the data are presented, and their interpretation discussed.

The $\Lambda(1520)$, is a hyperon with quark content uds and quantum numbers $J^P = \frac{3}{2}^-$ [27]. To produce it on a proton in photoproduction, which conserves strangeness and charge [28], it has to be produced together with a K^+ ($u\bar{s}$). The three main production mechanisms are pictured in Figure 2.1. In s-channel production (Figure 2.1a) an intermediate nucleon resonance decays

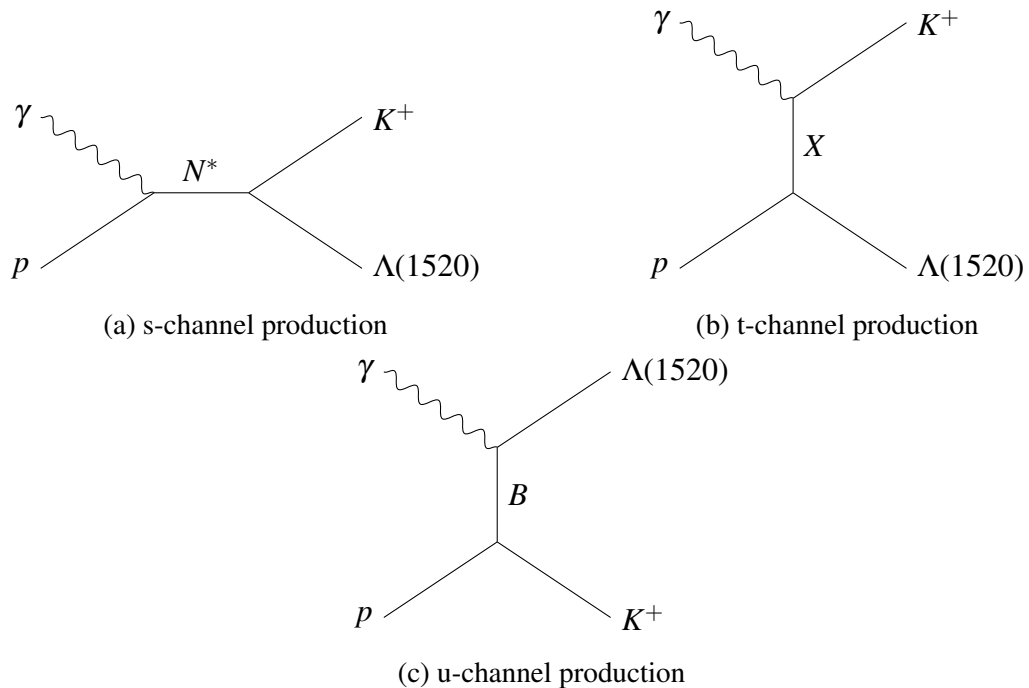


Figure 2.1: Three production mechanisms for $\Lambda(1520)$ photoproduction. (a) The s-channel production proceeds via a nucleon resonance (N^*). (b) In t-channel production a virtual meson (X) is exchanged. (c) In u-channel production a virtual baryon (B) is exchanged.

into a K^+ and a $\Lambda(1520)$. At $E_\gamma = 8.2\text{ GeV} - 8.8\text{ GeV}$ the intermediate state, however, would have a mass of about 5 GeV and there are no known states with such high masses. Although not impossible and certainly important at lower photon beam energies, this production mode seems unlikely for this work and is probably not dominant compared with the others. The t-channel production mechanism proceeds via the exchange of a virtual kaon (Figure 2.1b). This mechanism is found at a wide range of beam photon energies. At very high energies and small scattering angles the exchange between the incoming photon and target proton dominantly proceeds via a so called Pomeron, a hypothetical particle without electric or colour charge. In those reactions, the photon would diffractively dissociate into mesons and the proton would stay intact. The production of hyperons, such as the $\Lambda(1520)$, requires an exchange of strangeness. Therefore, it is not possible to produce the reaction of interest via this mechanism. The exchange of a virtual baryon, which would commonly be identified as a u -channel, is also possible (Figure 2.1c). Although the production mechanisms via t- and u-channel exchange are expected to dominate, the exact mechanism is not clear. Their relative strength as well as the types of exchanged particles is unknown. No data in the GlueX energy range exists so far for this reaction and, therefore, it is essential to perform measurements in order to improve the current understanding of the reaction.

The $\Lambda(1520)$ decays via the strong interaction and its most important decay modes are $N\bar{K}$ (45%), $\Sigma\pi$ (42%) and $\Lambda\pi\pi$ (10%) [15]. Due to isospin symmetry the $N\bar{K}$ decay mode can be assumed to evenly split into pK^- and $n\bar{K}^0$ with about 22.5% branching fraction each. The $n\bar{K}^0$ decay mode is challenging to measure in GlueX, which does not have a dedicated neutron detector. The $\Sigma\pi$ decay mode has three possible isospin combinations each having a branching ratio of about 14%. The Σ^0 baryon decays to the ground state Λ and a photon, while charged Σ decay weakly to a nucleon and a pion. The additional decays complicate the reconstruction and analysis, leaving the pK^- decay mode as the best suited to study this reaction in GlueX. It has a relatively large branching ratio and contains only three charged particles in the final state. Therefore, the reaction of interest for this work is

$$\vec{\gamma}p \longrightarrow K^+\Lambda(1520) \longrightarrow K^+K^-p$$

2.1 Spin-density matrix elements

A density matrix can be used to represent the spin polarisation of a particle, it can be used to describe pure and mixed quantum mechanical states. For a finite-dimensional system with pure states $|\psi\rangle$ one can write the density matrix as

$$\rho = \sum_i p_i |\psi_i\rangle\langle\psi_i| \quad (2.1)$$

with p_i being (positive) eigenvalues of the density matrix and $\sum_i p_i = 1$. A density matrix has the important properties of being Hermitian and having a trace of one [29]. Following Schilling [30] the density matrix for a linearly polarised photon, such as in GlueX, can be constructed from its wave function in helicity basis as

$$|\gamma\rangle = -\frac{1}{\sqrt{2}} (e^{-i\Phi}|\lambda_\gamma = +1\rangle - e^{i\Phi}|\lambda_\gamma = -1\rangle) \quad (2.2)$$

where λ_γ denotes the helicity of the photon and Φ denotes the angle between the polarisation vector and the production plane. The production plane is defined as the x-z plane in which incoming γp and outgoing $K^+\Lambda(1520)$ lie in the overall centre-of-mass (CM) frame, with the z-axis pointing in photon beam direction (see Figure 2.2). The photon density matrix can then be written as a linear combination of the 2×2 unit matrix I and the vector of the three Pauli matrices $\vec{\sigma}$, which form a complete set in the space of 2×2 hermitian matrices [30]

$$\rho(\gamma) = \frac{1}{2}I + \frac{1}{2}\vec{P}_\gamma \cdot \vec{\sigma} \quad (2.3)$$

with $\vec{P}_\gamma = P_\gamma(-\cos 2\Phi, -\sin 2\Phi, 0)$ and P_γ being the degree of polarisation of the photon.

The spin-density matrix for the $\Lambda(1520)$ in the reaction of interest is given by

$$\rho(\Lambda) = T\rho(\gamma)T^* \quad (2.4)$$

where T denotes the production amplitude. Using Eq. (2.3) and Eq. (2.4) we can write

$$\rho(\Lambda) = \rho^0 + \sum_{i=1}^3 P_\gamma^i \rho^i \quad (2.5)$$

with [30]

$$\rho^0 = \frac{1}{2}TIT^* \quad (2.6)$$

$$\rho^i = \frac{1}{2}T\sigma^iT^* \quad (2.7)$$

This nicely shows the decomposition of the $\Lambda(1520)$ spin-density matrix depending on the photon polarisation. Since $P_\gamma^3 = 0$ for photons with zero circular polarisation, we are left with three matrices measurable at GlueX.

To investigate the decay of the $\Lambda(1520)$, it is convenient to study it in a specific frame, the so called Gottfried-Jackson (GJ) or t -channel helicity frame [31]. The \hat{z} -axis is defined as opposite to the incoming target proton vector in the $\Lambda(1520)$ rest frame. The \hat{y} -axis is defined as normal

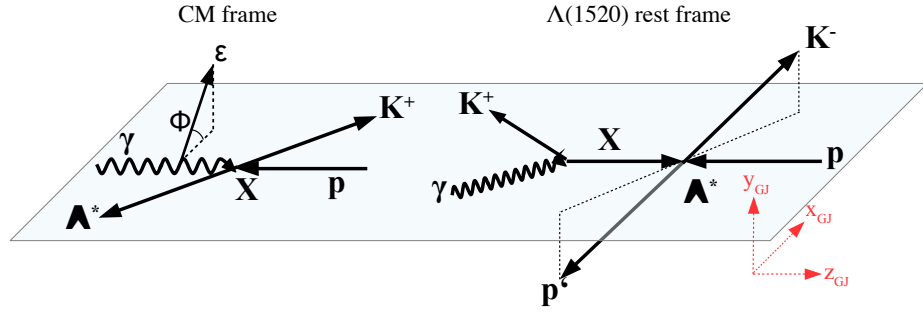


Figure 2.2: Definition of the Gottfried-Jackson frame for the reaction of interest. The X denotes the exchanged particle in a t -channel exchange (see Figure 2.1b).

to the production plane and the \hat{x} -axis completes the right-handed coordinate system

$$\hat{z} = \frac{-\vec{p}_p}{|-\vec{p}_p|} \quad \hat{y} = \frac{\vec{p}_\gamma \times \vec{p}_{K^+}}{|\vec{p}_\gamma \times \vec{p}_{K^+}|} \quad \hat{x} = \hat{y} \times \hat{z} \quad (2.8)$$

An illustration of this frame can be found in Figure 2.2. The usefulness of this frame becomes apparent if one studies the helicities of the involved particles. The helicity λ of a particle is defined as the projection of its spin on its momentum vector [32].

$$\lambda = \frac{\vec{s} \cdot \vec{p}}{|\vec{p}|} \quad (2.9)$$

Figure 2.2 shows that the exchanged particle X is collinear with the target proton in the GJ frame. Therefore any angular momentum between the two particles has a z -component of zero and the z -component of the produced baryon, the $\Lambda(1520)$ in this case, is given by $\lambda_p + \lambda_X$. This means that measuring the angular distribution of the decay products of the $\Lambda(1520)$ provides information on the spin of the exchanged particle X . For that reason we study the reaction in the GJ frame.

Using helicity amplitudes and Eq. (2.4) we can explicitly write out the three matrices as

$$\rho_{\lambda_\Lambda \lambda'_\Lambda}^0 = \frac{1}{2N} \sum_{\lambda_\gamma \lambda_p} T_{\lambda_\gamma \lambda_p \lambda_\Lambda} T_{\lambda_\gamma \lambda_p \lambda'_\Lambda}^* \quad (2.10)$$

$$\rho_{\lambda_\Lambda \lambda'_\Lambda}^1 = \frac{1}{2N} \sum_{\lambda_\gamma \lambda_p} T_{-\lambda_\gamma \lambda_p \lambda_\Lambda} T_{\lambda_\gamma \lambda_p \lambda'_\Lambda}^* \quad (2.11)$$

$$\rho_{\lambda_\Lambda \lambda'_\Lambda}^2 = \frac{i}{2N} \sum_{\lambda_\gamma \lambda_p} \lambda_\gamma T_{-\lambda_\gamma \lambda_p \lambda_\Lambda} T_{\lambda_\gamma \lambda_p \lambda'_\Lambda}^* \quad (2.12)$$

with $2N = \sum_{\lambda_\gamma \lambda_p \lambda_\Lambda} |T_{\lambda_\gamma \lambda_p \lambda_\Lambda}|^2$ so that $\text{Tr} \rho^0 = 1$. From parity it follows that [33]

$$T_{-\lambda_\gamma -\lambda_p -\lambda_\Lambda} = (-1)^{\lambda_p - \lambda_\Lambda} T_{\lambda_\gamma \lambda_p \lambda_\Lambda} \quad (2.13)$$

And therefore,

$$\rho_{\lambda_\Lambda \lambda'_\Lambda}^0 = (-1)^{\lambda_\Lambda - \lambda'_\Lambda} \rho_{-\lambda_\Lambda - \lambda'_\Lambda}^0 \quad (2.14)$$

$$\rho_{\lambda_\Lambda \lambda'_\Lambda}^1 = (-1)^{\lambda_\Lambda - \lambda'_\Lambda} \rho_{-\lambda_\Lambda - \lambda'_\Lambda}^1 \quad (2.15)$$

$$\rho_{\lambda_\Lambda \lambda'_\Lambda}^2 = -(-1)^{\lambda_\Lambda - \lambda'_\Lambda} \rho_{-\lambda_\Lambda - \lambda'_\Lambda}^2 \quad (2.16)$$

This definition of the spin-density matrix is useful to learn about the production amplitudes T , when $\rho(\Lambda)$ is known.

In order to determine $\rho(\Lambda)$ one must measure the angular distribution of the $\Lambda(1520)$ decay. This distribution can be described in terms of the decay amplitudes M . Following Schilling [30] and Chung [34] one can write the decay angular distribution as [35]

$$\frac{dN}{d\cos\theta d\phi} = W(\theta, \phi) = M\rho(\Lambda)M^* \quad (2.17)$$

$$= \frac{2J+1}{8\pi} \sum_{\lambda''} D_{\lambda_\Lambda \lambda''}^{(3/2)*}(\phi, \theta, -\phi) \rho_{\lambda_\Lambda \lambda'_\Lambda} D_{\lambda'_\Lambda \lambda''}^{(3/2)}(\phi, \theta, -\phi) \quad (2.18)$$

with $\lambda'' = \pm\frac{1}{2}$ being the difference of the two helicities of the decay products and $D^{(3/2)}$ being the Wigner-rotation matrix as defined in [36] which is given by

$$D_{\lambda_\Lambda \frac{1}{2}}^{(3/2)} = \left(-\sqrt{3} \cos^2 \frac{\theta}{2} \sin \frac{\theta}{2} e^{-i\phi}, \cos^3 \frac{\theta}{2} - 2 \cos \frac{\theta}{2} \sin^2 \frac{\theta}{2}, \right. \\ \left. \left[2 \cos^2 \frac{\theta}{2} \sin \frac{\theta}{2} - \sin^3 \frac{\theta}{2} \right] e^{i\phi}, \sqrt{3} \cos \frac{\theta}{2} \sin^2 \frac{\theta}{2} e^{2i\phi} \right) \quad (2.19)$$

$$D_{\lambda_\Lambda -\frac{1}{2}}^{(3/2)} = \left(\sqrt{3} \cos \frac{\theta}{2} \sin^2 \frac{\theta}{2} e^{-2i\phi}, \left[\sin^3 \frac{\theta}{2} - 2 \cos^2 \frac{\theta}{2} \sin \frac{\theta}{2} \right] e^{-i\phi}, \right. \\ \left. - \left[2 \cos \frac{\theta}{2} \sin^2 \frac{\theta}{2} - \cos^3 \frac{\theta}{2} \right], \sqrt{3} \sin \frac{\theta}{2} \cos^2 \frac{\theta}{2} e^{i\phi} \right) \quad (2.20)$$

Using Eq. (2.5) and Eq. (2.17) one can decompose the angular distribution as

$$W(\theta, \phi, \Phi) = W^0(\theta, \phi) + \sum_{i=1}^3 P_\gamma^i(\Phi) W^i(\theta, \phi) \quad (2.21)$$

The angles θ and ϕ are evaluated as the angles of the K^- in the GJ frame of the decay. Φ is the direction of the polarisation vector with respect to the production plane (Figure 2.2).

Since the $\Lambda(1520)$ is a spin-3/2 state, its spin-density matrix is a 4×4 matrix of complex numbers, which would mean the matrix is given by 32 real numbers. Since a spin-density matrix is

Hermitian, by definition one can reduce this number and write the matrix as

$$\rho = \begin{pmatrix} \rho_{33} & \rho_{31} & \rho_{3-1} & \rho_{3-3} \\ \rho_{13} & \rho_{11} & \rho_{1-1} & \rho_{1-3} \\ \rho_{-13} & \rho_{-11} & \rho_{-1-1} & \rho_{-1-3} \\ \rho_{-33} & \rho_{-31} & \rho_{-3-1} & \rho_{-3-3} \end{pmatrix} = \begin{pmatrix} \rho_{33} & \rho_{31} & \rho_{3-1} & \rho_{3-3} \\ \rho_{31}^* & \rho_{11} & \rho_{1-1} & \rho_{1-3} \\ \rho_{3-1}^* & \rho_{1-1}^* & \rho_{-1-1} & \rho_{-1-3} \\ \rho_{3-3}^* & \rho_{1-3}^* & \rho_{-1-3}^* & \rho_{-3-3} \end{pmatrix} \quad (2.22)$$

The matrix elements are written as $\rho_{2\lambda_\Lambda, 2\lambda'_\Lambda}$ for simplicity, i.e. the matrix element $\rho_{\frac{1}{2}, \frac{1}{2}}$ is written as ρ_{11} .

Making use of the parity relations defined in Eqs. (2.14), (2.15) and (2.16) it follows that

$$\text{Re}\rho_{1-1} = \text{Re}\rho_{3-3} = 0, \text{ for } i=0,1 \quad (2.23)$$

$$\text{Im}\rho_{1-1} = \text{Im}\rho_{3-3} = 0, \text{ for } i=2 \quad (2.24)$$

This results in the three accessible matrices

$$\rho^0 = \begin{pmatrix} \rho_{33}^0 & \text{Re}\rho_{31}^0 + i\text{Im}\rho_{31}^0 & \text{Re}\rho_{3-1}^0 + i\text{Im}\rho_{3-1}^0 & i\text{Im}\rho_{3-3}^0 \\ \text{Re}\rho_{31}^0 - i\text{Im}\rho_{31}^0 & \rho_{11}^0 & i\text{Im}\rho_{1-1}^0 & \text{Re}\rho_{3-1}^0 - i\text{Im}\rho_{3-1}^0 \\ \text{Re}\rho_{3-1}^0 - i\text{Im}\rho_{3-1}^0 & -i\text{Im}\rho_{1-1}^0 & \rho_{11}^0 & -\text{Re}\rho_{31}^0 + i\text{Im}\rho_{31}^0 \\ -i\text{Im}\rho_{3-3}^0 & \text{Re}\rho_{3-1}^0 + i\text{Im}\rho_{3-1}^0 & -\text{Re}\rho_{31}^0 - i\text{Im}\rho_{31}^0 & \rho_{33}^0 \end{pmatrix} \quad (2.25)$$

$$\rho^1 = \begin{pmatrix} \rho_{33}^1 & \text{Re}\rho_{31}^1 + i\text{Im}\rho_{31}^1 & \text{Re}\rho_{3-1}^1 + i\text{Im}\rho_{3-1}^1 & i\text{Im}\rho_{3-3}^1 \\ \text{Re}\rho_{31}^1 - i\text{Im}\rho_{31}^1 & \rho_{11}^1 & i\text{Im}\rho_{1-1}^1 & \text{Re}\rho_{3-1}^1 - i\text{Im}\rho_{3-1}^1 \\ \text{Re}\rho_{3-1}^1 - i\text{Im}\rho_{3-1}^1 & -i\text{Im}\rho_{1-1}^1 & \rho_{11}^1 & -\text{Re}\rho_{31}^1 + i\text{Im}\rho_{31}^1 \\ -i\text{Im}\rho_{3-3}^1 & \text{Re}\rho_{3-1}^1 + i\text{Im}\rho_{3-1}^1 & -\text{Re}\rho_{31}^1 - i\text{Im}\rho_{31}^1 & \rho_{33}^1 \end{pmatrix} \quad (2.26)$$

and

$$\rho^2 = \begin{pmatrix} \rho_{33}^2 & \text{Re}\rho_{31}^2 + i\text{Im}\rho_{31}^2 & \text{Re}\rho_{3-1}^2 + i\text{Im}\rho_{3-1}^2 & \text{Re}\rho_{3-3}^2 \\ \text{Re}\rho_{31}^2 - i\text{Im}\rho_{31}^2 & \rho_{11}^2 & \text{Re}\rho_{1-1}^2 & -\text{Re}\rho_{3-1}^2 + i\text{Im}\rho_{3-1}^2 \\ \text{Re}\rho_{3-1}^2 - i\text{Im}\rho_{3-1}^2 & \text{Re}\rho_{1-1}^2 & -\rho_{11}^2 & \text{Re}\rho_{31}^2 - i\text{Im}\rho_{31}^2 \\ \text{Re}\rho_{3-3}^2 & -\text{Re}\rho_{3-1}^2 - i\text{Im}\rho_{3-1}^2 & \text{Re}\rho_{31}^2 + i\text{Im}\rho_{31}^2 & -\rho_{33}^2 \end{pmatrix} \quad (2.27)$$

Combining Eqs. (2.18), (2.19), (2.20), (2.25), (2.26) and (2.27) one arrives at

$$\begin{aligned}
 W(\theta, \phi, \Phi) = \frac{3}{4\pi} \left\{ \rho_{33}^0 \sin^2 \theta + \rho_{11}^0 \left(\frac{1}{3} + \cos^2 \theta \right) \right. \\
 \left. - \frac{2}{\sqrt{3}} \text{Re} \rho_{31}^0 \sin 2\theta \cos \phi - \frac{2}{\sqrt{3}} \text{Re} \rho_{3-1}^0 \sin^2 \theta \cos 2\phi \right. \\
 \left. - P_\gamma \cos 2\Phi \left[\rho_{33}^1 \sin^2 \theta + \rho_{11}^1 \left(\frac{1}{3} + \cos^2 \theta \right) \right. \right. \\
 \left. \left. - \frac{2}{\sqrt{3}} \text{Re} \rho_{31}^1 \sin 2\theta \cos \phi - \frac{2}{\sqrt{3}} \text{Re} \rho_{3-1}^1 \sin^2 \theta \cos 2\phi \right] \right. \\
 \left. - P_\gamma \sin 2\Phi \frac{2}{\sqrt{3}} \left[\text{Im} \rho_{31}^2 \sin 2\theta \sin \phi + \text{Im} \rho_{3-1}^2 \sin^2 \theta \sin 2\phi \right] \right\} \quad (2.28)
 \end{aligned}$$

With condition $\text{Tr} \rho^0 = 1$ follows $\rho_{33}^0 = \frac{1}{2} - \rho_{11}^0$. Eq. (2.28) gives the angular distribution of the K^- in the GJ frame. This can be used to fit the data and extract the nine remaining independent SDMEs that are accessible with a linearly polarised photon beam.

Helicity frame

The discussion and definition of SDMEs is not only valid in the GJ frame but also equally valid in the so called s -channel helicity frame [30]. It is defined in the baryon rest frame by

$$\hat{z} = \frac{-\vec{p}_{K^+}}{|-\vec{p}_{K^+}|} \quad \hat{y} = \frac{\vec{p}_\gamma \times \vec{p}_{K^+}}{|\vec{p}_\gamma \times \vec{p}_{K^+}|} \quad \hat{x} = \hat{y} \times \hat{z} \quad (2.29)$$

The frame is constructed such that the \hat{z} -axis is defined in direction of the produced baryon in the CM system, which is equivalent to opposite of the produced meson in the baryon rest frame [37]. The frame is depicted in Figure 2.3. It is especially useful for cases where one wants to study s -channel helicity conservation. Both the helicity and the GJ frame have their \hat{y} -axis defined perpendicular to the production plane and their \hat{z} -axis in the production plane. Therefore, the

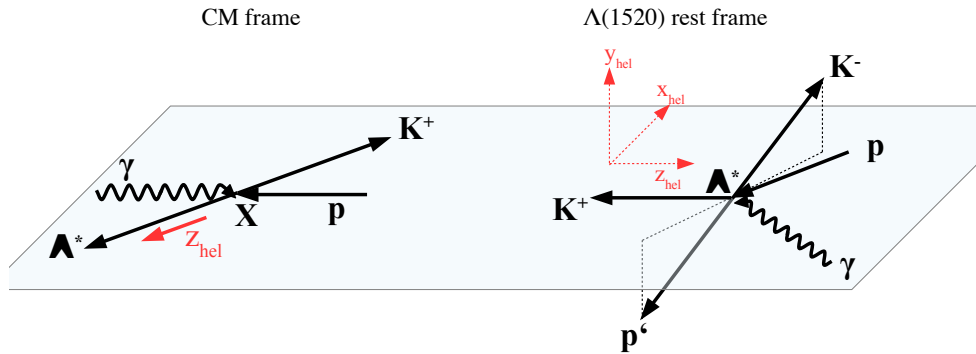


Figure 2.3: Definition of the s -channel helicity frame for the reaction of interest.

parity relations are the same in both frames and one can easily get from one frame to the other via a rotation with a small Wigner-d matrix

$$\rho_{mm'}^{\text{hel}} = \sum_{\lambda_\Lambda \lambda'_\Lambda} d_{m\lambda_\Lambda}^{3/2}(\alpha_{\text{hel} \rightarrow \text{GJ}}) \rho_{\lambda_\Lambda \lambda'_\Lambda}^{\text{GJ}} d_{m'\lambda'_\Lambda}^{3/2}(\alpha_{\text{hel} \rightarrow \text{GJ}})^* \quad (2.30)$$

where

$$\alpha_{\text{hel} \rightarrow \text{GJ}} = \arccos\left(\frac{\beta - \cos\theta}{\beta \cos\theta - 1}\right) \quad (2.31)$$

and β is the $\Lambda(1520)$ velocity in the CM frame and θ is the K^+ production angle in the CM frame [38]. Since both frames are connected by a rotation, they contain the same amount of information and measuring the SDMEs in one frame gives the results in the other as well. Nevertheless, both have their uses as they can simplify certain assumptions in the reaction model.

2.1.1 Naturality in the reflectivity basis

Spin-density matrix elements provide a parametrisation to describe the production and decay of the $\Lambda(1520)$ in terms of nine independent real-valued numbers. The interpretation of their values however, is neither obvious nor straightforward. This section aims to provide some guidance on the relation between the exchange mechanism and SDMEs. This interpretation is based on private communication with Vincent Mathieu (JPAC) [39].

The helicities in the reaction $\gamma(\lambda_\gamma)p(\lambda_p) \rightarrow K^+\Lambda(1520)(\lambda_\Lambda)$ are given by $\lambda_\gamma = \pm 1$, $\lambda_p = \pm 1/2$ and $\lambda_\Lambda = \pm 1/2, \pm 3/2$. The K^+ is a pseudoscalar and as such has helicity $\lambda_{K^+} = 0$. Following Schilling [30], $T_{\lambda_\gamma \lambda_p \lambda_\Lambda}$ denotes the production amplitudes as before. Taking the product of all combinations and adding the parity constraint from Eq. (2.13) results in $1/2 \times 2 \times 2 \times 4 = 8$ independent amplitudes. Each amplitude can be split in a positive (N, $\varepsilon = +1$) and negative (U, $\varepsilon = -1$) reflectivity component such that

$$T = T^{(+)} + T^{(-)} \quad (2.32)$$

and the amplitude is written in so called reflectivity basis as

$$T_{\lambda_p \lambda_\Lambda}^{(\varepsilon)} = \frac{1}{2} \left(T_{1\lambda_p \lambda_\Lambda} + \varepsilon T_{-1\lambda_p \lambda_\Lambda} \right) \quad (2.33)$$

Using Eq. (2.13) and Eq. (2.33) the parity relation for the amplitudes in reflectivity basis is given by

$$T_{-\lambda_p -\lambda_\Lambda}^{(\varepsilon)} = \varepsilon (-1)^{\lambda_p - \lambda_\Lambda} T_{\lambda_p \lambda_\Lambda}^{(\varepsilon)} \quad (2.34)$$

At high energies the reflectivity component corresponds to the naturality of the exchanged particle. The naturality η of a particle with spin-parity quantum numbers J^P is given by

$$\eta = P(-1)^J \quad (2.35)$$

Natural exchanges are therefore exchanges of a vector (e.g. $K^*(892)$) or a tensor (e.g. $K_2^*(1430)$) meson. Unnatural exchanges are exchanges of a pseudoscalar (e.g. $K(492)$) or axial-vector (e.g. $K_1(1270)$) meson.

Following on from the previous definitions in Eqs. (2.10)-(2.12), the SDMEs can be expressed in terms of reflectivity amplitudes as

$$\rho_{\lambda_\Lambda \lambda'_\Lambda}^0 = \frac{1}{N} \sum_{\lambda_p} T_{\lambda_p \lambda_\Lambda}^{(+)} T_{\lambda_p \lambda'_\Lambda}^{(+)*} + T_{\lambda_p \lambda_\Lambda}^{(-)} T_{\lambda_p \lambda'_\Lambda}^{(-)*} \quad (2.36)$$

$$\rho_{\lambda_\Lambda \lambda'_\Lambda}^1 = \frac{1}{N} \sum_{\lambda_p} T_{\lambda_p \lambda_\Lambda}^{(+)} T_{\lambda_p \lambda'_\Lambda}^{(+)*} - T_{\lambda_p \lambda_\Lambda}^{(-)} T_{\lambda_p \lambda'_\Lambda}^{(-)*} \quad (2.37)$$

$$\rho_{\lambda_\Lambda \lambda'_\Lambda}^2 = \frac{i}{N} \sum_{\lambda_p} T_{\lambda_p \lambda_\Lambda}^{(+)} T_{\lambda_p \lambda'_\Lambda}^{(-)*} - T_{\lambda_p \lambda_\Lambda}^{(-)} T_{\lambda_p \lambda'_\Lambda}^{(+)*} \quad (2.38)$$

and write the following combinations

$$\rho_{\lambda_\Lambda \lambda'_\Lambda}^0 + \rho_{\lambda_\Lambda \lambda'_\Lambda}^1 = \frac{2}{N} \sum_{\lambda_p} T_{\lambda_p \lambda_\Lambda}^{(+)} T_{\lambda_p \lambda'_\Lambda}^{(+)*} \quad (2.39)$$

$$\rho_{\lambda_\Lambda \lambda'_\Lambda}^0 - \rho_{\lambda_\Lambda \lambda'_\Lambda}^1 = \frac{2}{N} \sum_{\lambda_p} T_{\lambda_p \lambda_\Lambda}^{(-)} T_{\lambda_p \lambda'_\Lambda}^{(-)*} \quad (2.40)$$

One can nicely see that certain combinations of SDMEs separate amplitudes with positive and negative reflectivity. This can be taken a step further by denoting eight amplitudes by N_σ (natural) and U_σ (unnatural) with $\sigma = \lambda_p - \lambda_\Lambda = \{-1, 0, 1, 2\}$. The reflectivity amplitudes can then be written in terms of the exchange naturality

$$N_{-1} = T_{\frac{1}{2} \frac{3}{2}}^{(+)} \quad N_0 = T_{\frac{1}{2} \frac{1}{2}}^{(+)} \quad N_1 = T_{\frac{1}{2} -\frac{1}{2}}^{(+)} \quad N_2 = T_{\frac{1}{2} -\frac{3}{2}}^{(+)} \quad (2.41)$$

$$U_{-1} = T_{\frac{1}{2} \frac{3}{2}}^{(-)} \quad U_0 = T_{\frac{1}{2} \frac{1}{2}}^{(-)} \quad U_1 = T_{\frac{1}{2} -\frac{1}{2}}^{(-)} \quad U_2 = T_{\frac{1}{2} -\frac{3}{2}}^{(-)} \quad (2.42)$$

The combinations of SDMEs in these amplitudes are then given by

$$\rho_{11}^0 + \rho_{11}^1 = \frac{2}{N} (|N_0|^2 + |N_1|^2) \quad \text{Re}(\rho_{31}^0 + \rho_{31}^1) = \frac{2}{N} \text{Re}(N_{-1}N_0^* - N_2N_1^*) \quad (2.43)$$

$$\rho_{11}^0 - \rho_{11}^1 = \frac{2}{N} (|U_0|^2 + |U_1|^2) \quad \text{Re}(\rho_{31}^0 - \rho_{31}^1) = \frac{2}{N} \text{Re}(U_{-1}U_0^* - U_2U_1^*) \quad (2.44)$$

$$\rho_{33}^0 + \rho_{33}^1 = \frac{2}{N} (|N_{-1}|^2 + |N_2|^2) \quad \text{Re}(\rho_{3-1}^0 + \rho_{3-1}^1) = \frac{2}{N} \text{Re}(N_{-1}N_1^* + N_2N_0^*) \quad (2.45)$$

$$\rho_{33}^0 - \rho_{33}^1 = \frac{2}{N} (|U_{-1}|^2 + |U_2|^2) \quad \text{Re}(\rho_{3-1}^0 - \rho_{3-1}^1) = \frac{2}{N} \text{Re}(U_{-1}U_1^* + U_2U_0^*) \quad (2.46)$$

$$\text{Im}\rho_{31}^2 = \frac{2}{N} \text{Im}(N_2U_1^* + N_{-1}U_0^* - U_2N_1^* - U_{-1}N_0^*) \quad (2.47)$$

$$\text{Im}\rho_{3-1}^2 = \frac{2}{N} \text{Im}(U_2N_0^* + N_{-1}U_0^* - N_2U_0^* - U_{-1}N_1^*) \quad (2.48)$$

with the normalisation given by

$$N = 2(|N_{-1}|^2 + |N_0|^2 + |N_1|^2 + |N_2|^2 + |U_{-1}|^2 + |U_0|^2 + |U_1|^2 + |U_2|^2) \quad (2.49)$$

These equations show that various combinations of SDMEs are directly related to the naturality of the exchange and combinations of specific helicity amplitudes. In the discussion of the results in Chapter 7 this will be used to make statements about the exchange mechanisms at play in $\Lambda(1520)$ photoproduction.

2.1.2 Beam asymmetry

A commonly studied observable in pseudoscalar photoproduction experiments with a linearly polarised photon beam, is the photon beam asymmetry Σ . The differential cross-section for a linearly polarised beam and an unpolarised target is given by [40]

$$\frac{d\sigma}{dt} = \frac{d\sigma}{dt}|_{unpolarised} (1 - P_\gamma \Sigma \cos(2\Phi)) \quad (2.50)$$

where P_γ denotes the degree of linear polarisation of the photon beam and Φ is the angle between the polarisation vector and the production plane (see Figure 2.2). By choosing two perpendicular settings for the polarisation vector one can measure Σ by forming an asymmetry as

$$P_\gamma \Sigma = \frac{d\sigma_y - d\sigma_x}{d\sigma_y + d\sigma_x} \quad (2.51)$$

where $d\sigma_y$ denotes the differential cross section measured with the photon beam polarisation vector perpendicular to the production plane ($\Phi = 90^\circ$) and $d\sigma_x$ denotes the setting with the

vector in the production plane ($\Phi = 0^\circ$). This definition is commonly used because it simplifies the experimental determination of Σ , when corrected for the photon flux and polarisation in each setting. Assuming that the detector acceptance is the same in both settings, it cancels in the asymmetry.

The beam asymmetry can also be accessed through the measurement of SDMEs. Using Eq. (2.17) one can write

$$P_\gamma \Sigma = \frac{W(\Phi = \frac{\pi}{2}) - W(\Phi = 0)}{W(\Phi = \frac{\pi}{2}) + W(\Phi = 0)} \quad (2.52)$$

where $W(\Phi)$ means that the θ and ϕ angles were completely integrated over. Decomposing $W(\Phi)$ using Eq. (2.21) yields

$$W(\Phi) = \int d\Omega W = \int d\Omega W^0 - P_\gamma \cos 2\Phi \int d\Omega W^1 - P_\gamma \sin 2\Phi \int d\Omega W^2 \quad (2.53)$$

$$= 1 - P_\gamma \cos(2\Phi) 2(\rho_{11}^1 + \rho_{33}^1) \quad (2.54)$$

with $\int d\Omega W^2 = 0$. One can see straight away, that this is equivalent to the definition in Eq. (2.50). Comparing Eq. (2.50) to Eq. (2.54) it follows that

$$\Sigma = \int d\Omega W^1 = 2(\rho_{11}^1 + \rho_{33}^1) \quad (2.55)$$

In terms of (un)natural amplitudes one can then write

$$\Sigma = \frac{2}{N} \left(|N_{-1}|^2 + |N_0|^2 + |N_1|^2 + |N_2|^2 - |U_{-1}|^2 - |U_0|^2 - |U_1|^2 - |U_2|^2 \right) \quad (2.56)$$

which shows that a positive beam asymmetry means that there is a greater contribution to the production mechanism from natural exchanges and a negative beam asymmetry means there is a greater contribution from unnatural exchanges. This provides a simple interpretation of the reaction mechanism based on one observable.

As mentioned before, Σ can be accessed as a counting asymmetry, assuming that all acceptance effects drop out in the ratio. This provides a comparably easy way to gain some information on the production mechanism. It can be shown [41], however, that the assumption is not completely true for a decaying baryon. It only holds if the integration in Eq. (2.54) really is complete in θ and ϕ . If there are acceptance effects introducing gaps or cutoffs, these have to be accounted for. This is automatically done if the beam asymmetry is calculated from SDMEs via Eq. (2.55). In that case, one is guaranteed to measure the correct beam asymmetry. Since Σ is just a subset of the full set of SDMEs it is desirable to directly measure the nine independent SDMEs accessible through Eq. (2.28). This will provide the most comprehensive set of information to study the reaction of interest, available from the angular distribution of the final state particles.

2.2 Differential cross-section

Spin-density matrix elements give a full description of the angular decay distribution of the $\Lambda(1520)$. This is important information which allows the study of mechanisms involved in the production of this state. However, this is not enough information in order to get a complete picture of the reaction.

In quantum field theory the *coupling* describes the strength of an interaction at a vertex as shown in Figure 2.1. In order to write down a full reaction amplitude, that contains all the information about the reaction, one needs to know the coupling which can be determined from the *cross-section*. The cross-section is a measure of the probability for a reaction to take place and as such related to the strength at the vertex. It can generally be written as

$$\sigma = \frac{\text{number of reactions taking place}}{\text{number of incoming particles} \times \text{number of target particles}} \quad (2.57)$$

The number of incoming particles, also called *flux*, and the number of target particles are experimental parameters, that can be controlled. The number of reactions that occurred has to be measured. To do so, we must account for the detector *acceptance* η , which describes the fraction of reactions being measured (*yield*) of the total actually taking place, and is determined with the use of simulations (see Section 6.3.1). In this analysis the $\Lambda(1520)$ is only measured in one decay process, $\Lambda(1520) \rightarrow pK^-$. Therefore, it is also necessary to correct for the *branching ratio*, the fraction of particles decaying into a specific final state. Combining all, the *total cross-section* can be defined as

$$\sigma = \frac{Y}{F \cdot BR \cdot \rho \cdot \eta} \quad (2.58)$$

where Y denotes the yield, F is the flux, BR is the branching ratio, ρ is the target thickness and η denotes the acceptance.

It is common to study a reaction depending on some kinematic variable that the underlying production amplitudes are dependent on, e.g., the four-momentum transfer squared $t = (p_\gamma - p_{K^+})^2$ from the incoming photon to the outgoing K^+ . In this case, the *differential cross-section* can be defined as

$$\frac{d\sigma}{dt} = \frac{Y}{F \cdot BR \cdot \rho \cdot \eta \cdot \Delta t_{\text{bin}}} \quad (2.59)$$

where Δt_{bin} denotes the bin width in t . The total cross-section can be calculated from the differential cross-section by integrating the results over the kinematic variable. In general, this process is model dependent, as it requires a functional form for $\frac{d\sigma}{dt}$.

2.3 Choice of binning variable

The main aim of this work is to study the production mechanism in $\Lambda(1520)$ photoproduction through the measurement of polarisation observables and cross-sections. It is expected that this mechanism, and therefore the underlying production amplitudes, will depend on the reaction kinematics. As we wish to see how the amplitudes vary, a natural choice for binning the data is the four-momentum transfer squared t . This effectively varies the mass of the virtual particle exchanged by the beam and target in the reaction and is defined as

$$t = (p_\gamma - p_{K^+})^2 \quad (2.60)$$

Since t is negative its is convenient to use $-t$ for binning and plotting purposes.

It is important to recognise that there exists a minimum value of $-t$ which is constrained by the total energy in the CM frame s and the particles' masses m . It is given by [15]

$$t_{\min} = \left[\frac{-m_p^2 - m_K^2 + m_\Lambda^2}{2\sqrt{s}} \right]^2 - (p_{\gamma \text{ CM}} - p_{K^+ \text{ CM}})^2 \quad (2.61)$$

where p_{CM} denotes the particles' momenta in the CM frame, which are given by

$$p_{\text{CM}} = \sqrt{E_{\text{CM}}^2 - m^2} \quad (2.62)$$

with the particles' energies

$$E_{\gamma \text{ CM}} = \frac{s - m_p^2}{2\sqrt{s}} \quad E_{K^+ \text{ CM}} = \frac{s + m_{K^+}^2 - m_\Lambda^2}{2\sqrt{s}} \quad (2.63)$$

For the reaction kinematics in this work t_{\min} is very small, between $-0.026 \text{ GeV}^2/c^2$ and $-0.024 \text{ GeV}^2/c^2$. Nevertheless, it is accounted for properly by binning the data and results in bins of $-(t - t_{\min})$. This way the four-momentum transfer squared distribution always starts at $0 \text{ GeV}^2/c^2$.

In this Chapter the theoretical background and formalism to extract physics information from the data has been laid out. In the following, the current world data situation on this reaction and the status of theoretical description will be discussed.

Chapter 3

Current experimental situation

GlueX is the first experiment to perform photoproduction experiments with linearly polarised photons at energies around 8.8 GeV, therefore no data exists so far for the reaction of interest in this energy regime. However, there were earlier efforts to measure the $\Lambda(1520)$ photoproduction at lower energies in the LEPS, LAMP2, SAPHIR and CLAS collaborations as well as at higher energies at SLAC. In the following an overview of the obtained results will be given.

3.1 Previous measurements

The $\Lambda(1520)$ was first reported by Ferro-Luzzi, Tripp and Watson in [27] in 1962. They used a K^- beam on a proton target and reported an enhancement in the cross-section at around 1520 MeV which they identified as an excited hyperon with spin $3/2$. A year later they confirmed the extracted quantum numbers in a more sophisticated analysis [42]. In 1971 Boyarski *et al.* [43] used a tagged bremsstrahlung photon beam at the Stanford Linear Accelerator Center (SLAC) in combination with the SLAC 20 GeV spectrometer to measure hyperon photoproduction at five angles in the very forward region. They measured the outgoing K^+ and identified the $\Lambda(1520)$ in a missing mass spectrum (Figure 3.1). Since they did not use a linearly polarised photon beam they could not measure polarisation observables but they provided differential cross-section measurements. In 1980 Barber *et al.* [44], from the LAMP2 group, measured the $\Lambda(1520)$ in photoproduction at energies between 2.8 GeV and 4.8 GeV in the exclusive pK^-K^+ final state. They measured the total and differential cross-section (Figure 3.2) as well as mass and width of the $\Lambda(1520)$. They also managed to extract three independent, unpolarised spin-density matrix elements. Their results indicated that the production does not simply proceed via K exchange. In 2009 Muramatsu *et al.* (LEPS collaboration) measured differential cross-sections for $\Lambda(1520)$ photoproduction from the proton and deuteron in the SPring-8 LEPS experiment [45].

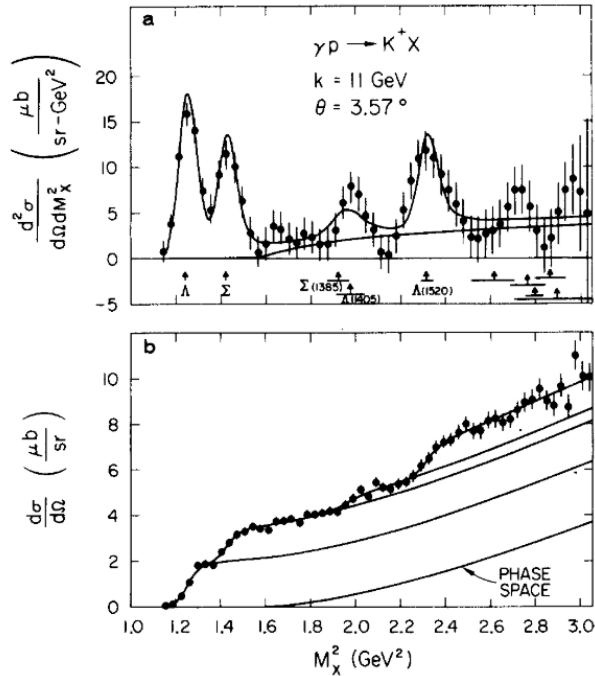


Figure 3.1: Missing mass squared spectrum reported by Boyarski *et al.* (SLAC) [43]. The bottom plot shows the measured yields with the curves representing fits consisting of phase space and steps corresponding to production of Λ , Σ , $\Sigma(1385) + \Lambda(1405)$ and $\Lambda(1520)$ [43]. The top plot shows the derivative of the measured yields. The $\Lambda(1520)$ shows up as a peak in the top spectrum at about $2.3 \text{ GeV}^2/c^4$.

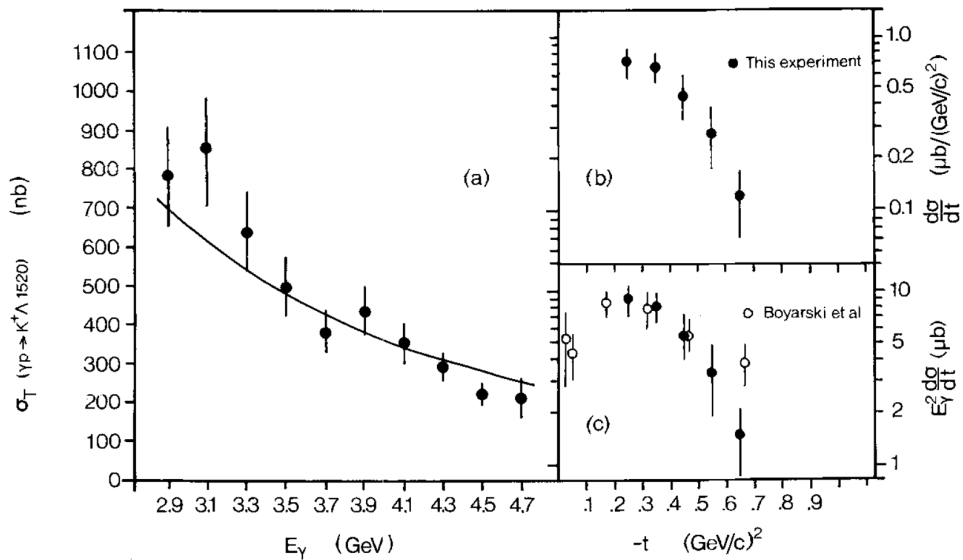


Figure 3.2: Total and differential cross-sections reported by Barber *et al.* (LAMP2) [44]. In the bottom right they show a scaled comparison to the previous SLAC data.

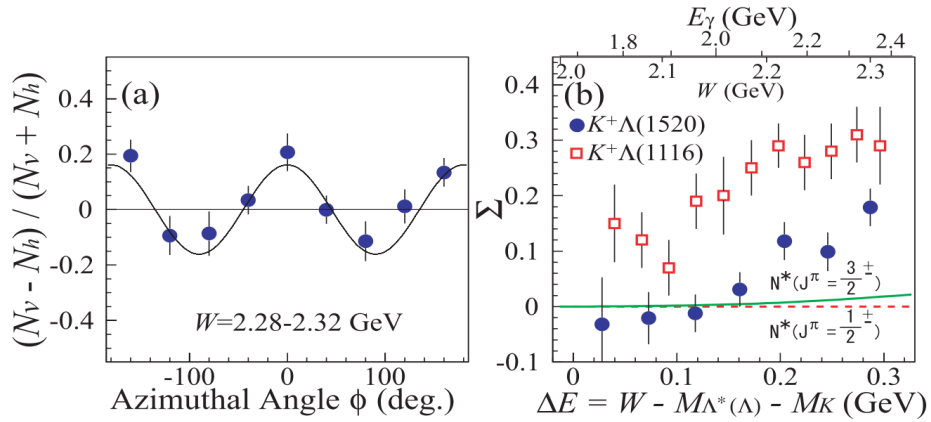


Figure 3.3: Photon beam asymmetry Σ reported by Kohri *et al.* (LEPS) [46]. The plot on the left shows an example fit. The plot on the right shows the beam asymmetry extracted for the $\Lambda(1520)$ at forward angles compared to previous data for the $\Lambda(1116)$ [47]. The solid green and dashed red lines show calculations of Σ by Nam *et al.* for the cases of two different nucleon resonances contributing to the production.

They used a linearly polarised photon beam with energies between 1.75 GeV and 2.4 GeV, and provided a measurement of the beam asymmetry Σ for K^+ angles below 60° . Their value is compatible with 0 which is interpreted as a dominance by the contact-term and only small t -channel K^* contribution in the production mechanism. In 2010 the LEPS collaboration published another paper where they extended the measurement of the differential cross-sections and also provided more data on Σ [46]. The results for the beam asymmetry are still compatible with 0 near threshold but indicate a rise at higher energies which might be due to higher t -channel K^* contributions (Figure 3.3). Also in 2010, Wieland *et al.* published results from the SAPHIR experiment at ELSA in Bonn [48]. They measured the $\Lambda(1520)$ production cross-section in various decay channels as a function of the photon energy as well as the Mandelstam variable t . They also measured differential cross-section in the t -channel helicity frame, to make deductions about the production mechanisms involved in the reaction.

The most recent data come from the CLAS collaboration in 2013. Moriya *et al.* measured the differential and total photoproduction cross-sections for $\Lambda(1520)$ production on the proton, for photon energies between 1.66 GeV and 3.71 GeV [49], and compared their results to theoretical predictions (Figure 3.4). In 2010 Zhao published his PhD thesis in which he measured the production cross-section for photon energies between 1.75 GeV and 5.5 GeV [52], in 2016 Levine published his PhD thesis in which he extracted unpolarised spin-density matrix elements for the reaction of interest [38]. Both of them used the CLAS detector at Jefferson Lab.

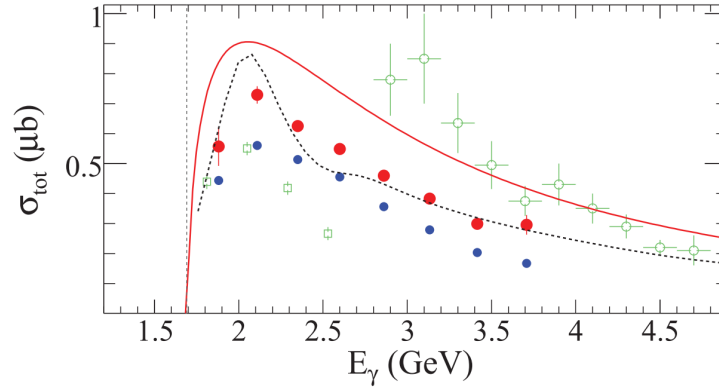


Figure 3.4: Total photoproduction cross-section for $\Lambda(1520)$ production on the proton reported by Moriya *et al.* (CLAS) [49]. The blue points show the CLAS results within detector acceptance, the red points show the extrapolation over all phase space. The dashed black and solid red curves are calculations by He *et al.* [50] and Nam *et al.* [51] respectively. The green squares and green circles are results from SAPHIR [48] and LAMP2 [44] respectively.

3.2 Status of theoretical description

In addition to the experimental results discussed so far, there was a lot of effort on the theory side to understand the $\Lambda(1520)$ and its production mechanism ([35, 51, 53, 54]). Since the data available until now was taken at lower energies than what GlueX is measuring at, most theoretical work covers only lower energies up to 5 GeV. Yu and Kong [35] however used the results from SLAC [43] to extrapolate their model predictions (Figure 3.5). They also provided predictions for the energy range of this work and their results will be used later for comparisons.

There have been some previous measurements of the reaction studied in this work, $\gamma p \rightarrow K^+ \Lambda(1520)$, mostly at low energies. The only measurements at high photon energies were performed at SLAC almost 50 years ago. Most measurements were made using an unpolarised beam and, therefore, little information exists on polarisation observables which provide key knowledge about the involved production mechanisms. There are no measurements of this reaction around 8.2 GeV-8.8 GeV photon energy. Furthermore, so far no measurements of polarised SDMEs have been performed at all. This work provides the first measurement of that kind and will help to fill in the large gap that exists between previous measurements at low energies and high energies. In the following chapter the GlueX experiment, which provides the data for this analysis, is presented.

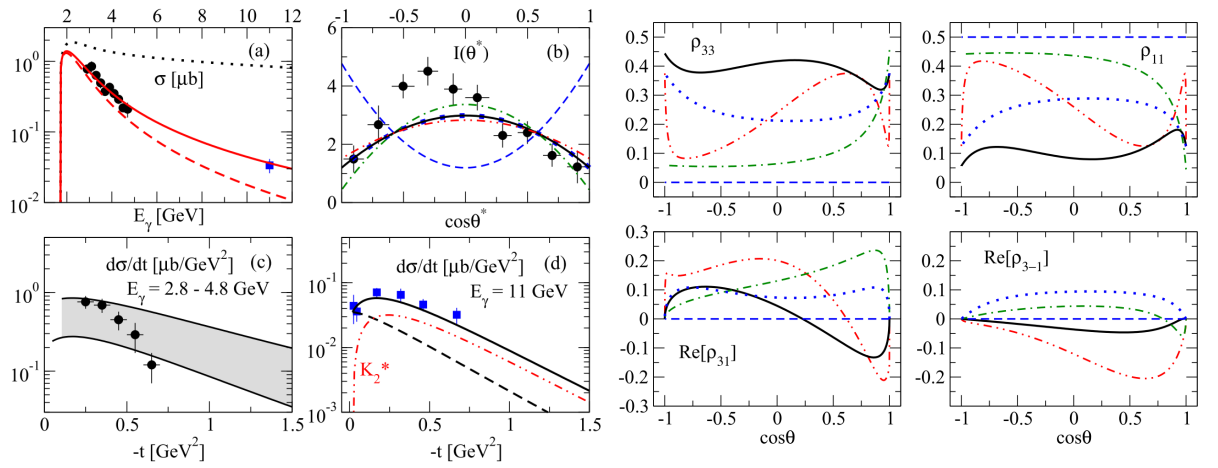


Figure 3.5: Fits and model predictions by Yu and Kong [35]. Black data points are results from LAMP2 [44], blue data points are results from SLAC [43]. (a), (c) and (d) show the total and differential cross-section and fits to the data. (b) shows the angular distribution of the K^- in the Gottfried-Jackson frame. The four plots on the right show calculations for four unpolarised SDMEs (three independent) at 3.8 GeV in the Gottfried-Jackson frame. The solid black line shows the result of the full calculation while the coloured lines show contributions from different kaon exchanges (K , K^* , and K_2^* in blue dashed, green dash-dotted and red dash-dot-dotted respectively).

Chapter 4

Experimental setup

In this chapter the GlueX experiment, where the research is carried out, is presented. Figure 4.1 gives an overview over the whole setup with the outline of a person for scale. In brief, the electron beam from the CEBAF accelerator strikes a diamond radiator to produce a linearly polarised photon beam, using the coherent bremsstrahlung technique. This beam is directed into the proton (i.e. liquid hydrogen) target at the centre of the GlueX superconducting solenoid, and outgoing charged and neutral particles are detected using a combination of drift chambers, scintillating fibres and calorimetry. In the following, the accelerator and components of the beam line and detector setup are discussed in detail.

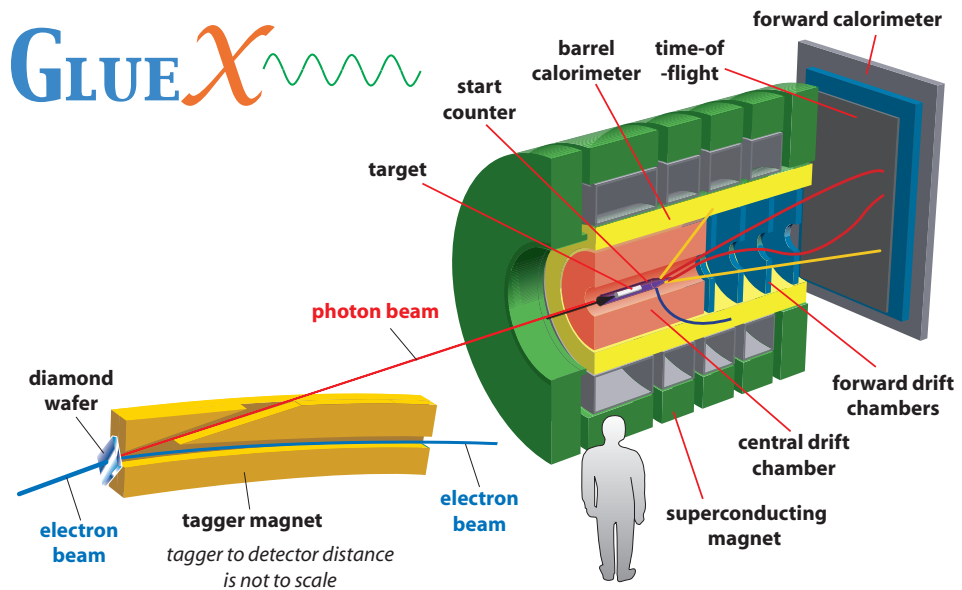


Figure 4.1: Overview of the GlueX experiment and its important subdetector systems. Taken from [55].

4.1 Continuous Electron Beam Accelerator Facility

The Continuous Electron Beam Accelerator Facility (CEBAF) is a continuous wave electron accelerator located in Newport News, VA, USA. It can deliver electrons with an energy of up to 12 GeV, with a total beam power of about 900 kW, which corresponds to a current of about $100\ \mu\text{A}$ [56]. Under normal running conditions between 150 nA and 180 nA of beam are delivered to the Hall D tagger hall. A schematic view of the accelerator can be found in Figure 4.2. A pulsed laser is directed at a GaAs crystal to release electrons [58] that are con-

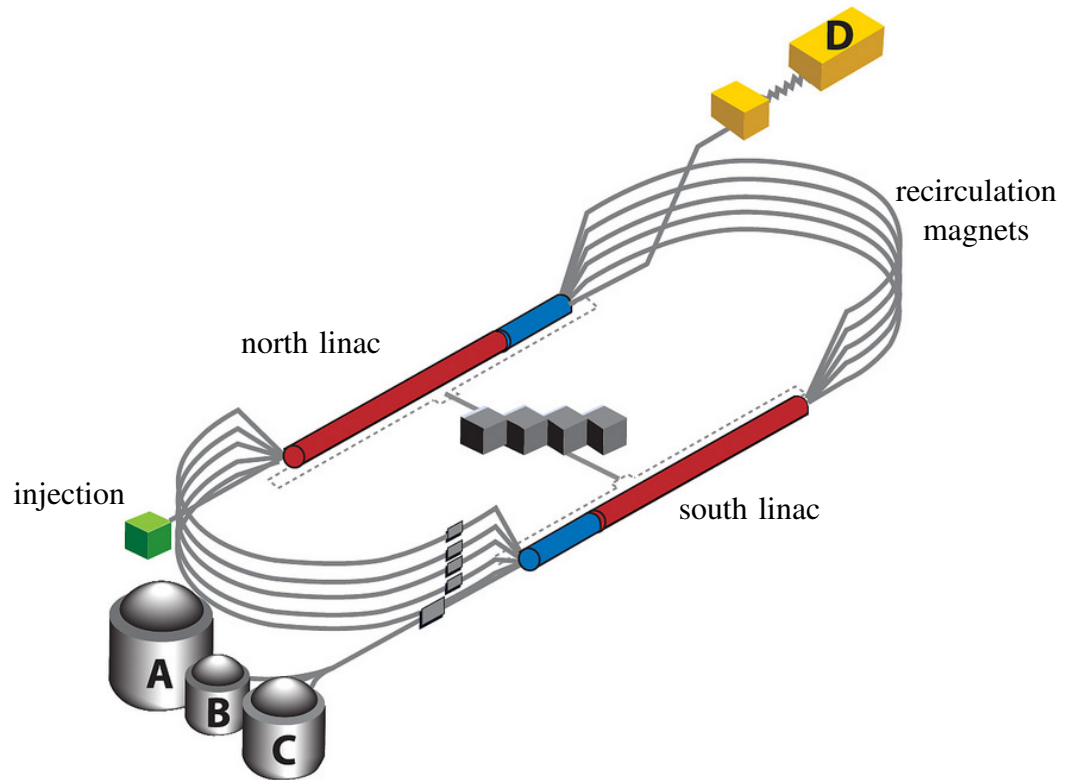


Figure 4.2: Schematic view of Jefferson Lab's accelerator site. Taken from [57] with added annotations.

sequently injected into the accelerator in bunches with a repetition rate of either 249.5 MHz or 499 MHz [59]. Hall D receives beam with 249.5 MHz, which corresponds to a beam bunch separation of 4.008 ns. The electron bunches are accelerated in two linear accelerators (linac) consisting of 25 cryogenic modules each [60]. The cavities providing the electromagnetic field responsible for the acceleration are made from niobium and held at a temperature of about 2 K using liquid helium [61]. Niobium becomes superconducting at these temperatures, making the whole acceleration process much more energy efficient and feasible. The two linacs are connec-

ted by beam lines within recirculation magnets that focus and steer the beam. This race track setup makes it possible to reuse the same linac multiple times to increase the electrons' energy, adding about 2.2 GeV with each pass [60]. Sitting at the end of the north linac, Hall D can get beam that passed the whole accelerator up to 5.5 times. This totals to the full 12 GeV that CEBAF can deliver. During the data taking periods in Spring 2017 the electron beam energy was lowered to about 11.6 GeV, to increase running stability of the accelerator.

4.2 Linearly polarised photon beam

The GlueX experiment uses linearly polarised, tagged photons produced by the coherent bremsstrahlung technique. A schematic view of the photon beam line and its components is shown in Figure 4.3. A short explanation of the concept of photon tagging is given here, together with details of the specific tagging systems used in the experiment. This is followed by a description of coherent bremsstrahlung and the hardware used to implement it, and to measure the flux and polarisation of the resulting beam.

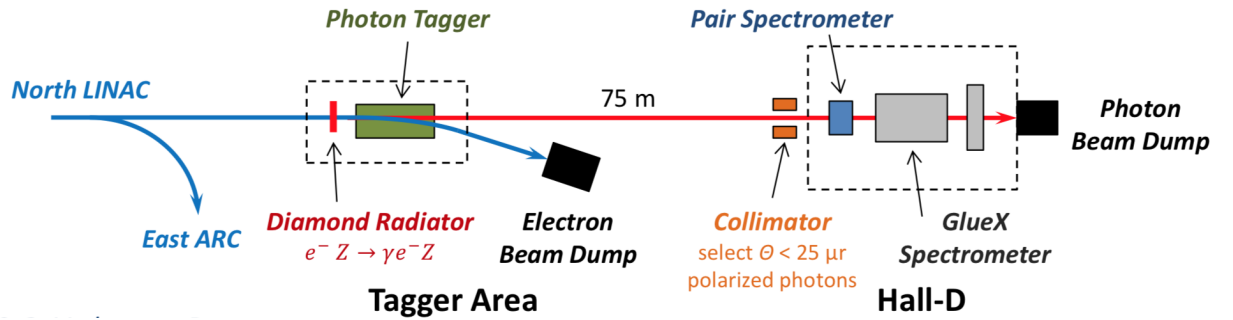


Figure 4.3: Schematic view of the Hall D beam line. Taken from [62].

4.2.1 Bremsstrahlung and photon tagging

GlueX is a real photon beam experiment. Since CEBAF is only capable of delivering electrons, GlueX produces its own photon beam via *bremstrahlung* (braking radiation), where a real photon is emitted by an electron, decelerated in the vicinity of an atomic nucleus [63] (see Figure 4.4). Knowing the energy of each photon triggering a reaction greatly improves the reaction identification capabilities of GlueX. For that reason the photon beam is tagged. The electron beam energy $E_{e^-, \text{beam}}$ is known to great precision. If the energy of the electron after emission, E'_{e^-} , is measured the photon energy is given as

$$E_\gamma = E_{e^-, \text{beam}} - E'_{e^-} \quad (4.1)$$

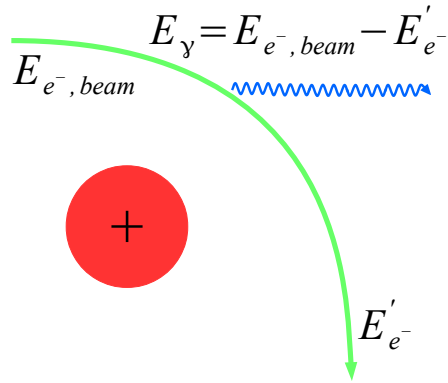
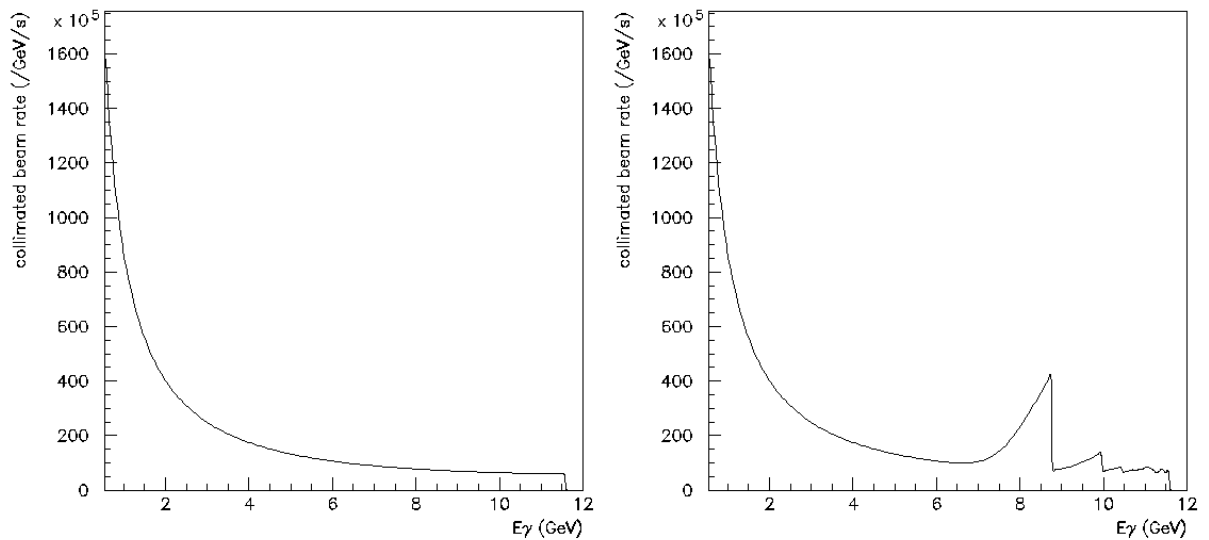


Figure 4.4: Diagram of the bremsstrahlung process.

In order to measure the energy of the scattered electron, a known magnetic field of about 1.5 T is used. After radiating a photon the electrons are bent by the Lorentz force with the curvature depending on their remaining momentum. Measuring the position of the electron on a focal plane (see Figure 4.7) together with a magnetic field map of the tagger magnet results in a precise momentum measurement. In order to know which photon triggered a reaction in the target, a timing coincidence is used. That makes it necessary to have very good timing resolution together with the position measurement on the focal plane. A bremsstrahlung photon energy spectrum follows a $1/E_\gamma$ distribution. A calculated photon rate can be seen in Figure 4.5a. One can see the sharp rise towards small photon energies and a flattening out towards higher energies.



(a) Amorphous radiator

(b) Diamond radiator

Figure 4.5: Calculated photon rate for different radiators [64].

4.2.2 Coherent bremsstrahlung

To produce linearly polarised photons the coherent bremsstrahlung technique is used. The electron beam is directed on a thin diamond wafer. If the diamond is precisely orientated in a way that the recoil momentum from an electron is transferred to the crystal lattice instead of a single nucleus, and is a multiple of the reciprocal lattice vector, then the Bragg condition is fulfilled and the produced photons can interfere constructively. In this case, one speaks of *coherent bremsstrahlung*. Photons coming from this process are linearly polarised. The coherent bremsstrahlung process is described in detail in [65]. The resulting photons have a characteristic energy distribution which depends on the orientation of the diamond. A calculated photon rate for linearly polarised photons can be seen in Figure 4.5b. One can see the underlying $1/E_\gamma$ distribution of unpolarised photons with a series of peaks superimposed. The first, most prominent, of these is referred to as the *coherent peak*, and contains photons with a high degree of linear polarisation. Its point of steepest decline on the right is referred to as the *coherent edge* and is often used as a reference point to describe the energy of the peak. The size of the coherent peak and the degree of polarised photons within the coherent peak can be improved by collimation but is ultimately limited by its energy relative to the incoming electron beam energy. The orientation of the electric field vector of the photon beam determines its polarisation angle. It can be controlled by precise orientation of the diamond.

4.2.3 Goniometer and radiators

The diamond radiator used for the production of coherent bremsstrahlung is mounted on a multi-axis goniometer (see Figure 4.6). It allows for precise movement in two linear directions (x, y) and three rotations (roll, pitch, yaw). This precise positioning makes it possible to align the diamond such that optimal beam polarisation is achieved at the desired photon beam energy. Multiple diamond radiators are mounted in the centre of the goniometer. This allows for fast changes if the experimental requirements change. A diamond with 58 μm thickness was used throughout data taking for this work. The goniometer is not located in the main experimental hall, but in a separate building, together with the tagging spectrometer (see Section 4.2.4). This is situated approximately 70 m upstream of the main detector building, and was designed this way to allow tight collimation of the photon beam by having the radiator a long way from the collimator inside the main hall (see Section 4.2.5). In addition to the diamond radiator, an amorphous aluminium radiator was used for about 15% of data taking. This type of radiator produces only unpolarised photons and is used for normalisation and systematic studies, and is needed to determine the degree of linear polarisation via a shape analysis of the coherent bremsstrahlung spectrum [67]. The amorphous radiator is not mounted on the goniometer but instead on a separate rail 61.5 cm downstream of the goniometer [68].

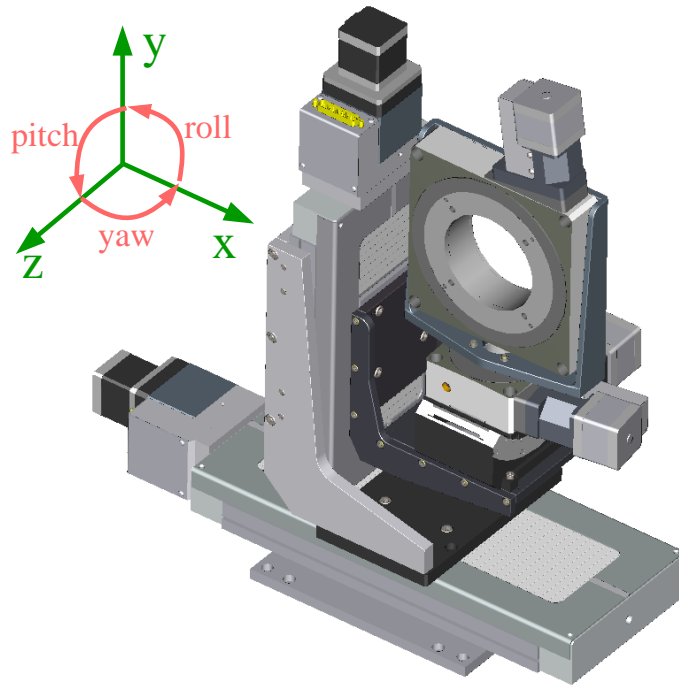


Figure 4.6: 3D drawing of the goniometer. The diamond radiator is mounted in the centre of the circular hole. Taken from [66] (modified).

4.2.4 Tagger hodoscope and microscope

To measure the photon beam energy GlueX uses two photon taggers. They are situated behind the radiator in a known magnetic field of about 1.5 T. The tagger hodoscope (TAGH) consists of 218 scintillators that sample about 30 – 50% of the region between 3.0 GeV and 8.2 GeV and the full energy region between 9.2 GeV and 11.78 GeV [69]. The tagger microscope (TAGM) consists of 102 columns of five scintillating fibres covering the energy range between 8.2 GeV and 9.2 GeV [68]. The TAGM has a much finer granularity since this is the region of highest interest. This is where the coherent edge and therefore the bulk of the linearly polarised photons are (see Section 4.2.2). Having a higher granularity here results in a better energy resolution and increased rate capability. Figure 4.7 shows a schematic of both tagging detectors and the magnet. The blue dots indicate the instrumented focal plane with the TAGM in the central part. The energy scale in the figure (red dots) is given as ratio of photon energy (k) to incoming beam energy (E_0). Electrons that did not undergo bremsstrahlung still have the full energy and are bent into a beam dump by the tagger magnet. To make sure that the photon beam is not contaminated with charged particles sweeping magnets are installed that deflect them out of the beam line.

Both the TAGH and TAGM have excellent timing resolutions of less than 230 ps [68] to allow for a timing coincidence with the detector setup, to identify the photon that triggered the reaction.

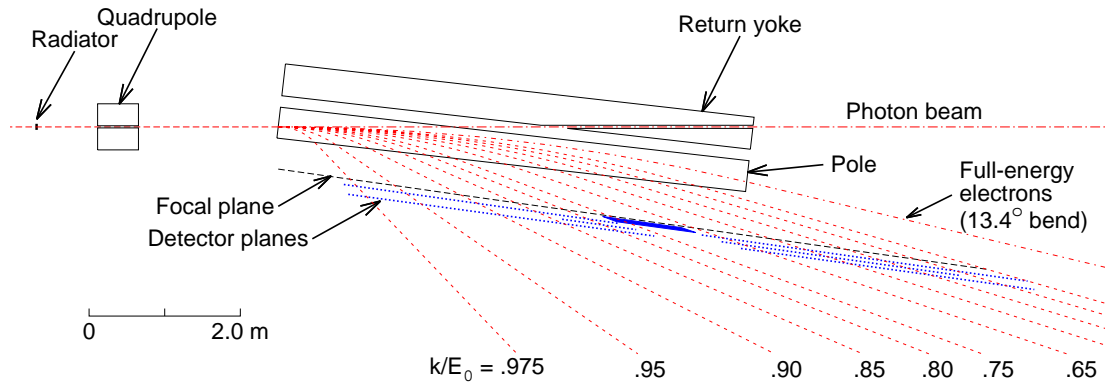


Figure 4.7: Schematic view of the tagger hodoscope and microscope. Taken from [68].

4.2.5 Collimation and beam monitoring

Since the linearly polarised photons are predominantly produced under small forward angles, collimation of the beam can help to increase the degree of linear polarisation. This is the reason for having the diamond radiator, where the photons are produced, a long distance upstream from the detector setup. The photon beam travels through a beam pipe for 70 m and is then collimated with a 5 mm *active collimator*. The collimator is called active because it is equipped with eight photon detectors that measure the beam halo, to calculate the beam position. This information can then be fed into a feedback loop and the steering magnets, that control the electron beam on the diamond, can be automatically adjusted [68]. With that, it is possible to run with a very stable beam position despite the very long collimation distance. All remaining detector components discussed here are situated downstream of the collimator.

In addition to the active collimator, beam profilers can be inserted into the beam line to monitor the beam position and size. These diagnostic tools are very important to ensure good running conditions. For measurement and monitoring of the beam polarisation and flux the GlueX beam line is equipped with three other major monitoring systems that are discussed in the following.

Triplet polarimeter

For most measurements planned at GlueX, including the measurements for this work, it is important to know the degree of linear polarisation in the photon beam. GlueX has a detector component specifically designed to directly measure this quantity. It takes advantage of the angular dependence of triplet production with linearly polarised photons. In pair production the incoming photon recoils against an atomic nucleus and produces an electron-positron pair. In the triplet process the production happens on an atomic electron, which will then be knocked out at large polar angles, with an azimuthal angular distribution related to the incoming photon polarisation [70].

The triplet polarimeter (TPOL) is situated after the collimator and consists of a $75\ \mu\text{m}$ thick beryllium foil surrounded by a silicon strip detector, segmented into 32 azimuthal sectors [70]. These can be used to measure the knocked out electron in coincidence with a pair detected in the pair spectrometer (see below). Analysing the resulting angular distributions allows for a direct measurement of the linear polarisation [71]. This technique was used to measure the degree of linear polarisation for this work. Further information on the beam polarisation during the data taking period for this work can be found in Section 4.2.6.

Pair spectrometer

In order to measure cross-sections, it is very important to know the photon flux with high precision. In GlueX this measurement is done with a pair spectrometer (PS) (see Figure 4.8). It

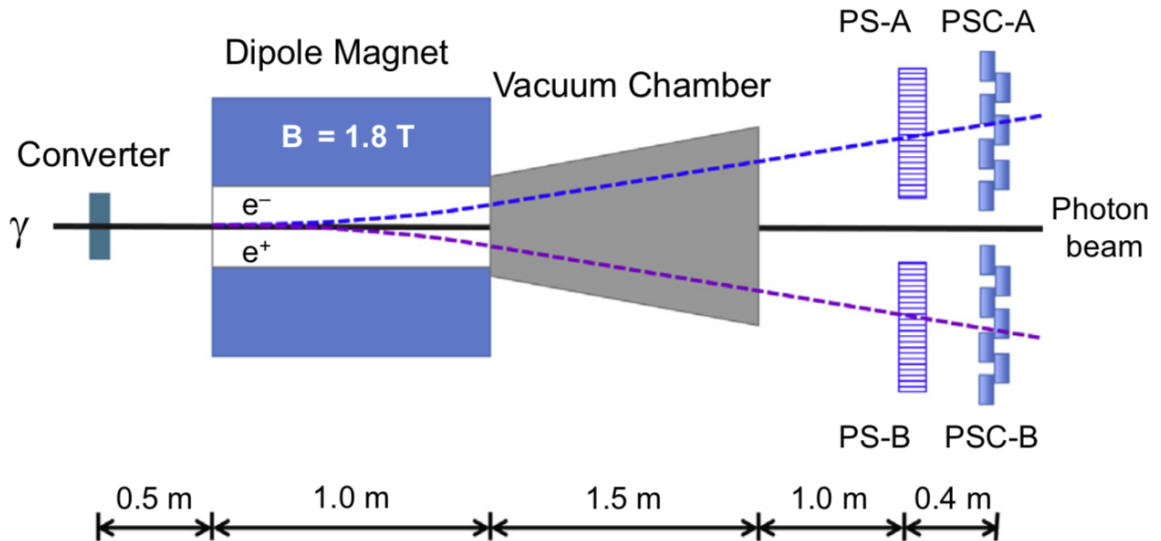


Figure 4.8: Schematic view of the pair spectrometer, which is used for flux measurements at GlueX. Taken from [72].

consists of a thin foil converting photons into electron-positron pairs via pair production. Since the PS is located after the TPOL in normal running conditions its own foil is retracted and the electron-positron pairs originating from the TPOL foil are used for the measurement. A strong magnet of about 1.8 T is used to separate the pair, whose trajectories depend on their energies. The backplane is instrumented with a high granularity hodoscope with 290 scintillators (PS-A/B) read out by silicon photomultipliers (SiPM) [72]. The high granularity means that the PS-A/B provide a good energy resolution. Behind that is a coarse array of sixteen scintillators (PSC-A/B) read out by photomultiplier tubes. These are optimised to provide a trigger signal and reduce background by ensuring coincidence between the electron and positron.

In order to measure the flux, the acceptance of the PS has to be determined. This is done by Monte Carlo simulations, as well as dedicated measurements using the total absorption counter.

Total absorption counter

The total absorption counter (TAC) is used to determine the analysing power of the PS experimentally. This quantity is very important to measure the photon flux with good precision. The TAC consists of an SF-5 lead glass block with a length of 40 cm and a height and width of 20 cm [73]. At low beam currents the TAC can measure the photons in the beam with an efficiency of nearly 100% and can then be used to determine the efficiency of the PS. For this purpose dedicated TAC runs are performed throughout a beam time, during which the number of beam photons identified by the PS is compared to the total number of photons in the beam, as determined by the TAC. At normal running conditions the TAC is removed, in order to protect it from radiation damage.

4.2.6 Beam polarisation and orientation

In order to reduce systematic uncertainties and to aid with the measurement of asymmetries, four different diamond settings were used during data taking, corresponding to two sets of two orthogonal polarisation angles, $0^\circ/90^\circ$ and $45^\circ/135^\circ$. The coherent edge was set to 8.8 GeV for all four settings and the photon beam energy range used for analysis is 8.2 GeV to 8.8 GeV. The degree of linear polarisation for each setting is determined by measuring the angular distribution of triplet production in the TPOL. The method is presented in [71]. Figure 4.9 shows the photon beam polarisation obtained with the TPOL and flux obtained with the PS in bins of energy, as provided by the detector experts. The numbers provided by the analysers and used in this analysis are summarised in Table 4.1. They are the average polarisation of the beam photons within the specified energy range. The absolute orientation of the polarisation vector,

| setting | degree of polarisation | orientation |
|-------------|------------------------|-----------------------------|
| 0° | 0.3536 ± 0.0100 | $1.8^\circ \pm 0.6^\circ$ |
| 90° | 0.3472 ± 0.0098 | $94.5^\circ \pm 0.5^\circ$ |
| 45° | 0.3484 ± 0.0102 | $47.9^\circ \pm 0.5^\circ$ |
| 135° | 0.3513 ± 0.1020 | $138.4^\circ \pm 0.6^\circ$ |

Table 4.1: Polarisation and exact orientation of the photon beam between 8.2 GeV and 8.8 GeV photon energy for the four diamond settings.

as measured in the detector reference frame, is an important quantity. It is best determined from data in a high statistics channel. For this analysis the angular offsets determined in the beam asymmetry measurements in $\gamma p \rightarrow \rho p$ are used [74]. The numbers can be found in Table 4.1.

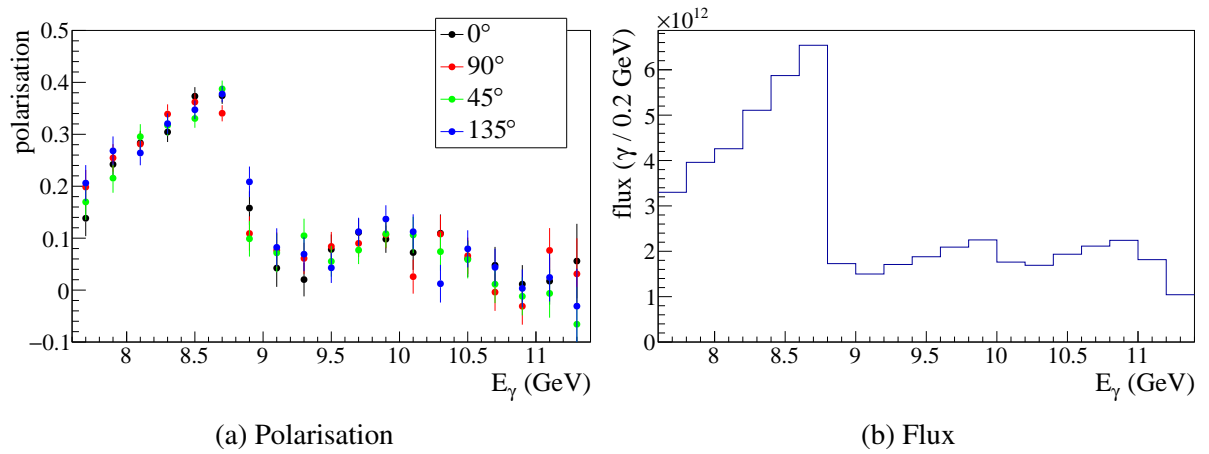


Figure 4.9: The photon beam polarisation for the four separate diamond settings and the photon flux in bins of photon energy.

Systematic effects of these measurements on the final results for the extracted observables are discussed in Sections 6.1.6 and 6.2.5.

4.3 Liquid hydrogen target

The target used at GlueX is provided by the JLab target group. They are specialised in cryogenic targets for nuclear physics experiments. The target consists of liquified hydrogen at a temperature of about 20 K and a pressure of about 1.31 bar [68]. It is 30 cm long and conical in shape. The diameter reduces from 2.42 cm at the entrance window to 1.56 cm at the exit window [75].

4.4 The GlueX detector

In the following, the important subsystems of the GlueX spectrometer are discussed in detail.

4.4.1 Solenoid magnet

GlueX's main component is the 2 T superconducting solenoid magnet. It has a diameter of about 2 m and length of about 4.8 m. It is cooled down to 4.5 K using liquid helium and is operated at 1350 A [68]. It surrounds the tracking detectors and enables the momentum measurement of charged particles by bending them on a momentum dependent helical trajectory. To reconstruct the momentum from the particle's track, the solenoid's magnetic field needs to be known. It was

calculated, and the calculations confirmed by measurements. The calculated magnetic field map is used for momentum reconstruction of charged particles.

4.4.2 Start counter

The innermost detector surrounding the target is the start counter (SC). It consists of 30 scintillator paddles arranged in a cigar-like shape [76] (see Figure 4.10). The SC covers approximately 90% of the solid angle [76]. Its main purpose is to help with the identification of the beam bunch that triggered the reaction, for which it provides excellent timing resolution of less than 825 ps (FWHM) [76]. In addition, it can contribute to particle identification by measuring the deposited energy for a dE/dx measurement and the flight time of the particles for a time-of-flight measurement.

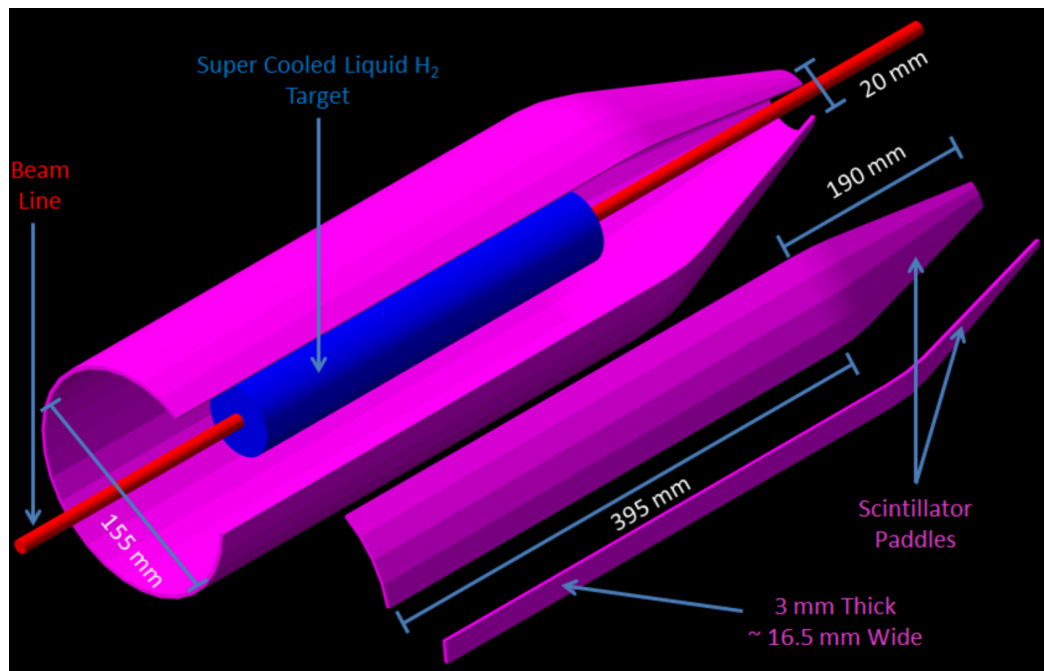


Figure 4.10: Schematic view of the start counter detector and its dimensions. Taken from [77].

4.4.3 Drift chambers

After particles pass the SC, they enter the drift chambers. These two detectors, one barrel-shaped surrounding the target and one in forward direction, provide tracking information for charged particles. When a charged particle passes through the drift chamber it ionises the gas within. An electromagnetic field in the detector causes the ions to drift towards the wires and to induce a current that can be measured. Using multiple layers of wires with different orientations makes

it possible to track a particle through the drift chamber. In order to also extract momentum information the drift chambers are contained within the superconducting magnet with a solenoidal field of about 2 T (see Figure 4.1). This results in a momentum resolution of $\sigma_p/p \approx 1 - 5\%$ for charged particles [68].

Central drift chamber

The central drift chamber (CDC) is a barrel shaped straw tube chamber consisting of 3522 tubes. They have a diameter of 16 mm and are arranged in 28 layers with an alternating orientation of $\pm 6^\circ$ relative to the beam axis. Figure 4.11 shows two of the layers during construction of the detector. The active length of the CDC is 150 cm [78] and it covers polar angles from 6° to



Figure 4.11: The CDC during construction. Taken from [78].

168° [79] with optimal coverage from 29° to 132° [78]. In addition to the information required for charged track reconstruction the CDC can also be used to measure dE/dx , the deposited energy over a certain distance, to perform particle identification (see Section 5.4). This is especially useful to discriminate protons against other charged particles. Figure 4.12 shows the dE/dx spectrum for positively charged particles plotted against their momentum. Low momentum protons have a considerably larger energy deposition and can therefore be easily identified as a band.

Forward drift chambers

The forward drift chambers (FDC) cover polar angles below 20° and are an array of 24 1 m-diameter cathode drift chambers arranged in four groups [80]. Each cathode drift chamber is

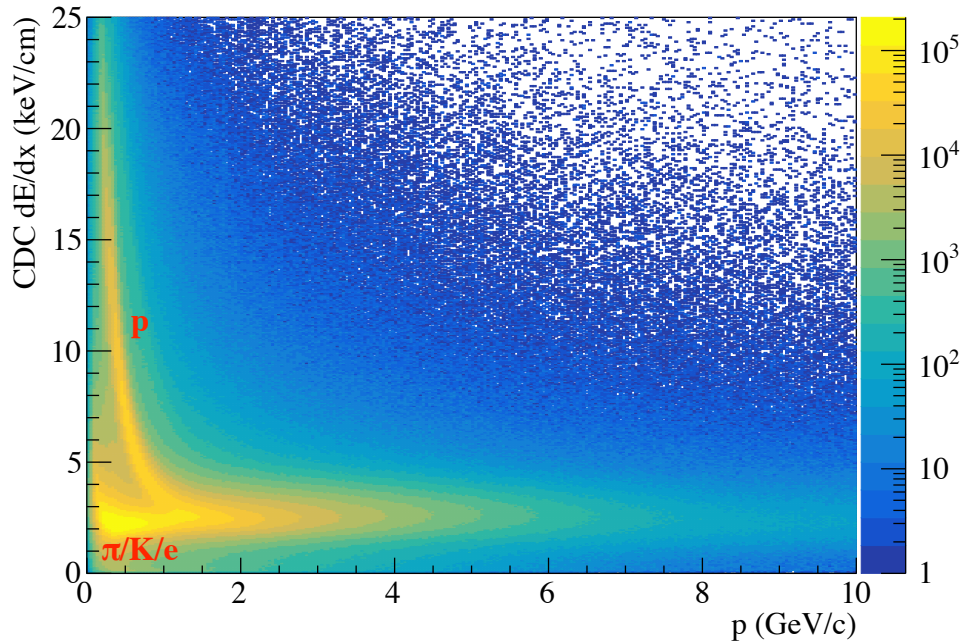


Figure 4.12: The CDC dE/dx spectrum for positively charged particles is plotted against their momentum. Low momentum protons can easily be identified due to their higher energy deposition.

oriented with an offset of 60° relative to its neighbours and consists of two layers of cathode strips with a relative orientation of 75° and 105° to the wires [79].

4.4.4 Calorimetry

Many final states of interest for GlueX contain at least one neutral particle. In order to measure them, the GlueX spectrometer includes two calorimeters, one surrounding the drift chambers and another one in very forward direction (see Figure 4.1). Calorimeters measure the total energy of a particle. The calorimeters in GlueX are electromagnetic calorimeters. Photons and charged particles entering the calorimeter will produce an electromagnetic shower which is proportional to the energy of the particle. This shower will cause scintillation which can then be measured and converted to electric signals. In order to measure the total energy of a particle, it has to be stopped inside the detector. Therefore, materials with high atomic number Z are often used, which have a high stopping power for photons and charged particles.

Barrel Calorimeter

The Barrel Calorimeter (BCAL) is an electromagnetic calorimeter consisting of 48 modules each 390 cm long with a trapezoidal cross-section. The modules have a height of 22.2 cm and are ar-

ranged in a barrel with an inner diameter of 130 cm and an outer diameter of 180 cm. The calorimeter covers the polar angle between 11° and 126° (see Figure 4.13). Each module is manufactured from 185 layers of 0.5 mm lead sheets interleaved with 184 layers of 1 mm plastic scintillator fibres [81]. They are read out from both sides with 40 SiPMs making it a total of 3840 large area SiPM arrays. The BCAL has an energy resolution of $\sigma_E/E = 5.2\%/\sqrt{E(\text{GeV})} \oplus 3.6\%$, where \oplus means the terms are added in quadrature, for neutral particles between 0.5 GeV and 2.5 GeV. The first term originates from sampling fluctuation and photoelectron statistics, while the second term contains effects from mechanical imperfections, material effects, calibration variations, instability with time, and shower leakage [81]. The timing resolution is about 150 ps for 1 GeV electromagnetic showers and 200 ps for pions greater than 1 GeV [81]. This excellent timing resolution makes it possible to use the BCAL as a time-of-flight detector for particle identification (see Section 5.4).

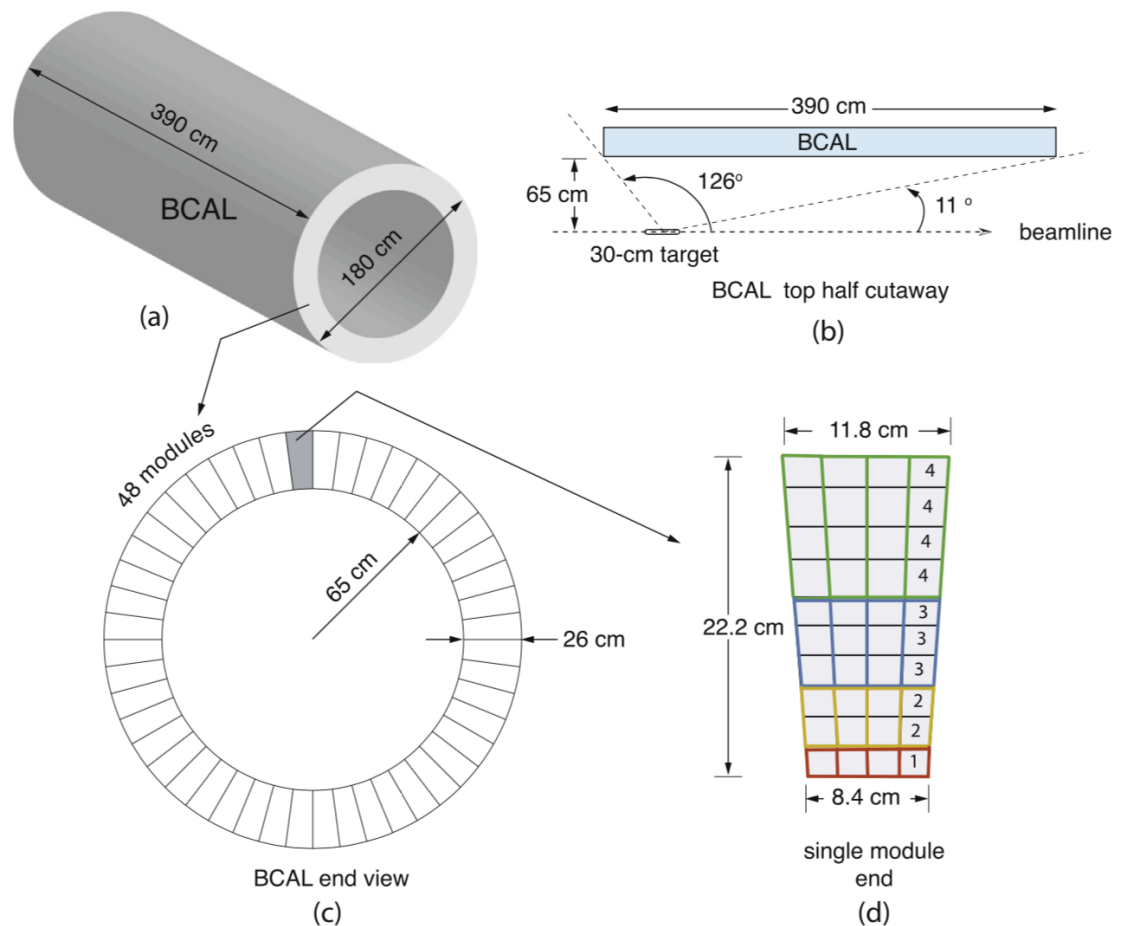


Figure 4.13: Various schematic views of the BCAL detector. Taken from [81].

(a) overall view of the arrangement of the modules. (b) polar angle covered by the BCAL. (c) cross-section view of (a). (d) matrix of read-out areas.

Forward Calorimeter

The forward calorimeter (FCAL) is an electromagnetic calorimeter consisting of 2800 lead glass blocks with dimensions of $4 \times 4 \times 45 \text{ cm}^3$ [82]. Each block is read out with a photomultiplier tube. The blocks are arranged in a circular shape, with the central nine blocks removed to allow for the beam that did not interact in the target to pass (see Figure 4.14). The FCAL is situated behind the Time-of-Flight detector. It has an energy resolution of about $\sigma_E/E = 6.2\%/\sqrt{E(\text{GeV})} \oplus 4.7\%$ [68], where the same parametrisation as for the BCAL was used. The FCAL has a position resolution of about $6.4 \text{ mm}/\sqrt{E}$ and a timing resolution of about 400 ps [82]. Despite the FCAL not having the best timing resolution its distance of about 560 cm away from the target cell means it can still be used for some time-of-flight particle identification (see Section 5.4).

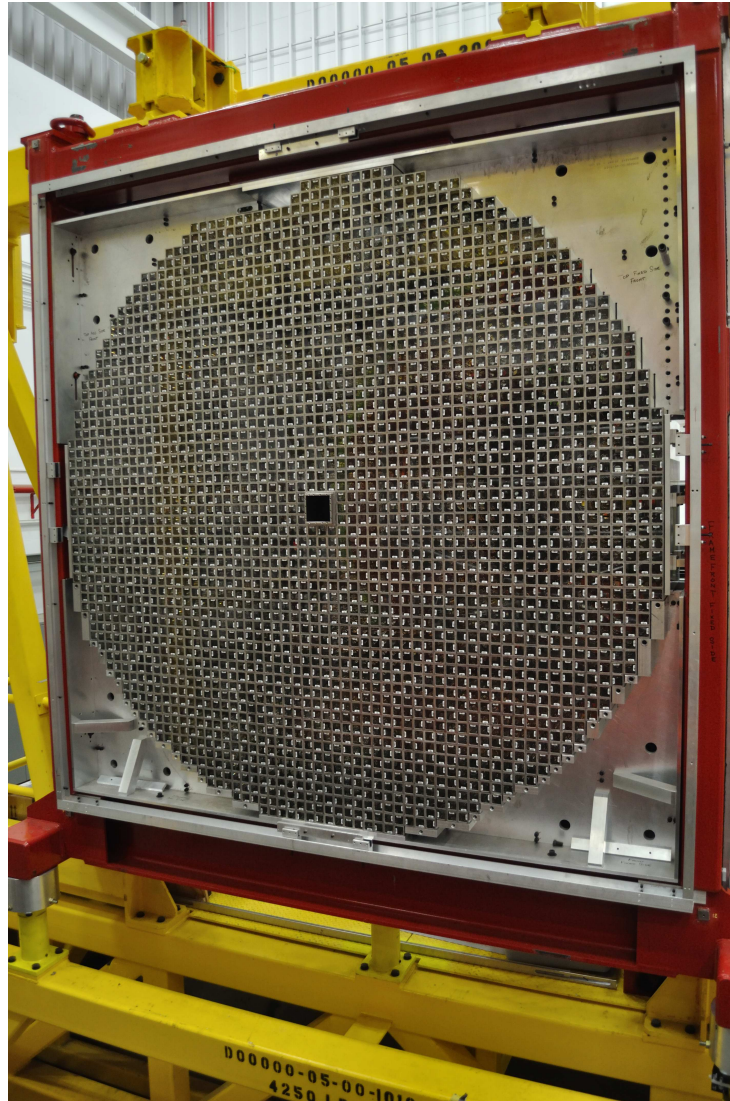


Figure 4.14: Picture of the FCAL detector in its support structure in Hall D. The diameter of the detector is about 2.4 m. Taken from [83].



Figure 4.15: Picture of the TOF wall in its support structure in Hall D. The length and height of the detector is about 2.5 m. Taken from [84].

4.4.5 Time-of-flight detector

During data taking for this work GlueX had one detector with the specific purpose of identifying particles. It uses the time-of-flight method to discriminate between different charged particles. The Time-of-Flight detector (TOF) consists of scintillation bars arranged in a wall with a gap in the middle to let the beam that did not interact with the target pass through (see Figure 4.15). It is read out by 176 PMTs and has an excellent timing resolution of about 90 ps to 95 ps [82]. The TOF is located just before the FCAL. The long distance from the interaction point in combination with the excellent timing resolution makes the TOF a powerful particle identification detector. Figure 4.16 shows a spectrum of calculated relativistic β factor against particle momentum. Bands of different particle types are clearly visible. The TOF provides GlueX with good π/K separation of up to 2 GeV and π/p separation of up to 4 GeV particle momentum.

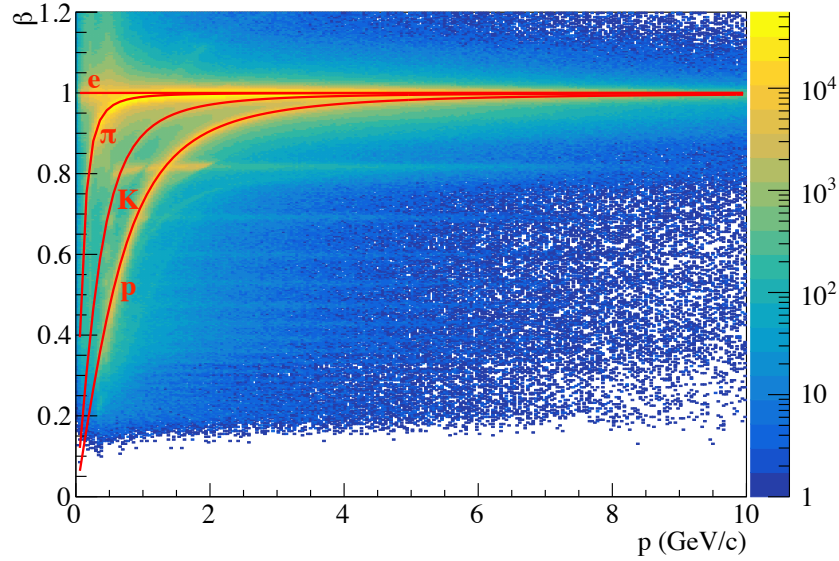


Figure 4.16: The Lorentz factor, β , measured for various particles is plotted against their momentum. The different bands correspond to the different particles and can be used for particle identification. The theoretical curves are plotted in red.

4.5 Event recording and trigger

GlueX is a continuously digitising experiment. Portions of the data stream, which are selected according to certain criteria to include reactions of interest, are saved for further analysis. This is analogous to a conventional trigger. It uses Flash-Analog-to-Digital-Converter (FADCs) to digitise the signals coming from BCAL and FCAL at a sampling rate of 250 MHz [68]. The digitised signal is stored in a pipeline until it is reduced to key quantities, such as pulse height and integral, and readout via VME, if the trigger condition is fulfilled. The trigger conditions used during the data taking period in Spring 2017 were a minimum bias trigger. That means that as many hadronic reactions as possible should be recorded. The general approach was, to set energy thresholds for the calorimeters. If more than a certain energy was measured in the detectors the event was recorded. The calculation of the energy sum was performed on Field-Programmable Gate Arrays (FPGAs) using the digitised signals stored in the pipeline. Since the rates in the two innermost rings in the FCAL are very high due to their proximity to the beam line they were masked from the trigger. The trigger conditions used are summarised in Table 4.2 [85]. These were used simultaneously as they complement each other. The PS coincidence trigger was used for beam flux monitoring and recorded events with a time coincidence in both arms of the PS. In addition, a random trigger was in operation to record events at a fixed rate of 100 Hz. These are used to add random detector background to detector simulations, to get more realistic efficiencies and acceptances. The total trigger rate during data taking was about 40 kHz. This corresponds to a data rate of about 600 MB/s [68].

| trigger condition | FCAL rings masked |
|---|-------------------|
| $E_{FCAL} + 0.5 \cdot E_{BCAL} > 0.5 \text{ GeV}$ $E_{FCAL} > 0 \text{ GeV}$ | 2 |
| $E_{BCAL} > 1.2 \text{ GeV}$ | 0 |
| PS coincidence | 0 |
| Random trigger 100 Hz | 0 |

Table 4.2: Trigger conditions used in the Spring 2017 beam time. The first two trigger types are physics trigger, the second two additional triggers used for flux determination and efficiency studies.

4.6 Detector simulation

Many GlueX analyses, including the one presented here, rely on a very good understanding of the whole detector setup. That means, that the geometric effects of the detector on the reconstructed data, as well as resolutions, and reconstruction probabilities have to be known. For that purpose a simulation software called *hdgeant4* has been developed [86]. It is based on Geant4 [87], a simulation framework widely used within the nuclear and particle physics communities.

hdgeant4 allows for events to be generated in external *event generators*, producing position and momentum four-vectors of final state particles, which are then run through the simulation. The simulation tracks each particle through the detector setup and simulates its interaction with the material. The simulation output can then be treated as real data and analysed in the same way. Although *hdgeant4* aims to simulate all interactions as realistically as possible, it was found that some of the extracted resolutions are slightly better than seen in real data. In an attempt to make the simulation output appear more realistic, the simulated data is *smeared*. This means that the resulting energy and timing distributions are convoluted with Gaussian functions whose widths are determined in careful studies. In addition, the random trigger events are folded into the simulated output to achieve more realistic tracking efficiencies, which are distorted by noise and background events in the detector.

To simulate the run conditions as closely as possible, run dependent variables, such as photon flux or coherent peak orientation, are matched to the real data. That means that if a dataset is simulated, the proportion of the different orientations is the same in simulation as in data. This is also the case for run dependent calibrations, which are matched in simulation.

Another very important detail is the emulation of the trigger condition. This is done by recreating the trigger conditions in software. While the simulated data is reconstructed, the conditions can be checked for each event. This also makes it possible to study the effects of different trigger setups in the simulation.

| sample | events generated | purpose | additional information |
|--------|-------------------|------------------------------|---|
| A | 10^9 | study event selection | bggen (Pythia) event generator using full hdgeant4 simulation |
| B | 2×10^6 | Σ validation | toy MC with imposed Σ |
| C | 250×10^6 | Σ and SDME validation | with imposed SDMEs using full hdgeant4 simulation |
| D | 50×10^6 | acceptance correction | phase space distributed using full hdgeant4 simulation |

Table 4.3: Summary of MC simulations produced for this work. More information about the purpose and contents of each simulated sample can be found in the appropriate sections.

Table 4.3 summarises the four large sets of MC simulations that were produced for this work. This summary shall serve as a reference for the following chapters. More information regarding each set of MC simulations can be found in the appropriate section.

The GlueX beam line and detector are set up to measure hadronic reactions in photoproduction with a linearly polarised photon beam. A summary of its specifications can be found in Table 4.4. GlueX provides good energy and momentum resolution for charged and neutral final state

| | | |
|----------|---|--|
| beam | tagged linearly polarised photons | $\sim 40\%$ polarisation in coherent peak data taken in four polarisation settings |
| target | protons | liquid hydrogen |
| detector | magnet start counter (SC) tracking (CDC, FDC) calorimetry (BCAL, FCAL) time-of-flight (TOF) | 2 T solenoid good timing resolution provides start time momentum resolution $\sigma_p/p \approx 1 - 5\%$ good energy and timing resolution good timing resolution |
| trigger | minimum bias | energy sum |

Table 4.4: Summary of GlueX specifications.

particles. The next chapter shows how these capabilities are used to identify the reaction of interest.

Chapter 5

Data analysis and event selection

In order to extract physics information from the data taken with the GlueX detector setup, various steps have to be performed. Before the data can be analysed, it has to be calibrated and the events processed to reconstruct particle momenta. Afterwards, the data can be scanned for the reaction of interest by identifying events that contain the desired particles. Figure 5.1 visualises the analysis flow from reconstruction to observable extraction (see Chapter 6). In the following, the important steps towards physics extraction are explained in more detail.

5.1 Dataset

The data used in this analysis were acquired in the Spring 2017 beam time between February 4 and March 9, 2017. The beam current provided by CEBAF was about 100 nA in the first part of the beam time (low intensity) which then increased to about 150 nA for the second part (high intensity). The data were mostly taken with a 58 μm diamond radiator, which was used in four different orientations to produce data with different polarisation plane angles (see Section 4.2). In addition, some data were taken with an amorphous aluminium radiator. Table 5.1 summarises the number of triggers recorded in each radiator configuration. In order to facilitate data handling, the data were taken in *runs*. Each run lasted for about two hours and the data for each run was saved across multiple files to keep the size of each file under 20 GB. The raw data format used was *EVIO* [89], a format developed for the use with *CODA* (CEBAF Online Data Acquisition) [90], Jefferson Lab's data acquisition framework. In total, about 900 TB of raw data were generated during the beam time and are stored on tape at Jefferson Lab. 347 runs were identified as physics quality, i.e. the beam and detector were stable during the data taking and no issues with the data acquisition were encountered.

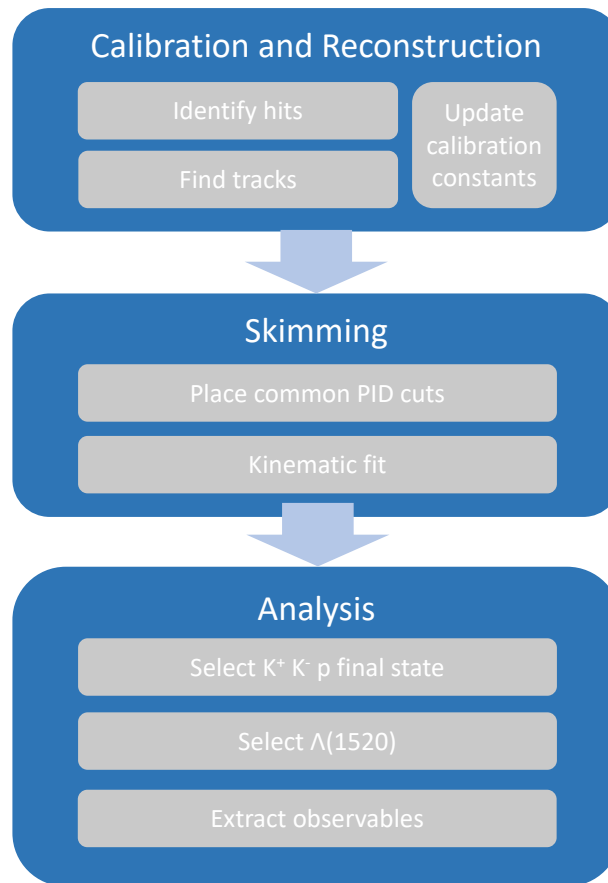


Figure 5.1: Visualisation of the analysis flow from calibration and reconstruction to observable extraction.

5.2 Calibrations

Signals measured in the taggers and detectors are usually timing signals, measured by time-to-digital converters (TDCs), and charge collected proportional to energy depositions, measured by charge-to-digital converters (QDCs). For those signals to be useful, it was necessary to make sure that all timing signals were measured relative to the same reference time. Otherwise, it would not be possible to assign signals from different detectors to the same event trigger and to use them for particle identification or to establish coincidences to identify the beam photon that triggered the reaction. In addition, proportionality factors had to be determined to relate the collected charge to the energy deposited in the detector. This procedure is referred to as calibration and involved many, sometimes iterative, steps. This was done directly after data taking, using the calibration constants from a previous run period as starting parameters. The calibrations were performed by members of the GlueX collaboration and are shared with the whole collaboration. In the following an overview of the most important steps is given.

| radiator setting | triggers collected | |
|------------------|--------------------|-------------------|
| | low intensity | high intensity |
| 0° | 5.8×10^9 | 4.6×10^9 |
| 90° | 5.8×10^9 | 5.2×10^9 |
| 135° | 5.6×10^9 | 4.6×10^9 |
| 45° | 5.7×10^9 | 4.3×10^9 |
| amo | 4.1×10^9 | 3.9×10^9 |

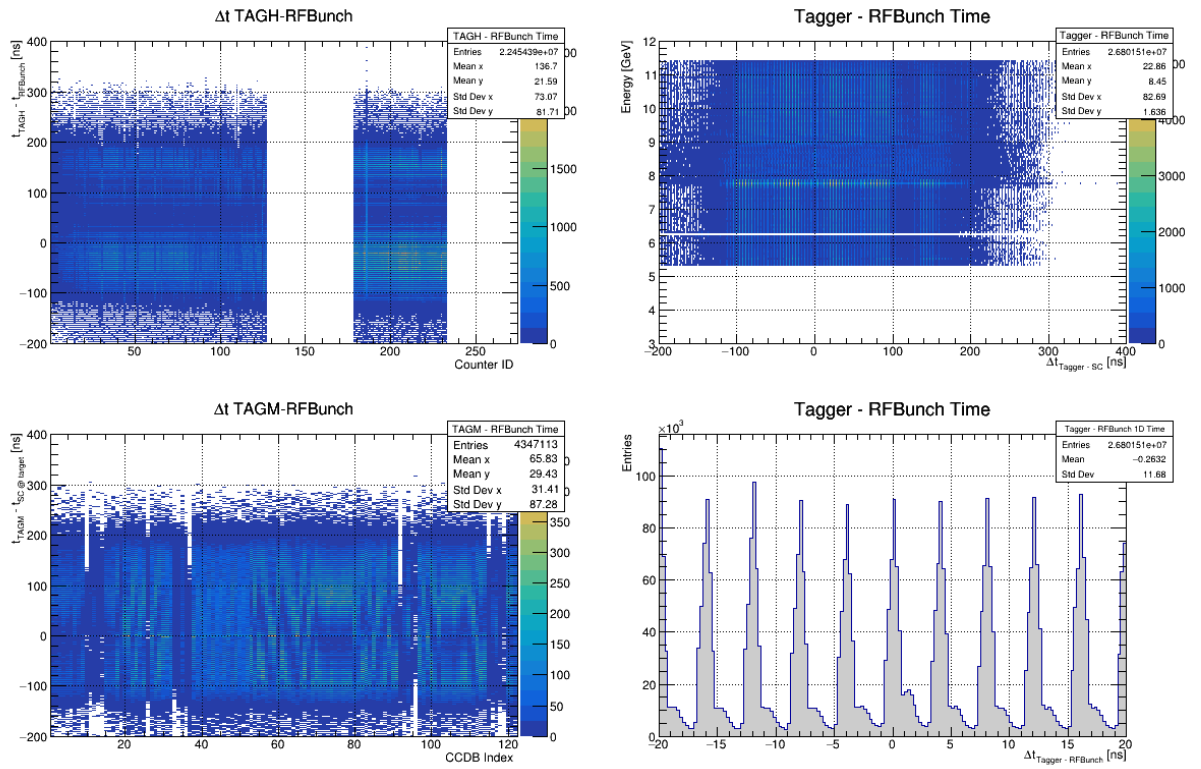
Table 5.1: Number of triggers collected for each diamond orientation and amorphous radiator during the Spring 2017 beam time [88].

5.2.1 Timing calibrations

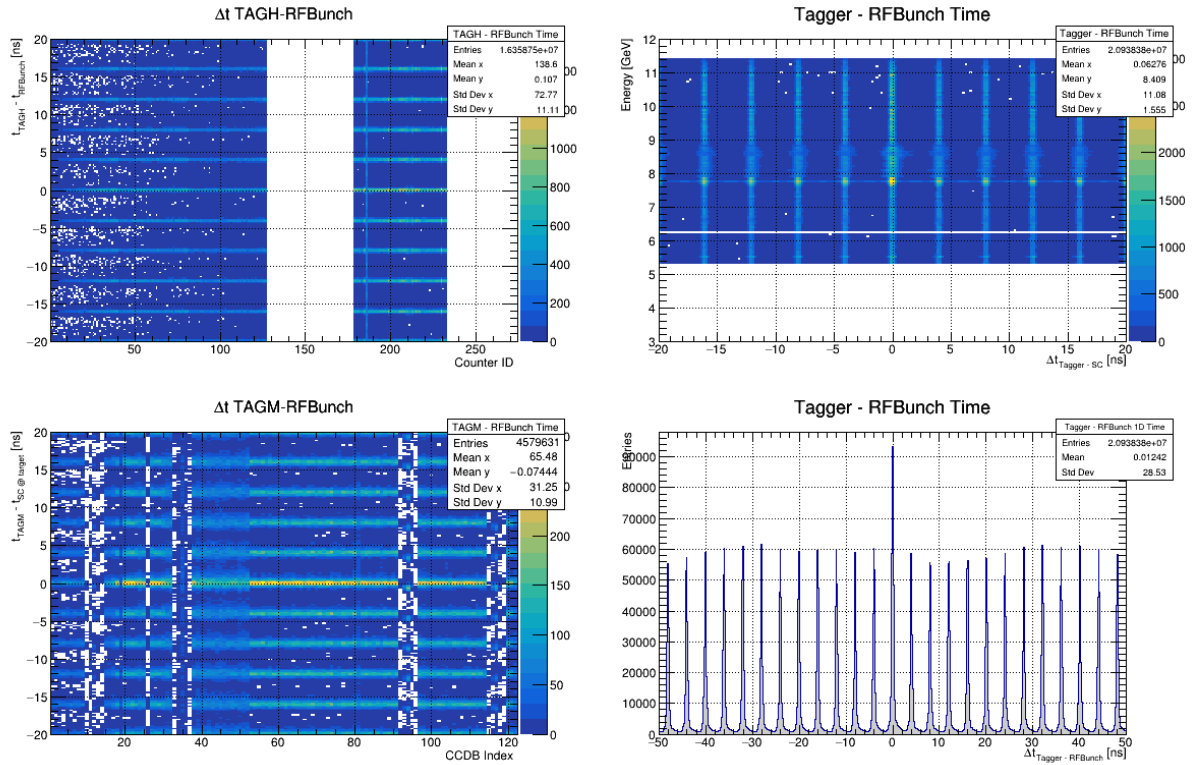
The most precise timing signal available for synchronisation in GlueX comes from CEBAF in form of a 499 MHz radio frequency (RF) clock. It was read out at the TOF crate and used as the overall reference time.

The GlueX detectors consist of many channels. Most detectors are instrumented with both TDCs and QDCs (CDC and FCAL have QDC-only readout). The QDC also provides a timing signal, although with poorer resolution. These two needed to be aligned to each other for each channel. A timing alignment was then performed for all channels within a detector and then the overall detector time was aligned to the RF clock. In addition, a *timewalk* correction was applied to the TDC signals. It corrected for the timing signal dependency on the amplitude of the signal pulse in the leading edge discriminators used in GlueX. Figure 5.2 shows example plots of the tagger timing signal relative to the RF clock before and after calibrations. The top and bottom left plots show the signal plotted versus detector elements for the tagger hodoscope and microscope, respectively. The top right plot shows the signal plotted versus photon energy and the bottom right shows a histogram of the signal. In all cases one would expect to see a dominant peak at 0 ns and smaller peaks in multiples of 4.008 ns, which corresponds to the accelerator beam bunch frequency. The improvements through the calibration are clearly visible. Before calibration the peaks are not well defined and the peak centred at 0 ns is not more dominant than the surrounding peaks. After the calibration the expected narrow peak structure is clearly visible.

In addition to these basic timing calibrations, the time differences between signals coming from the two ends of a TOF paddle were calibrated so the timing can be used to determine the position along the length of the paddle [92]. Similarly, there was also an additional timing calibration in the BCAL to determine the shower z-position, by calibrating signals coming from the upstream and downstream readout [81]. Most of these calibrations were performed once for the whole run period. The PS, tagger and TOF calibrations were done on a run-by-run basis.



(a) before calibration



(b) after calibration

Figure 5.2: Example plots of tagger timing signal relative to the RF clock showing the effect of timing calibrations on the tagger time spectra for run 30999. Top and bottom left plots: Signal plotted versus detector elements for TAGH and TAGM, respectively. Top right: Signal plotted versus photon energy. Bottom right: Histogram of the signal. Taken from [91].

5.2.2 Gain calibrations

In general, the charge collected in a QDC is proportional to the energy deposited in the detector. In order to relate the charge deposition to the energy, a *gain calibration* is necessary. These calibrations were done for the CDC, BCAL and FCAL.

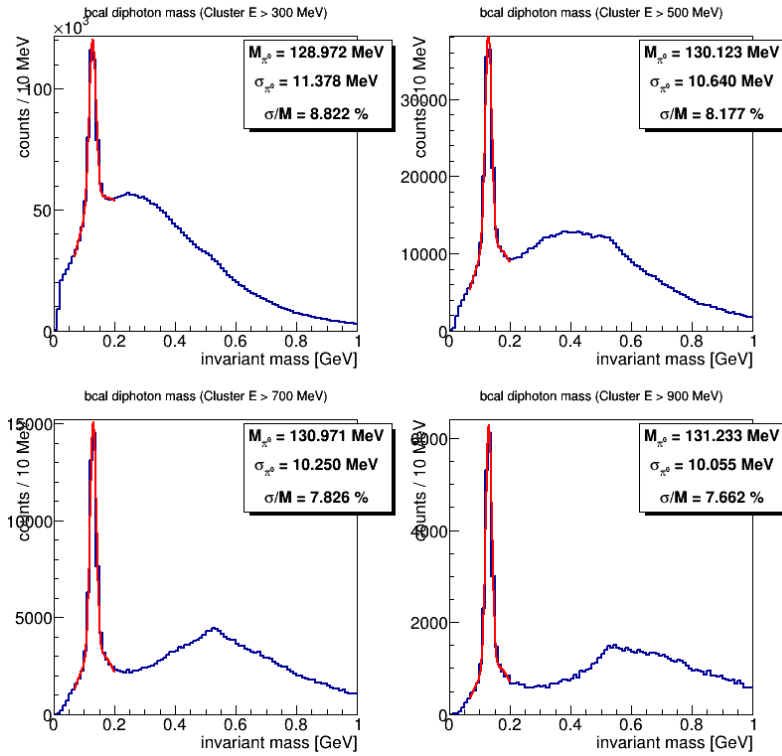
For the calorimeters the gains were calibrated using events with a π^0 decaying to two photons. The mass of the π^0 is known, so the gains were adjusted in order for the peak of the measured invariant mass to coincide with the PDG mass of 135 MeV [81]. This was an iterative process that was performed for the beam time as a whole. The gain was calibrated on a channel-by-channel basis and then the data had to be analysed again. After a few iterations of gain calibrations the peak of the measured invariant mass was at the correct position and, more importantly, the width was minimised. Shower based non-linearity corrections were applied to the data after the gain calibrations of both calorimeters. Example plots for the BCAL before and after calibration can be found in Figure 5.3. The blue histograms show the di-photon invariant mass distributions with the expected peaks in the π^0 mass range. The red lines show fits to the data using gaussian function which are used to extract mean and width of the π^0 peak. The data for this figure was divided up into four subsets according to the cluster energy of the photons as indicated by the individual plot titles. After the calibration the mass is at the correct value of about 135 MeV for all four plots, and in addition the width improved as well.

The CDC is used to measure energy deposition by a charged particle in a thin layer of material for particle identification (dE/dx). The calibration was based on minimum ionising particles depositing constant energy in the detector. The CDC gain calibrations were done on a run-by-run basis since they were very much dependent on the temperature and pressure within the detector and sensitive to fluctuations.

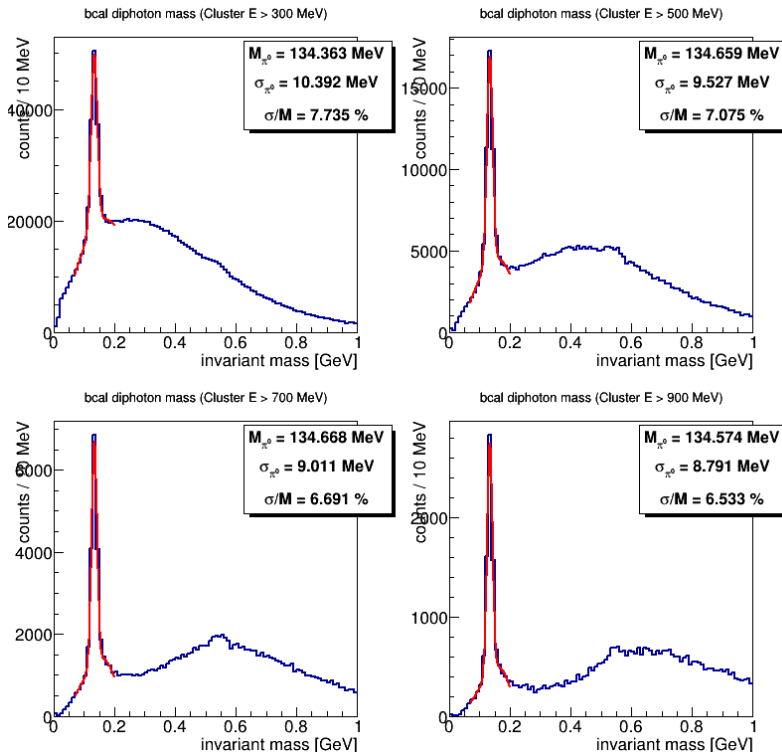
5.2.3 Additional calibrations

In addition to timing and gain calibrations, other calibrations were required. The wire chamber alignment was calibrated and checked using data without magnetic field. In that case, the particles move on straight tracks, which can be used to correct for wires sagging from their nominal position due to gravity [78, 79].

An iterative time-to-distance calibration was done for the CDC to properly account for the drift time of charge inside the straw tube. Both of these improve the CDC position and energy resolution.



(a) before calibration



(b) after calibration

Figure 5.3: Example plots showing the effect of BCAL gain calibrations on the π^0 mass and width for run 30999. Blue: Di-photon invariant mass distribution. Red: Fits using gaussian functions. The data was split into four subsets according to the cluster energy of the photons (see plot titles). Taken from [93].

5.3 Event reconstruction

In order to extract information about the reaction that triggered an event, it was important to identify the particles in the final state. The information from all detector components were combined for that purpose. For neutral particles clusters were identified in the calorimeters. The measured energies of the clusters were then used as the energy of the neutral particles. For charged particles, hits in the wire chambers were linked up and associated with clusters in the calorimeters and hits in the scintillation detectors. The resulting tracks were then analysed for their curvature, which, in combination with knowledge of the magnetic field map from within the detector, provided a measurement of the particles' momenta.

The process of linking up the hits created by charged particles in the wire chambers is called *tracking*. It was done in three stages. The first stage linked hits within FDC packages and adjacent CDC rings to create track segments. These were further combined to track candidates which served as starting parameters for the second stage. For this a Kalman filter [94, 95] was used to find the track parameters at the point of closest approach to the beam line. The Kalman filter started from the outside and stepped towards the centre of the detector updating the track parameters at each step. It accounted for energy loss, multiple scattering and the magnetic field within the detector. At this point, for the Kalman filter every track candidate with $p > 0.8 \text{ GeV}/c$ was assumed to be a pion while track candidates with less momentum were also fitted with a proton hypotheses. In the last stage the track was matched to the scintillation detectors or calorimeters to determine a start time. Using this information the drift time was taken into account and the track was refitted with an electron, pion, kaon and proton hypotheses [68].

The number of charged tracks in the detector reached ten or more and the number of hits in the wire chambers were accordingly very high (> 200). Therefore the possibility of reconstructing *fake tracks*, either through incorrectly linking up hits from two tracks or through combining a real track with random noise, was significant. These events were removed from the data sample in consecutive analysis steps.

The reconstruction procedure was computationally very expensive. For that reason it was coordinated for the whole collaboration and the results were saved in *hddm* (Hall-D Data Model) files. These did not contain all the hit information from the detectors but only the higher level track information. This reduced the size of the data set from 900 TB to 120 TB. The whole procedure required about six million CPU hours and was done using the computer resources at Jefferson Lab.

| | BCAL/RF ΔT (ns) | TOF/RF ΔT (ns) | FCAL/RF ΔT (ns) | SC/RF ΔT (ns) | CDC dE/dx (keV/cm) |
|-------|----------------------------|---------------------------|----------------------------|--------------------------|------------------------------|
| p | ± 1.0 | ± 0.6 | ± 2.0 | ± 2.5 | $> 1.0 + \exp(-4.0p + 2.25)$ |
| K^+ | ± 0.75 | ± 0.3 | ± 2.5 | ± 2.5 | $< 6.2 + \exp(-7.0p + 3.0)$ |
| K^- | ± 0.75 | ± 0.3 | ± 2.5 | ± 2.5 | $< 6.2 + \exp(-7.0p + 3.0)$ |

Table 5.2: Cuts applied to the data during the generation of ROOT trees in the skimming process [97]. ΔT , as defined in Eq. (5.1), is the time difference between a measured particle track and the time calculated under a certain mass hypothesis. dE/dx is the energy loss of a particle per distance travelled and is characteristic for different particle types. p denotes the particle's momentum.

5.4 Skimming and kinematic fitting

Although the reconstruction process already reduces the amount of data by storing track instead of hit information, it was still too much data to efficiently analyse it. To further reduce the data size the data was *skimmed* at Jefferson Lab, i.e. split in different sub data sets according to different event criteria. The resulting data was stored in ROOT trees [96], a data storage and handling solution commonly employed in nuclear and particle physics experiments developed at CERN.

For this analysis a pK^+K^- skim was used. Events fitting this topology, i.e. having at least one negatively and two positively charged tracks, were passed on to the ROOT tree. It was not required to have exactly two positively and one negatively charged track but up to three additional tracks were allowed in each event. This was to make sure that a spurious track, e.g. coming from noise in the detector, did not result in a good event being discarded. For each event multiple hits were recorded on the tagger, each corresponding to a beam photon. Only beam photons that had an associated time between -18.036 ns and 18.036 ns relative to the event reference time were kept (see Section 5.6.6). Each possible combination of beam photons and final state particles was then treated as a separate pK^+K^- event. During the generation of ROOT trees loose particle identification cuts were applied to help with the identification and to reduce the file size further. They are summarised in Table 5.2. dE/dx is a characteristic quantity for each particle type and has a momentum dependence. ΔT is the time difference between a measured particle track and the time calculated under a certain mass hypothesis as

$$\Delta T = t_{track} - \left(t_{RF} + \frac{z_{track} - z_{target}}{c} \right) \quad (5.1)$$

where t_{track} denotes the time of the track at its origin, t_{RF} denotes the overall event reference time, calculated as if the reaction happened in the target center, z denotes the z-position of either origin of the track or the target and c denotes the speed of light. The mass dependence is built-in into t_{track} which was calculated during the track reconstruction for different particle, and hence mass, hypotheses. In case of a detector with perfect resolution and correct particle ID

assignment, one would expect $\Delta T = 0$ ns.

Further criteria an event had to fulfil in order to pass into the ROOT tree were [97]:

- For a given charged track, at least one particle hypothesis must have had a hit in either: BCAL/FCAL/TOF/SC
- Timing cuts were applied only on the system with the best timing information available, in the order: BCAL/TOF/FCAL/SC. In other words, if a track had a hit in the TOF, then no cut was applied on the FCAL or SC time
- If the SC is the best-available detector, no cut was placed on the timing if the track has been matched to more than one SC hit, unless it was the only track in the combination
- Also, all kaons were cut that
 - Did not have a hit in one of these timing detectors
 - Did not have enough hits in the CDC to compute dE/dx
- A cut on the missing energy: $-3.0\text{GeV} < \text{missing energy} < 3.0\text{GeV}$

After this initial filtering and combinatorial selection a *kinematic fit* was performed for each possible combination (for details see [98]). It implemented both four-momentum conservation and the constraint that all tracks must have originated from the same position vertex to calculate a confidence level (CL) which quantified how well the given event matched the expected topology based on the kinematics and experimental resolutions. The CL was calculated by determining how much the particle kinematics, i.e. their momentum and position vectors, had to be changed to achieve perfect conservation of four-momentum and the same vertex for all three particles. The more the kinematics had to be adjusted the lower the CL. If an event had a high CL it meant that it matched the pK^+K^- topology well without significant change. The kinematic fit provided updated four-vectors for the particles which fulfil all constraints. These could be used instead of the measured kinematics to improve resolutions but introduced a possibility of biasing the results by forcing events to look like the specified topology. If not explicitly stated otherwise, this analysis used the measured parameters. The event criteria above were re-evaluated after the kinematic fit, using updated momentum and vertex information

The skimming process reduced the data from about 120 TB to 880 GB. This large reduction in data size and made it feasible to copy the data to Glasgow where the remaining analysis was performed.

| | BCAL/RF ΔT (ns) | TOF/RF ΔT (ns) |
|-------|----------------------------|---------------------------|
| p | ± 1.0 | ± 0.5 |
| K^+ | ± 0.5 | ± 0.3 |
| K^- | ± 0.5 | ± 0.3 |

Table 5.3: Timing cuts applied to combinations in ROOT trees during the pre-selection.

5.5 General event selection

After producing analysis trees from the reconstructed data, a DSelector [99], a GlueX specific analysis tool based on ROOT's TSelector, was used to analyse them within the ROOT data analysis framework.

In order to further reduce the amount of event combinations that did not fit the pK^+K^- reaction hypothesis, the following cuts were applied.

5.5.1 Photon beam energy cut

The extraction of the physics observables required a linearly polarised photon beam. As mentioned in Section 4.2.6 the degree of linear polarisation was determined for the photon range between 8.2 GeV and 8.8 GeV. Therefore, a cut was placed on the energy of the photon as measured by the photon tagger:

$$8.2 \text{ GeV} < E_\gamma < 8.8 \text{ GeV} \quad (5.2)$$

5.5.2 PID cuts

The cuts applied during the skimming process were not fully optimised and were chosen so as not to cut away any signal. In order to get a cleaner data sample, some of these cuts were tightened. The timing cuts applied to improve the particle identification are summarised in Table 5.3. Figure 5.4 shows ΔT plots after the skimming process. Each plot shows the time difference for a particle track with momentum p under the assumption it was either a proton or kaon calculated with Eq. (5.1). The different detectors shown correspond to different regions in the detector. The BCAL covers the central part, while the TOF covers the forward region. The red horizontal lines indicate the tighter cuts placed at this stage (see Table 5.3). The spectra show the expected distribution along $\Delta T = 0$ with some width due to resolution effects. In addition, bands coming in from either above or below 0 ns, stemming from misidentified particle tracks, are clearly visible. The cuts were chosen such that the background from these misidentified

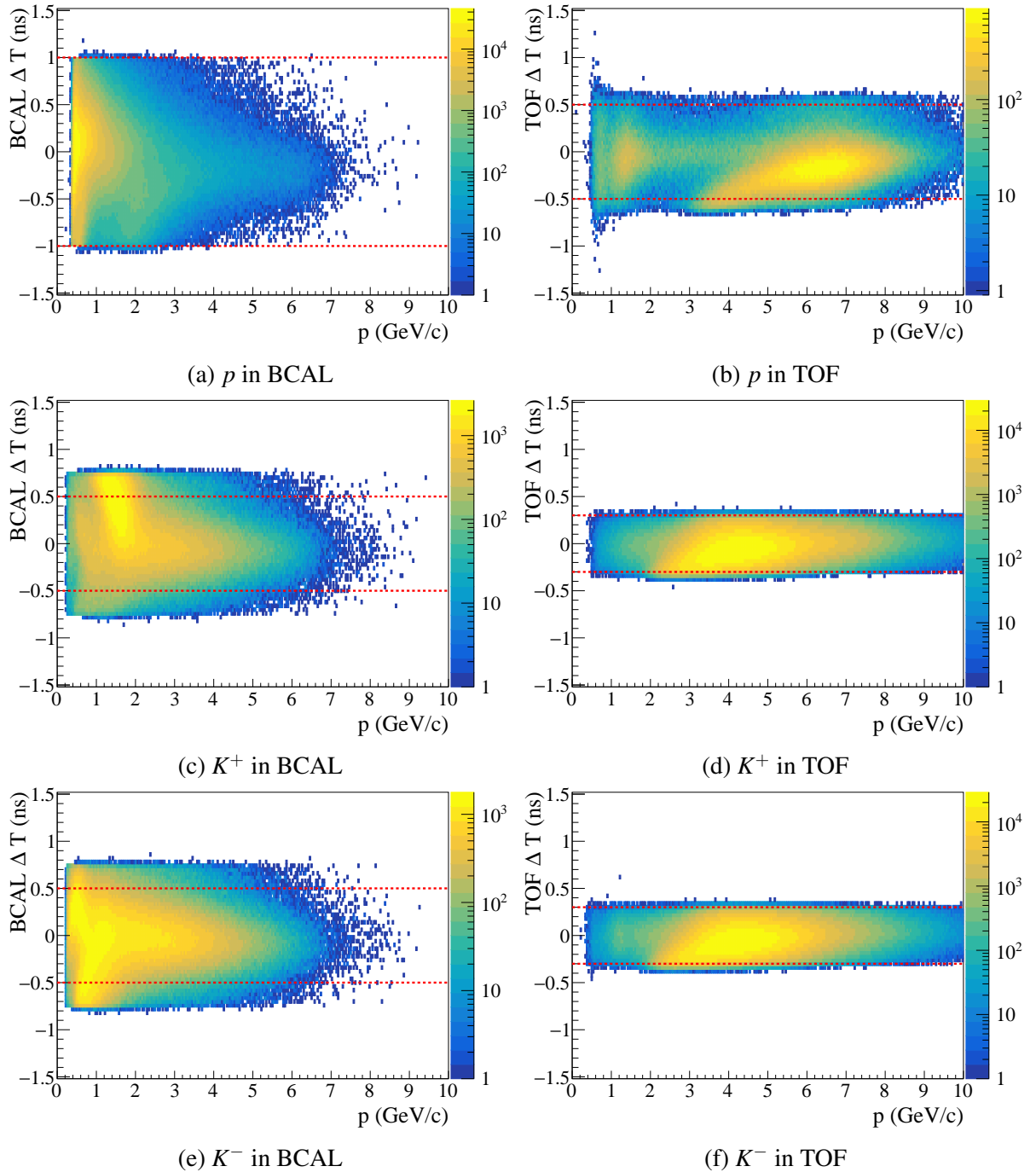


Figure 5.4: Difference between the timing signal of the measured track and a particle for a given momentum in the specified detector (see Eq. (5.1)). In a perfect scenario, one would expect a line at $\Delta T = 0$ ns. Bands coming in from above and below 0 ns stem from misidentified particle tracks. The red lines indicate the cut limits applied in the general event selection step (see Table 5.3).

particles was largely removed without removing the signal events. The cuts could have been optimised further by choosing momentum dependent cut limits but it was found that this was not necessary for this analysis (see Section 5.6.5).

5.5.3 Vertex cuts

To select reactions originating within the LH₂ target the reconstructed vertex was used to veto combinations with tracks not coming from inside the target cell:

$$51 \text{ cm} < z < 78 \text{ cm} \quad (5.3)$$

$$r < 1 \text{ cm} \quad (5.4)$$

where z denotes the z -coordinate of either of the particles in the final state in the GlueX lab frame and r denotes the distance of the vertex from the beamline. Figure 5.5 shows the xy - and z -spectra before and after event selection and the applied cuts. The xy -distribution clearly shows that most events originated from within the target cell. The z -distribution shows most events originating from within the target cell but also a few features in addition. The exit window of the scattering chamber can be seen at around 84 cm and much further downstream more structure is visible in the region between the CDC and FDC (around 180 cm). Before any cuts were placed it seems like more events came from the downstream side of the target cell than from the upstream side. This is not fully understood, but after applying the event selection the effect was not visible anymore. The distribution is fairly flat in the central region with fewer events very close to the cut limits. This is due to the fact that the cuts were not applied on the combined event vertex but for each track individually.

5.6 Exclusive event selection

All cuts discussed so far are valid to select protons and kaons in the final state. In a traditional analysis exclusive events would be selected by making a series of cuts, based on energy and momentum conservation, on quantities such as the missing mass squared or angles. In this work, a kinematic fit was performed to calculate a confidence level which is highly correlated with these quantities. Therefore, a cut on the CL would implicitly cut on them as well. However, it was important to confirm this by checking their distributions with and without CL cut.

To select the exclusive reaction $\vec{\gamma}p \rightarrow K^+\Lambda(1520) \rightarrow K^+K^-p$ the following cuts were applied.

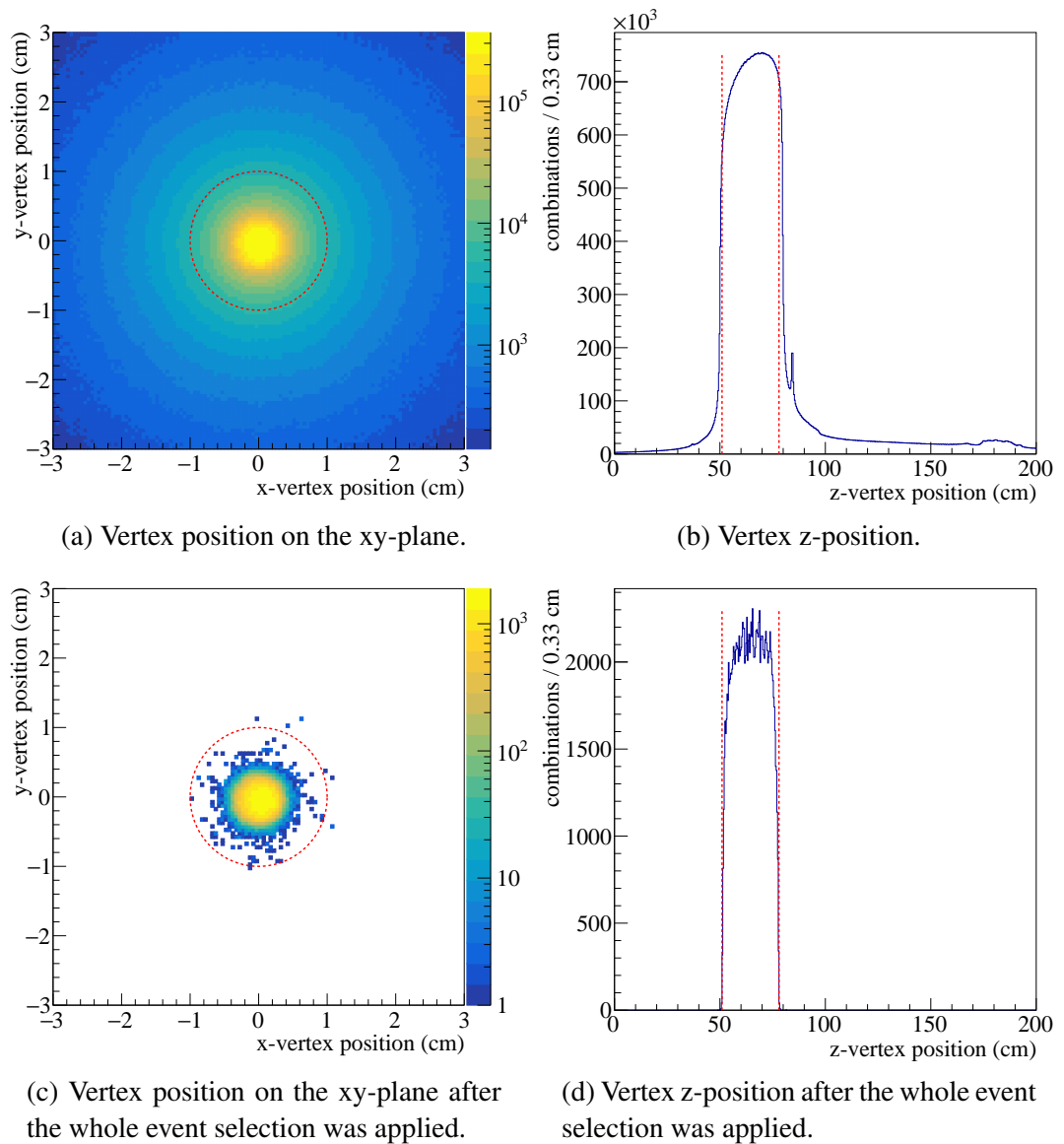


Figure 5.5: Vertex position in xy-plane and in z-direction before and after the full event selection. The red lines indicate the cut limits.

5.6.1 Confidence level cut

The most important cut was placed on the confidence level resulting from the kinematic fit with vertex and four-momentum conservation constraints (see Section 5.4). The determination of the CL was a complicated process dependent on many tuning parameters, such as resolutions of the many detector components. There was not a straightforward answer to what the best value for a CL cut was, so the effect of this cut was investigated.

To study the effect of the choice of the CL cut value, the pK^- invariant mass spectrum between $1.44 \text{ GeV}/c^2$ and $1.62 \text{ GeV}/c^2$ was plotted for 100 CL values between 10^{-10} and 10^{-1} . Then a gaussian function plus a first order polynomial was fitted to the data, to extract an estimate

for the $\Lambda(1520)$ signal and the background yields by integrating the functions over the specified range. The signal and background yields were then used to calculate a figure-of-merit (FOM):

$$\text{FOM} = \frac{\text{signal}}{\sqrt{\text{signal} + \text{background}}} \quad (5.5)$$

This FOM is a good choice in cases where the signal rate is to be determined accurately (Chapter 39, [15]). That means that the yield of a certain signal has to be measured. Since this involves optimising the signal this FOM is a good choice to study the effect of the CL cut. A selection of the fits used to determine signal and background is plotted in Figure 5.6. The extracted FOMs are depicted in Figure 5.7. The results indicate that a CL cut of around $\text{CL} = 10^{-6}$ yields the best FOM. It was therefore chosen as cut limit and is indicated by the dashed line in Figure 5.7. Only events with

$$\text{CL} > 10^{-6} \quad (5.6)$$

were kept. Figure 5.8a shows the CL distribution before and after the complete event selection in this Chapter. The bin width on the x-axis is logarithmic to have equally spaced CL bins on this log-log plot. The red histogram shows the CL distribution after the skimming was done. The blue histogram shows the CL distribution after the full event selection. Since the bin width is much larger towards high CL one can see a rising slope. Figure 5.8b shows the CL distribution after the complete event selection with a linear x-axis.

5.6.2 Missing mass squared

Since the reaction of interest was measured in a fully exclusive final state, energy and momentum conservation required that the following relation, also known as the missing mass squared, holds true

$$MM^2 = (P_\gamma + P_{\text{target}} - P_p - P_{K^-} - P_{K^+})^2 = 0 \text{ GeV}^2/c^4 \quad (5.7)$$

where P denotes the particles' four-momenta. For a real experiment with finite resolutions the missing mass squared has a distribution around $0 \text{ GeV}^2/c^4$. Note that this quantity is strongly correlated to the CL of the kinematic fit. Therefore, a cut on the CL will implicitly cut on the missing mass. The distribution of the missing mass squared before and after the CL cut are shown in Figure 5.9. The blue histogram shows the MM^2 distribution before the CL cut was applied and the green histogram shows the same distribution after the CL cut was applied. It is clear that the CL cut removed predominantly event combinations that did not fulfil Eq. (5.7). Combinations close to $0 \text{ GeV}^2/c^4$ were kept. The structure visible to the right of the main peak before the CL cut was applied, which probably stemmed from misidentified pions, was removed.

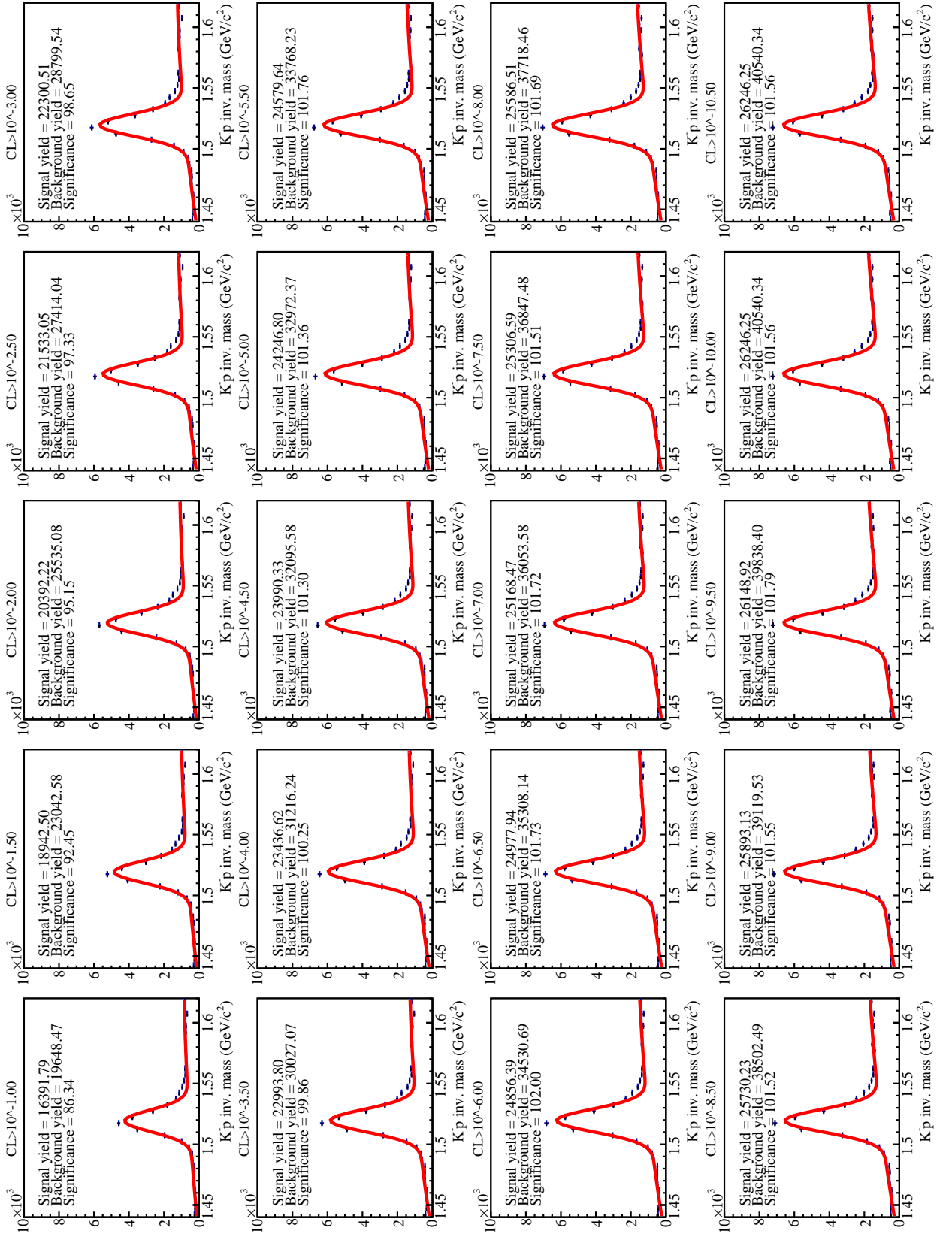


Figure 5.6: Invariant mass of pK^- between $1.44 \text{ GeV}/c^2$ and $1.62 \text{ GeV}/c^2$ with a fit to determine a figure-of-merit for various kinematic fit CL cuts.

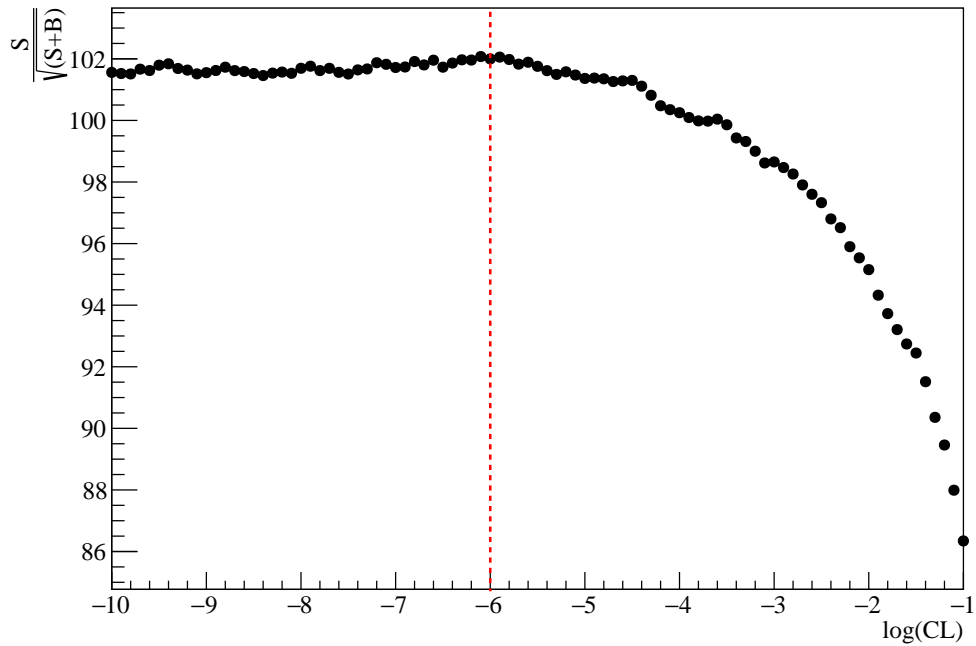
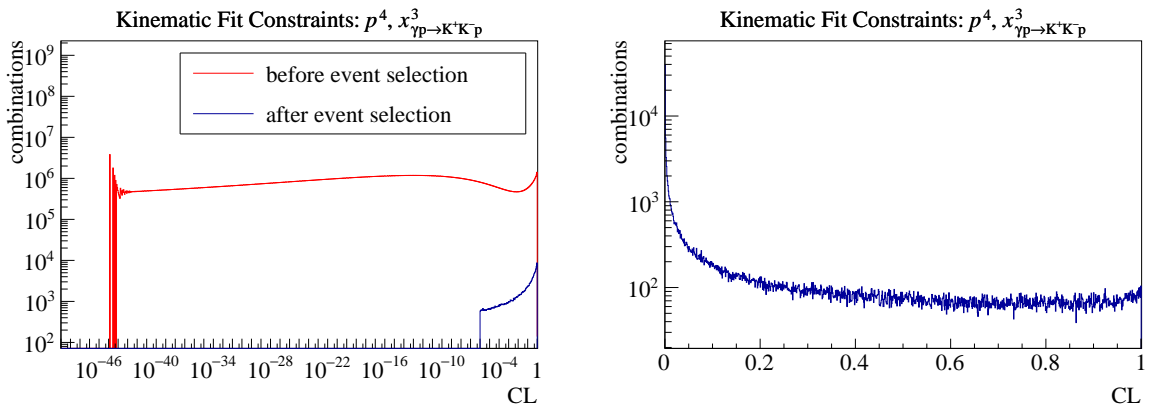


Figure 5.7: The figure-of-merit as extracted from fits as in Figure 5.6 is plotted against $\log(\text{CL})$. The red dashed line indicates the CL cut value chosen for this analysis.



(a) CL distributions with logarithmic x-binning.

(b) CL distribution after event selection with linear x-axis binning.

Figure 5.8: CL distributions before and after the event selection with logarithmic and linear x-binning. The rising slope approaching a CL of one in the left plot is due to the logarithmic binning in CL.

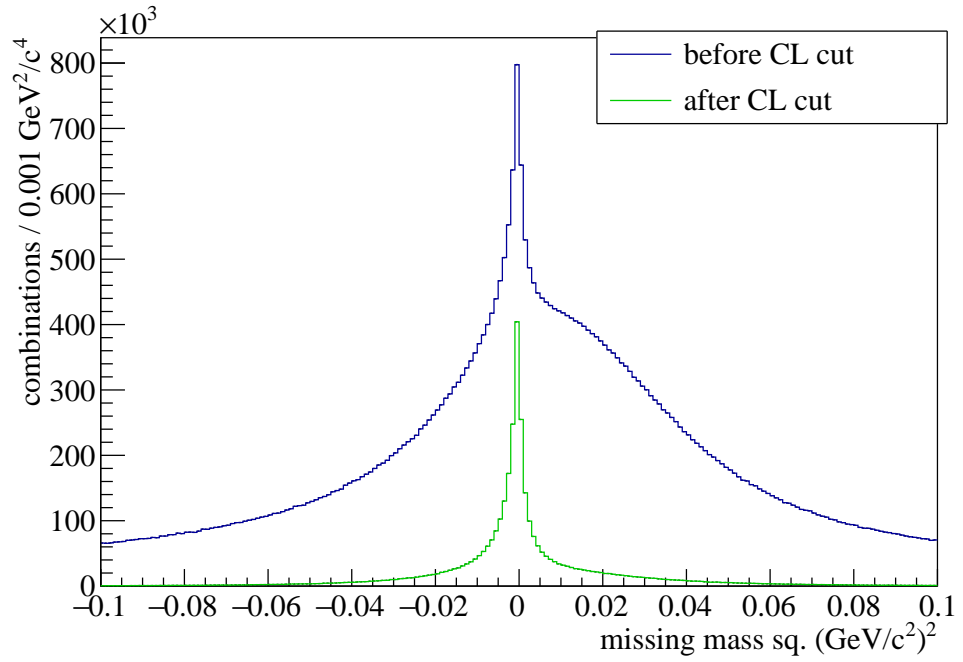


Figure 5.9: Missing mass square distribution before and after the CL cut.

5.6.3 ϕ and θ difference

The reaction kinematics also require that the following relations hold true

$$\phi_{\Lambda, \text{lab}} - \phi_{K^+, \text{lab}} = 180^\circ \quad (5.8)$$

$$\theta_{\Lambda, \text{CMS}} - \theta_{K^+, \text{CMS}} = 180^\circ \quad (5.9)$$

where ϕ and θ denote the particles' angles in the laboratory (lab) or overall centre-of-mass frame (CMS). The relations arise from the fact that the $\Lambda(1520)$ and K^+ are produced back-to-back in the CMS. These relations were included in the kinematic fit through conservation of momentum. Therefore, a cut on the CL will also implicitly cut on the angles. The differences of both angular distributions, before and after the CL cut was applied, are shown in Figure 5.10. The ϕ difference shows the expected distribution around 180° before and after the CL cut. This distribution was not affected by misidentification but would have shown differences if there was a significant amount of unbalanced transverse momentum, i.e. more or less than three particles in the final state. The θ_{CMS} difference, however, shows the histogram before the CL cut shifted towards larger differences. After the CL cut was applied the distribution peaked at 180° . The θ_{CMS} difference was calculated in the CMS. Particle misidentification, which was seen before in the MM^2 (see Figure 5.9), could have caused this change in shape which was recovered by cutting on the CL.

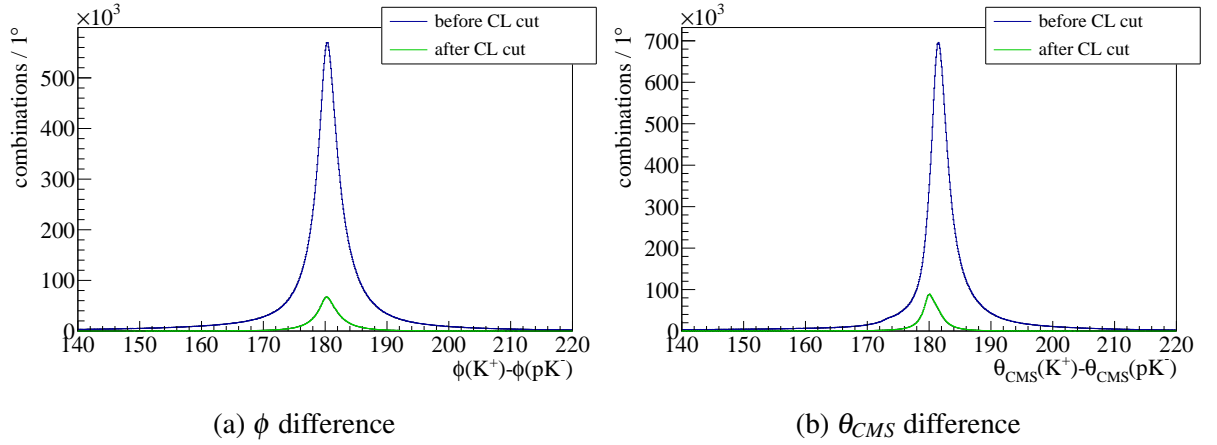


Figure 5.10: The plots show the ϕ and θ_{CMS} differences between the K^+ and the combined pK^- in the lab and overall centre-of-mass system according to Eqs. (5.8) and (5.9).

5.6.4 Invariant Mass cut

The resulting pK^- spectrum after all of the cuts were placed is depicted in Figure 5.11. The $\Lambda(1520)$ peak is clearly visible at around $1.52 \text{ GeV}/c^2$.

A large background for the study of hyperons in the pK^-K^+ final state arises from $\phi(1020)$ mesons that are produced with a large cross-section and decay to K^+K^- . To assess the proportion of $\phi(1020)$ in the background under the $\Lambda(1520)$ the K^+K^- and pK^- invariant masses squared are plotted on a Dalitz plot (Figure 5.12). One can see a strong band of $\phi(1020)$ mesons and even a band of $\rho(770)$ mesons decaying to misidentified $\pi^+\pi^-$. Since the production cross-section of the ρ is much bigger than that of the $\phi(1020)$ and the momenta of the decay particles are very high, it is expected to see a small fraction of pions being misidentified as kaons. A $\rho(770)$ with its decay products misidentified as kaons shows up at a mass of about $1.22 \text{ GeV}/c^2$, which agrees with the band seen in Figure 5.12. No overlap is seen between the $\phi(1020)$ and the $\Lambda(1520)$ bands for the kinematics under study. Also the $\rho(770)$ band does not stretch down to the $\Lambda(1520)$ band. At small pK^- invariant masses the momentum of the K^- is small and misidentification of a pion as a kaon is much less likely. Figure 5.13 shows the pK^- invariant mass with and without an additional cut to veto the two mesons as indicated by the red dashed line in Figure 5.12. It is clear that there is no $\phi(1020)$ and $\rho(770)$ background below $1.8 \text{ GeV}/c^2$, so these mesons did not contribute to the background of this analysis.

To remove combinations not coming from a $\Lambda(1520)$ decay a cut, as indicated by the red dashed lines in Figure 5.11 was placed

$$1.46 \text{ GeV}/c^2 < \text{inv. mass } (pK^-) < 1.58 \text{ GeV}/c^2 \quad (5.10)$$

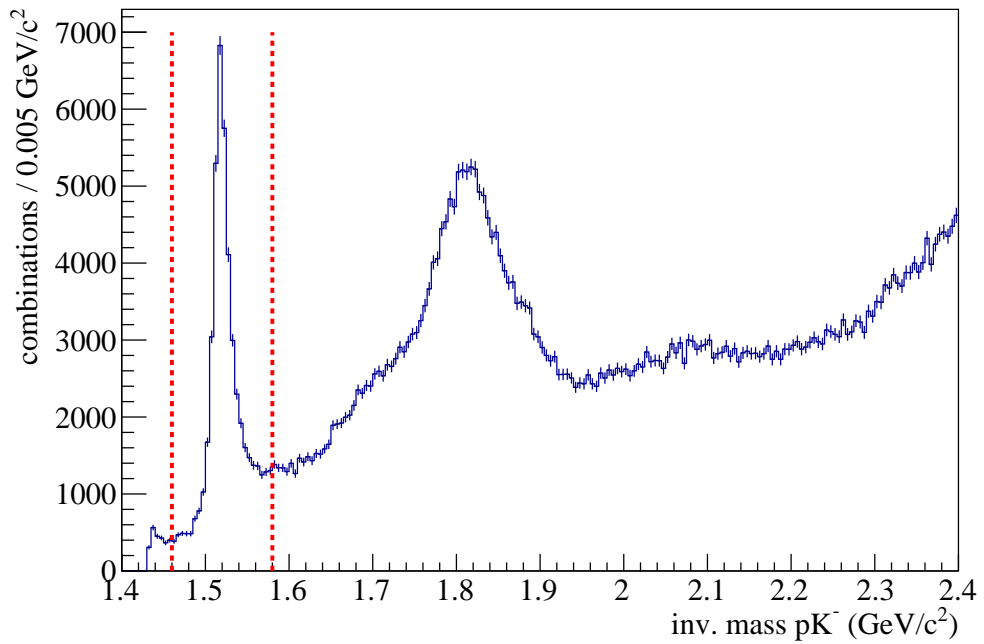


Figure 5.11: Invariant mass of pK^- after all cuts. The red dashed lines indicate the cut placed on the data to single out the $\Lambda(1520)$.

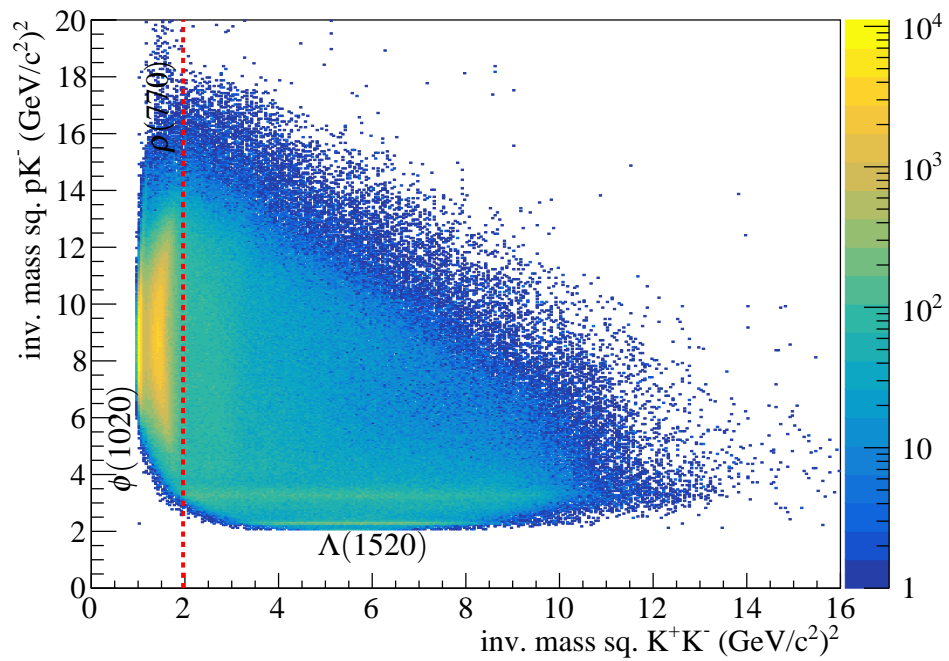


Figure 5.12: Dalitz plot of pK^-K^+ after all cuts. The red dashed line indicates the cut tried on the data to veto the $\phi(1020)$ and $\rho(770)$.

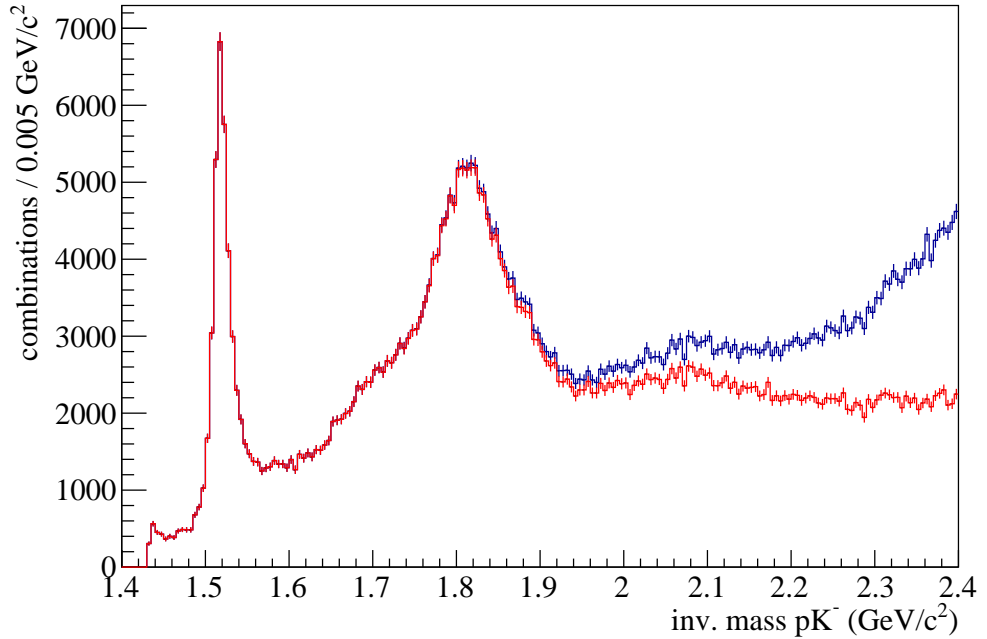


Figure 5.13: Comparison of invariant mass of pK^- after all cuts (blue) with additional cut against $\rho(770)$ meson (red).

In general, it can be assumed that it is desirable for an analysis to have as few cuts as possible. It was shown that a CL cut alone yielded the distributions in MM^2 , ϕ difference and θ_{CMS} difference, that were expected in an exclusive final state. In connection with a cut on the pK^- invariant mass around the $\Lambda(1520)$ mass this resulted in an event sample almost free from non- pK^+K^- events.

5.6.5 PID after cuts

To check the quality of the event selection and the rejection of non- pK^-K^+ background the ΔT PID plots were studied again. Figure 5.14 shows the same PID plots as before (Figure 5.4) but with the discussed event selection applied. In general, one can see that the event sample contains far fewer misidentified particle tracks than before. It is interesting to note that there seems to be a high momentum/low momentum split in the data. For the following extraction of polarisation observables the data was binned in momentum transfer squared (see Section 5.6.9) and the highest $-(t - t_{\text{min}})$ -bin had an upper limit of $2 \text{ GeV}^2/c^2$. If this cutoff was imposed on the PID plots the low momentum part of the K^+ as well as the high momentum part of the p and K^- vanished. This is shown in Figure 5.15. The kinematics of $\Lambda(1520)$ production and decay favoured a low momentum K^- and proton. These could be identified well by the GlueX detector setup. Due to strangeness conservation, the third (positively charged, high momentum) track was therefore very likely to be a K^+ . Figure 5.15 shows very clean distributions confirming this.

The fact that there was a high momentum p/K^- and low momentum K^+ part seemed to indicate that there were possibly two or more different reaction mechanisms at play. Unfortunately, the statistics in this dataset were not sufficient to analyse the other mechanisms. Future analyses using the full GlueX statistics might be able to shine more light on this issue.

5.6.6 Tagger accidentals

The electron beam provided by CEBAF has a bunch structure with a frequency of 249.5 MHz (i.e. timing separation of 4.008 ns between bunches). For every recorded event there were about 60-80 hits on the tagger system but only one corresponded to the photon that produced the triggered event. Even after applying all the cuts in the event selection, as discussed above, there were still multiple tagger hits per event. They are referred to as *random background*, or *tagger accidentals*. In order to account for the random tagger photons in the data, a background subtraction has been performed. To do that, events from four beam bunches before and after the bunch in coincidence with the event in the main GlueX detector were analysed. The regions spanned by these bunches are referred to as *side bands*. The timing spectrum of these events is depicted in Figure 5.16.

The underlying assumption for the background subtraction is that the random tagger photons contributed as much to the background under the coincidence peak as they did to the side bands. Each event combination was given a weight, assigned depending on the timing of its tagger photon. Combinations from the main bunch and its two nearest neighbours, i.e. three bunches, got the weight 1, while combinations from the side band peaks were given the weight -0.5 , as six bunches were included. Taking into account the two nearest neighbours of the coincidence peak made it possible to assess if any signal from the prompt peak leaked into the side bands. It is clear from Figure 5.16 that this is not the case.

5.6.7 Handling of multiple combinations in final state

Even after the event selection described above was applied, it could happen that more than one combination of final state particles and tagger hits was left. In the case these supernumerary combinations arose from multiple tagger photons, the previously discussed tagger random background subtraction accounted for them. In less than 1% of the cases it happened that more than one combination of final state particles, e.g. through background tracks that were allowed through the skimming process, survived all cuts. That meant that the event selection could not unambiguously identify a pK^+K^- event from the given tracks. In this case the whole event was discarded. This made sure that the angular distributions were not distorted by wrong combinations, that could have a very different angular distribution from the true events.

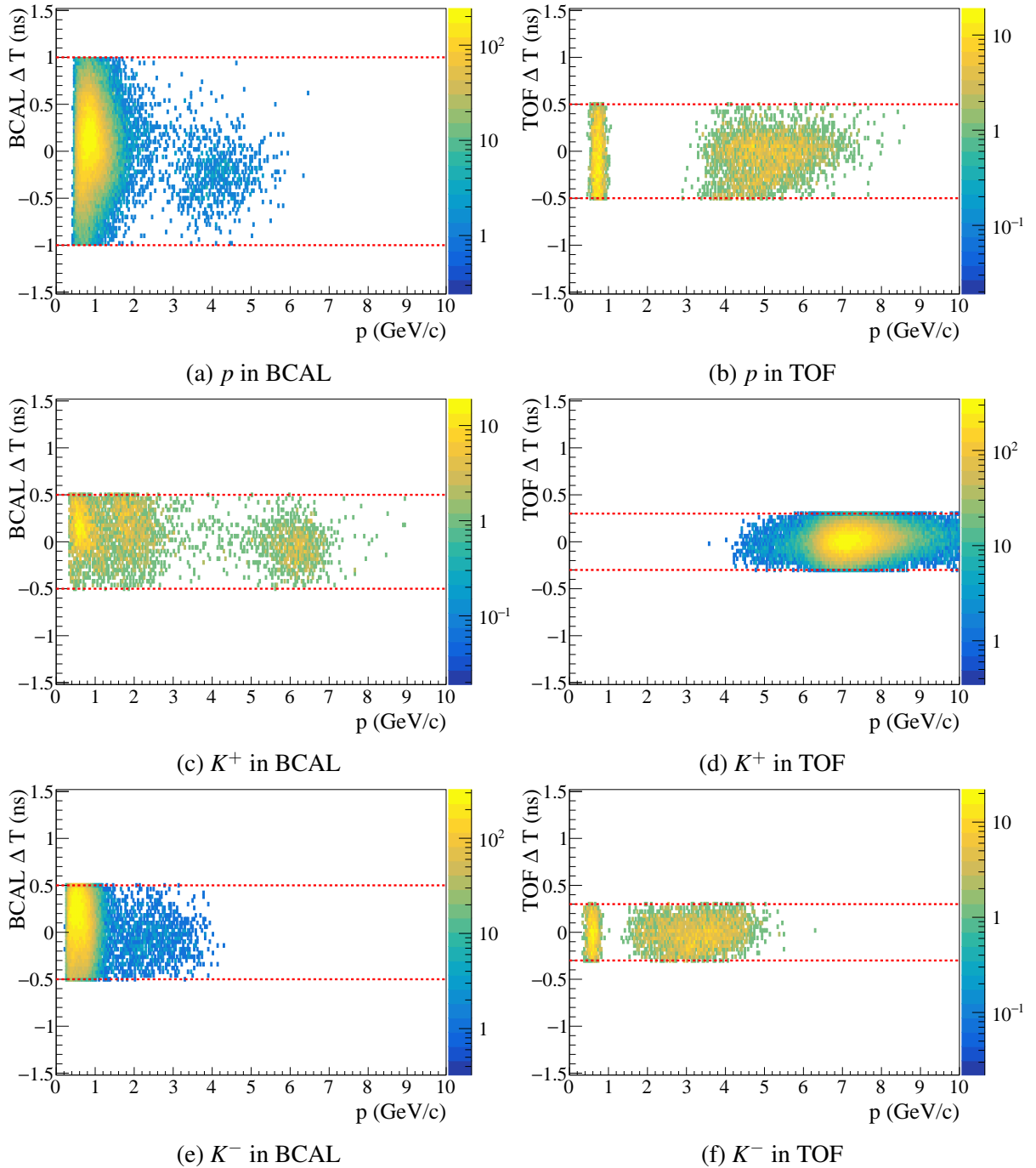


Figure 5.14: Difference between the timing signal of the measured track and a particle for a given momentum in the specified detector after previously discussed cuts were applied. In a perfect scenario one would expect a line at $\Delta T = 0$. The red lines indicate the cut limits applied in the general event selection (see Table 5.3).

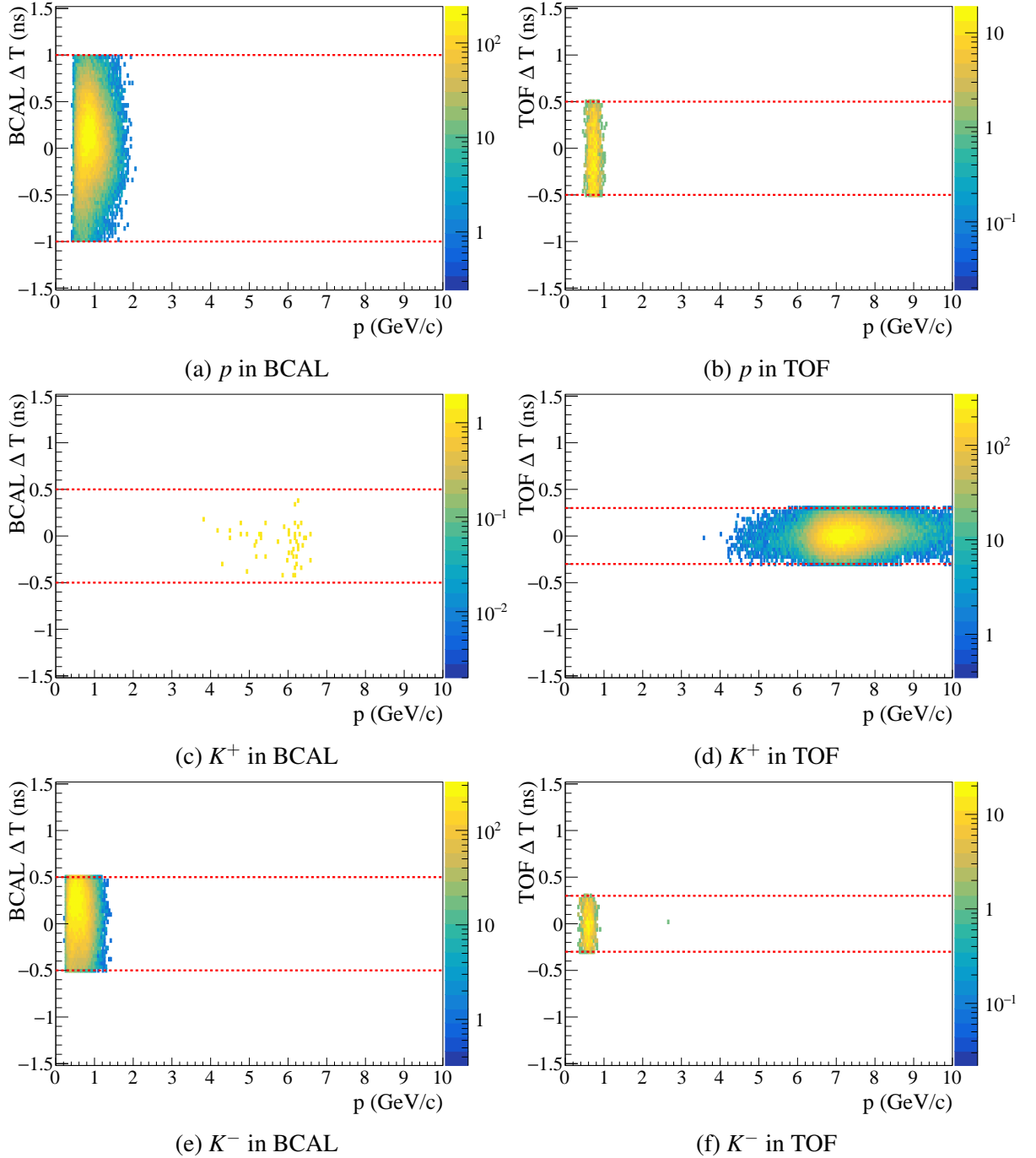


Figure 5.15: Difference between the timing signal of the measured track and a particle for a given momentum in the specified detector after previously discussed cuts and an additional $-(t - t_{\min}) < 2\text{GeV}^2/c^2$ cut were applied. In a perfect scenario one would expect a line at $\Delta T = 0$. The red lines indicate the cut limits applied in the general event selection (see Table 5.3).

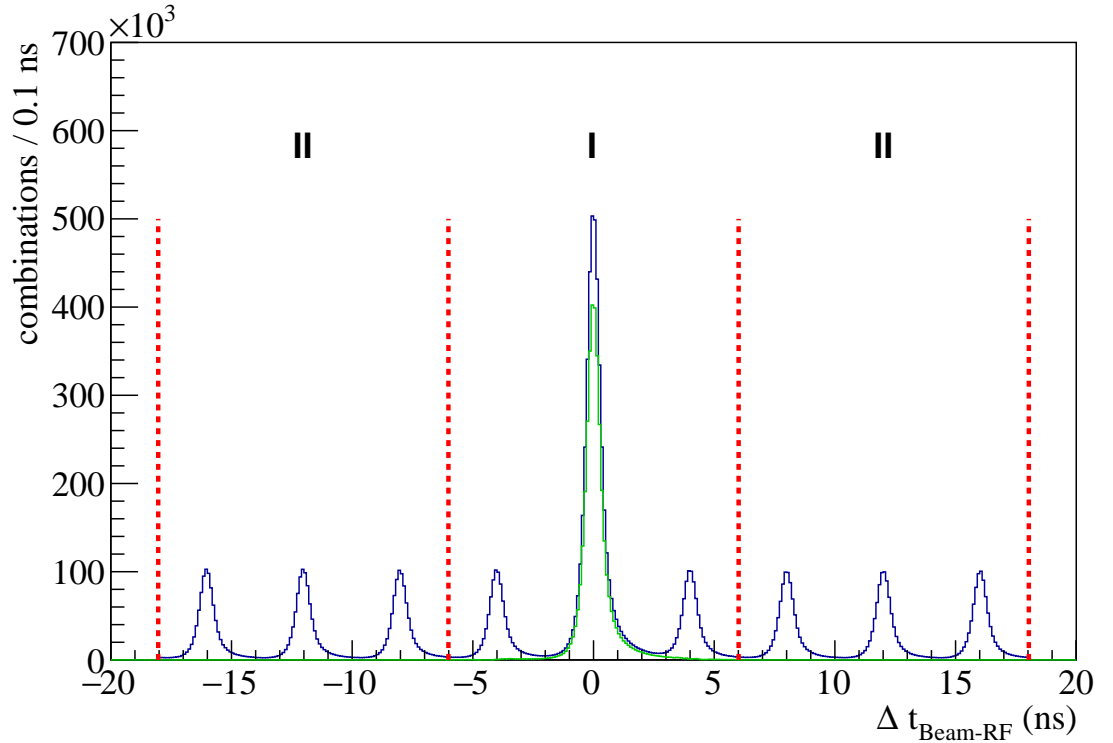


Figure 5.16: Timing spectrum of pK^-K^+ events. The red lines indicate the regions called *side bands* (II) and *coincidence peak* (I). The blue histogram shows the full timing spectrum while the green histogram shows what is left after the random subtraction has been performed.

5.6.8 sPlot technique

After applying all cuts the $\Lambda(1520)$ baryon appeared as a clear peak in the pK^- invariant mass spectrum (see Figure 5.11). Although the cuts already removed most of the background, there was still some left under the peak. This background was of the same final state but produced by a different mechanism. Therefore, it could not be removed by cuts. In order to separate it from $\Lambda(1520)$ events the so-called sPlot technique was used. It was introduced by Pivk and Le Diberder in 2005 [100]. Their paper gives a very good account of how it works and how to use it, and they discuss the underlying statistical and mathematical principles extensively. Therefore, only a summarising overview of the sPlot technique will be given here. The sPlot technique is well established and was used in many peer-reviewed publications by LHCb (e.g. [101]) but also in low-energy hadron physics experiments (e.g. [102]).

The aim of sPlot is to unfold data distributions. In this case $\Lambda(1520)$ events should be separated from pK^+K^- background events. To do that, a *discriminatory variable* is required. This variable has different (known) distributions for signal and background. The discriminatory variable has to be uncorrelated with the variable whose signal and background distributions have to be unfolded. In the case of the current analysis, the angular distributions of the final state particles needed to be fitted (see Sections 6.1 and 6.2) and the invariant mass distribution of pK^- was chosen as

discriminatory variable. The $\Lambda(1520)$ was visible with a clear peak while the background was assumed to be described by a polynomial over that region.

In the next step, an event-by-event extended maximum likelihood fit to the discriminatory variable was performed to determine the contributions coming from $\Lambda(1520)$ and other pK^+K^- background. For this work a $\Lambda(1520)$ shape was produced from Monte Carlo generated $\Lambda(1520)$ events with a relativistic Breit-Wigner distribution including a Blatt-Weisskopf barrier factor for orbital angular momentum $L = 2$ [103]. Mass ($1519.5 \text{ MeV}/c^2$) and width ($15.6 \text{ MeV}/c^2$) were set to PDG values [15]. As background a 2nd degree Chebychev polynomial was used. The fit was performed within the *brufit* framework [104] which utilises RooFit [105], an extension to the ROOT data analysis framework.

The resulting fits for all $-(t - t_{\min})$ -bins are shown in Figures 5.17 to 5.24. On the left hand side of each plot the overall fit result is shown in red with the $\Lambda(1520)$ component depicted as dashed black line and the Chebychev as dashed red line. On the right hand side of each plot the fit residuals are shown on the top plot and the pull histogram is shown on the bottom plot. In addition to the free parameters describing the Chebychev polynomial and the yields of the fit components, three parameters were included to account for systematic uncertainties in the $\Lambda(1520)$ shape. The *alpha* parameter was the width of a gaussian function that was convoluted with the $\Lambda(1520)$ shape. The *off* parameter allowed for an offset in x in case the mass used for generation was not exactly the mass seen in data. The *scale* parameter was a factor applied to the x-axis of the $\Lambda(1520)$ shape. It accounted for the difference in width. If a perfect model would have been used *alpha* and *off* would have been zero and *scale* would have been one. One can see in the fits that in all cases the fit quality is very good. *alpha* and *offset* were almost always compatible with zero and the *scale* parameter was close to one. The width used in the simulation seemed to be slightly smaller than the width in data.

The yields and covariance matrices extracted from the fits were used in a second step to calculate event-by-event *sWeights* for signal and background. These weights were applied to the angular distributions on an event-by-event basis. This could not only be done for the signal but also for the background. The angular distribution of the K^- in the Gottfried-Jackson frame (see Figure 2.2), which was used to determine spin-density matrix elements (see Section 6.2), is shown in Figure 5.25. There one can see that the ϕ_{GJ} distribution looked very different in signal and background. The θ_{GJ} distributions were fairly similar with the background distribution being slightly broader and flatter. Note that the background distribution was scaled such that signal and background have the same integral. This was done for easier comparison between the distributions.

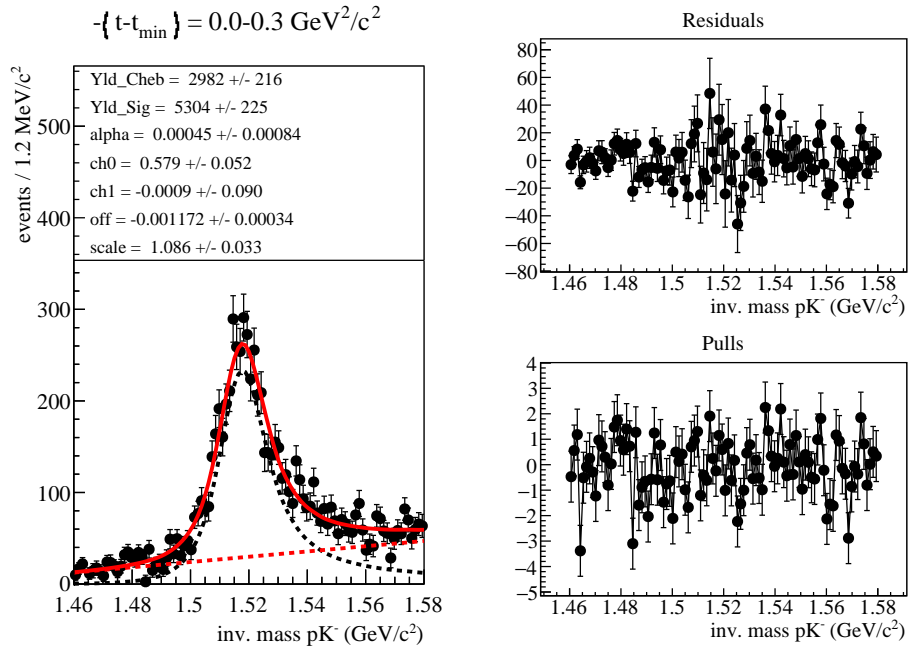


Figure 5.17: Left: sFit of the pK^- invariant mass. The red dashed line is a Chebychev function used to approximate background. The black dashed line is the simulated Breit-Wigner shape for a $\Lambda(1520)$. The solid red line is the resulting fit to the data.

Right: Fit residual on top and pull distribution on bottom.

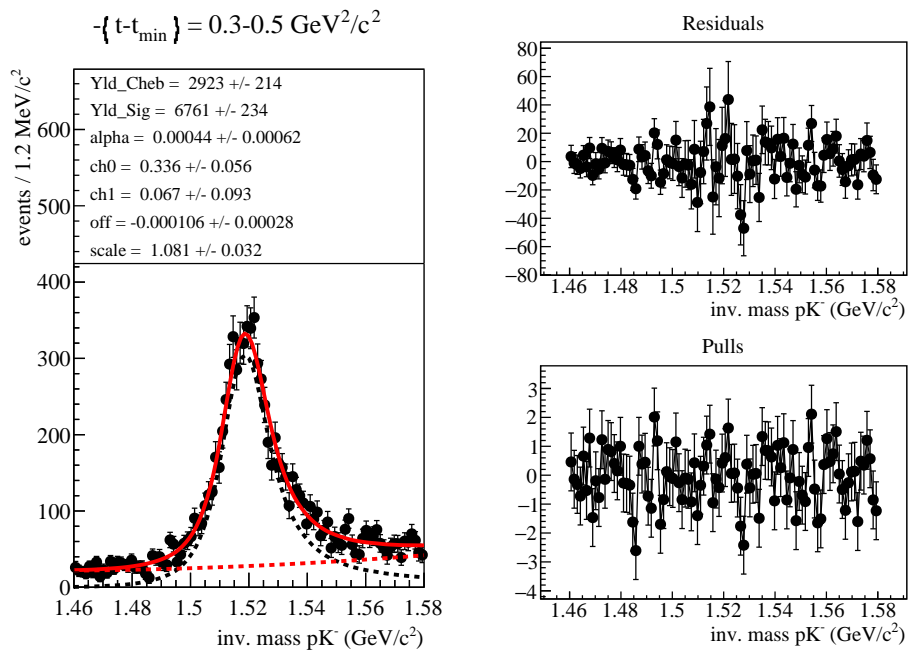


Figure 5.18: Left: sFit of the pK^- invariant mass. The red dashed line is a Chebychev function used to approximate background. The black dashed line is the simulated Breit-Wigner shape for a $\Lambda(1520)$. The solid red line is the resulting fit to the data.

Right: Fit residual on top and pull distribution on bottom.

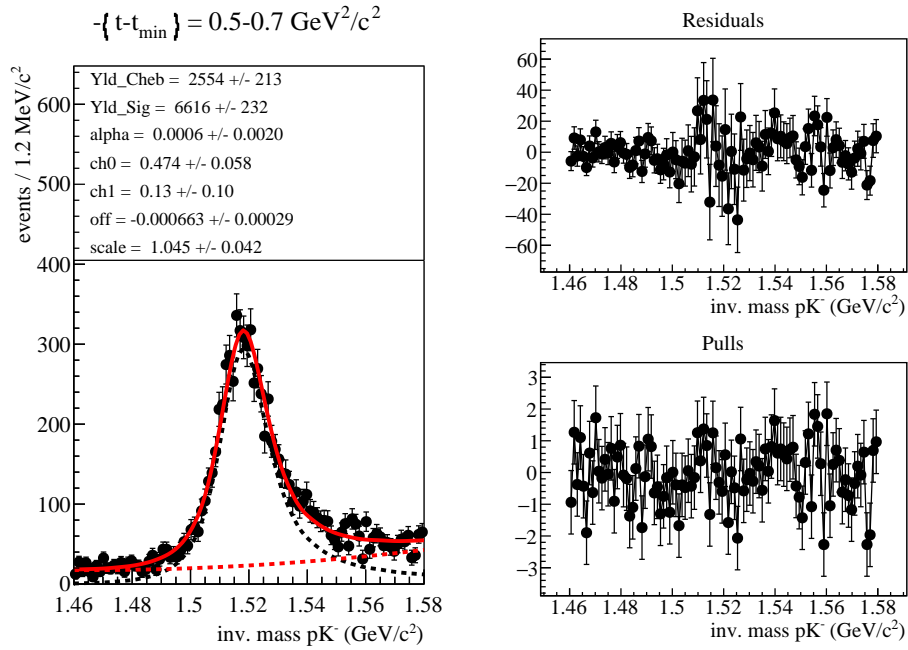


Figure 5.19: Left: sFit of the pK^- invariant mass. The red dashed line is a Chebychev function used to approximate background. The black dashed line is the simulated Breit-Wigner shape for a $\Lambda(1520)$. The solid red line is the resulting fit to the data. Right: Fit residual on top and pull distribution on bottom.

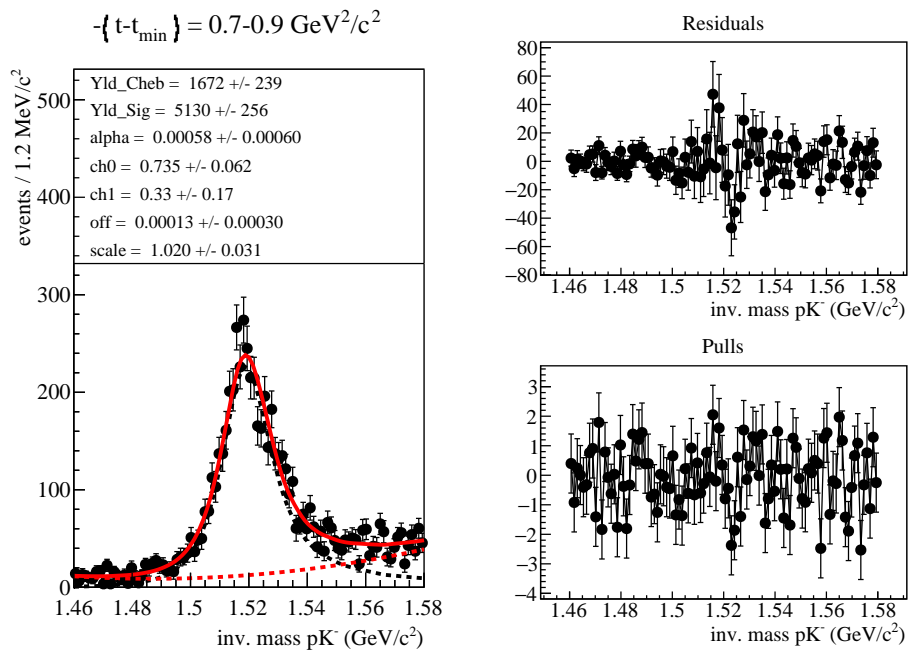


Figure 5.20: Left: sFit of the pK^- invariant mass. The red dashed line is a Chebychev function used to approximate background. The black dashed line is the simulated Breit-Wigner shape for a $\Lambda(1520)$. The solid red line is the resulting fit to the data. Right: Fit residual on top and pull distribution on bottom.

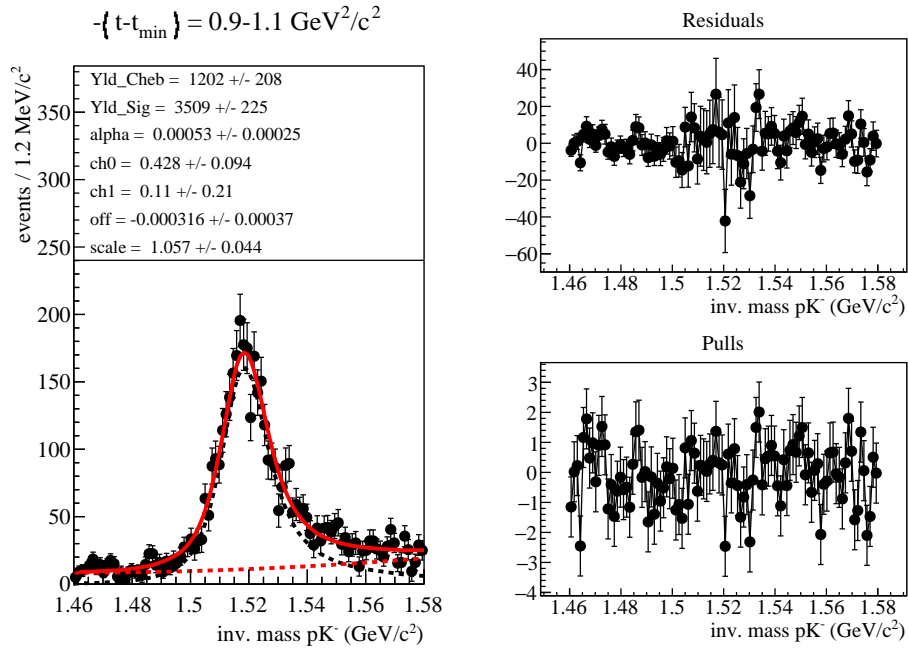


Figure 5.21: Left: sFit of the pK^- invariant mass. The red dashed line is a Chebychev function used to approximate background. The black dashed line is the simulated Breit-Wigner shape for a $\Lambda(1520)$. The solid red line is the resulting fit to the data. Right: Fit residual on top and pull distribution on bottom.

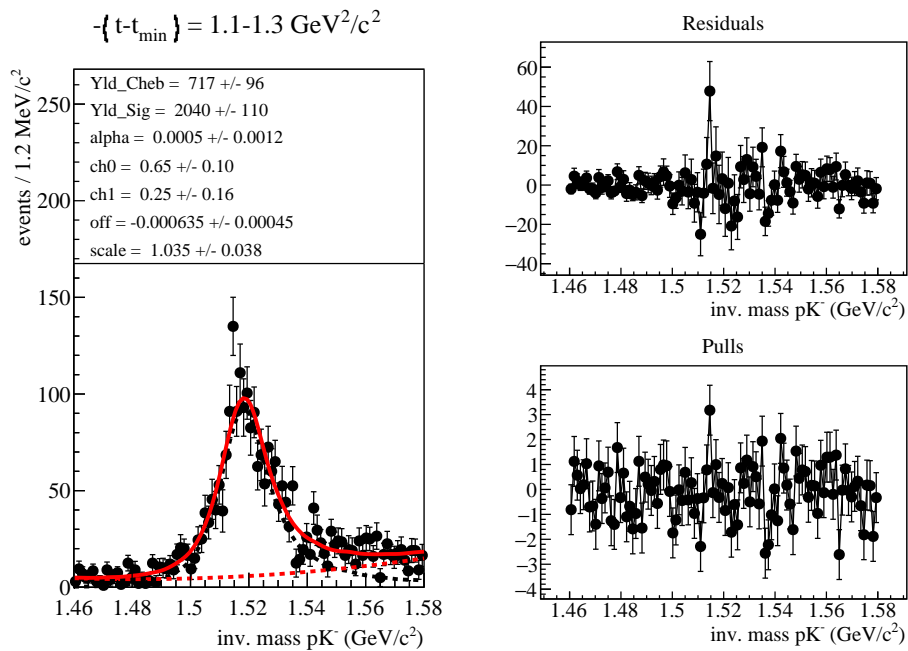


Figure 5.22: Left: sFit of the pK^- invariant mass. The red dashed line is a Chebychev function used to approximate background. The black dashed line is the simulated Breit-Wigner shape for a $\Lambda(1520)$. The solid red line is the resulting fit to the data. Right: Fit residual on top and pull distribution on bottom.

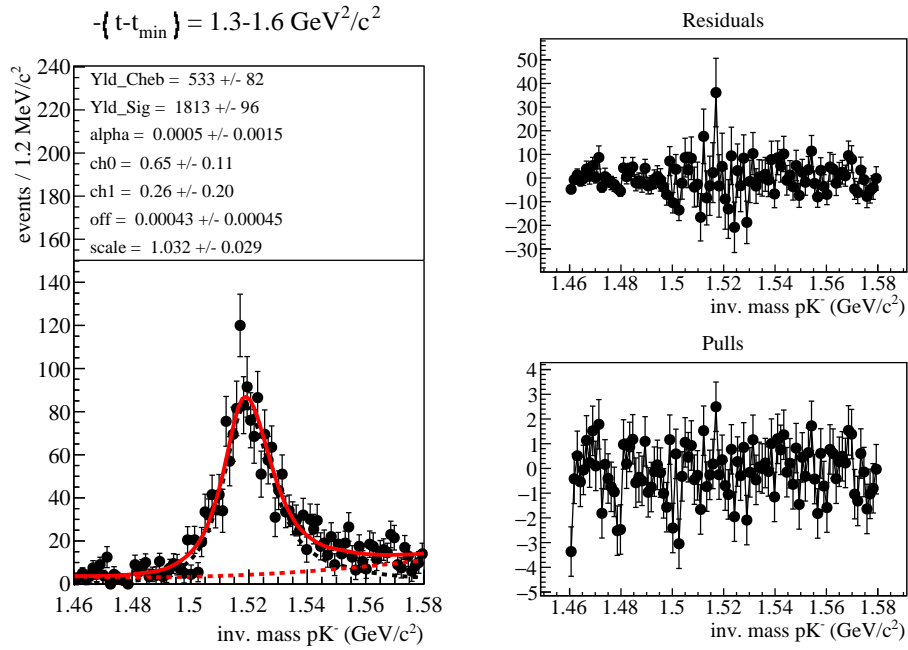


Figure 5.23: Left: sFit of the pK^- invariant mass. The red dashed line is a Chebychev function used to approximate background. The black dashed line is the simulated Breit-Wigner shape for a $\Lambda(1520)$. The solid red line is the resulting fit to the data.

Right: Fit residual on top and pull distribution on bottom.

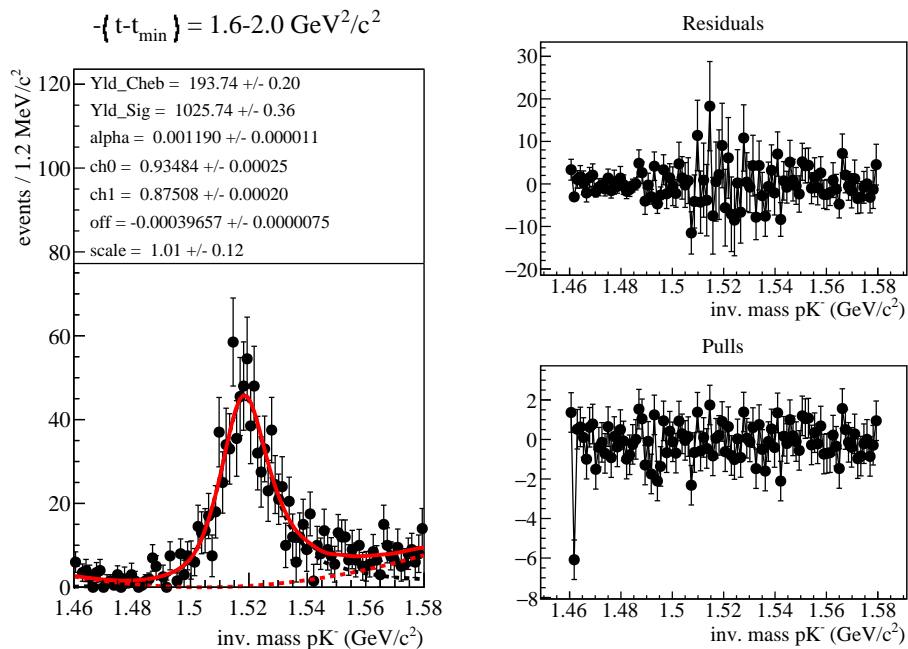


Figure 5.24: Left: sFit of the pK^- invariant mass. The red dashed line is a Chebychev function used to approximate background. The black dashed line is the simulated Breit-Wigner shape for a $\Lambda(1520)$. The solid red line is the resulting fit to the data.

Right: Fit residual on top and pull distribution on bottom.

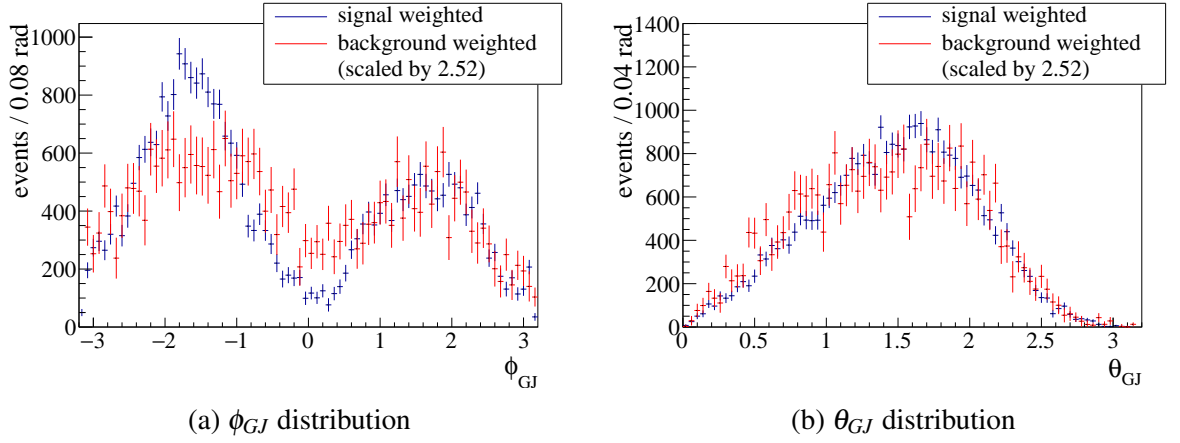


Figure 5.25: Comparison of angular distribution of K^- in Gottfried-Jackson frame with signal (blue) and background (red) weights applied.

5.6.9 Momentum transfer distribution

The sWeights are applied on an event-by-event basis to have a background free sample of $\Lambda(1520)$. Figure 5.26 shows the resulting distribution of momentum transfer squared $-(t - t_{\min})$. The blue crosses show the data and the red line indicates the acceptance over this region. To

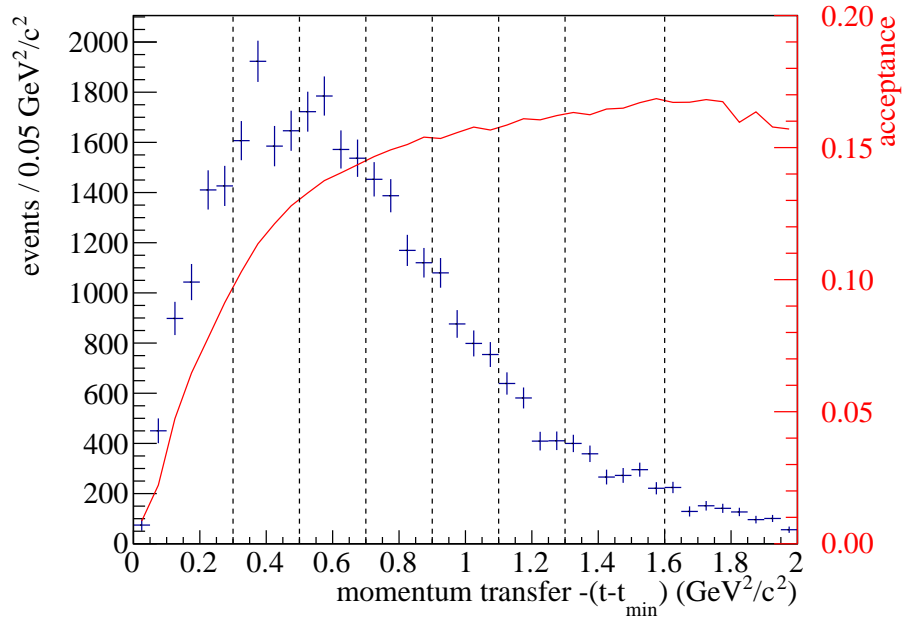


Figure 5.26: Distribution of momentum transfer $-(t - t_{\min})$ (blue) and the acceptance over this range (red). The vertical black lines indicate the limits used for binning.

generate the acceptance, a MC sample with a realistic angular distribution of final state particles was produced. The MC sample was analysed in the same way as the real data and the number of accepted events in a small range in $-(t - t_{\min})$ was divided by the amount of generated events in that range. The vertical lines in Figure 5.26 show the bin limits chosen for this work.

5.6.10 Comparison to bggen

A large generic MC sample of one billion events that was reflecting the Spring 2017 run conditions was produced using the Pythia 6.2 [106] based bggen event generator [107] and hdeant4 (see Section 4.6; set A, Table 4.3). It contained some of the most prominent final states and produced them according to the known physics processes. Although it did not contain the $\Lambda(1520)$ it was still useful to compare it to real data. It might reveal dominating background processes or potential issues in the event selection. For that purpose the ΔT PID plots shown before (Figure 5.4) were produced. They can be seen in Figure 5.27, which shows that the momentum distributions of the MC events are not entirely similar to the data. This is not unexpected since bggen is not able to accurately produce pK^+K^- events. Nevertheless, we can see the placed cuts seemed reasonable on the MC sample.

To further investigate this the same event selection as discussed before was applied. There were only very few events left since there was no $\Lambda(1520)$ signal in the sample. The ΔT PID plots for this are shown in Figure 5.28. The agreement between data and MC was reasonable and therefore the ΔT cuts had similar effects.

Figure 5.29 shows a stacked histogram of the pK^- invariant mass distribution where one would expect to see the $\Lambda(1520)$. The entries are coloured according to the thrown event topology and plotted such that one topology is stacked on top of the other, to better visualise their overall proportion of the simulated data. Since the $\Lambda(1520)$ was not included in the generated event sample, no peak is visible. Nevertheless, it was interesting to study the background distribution to rule out that other channels contaminated the event sample. By far the biggest part of the events that survived the event selection came from non-resonant pK^+K^- production (black), other event topologies only survived in very small quantities. This was quantified in Figure 5.30, which shows that almost 90% of the surviving event combinations came from non-resonant pK^+K^- production. It is important to keep in mind that in real data most events in this mass region came from $\Lambda(1520)$ production. Therefore the real background of non- pK^+K^- events was much smaller than 10%. Figure 5.31 shows the full invariant mass range from $1.4 \text{ GeV}/c^2$ - $2.4 \text{ GeV}/c^2$. It is clear that the biggest source of background in this final state, ρ mesons decaying to $\pi^+\pi^-$, only affects the invariant mass region above $2 \text{ GeV}/c^2$ (c.f. Figure 5.12).

This chapter has shown how the data taken with the GlueX detector was prepared for physics observable extraction. It had to be calibrated, reconstructed and skimmed before cuts were applied to select events that contain the pK^+K^- final state. The sPlot technique was presented to remove the remaining non- $\Lambda(1520)$ background from the sample of pK^+K^- events. This analysis was also performed on a large MC sample, to study its effects.

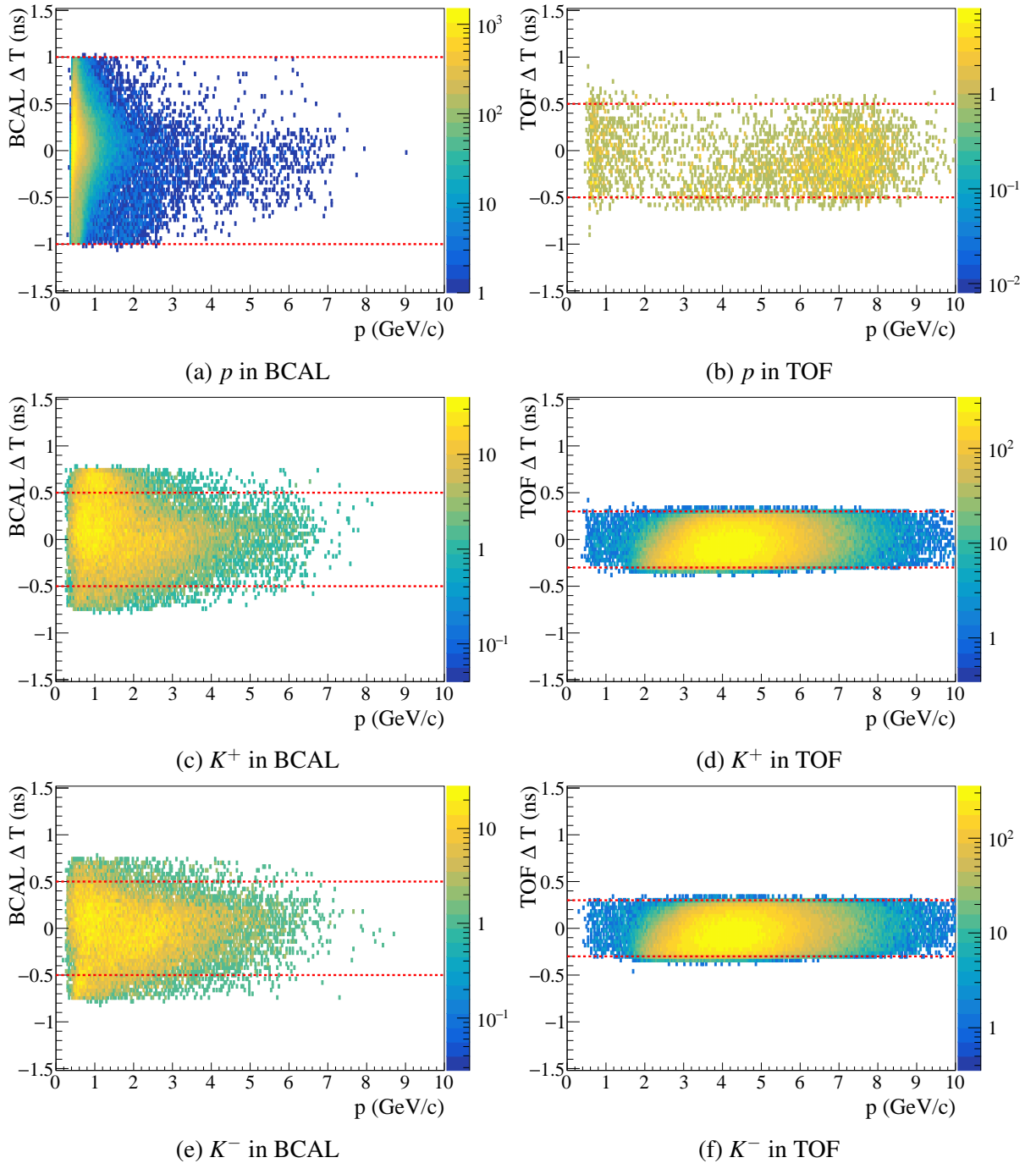


Figure 5.27: Difference between the timing signal of the measured track and a particle for a given momentum in the specified detector for a bggen MC sample. In a perfect scenario one would expect a line at $\Delta T = 0$. The red lines indicate the cut limits applied in the general event selection (see Table 5.3).

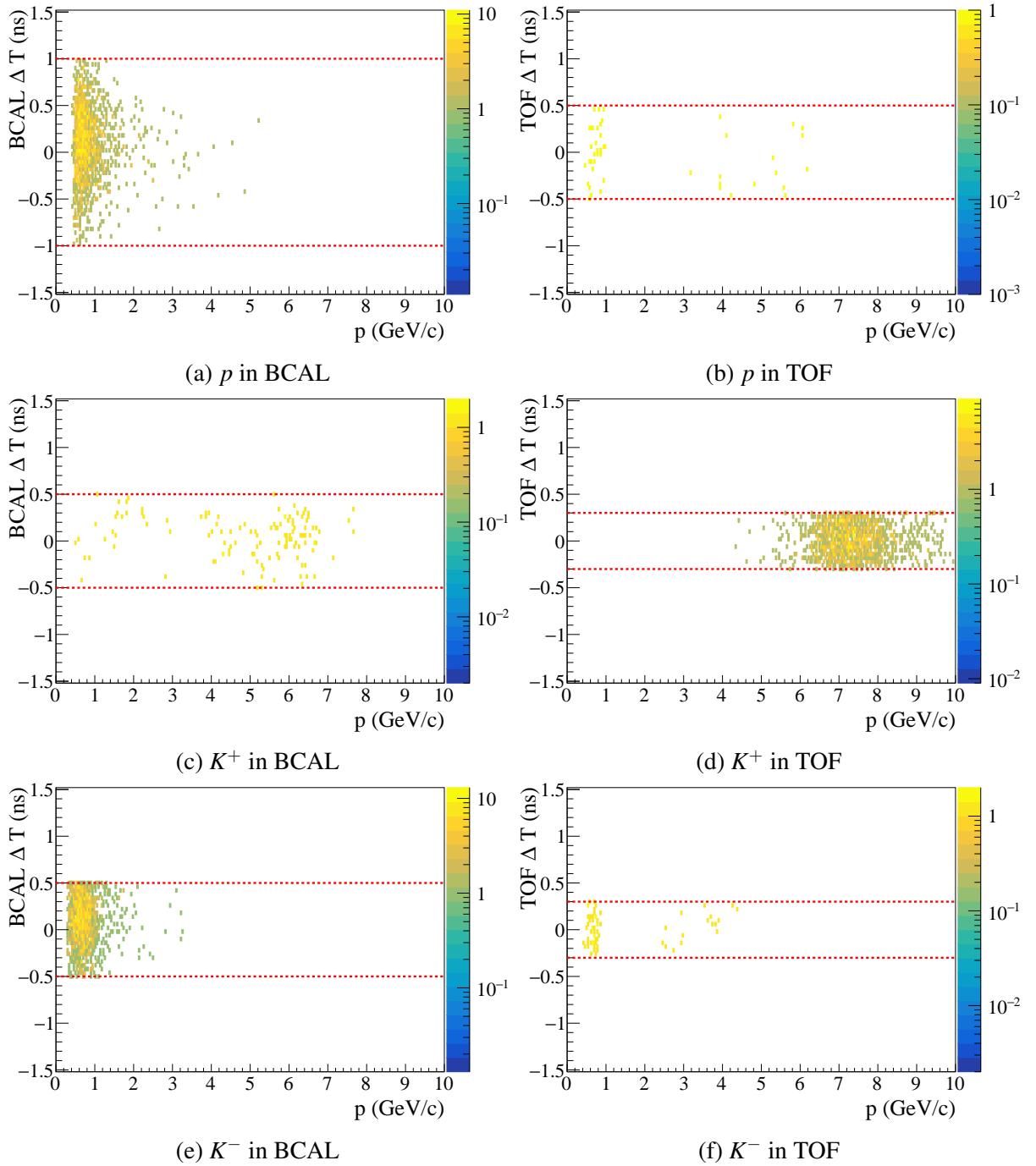


Figure 5.28: Difference between the timing signal of the measured track and a particle for a given momentum in the specified detector after previously discussed cuts were applied to a bggen MC sample. In a perfect scenario one would expect a line at $\Delta T = 0$. The red lines indicate the cut limits applied in the general event selection (see Table 5.3).

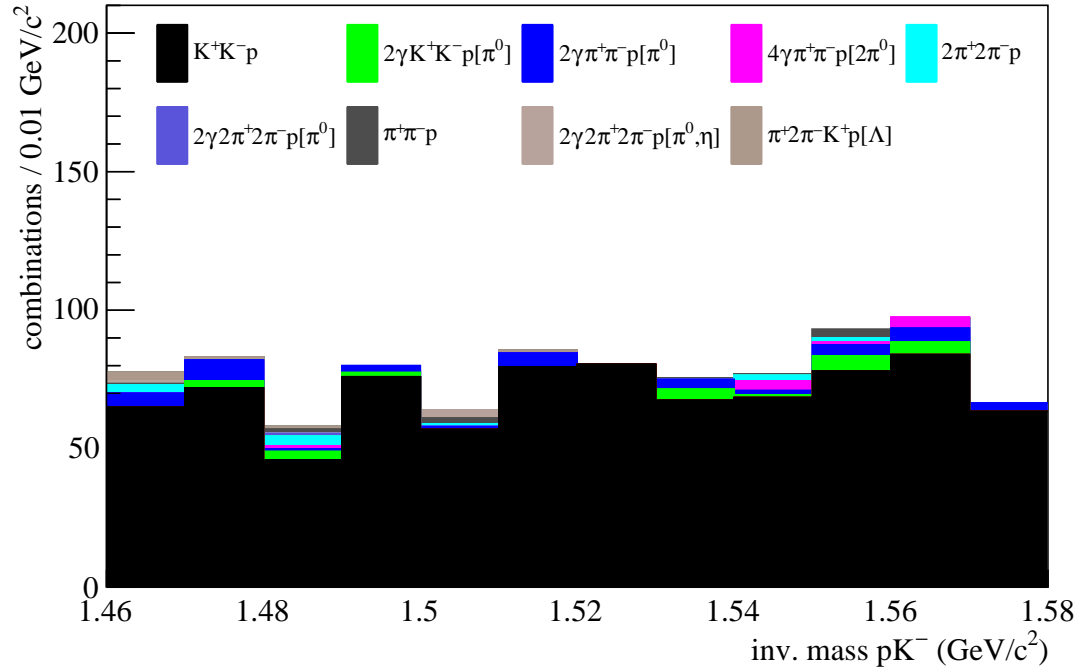


Figure 5.29: Stacked histogram of bggen events surviving the event selection. The color indicates the thrown topology. The K^+K^-p final state is dominating all the others.

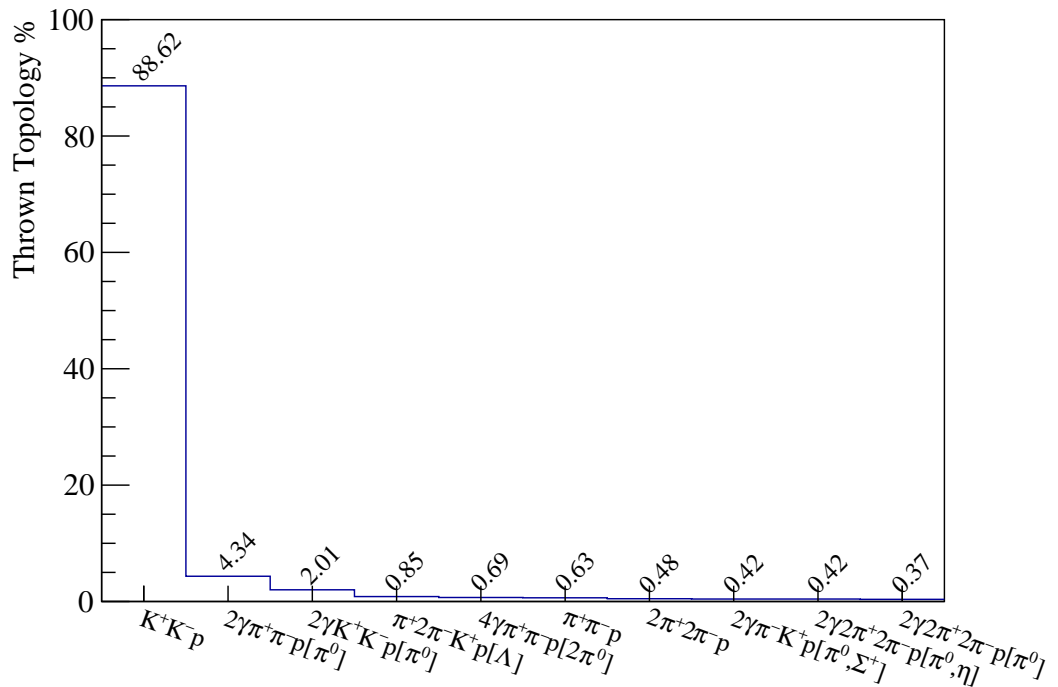


Figure 5.30: Each bin represents the amount of events of a certain thrown topology that survives the event selection. Almost 90% come from non-resonant K^+K^-p production.

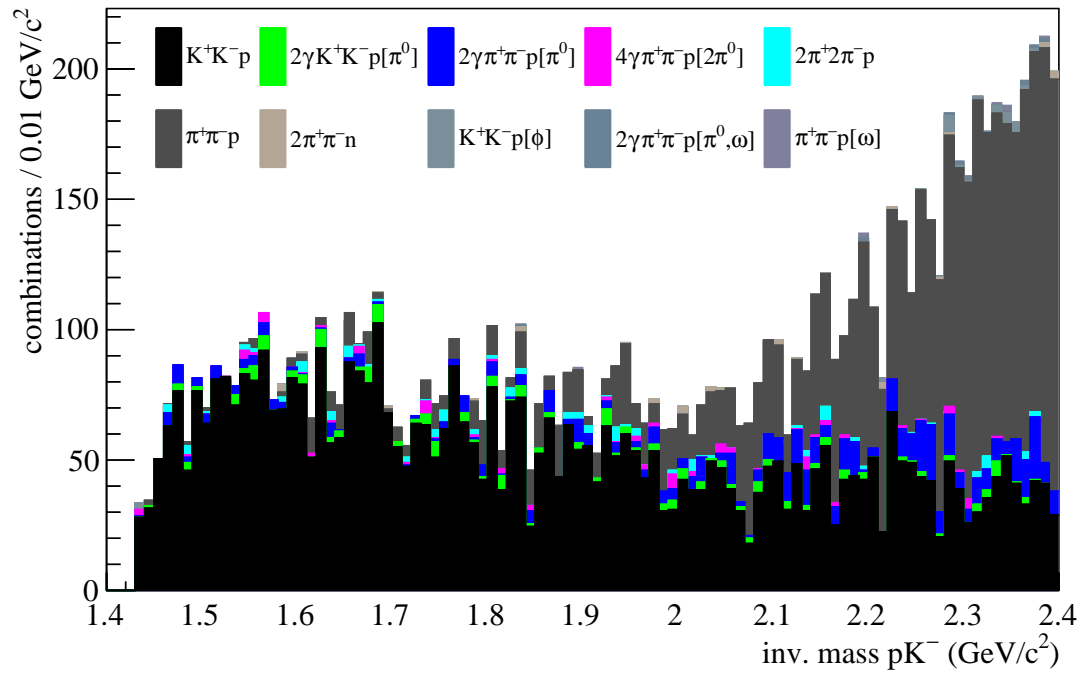


Figure 5.31: Stacked histogram of bkg events surviving the event selection (without invariant mass cut). The colour indicates the thrown topology.

At this stage a sample of $\Lambda(1520) \rightarrow pK^-$ signal events was extracted from the dataset. In the following chapter the analysis of their angular distributions, in order to extract physics observables, is presented.

Chapter 6

Observable extraction

In the previous chapter it was shown how a clean sample of $\Lambda(1520)$ events was selected from the data. These can now be used to extract the physics observables discussed in Chapter 2. For that purpose the angular distributions of final state particles in each event were studied.

6.1 Beam asymmetry

As shown in Section 2.1.2 the beam asymmetry Σ can be accessed by using a linearly polarised photon beam. It was shown that Σ contains information on the production process of the reaction since it is related to the naturality of the t-channel exchange. A beam asymmetry of 1 indicates purely natural exchange while a beam asymmetry of -1 indicates purely unnatural exchange.

6.1.1 Counting asymmetry

In order to measure Σ , a *counting asymmetry* was formed. To do that, the reaction was measured with four different polarisation orientations that were pairwise perpendicular to each other. For the measurements two perpendicular settings (\perp / \parallel) were used at a time for the asymmetry. Using Eq. (2.50) and assuming that the flux and polarisation was the same for all settings an asymmetry can be written as

$$\frac{N_{\perp} - N_{\parallel}}{N_{\perp} + N_{\parallel}} = P\Sigma \cos(2\Phi) \quad (6.1)$$

where $N_{\perp/\parallel}$ denotes the number of events in a certain region of Φ , the angle between the polarisation vector and the production plane, and P is the degree of linear polarisation. One can

immediately see that the counting asymmetry will follow a $\cos(2\Phi)$ distribution and its amplitude is equal to $P\Sigma$. To correct for differences in flux and polarisation for the different settings one can derive the following fit function [108] (for derivation see Appendix A):

$$\frac{N_{\perp} - N_{\parallel}}{N_{\perp} + N_{\parallel}} = \frac{A - 1 + \frac{AB+1}{B+1}2C \cos(2(\Phi - D))}{A + 1 + \frac{AB-1}{B+1}2C \cos(2(\Phi - D))} \quad (6.2)$$

with $A = \frac{F_{\perp}}{F_{\parallel}}$, $B = \frac{P_{\perp}}{P_{\parallel}}$, $C = \Sigma \frac{P_{\perp} + P_{\parallel}}{2}$ and $D = \Phi_{\text{off}}$. $F_{\perp/\parallel}$ denotes the photon flux, $P_{\perp/\parallel}$ the photon polarisation and Φ_{off} is a term correcting for a slight misalignment between the two settings. The advantage of a measurement like this is that possible acceptance effects in the detector cancel out in the ratio, to first order. That makes this measurement a good starting point for the observable extraction.

For the reaction $\vec{\gamma}p \rightarrow K^+ \Lambda(1520) \rightarrow K^+ K^- p$ the ϕ -distribution of the K^+ , which corresponds to Φ , was measured. Using the sWeights calculated in Section 5.6.8, ϕ -distributions of the outgoing K^+ were plotted for signal weighted events. That means events within the $\Lambda(1520)$ peak in the pK^- invariant mass spectrum with the background under the peak subtracted. Then the asymmetry was formed and fitted using the expression given in Eq. (6.2). Ideally the statistics are good enough to extract all parameters, excluding \bar{P} , from the fit. This was not the case in this measurement. Therefore, the parameters were fixed using data provided from parallel measurements. Parameter A , the ratio of the photon beam fluxes in both settings, was taken from direct flux measurements using the pair spectrometer. The parameter B and the mean polarisation \bar{P} were fixed using data from the triplet polarimeter (see Table 4.1). Parameter D was fixed to the polarisation plane angle extracted with a very high statistics analysis of $\gamma p \rightarrow \rho p$ [74] (see Table 4.1).

ROOT's standard MINUIT [109] χ^2 minimiser was used to find the optimal Σ , with the function value integrated over the data bin and normalised by its width. Data were taken at four different diamond orientations. Therefore, the beam asymmetry was measured with the photon polarisation plane at $0^\circ/90^\circ$ and $45^\circ/135^\circ$. This was used to check for systematic deviations. The results for $0^\circ/90^\circ$ are shown in Figure 6.1a and the results for $45^\circ/135^\circ$ are shown in Figure 6.1b. Each plot contains an asymmetry fit for events within a certain range of $-(t - t_{\text{min}})$ as specified in the histogram title. The beam asymmetries extracted from the asymmetry fits are shown in Figure 6.2. The black points are the results from the $0^\circ/90^\circ$ setting and the green points come from the $45^\circ/135^\circ$ setting. Each point is centered at the mean value of the momentum transfer and the horizontal error bars indicate the RMS of the momentum transfer within the bin. The data points from the two settings agree with each other. The beam asymmetry is large over the whole range.

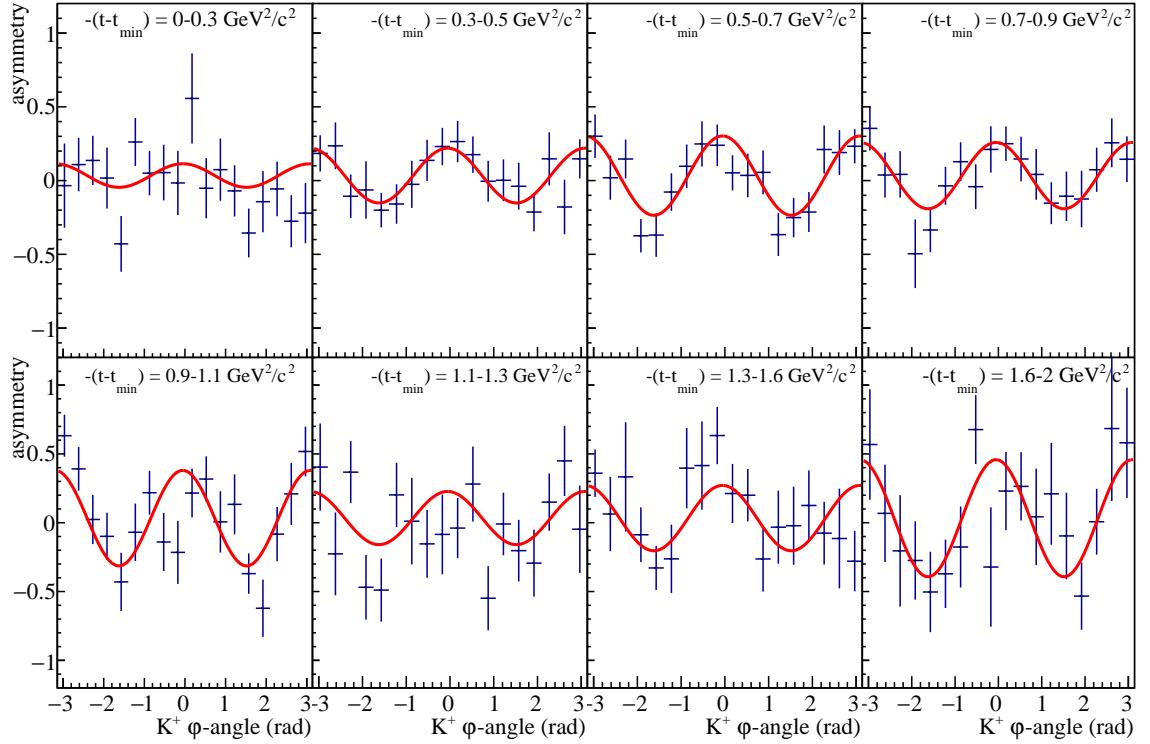
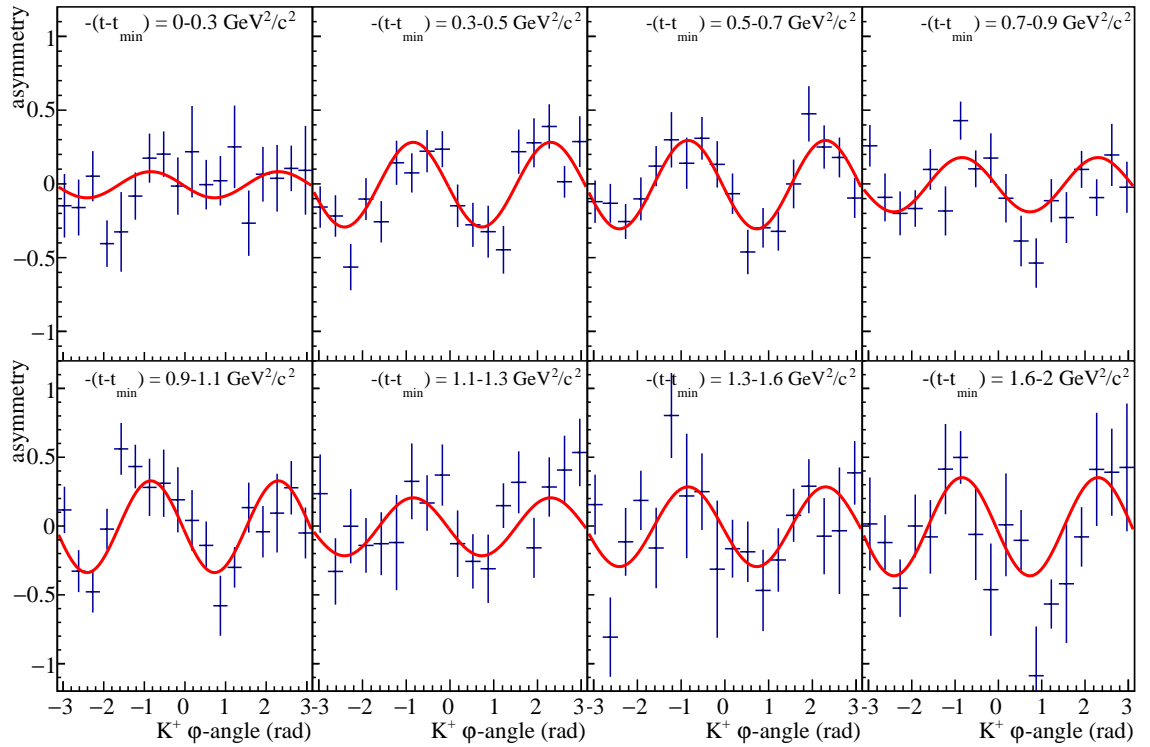
(a) $0^\circ/90^\circ$ setting(b) $45^\circ/135^\circ$ setting

Figure 6.1: The two settings of K^+ ϕ -angle distributions for eight bins in four-momentum transfer squared $-(t - t_{\min})$, fitted with Eq. (6.2) (red).

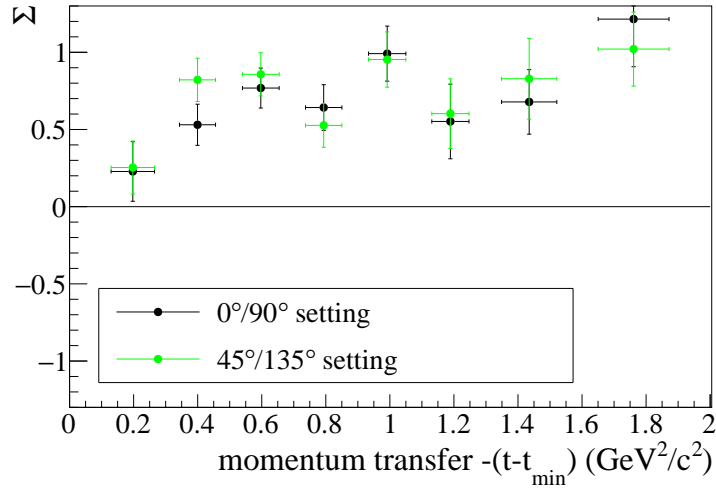


Figure 6.2: Results for the beam asymmetry Σ dependent on the four-momentum transfer squared $-(t - t_{\min})$ for two settings.

6.1.2 Validation of results for sPlot and counting asymmetry

In order to validate the results and errors for the asymmetry fit method, 500 *toy MC* samples, simulations without detector resolution or acceptance effects, were generated (set B, Table 4.3). The samples consisted of the invariant mass of pK^- and the $K^+ \phi$ angle as used in the beam asymmetry fit. The pK^- mass was modelled with a Breit-Wigner signal distribution with a mean of 1519.5 MeV and width of 15.6 MeV, and Chebychev polynomial for the background. Each sample contained 4000 events of which 2/3 were signal events and 1/3 were background. A beam asymmetry of 0.2 and 0.3 was imposed on the signal and background respectively. These values were chosen to have a fairly small asymmetry for the signal with a comparably large asymmetry in the background. This was not necessarily expected in the data but was to provide a stringent test of the rigour of the fits in the study. The same code that was used for the analysis of real data was used to analyse the toy samples. If the analysis procedure works as intended the sPlot technique should be able to unfold signal and background and the fit function Eq. (6.2) should be able to extract the imposed asymmetry with the correct error associated. Then a pull distribution was produced as follows

$$\text{pull} = \frac{\text{measured } \Sigma - \text{true } \Sigma}{\Delta(\text{measured } \Sigma)} \quad (6.3)$$

where Δ denotes the error as provided by the fit to the asymmetry. The result is shown in Figure 6.3. The resulting pull distribution was fitted with a Gaussian function. If the uncertainties are propagated correctly one would expect a pull distribution that is normally distributed with a mean of 0 and a width of 1. The fit to the pull distribution had a reduced χ^2 of 56.52/54 with a mean of -0.0298 ± 0.0492 and a width of 1.0005 ± 0.0435 . Therefore, it can be concluded that the extracted values for the beam asymmetry in this test are statistically correct. That implies that

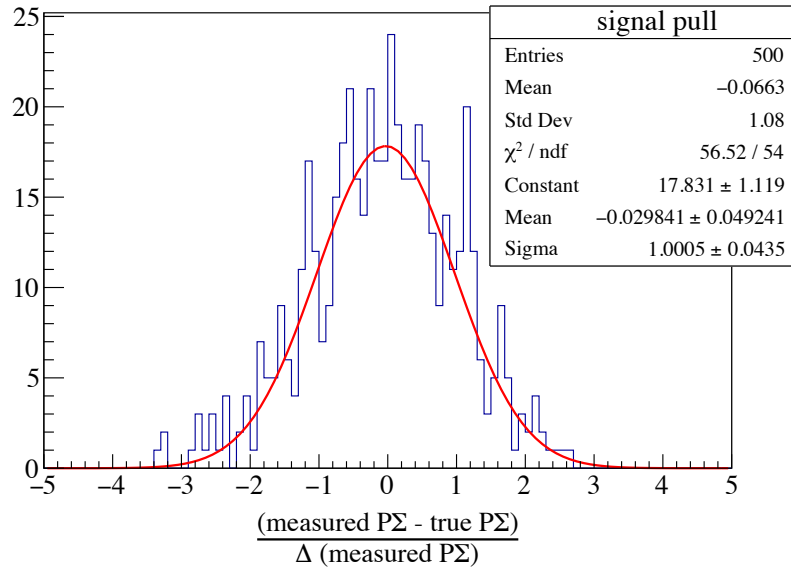


Figure 6.3: Pull distribution of MC simulations to validate the method used to extract the beam asymmetry from the data. The red line shows a Gaussian fit used to evaluate mean and width of the distribution.

the sPlot technique is working properly and is able to unfold signal and background distributions which have an asymmetry even if the background asymmetry is considerably larger.

The toy MC samples used in this validation process had full acceptance and no resolution effects. As part of a very thorough study of the extraction method for SDMEs (see Section 6.2.4) a different more detailed very large MC sample was produced that ran through the full GlueX hdgeant4 simulation (see Section 4.6; set C, Table 4.3). This sample was then also used to repeat the validation for the binned Σ fit. Details on this MC sample can be found in Section 6.2.4. For this study the important parameters were that the sample contained signal with a beam asymmetry of $\Sigma = 0.6$ and background without beam asymmetry. The four-momentum squared distribution of the generated events, as well as the relative proportions of signal-to-background, were chosen to match real data. The large sample was split in 400 statistically independent samples which were treated like real data. The samples were binned in $-(t - t_{\min})$ with the same binning as the real data and the sPlot technique was used to extract signal sWeights. The sWeighted samples were then binned in ϕ and fitted with Eq. (6.2). From the 400 fit results the pull distributions of Eq. (6.3) were created and are summarised in Figure 6.4. The top plot shows the means of the pull distributions, created for each $-(t - t_{\min})$ -bin individually, as extracted from a Gaussian fit to the pull, the middle plot shows the associated widths. The bottom plot shows the mean of the distribution of differences between the extracted Σ and real Σ for each fit. The errors given for the mean and width of the pull are taken as the uncertainties of the fit parameter while the error plotted in the bottom plot is the width of the distribution of differences. There seems to be a systematic shift of the results towards smaller values. The average difference

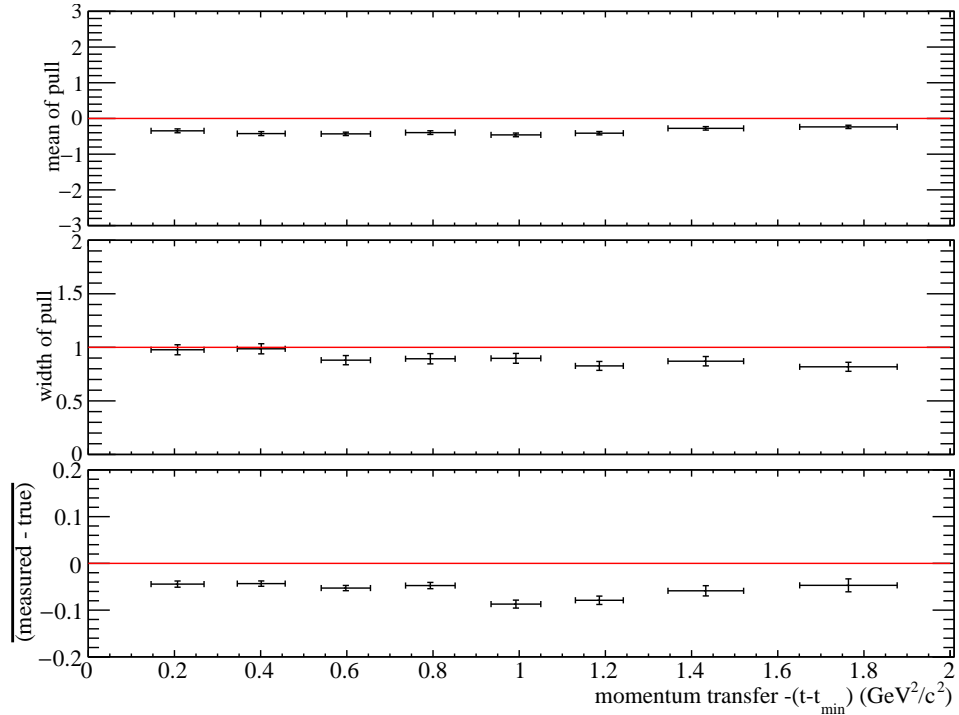


Figure 6.4: Mean (top) and width (middle) of pull distributions from a binned fit for a full simulation with background subtracted. Also shown is the absolute difference. The true value for the simulated beam asymmetry is 0.6.

is roughly 0.05 with the means of the pulls being shifted by about 0.3-0.5. The reported errors seem to be slightly overestimated for higher momentum transfer $-(t - t_{\min})$. It could be that this was due to some dilution coming from a very small amount of background remaining after the sPlot technique was applied. This has been studied in detail, and is discussed in Section 6.2.4.

6.1.3 Unbinned maximum likelihood fit

Binning data is always associated with loss of information and therefore the extracted results might not be as precise as achievable given the data. In an attempt to improve on this, the extraction of the beam asymmetry is repeated using an unbinned extended maximum likelihood fit (EML) [110] with the minimisation performed through MINUIT2 [111]. Using an unbinned fit makes it possible to fit all four settings of the polarisation plane simultaneously instead of fitting pairwise perpendicular settings.

In order to perform an EML fit, first of all an intensity function that describes the expected angular distribution is defined as

$$\mathcal{I}(\phi_{K^+}) = 1 - P_{\gamma}\Sigma \cos(2(\phi_{K^+} - \phi_0)) \quad (6.4)$$

where P_γ is the degree of polarisation and ϕ_0 is the orientation of the polarisation plane of the linearly polarised photon beam as in Table 4.1. A log-likelihood function containing a term to account for the expected number of events, assuming a Poisson distribution, was written as

$$\ln \mathcal{L} = \sum_{i=1}^N \ln \mathcal{S}(\phi_{K^+}) - \int d\phi_{K^+} \mathcal{S}(\phi_{K^+}) \eta(\phi_{K^+}) \quad (6.5)$$

where η denotes the detector acceptance which has to be taken into account. The summation runs over all N events in the data. The normalisation integral was evaluated by summing generated phase space MC events that had been passed through the full detector simulation and reconstruction (set D, Table 4.3). They were produced with a polarisation and polarisation plane orientation reflecting real data. This corrected for any acceptance effects introduced by the detector. The likelihood function was maximised by minimising $-\ln \mathcal{L}$ using MINUIT2, by finding a parameter Σ that best fits the data.

Since the sPlot technique was used in this analysis, care was taken in order to obtain correct fit results and their associated uncertainties. For that reason Eq. (6.5) was slightly modified

$$\ln \mathcal{L} = s_w \left(\sum_{i=1}^N s w_i \ln \mathcal{S}(\phi_{K^+}) - \int d\phi_{K^+} \mathcal{S}(\phi_{K^+}) \eta(\phi_{K^+}) \right) \quad (6.6)$$

with $s_w = \frac{\sum_{i=1}^N s w_i}{\sum_{i=1}^N s w_i^2}$. The weights $s w_i$ are the signal weights from the sPlot sideband subtraction. s_w is a constant factor taking into account the effect of the sideband subtraction on the statistical uncertainty and was found by other analyses to work well (see e.g. [101]). To show that this is a valid way of taking the weights into account a validation was performed (see Section 6.1.4). Ignoring this factor would lead to wrong uncertainties being reported by the fits.

The results of the unbinned fit method are shown in Figure 6.5. In order to see how well the

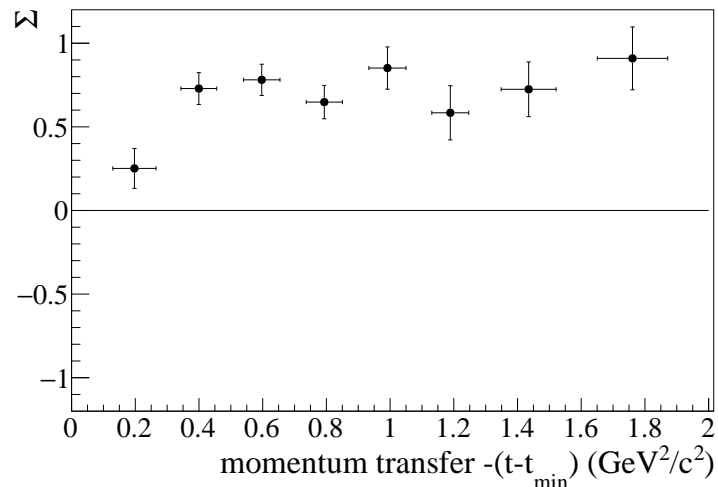


Figure 6.5: Results for the beam asymmetry Σ from an unbinned maximum likelihood fit.

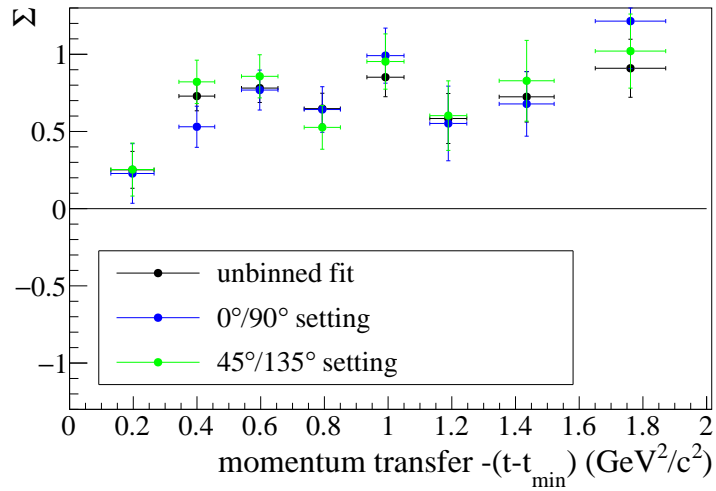


Figure 6.6: Results for the beam asymmetry Σ from an unbinned maximum likelihood fit compared to the results from the binned fit.

unbinned fit agrees with the binned fits they are all plotted together in Figure 6.6. The agreement between the methods is good. All results agree within statistics. This is a very important finding that shows, that the acceptance correction which was necessary for the unbinned fit is working properly. This will be also needed in Section 6.2 and was therefore important to demonstrate.

6.1.4 Validation of results for sPlot and unbinned fit

In order to validate that this method yields the correct results and associated uncertainties, a study similar to Section 6.1.2 was performed. The full detector simulation was used (set C, Table 4.3) and as before the MC data was split up in 400 statistically independent samples which were treated like real data. The result of the study can be seen in Figure 6.7. The widths of the pulls being close to one suggest that the errors associated with the measurements were estimated correctly. The means indicate a slight shift towards smaller asymmetries. The average difference of the measured and true beam asymmetry is about 0.02. The exact cause of this shift is hard to determine. Extensive studies have been performed to determine systematic uncertainties in the extraction of SDMEs (see Section 6.2.4) and further discussion can be found there. For now it remains to conclude that a small systematic shift is observed. Therefore, a systematic uncertainty on the extraction method of about 0.02 is assumed.

6.1.5 Invariant mass sideband studies

Often it can be interesting to look at the asymmetry in the sideband of a reaction. For that purpose the beam asymmetry was determined in bins of invariant mass of pK^- over the range

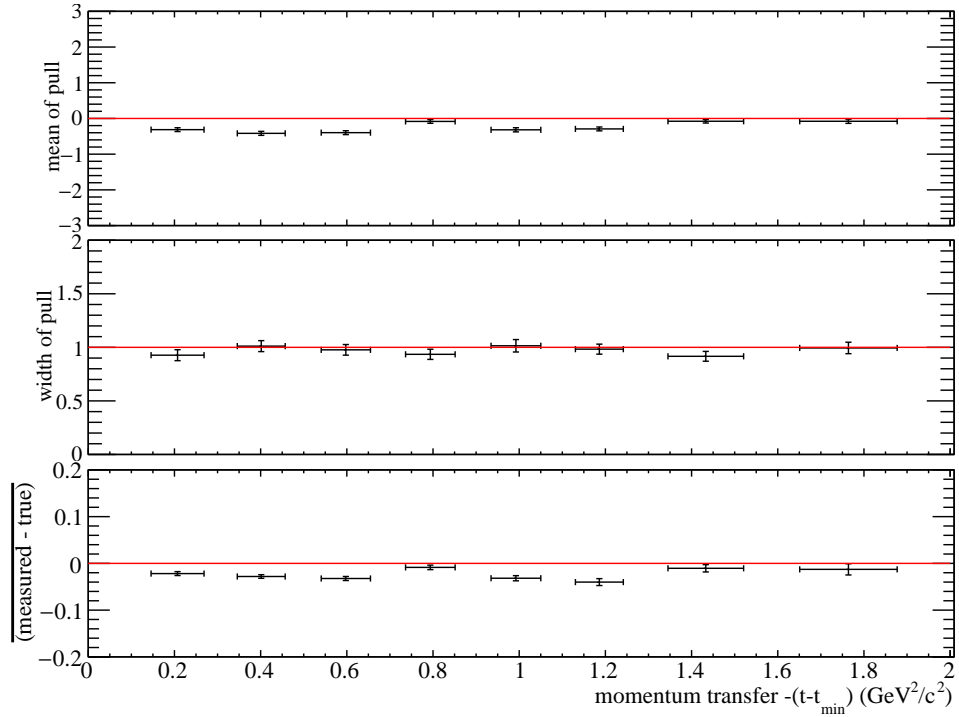


Figure 6.7: Mean (top) and width (middle) of pull distributions from an unbinned fit for a full simulation with background subtracted. Also shown is the absolute difference. The true value for the simulated beam asymmetry is 0.6.

of the sPlot fits. For this the sWeights were not used. This exercise gives a better idea of what the asymmetry left and right of the $\Lambda(1520)$ peak looks like. The result is plotted in Figure 6.8. The black points show the beam asymmetry Σ . Plotted in red is the pK^- invariant mass distribution. One can clearly see that the sideband of the $\Lambda(1520)$ also shows a non-zero beam asymmetry. This can also be observed when plotting the K^+ ϕ -angle distribution for events with background weights applied as shown in Figure 6.9. There seems to be an asymmetry present in the background. This was not a problem since the study in 6.1.4 has shown that the sPlot technique is fully capable of disentangling distributions based on an appropriate discriminatory variable (in this case the invariant mass). To understand the origin of the sideband asymmetry it is important to keep in mind what the beam asymmetry means. It makes a (limited) statement on the production process involved in the reaction. The kinematics of the region around the $\Lambda(1520)$ peak favour a reaction in which the K^+ has high momentum and is very forward going. In that case the likely production mechanism is strangeness exchange of a (virtual) kaon. This is true independent of whether a $\Lambda(1520)$ or other hyperon was produced. Therefore, it was not surprising to see similar beam asymmetries in the sidebands of the $\Lambda(1520)$. Using the sPlot technique they were properly taken care of and the extracted results are reliable.

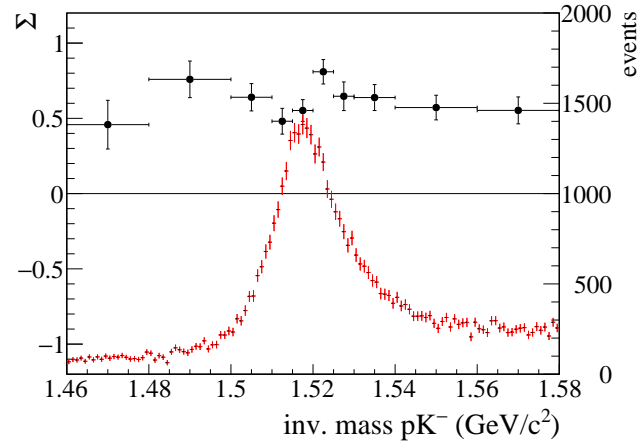


Figure 6.8: Beam asymmetry (black) over the invariant mass range near the $\Lambda(1520)$ extracted with an unbinned maximum likelihood fit. The red points show the inv. mass distribution of the events.

6.1.6 Further systematic studies

In order to assess the potential systematic uncertainty induced by various aspects of this analysis, several studies were carried out. Since the unbinned extraction of Σ is more relevant to the further analysis, the studies of systematic uncertainties were only carried out for that extraction.

Event selection

In order to study the influence of cuts during the event selection on the final results, the whole analysis chain was performed several times, while one parameter at a time was changed. In total 26 different variations of the event selection discussed in Chapter 5 were tested, which can be found in Table 6.1. They were chosen as reasonable ranges over which the cuts could have been placed. For each setup the full analysis was performed. In order to assess if a significant systematic shift was observed or not, the Barlow test as described in [112] was performed. For each measurement the quantity $\sigma_B = \sqrt{|\sigma^2 - \sigma'^2|}$ was calculated where σ denotes the error as reported by the fit for the baseline setting and σ' the reported error for the variation. Then the difference between the baseline result and the varied result is divided by σ_B . The resulting number can be treated as a significance. Barlow states that a significance smaller (larger) than (minus) one is not significant, a significance larger (smaller) than (minus) four indicates a significant systematic effect, the region in between is left to judgement. For this work a value of four as indication of systematic effects was adopted as guidance. This is in line with other GlueX analyses and might be different in other collaborations. In case of real systematic effects one would expect to see a trend of significant values across the analysed $-(t - t_{\min})$ range. Even significances smaller than four can indicate a systematic shift if they show a clear, continuous trend across the whole range.

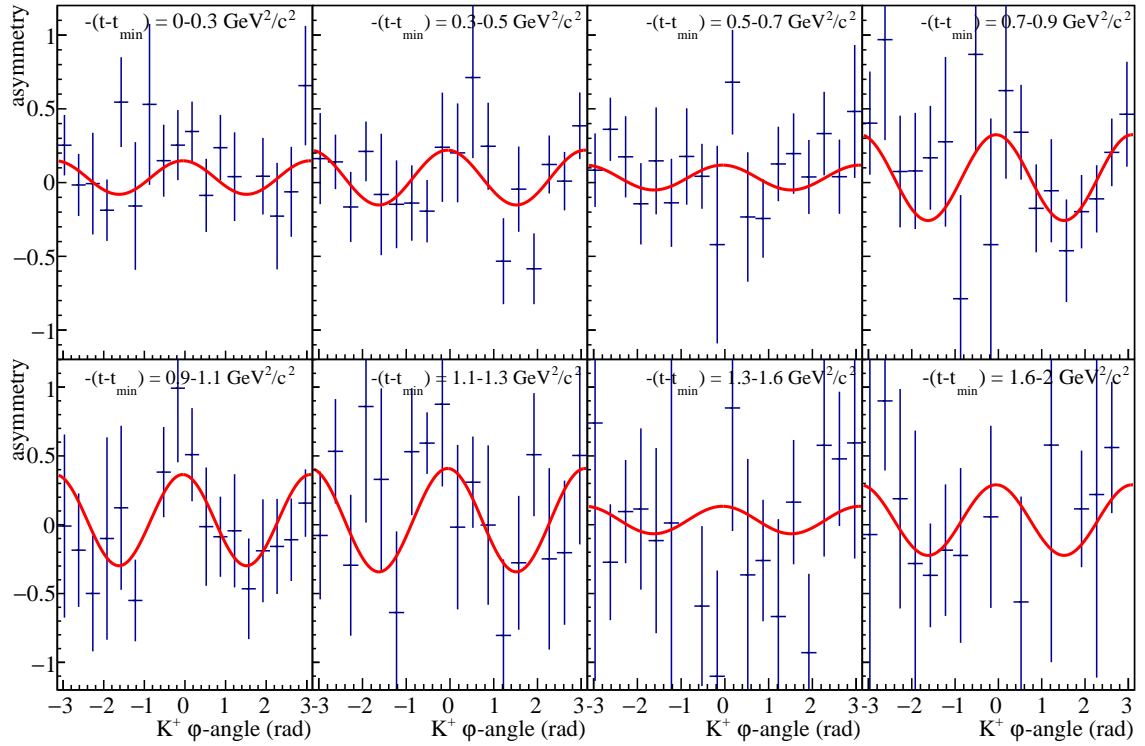
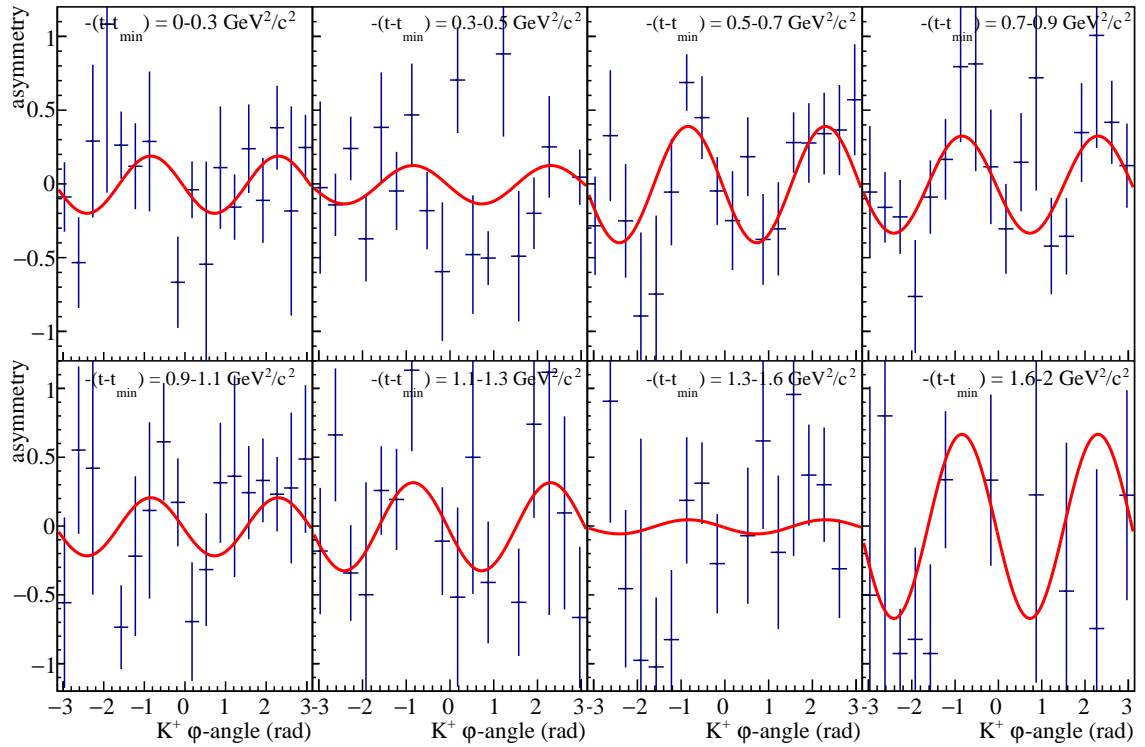
(a) $0^\circ/90^\circ$ setting(b) $45^\circ/135^\circ$ setting

Figure 6.9: The two settings of K^+ ϕ -angle distributions with background weights applied for eight bins in momentum transfer $-(t - t_{\min})$, fitted with Eq. (6.2) (red).

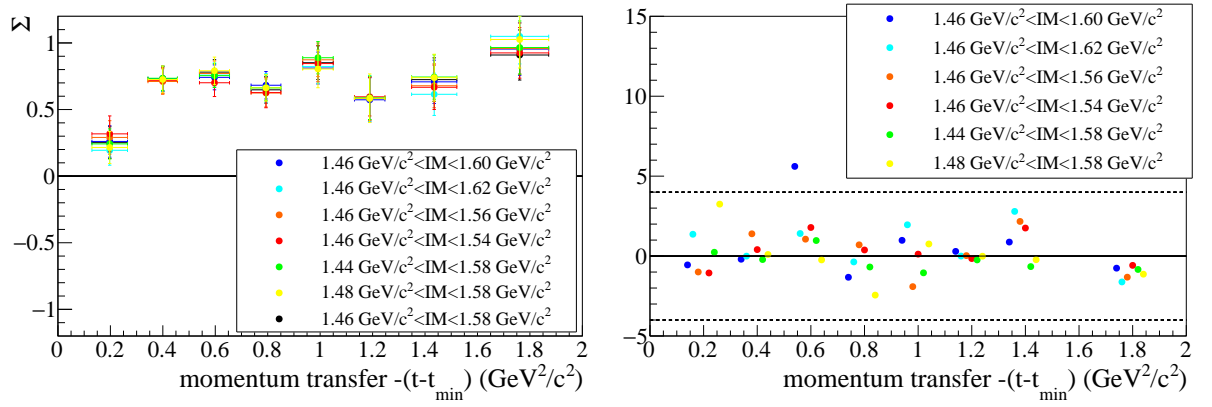
| setup | change | new limit | setup | change | new limit |
|-------|---------------|------------------------------|-------|-----------------------|-------------|
| 1 | IM | 1.46-1.60 GeV/c ² | 14 | vertex z | 52 cm-77 cm |
| 2 | IM | 1.46-1.62 GeV/c ² | 15 | ΔT BCAL K^+ | 0.6 ns |
| 3 | IM | 1.46-1.56 GeV/c ² | 16 | ΔT BCAL K^+ | 0.4 ns |
| 4 | IM | 1.46-1.54 GeV/c ² | 17 | ΔT TOF K^+ | 0.25 ns |
| 5 | IM | 1.44-1.58 GeV/c ² | 18 | ΔT TOF K^+ | 0.2 ns |
| 6 | IM | 1.48-1.58 GeV/c ² | 19 | ΔT BCAL K^- | 0.6 ns |
| 7 | CL | 1E-4 | 20 | ΔT BCAL K^- | 0.4 ns |
| 8 | CL | 1E-5 | 21 | ΔT TOF K^- | 0.25 ns |
| 9 | CL | 1E-7 | 22 | ΔT TOF K^- | 0.2 ns |
| 10 | CL | 1E-8 | 23 | ΔT BCAL p | 0.9 ns |
| 11 | vertex radius | 1.5 cm | 24 | ΔT BCAL p | 0.8 ns |
| 12 | vertex radius | 0.5 cm | 25 | ΔT TOF p | 0.6 ns |
| 13 | vertex z | 50 cm-79 cm | 26 | PID TOF p | 0.4 ns |

Table 6.1: Table with all the setups used to assess systematic uncertainties.

The results for the first six variations of the event selection are shown in the following. The remaining results are discussed here while the resulting plots are shown in Appendix C.1.

Invariant mass cut First of all, the range in the pK^- invariant mass used for the analysis was changed (Table 6.1, setups 1-6). This impacted the range of the sPlot fits. Figure 6.10a shows the beam asymmetry results for the baseline cut (black points) and six different variations. There is excellent agreement between all results. To quantify the agreement the Barlow test was performed. The result is shown in Figure 6.10b. The plots show that the vast majority of tests resulted in an insignificant change, only one test flagged up. Strictly following Barlow would mean including a systematic uncertainty in the final result. In this case there should be some consideration of the fact that a systematic shift caused by the choice of the invariant mass range would very likely affect not only one $-(t - t_{\min})$ -bin but also the neighbours. It is fair to assume some continuity in the systematics. This was not seen in the test result. In fact a direct neighbour showed a significance of $\ll 1$. Therefore, this one test is considered an outlier and no systematic uncertainty will be added for the invariant mass range.

Confidence Level cut It turned out that the most important cut in the event selection was the cut on the confidence level of the kinematic fit. Therefore it was very important to check its influence on the final result. In addition to the baseline cut of $CL > 10^{-6}$ four cuts, two tighter and two looser, were chosen based on a similar FOM (see Figure 5.7) and the whole analysis was performed (Table 6.1, setups 7-10). The results for the beam asymmetry can be found in Figure C.1a. Again the results seem to agree and the Barlow test is performed. The results of the test are shown in Figure C.1b. Similar to the test for the invariant mass cut most of the significances indicate no systematic shift. Five tests show results > 4 . However there seems to



(a) Results for the beam asymmetry Σ for the baseline setting (black points) and six variations.

(b) The significance as defined in the Barlow test is plotted for each bin and each variation.

Figure 6.10: Results for the invariant mass cut study (see Table 6.1 setups 1-6).

be no reasonable continuity again. The change from one bin to the other was random, therefore, it was not appropriate to include a systematic uncertainty in this case.

Vertex cut The vertex cut was chosen such that events originate from within the hydrogen target. To test the sensitivity of the beam asymmetry on the chosen cut range, it was varied in both radius and length (Table 6.1, setups 11-14). A looser and a tighter cut were applied respectively and the complete analysis was performed. The results are shown in Figure C.2. Only one test seems to indicate a systematic effect. Due to the same arguments as before a systematic uncertainty was not assigned to the results.

PID cut To test the influence of the PID cuts on the extraction of Σ , one PID cut limit at a time was varied and the whole analysis was repeated (Table 6.1, setups 15-26). In an attempt to quantify the significance of the change the Barlow test was performed. All results for the beam asymmetries and Barlow tests can be found in Figures C.3 to C.5. One test for each final state particle showed up as significant. Similar to the other tests that did not pass the Barlow test the direct neighbours of the bins in question do not show a significant variation. Therefore, no systematic uncertainty was added for the PID ΔT cuts.

Background shape for sPlot An important part of the analysis was the sPlot fit to subtract background under the $\Lambda(1520)$. The signal shape is well known but the shape for the background was chosen as a second order Chebychev polynomial, since a continuous distribution without any peaks is assumed. To test the influence of the chosen Chebychev polynomial on the final result, the analysis was repeated with a first, third, and fourth order polynomial. The results

can be seen in Figure C.6. The extracted beam asymmetry is independent of the chosen background distribution. In an attempt to quantify the agreement the Barlow test was performed. The results are shown in Figure C.6b. None of the tests showed a significant effect. No systematic uncertainty was added for the sPlot background shape.

Beam properties

The polarisation and orientation of the beam were determined in separate analyses. The values used here are summarised in Table 4.1.

Degree of polarisation The polarisation acts as an overall scaling factor to all results, hence its uncertainty is given in relative terms. The systematic uncertainty on the polarisation measurement is quoted as 1.5% [70]. The statistical uncertainty is about 3%. Therefore, the combined systematic uncertainty on the overall scaling of the beam asymmetry is $\frac{\sigma_p}{p} = \sqrt{0.015^2 + 0.03^2} = 3.5\%$.

Offset of polarisation plane To determine the influence of the uncertainty on the offset measurement on the final results, the unbinned fit was repeated twice more with offsets that were increased/decreased by three standard deviations, then the Barlow test was performed. The results for the beam asymmetry can be found in Figure C.7. None of the tests show a significant result. Therefore, no systematic uncertainty was added for the beam polarisation offset.

Combined systematic uncertainty

There were no significant systematic uncertainties arising from the detailed studies performed in Section 6.1.6. Only the extraction method studied in Section 6.1.4 and the systematic uncertainty on the degree of linear polarisation contribute to the final systematic uncertainty. The identified significant systematic uncertainties are summarised in Table 6.2.

| source | uncertainty |
|------------------------|-------------|
| extraction method | 0.02 |
| degree of polarisation | 3.5% |

Table 6.2: Numerical results for systematic uncertainties on the beam asymmetry Σ .

6.2 Spin-density matrix elements

The spin-density matrix elements incorporate information from all final state particles. Therefore, they provide more information about the production and decay of the $\Lambda(1520)$ than the beam asymmetry Σ . A common frame to extract SDMEs is the Gottfried-Jackson (t-channel helicity) frame [31] (see Figure 2.2). To evaluate the decay kinematics the ϕ_{GJ} and θ_{GJ} angle of the K^- are used together with Φ , the difference between the production plane and the beam polarisation axis, defined in the CM frame. The intensity function describing the K^- angular distribution in the GJ frame is given by Eq. (2.28). It contains nine fit parameters with three fit variables. This makes the measurement of SDMEs a very complex and challenging problem and an approach similar to 6.1.3 did not yield satisfactory results. First and foremost the error matrix came out wrong. The error bars were far too small or unrealistically large. For that reason, a different approach to estimate the fit parameters was chosen.

6.2.1 Markov chain Monte Carlo method

Markov Chain Monte Carlo (MCMC) is a very powerful tool for parameter estimation for problems with high dimensionality. A good description can be found in [113]. In the following, a brief overview of the main ideas behind the technique is given.

The general idea behind MCMC is that the possible parameter space is explored numerically. This is done by calculating a likelihood as in Eq. (6.6), with $\mathcal{L} = W(\theta, \phi, \Phi)$ from Eq. (2.28), and then stepping through the SDME parameter space. This is achieved by changing one parameter at a time and then recalculating the likelihood. If it is higher than in the previous step the changed parameter will be accepted, if the likelihood is lower the changed parameter will be accepted with a certain probability, proportional to the ratio of previous and new likelihood. This helps to overcome local minima in the negative log-likelihood. The set of parameters that were accepted during the stepping procedure form the eponymous chain.

Bayes' theorem

Bayes' theorem plays an important role in the MCMC method. For a set of parameters θ that describe the reaction and a dataset Z it can be written as [113]

$$P(\theta|Z)P(Z) = P(Z|\theta)P(\theta) \quad (6.7)$$

$P(Z|\theta)$ is the probability to measure dataset Z , given that θ is the set of parameters. This is the same as the likelihood \mathcal{L} used in a maximum likelihood fit. $P(\theta)$ is the probability of the

parameters θ within the model. It does not depend on the data and is often referred to as *prior probability*. It reflects the belief of the analyser in the parameters of the model and introduces a subjective element into the equation. $P(Z)$ is the probability to collect dataset Z . For the purpose of this analysis this quantity is not of much interest and it will be shown that it is not going to affect the results. $P(\theta|Z)$ denotes the conditional probability to measure a set of parameters θ , given the dataset Z . This is the quantity that is ultimately of interest since it is the probability for a set of parameters θ based on the data. It is also referred to as *posterior probability*.

Metropolis-Hastings algorithm

The algorithm used to step through the likelihood space is called Metropolis-Hastings [114,115]. It can be divided up in four separate parts [113]

1. choose a set of start parameters θ^0 that start the chain
2. propose a candidate for the next step in the chain θ' :
The candidate is proposed according to a *proposal distribution* $q(\theta'|\theta^n)$, where θ^n denotes the set of parameters at the current step.
3. calculate an acceptance probability $\alpha(\theta'|\theta^n)$ based on a *prior distribution* $P(\theta)$:
The acceptance probability is the probability to go from θ^n to θ' and is defined as

$$\alpha(\theta'|\theta^n) = \min \left\{ \frac{\pi(\theta') q(\theta^n|\theta')}{\pi(\theta^n) q(\theta'|\theta^n)}, 1 \right\} \quad (6.8)$$

where $\pi(\theta')$ denotes the *posterior distribution* of candidate θ' . This can be rewritten in terms of known quantities by making use of Bayes' theorem in Eq. (6.7)

$$\alpha(\theta'|\theta^n) = \min \left\{ \frac{P(Z|\theta') P(\theta') q(\theta^n|\theta')}{P(Z|\theta^n) P(\theta^n) q(\theta'|\theta^n)}, 1 \right\} \quad (6.9)$$

Now the acceptance probability only depends on the likelihood to measure the dataset Z given the parameters θ' and θ^n , the *prior distribution*, and the *proposal distribution*, all of which can either be calculated or are chosen explicitly.

4. accept the proposed candidate with probability $\alpha(\theta'|\theta^n)$ and go back to step 2. If the candidate is not accepted the current set of parameters θ^n is added to the chain again.

This algorithm results in a Markov Chain with distribution $P(\theta|Z)$ [113]. That means it gives the probability distribution for the set of parameters given the data.

Figure 6.11 illustrates the Metropolis-Hastings algorithm. One starts with an *initial sample* (start values) of parameters (θ^0). The next step in parameter space is proposed and the acceptance

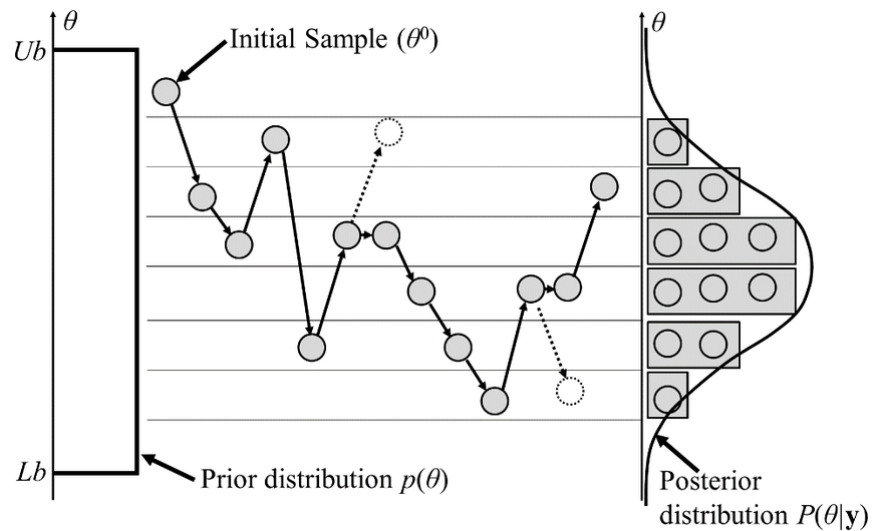


Figure 6.11: Visualisation of Metropolis-Hastings MCMC algorithm. Taken from [116].

probability is calculated using a *prior distribution* (uniform in the example with upper bound Ub and lower bound Lb). With the first two steps the likelihood increases and therefore the new set of parameters is accepted. In the third step the likelihood decreases but nevertheless the new parameters were accepted. Steps four and five again increase the likelihood and get accepted automatically. The proposed step six decreases the likelihood and this time the proposed new parameters do not get accepted. Therefore, the parameters stay the same for an additional step. One can continue with this as long as desired. Histogramming the accepted parameters yields the *posterior distribution*. The longer the Markov Chain that is used to step through the parameter space, the more accurate will the resulting posterior distribution reflect the real likelihood distribution of the parameters. From the resulting posterior distribution one can then infer the set of parameters that best fit the data (e.g. mean or mode).

For this work the Metropolis-Hastings implementation in RooStats, a RooFit based framework [117], was used. As for the extraction of the beam asymmetry, it was run through the brufit framework. A *sequential proposal* function was used. It randomly changes one parameter at a time and the next value is proposed based on a Gaussian distribution around the current value. The width of the Gaussian is related to a step size parameter, which was tuned such that an acceptance rate of 10 – 20% was achieved. Since this method is computationally expensive, one wants to make sure that a lot of proposed parameters get accepted. This implies using a new parameter value close to the previous, so the likelihood does not change significantly. On the other hand, if the acceptance rate is too high this could indicate that the likelihood space is not mapped out properly and that the Markov Chain spends too much time evaluating parameter values with a low likelihood. The starting values for all SDMEs were set to 0 and a uniform prior probability with range $[-1, 1]$ was used, which reflects the lower and upper limit for the allowed range of the SDMEs.

6.2.2 Results

The results of a typical example of the parameter estimation are shown in Figures 6.12 and 6.13 (see all plots in Appendix B). The so called *timeline plots* show the evolution of each parameter with respect to the steps taken in the Markov Chain. Each point in this timeline is the value of the specified parameter for the given step (see Figure 6.11). The *corner plots* [118] show 1D and 2D posterior distributions for the parameters. In order to get good sampling of the likelihood space, which results in more precise estimation of the final results and their uncertainties, the chain consisted of 50,000 steps. The first 100 steps were discarded from the chain to minimise the effect of the choice of start parameters. This is commonly called *burn-in*. The timeline plots show that all fits found stable solutions for all SDMEs and the yield. Corner plots visualise very nicely the spreads and correlations of the results. One can see that there is a strong correlation between the ρ_{11}^1 and ρ_{33}^1 but the other SDMEs seem mostly uncorrelated. The correlation can be easily explained as the beam asymmetry Σ is proportional to the sum of these two matrix elements (see Eq. (2.55)). To estimate the SDMEs and their associated uncertainties the means and widths of the posterior distributions were determined.

To visually assess the quality of the parameter estimation one can use a flat MC sample that was run through `hdgeant4` to include acceptance effects (set D, Table 4.3). The same MC sample as for the acceptance correction in the likelihood function was used for that purpose (see Section 6.1.3). The sample was then weighted with the SDMEs extracted from the posterior distributions and compared to the data. If the parameters were estimated correctly then the weighted MC sample should agree with the data projections. One example for resulting plots is shown in Figure 6.14 (see all plots in Appendix B). The weighted MC sample is shown as red line and the data is shown in black with statistical error bars. There is very good agreement for all eight bins.

The extracted SDME parameter for eight bins in $-(t - t_{\min})$ are shown in Figure 6.15. The error bars on the polarised SDMEs are larger due to the fact that they are scaled by a factor of $1/P_\gamma$. Additionally the runs without polarisation (amorphous radiator) add statistics which contribute only to the unpolarised SDMEs.

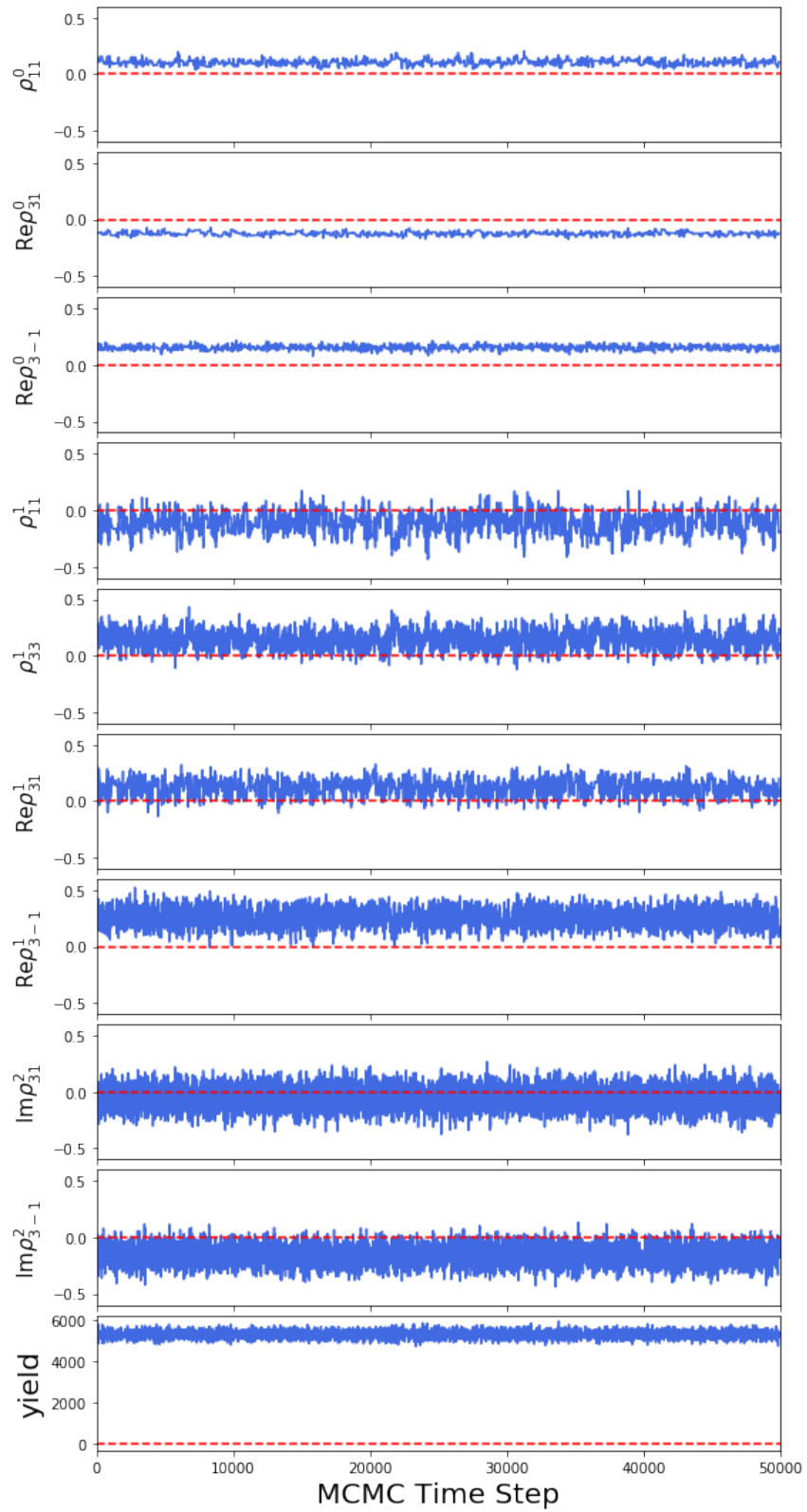


Figure 6.12: SDME timeline plots for $-(t - t_{\min}) = 0 \text{ GeV}^2/c^2 - 0.3 \text{ GeV}^2/c^2$.

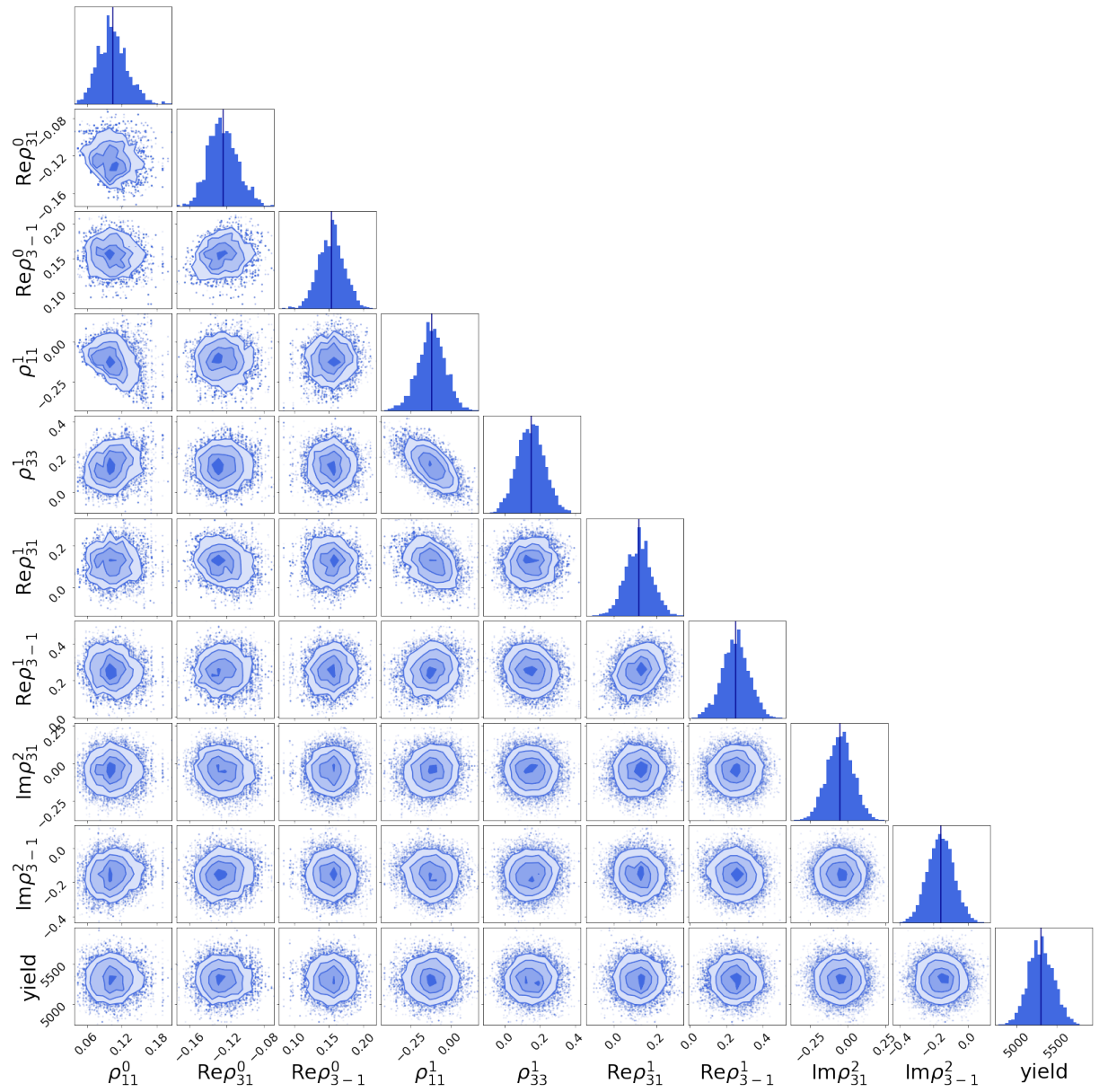


Figure 6.13: SDME corner plot for $-(t - t_{\min}) = 0\text{GeV}^2/c^2 - 0.3\text{GeV}^2/c^2$. The vertical blue line in the 1D distribution indicates the mean.

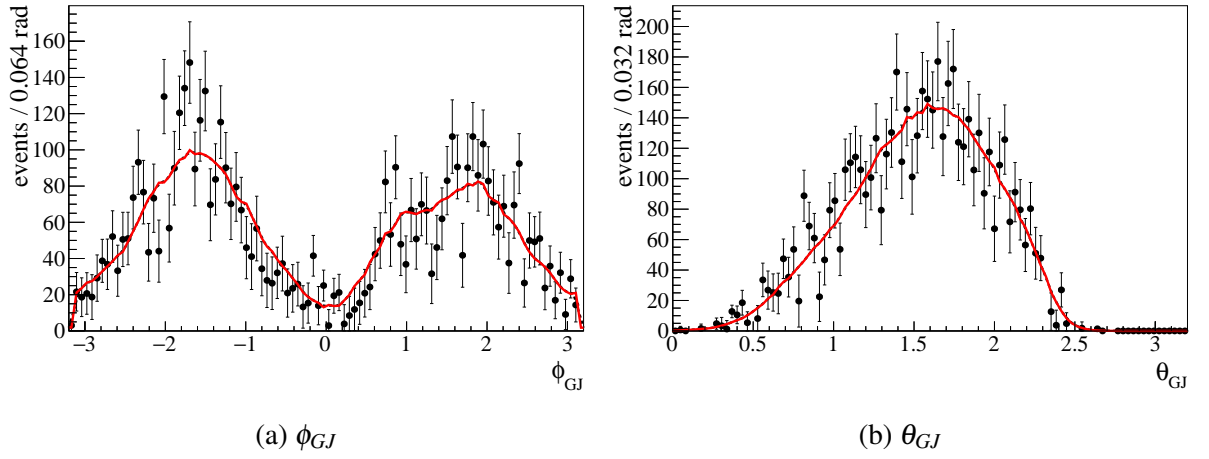


Figure 6.14: Projections of sPlot subtracted data (black points) and acceptance weighted fit results (red lines) for $-(t - t_{\min}) = 0 \text{ GeV}^2/c^2 - 0.3 \text{ GeV}^2/c^2$.

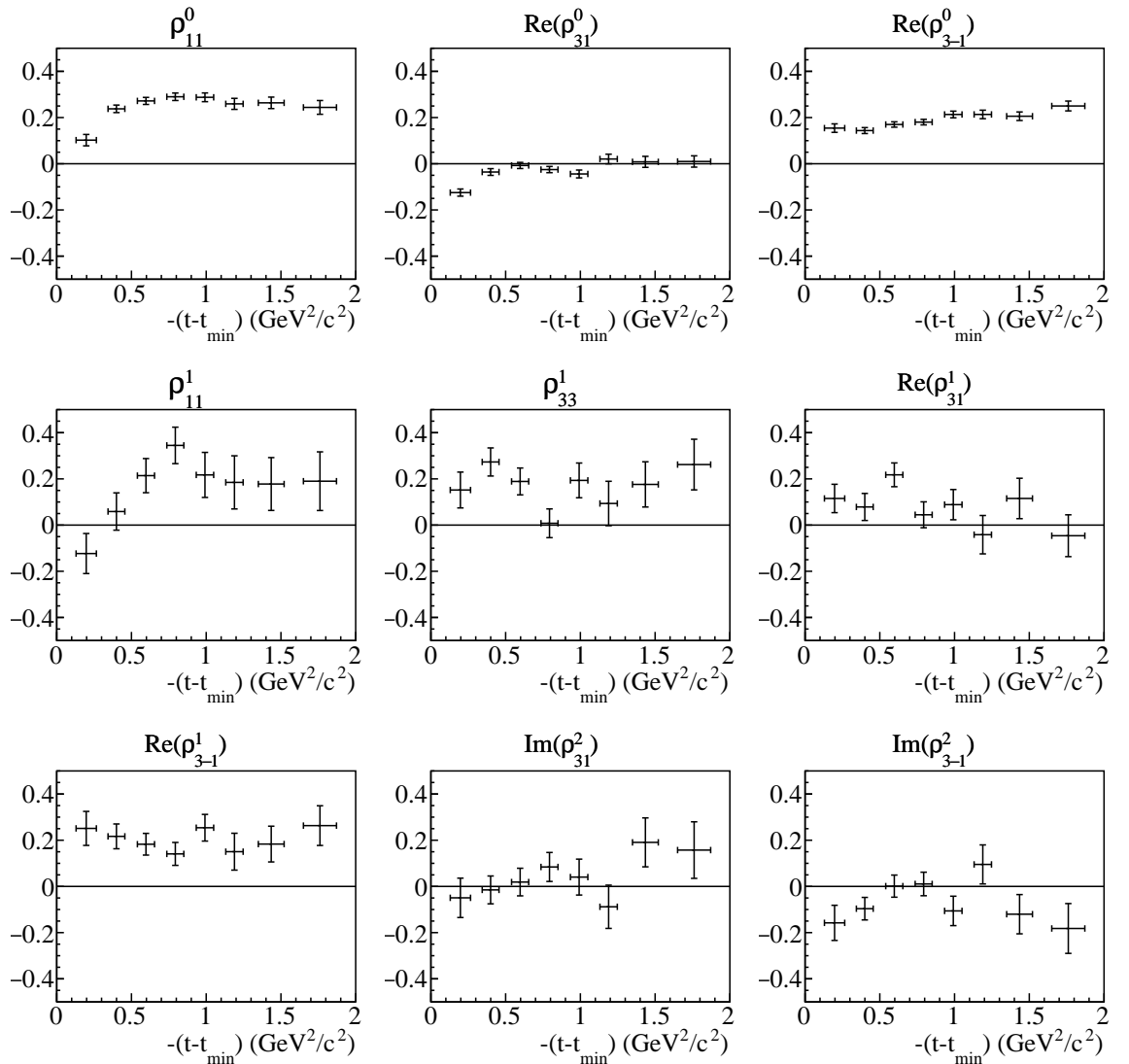


Figure 6.15: SDME results in the Gottfried-Jackson frame as a function of four momentum transfer squared.

As shown before in Eq. (2.55), there is a relationship between the beam asymmetry Σ and two of the nine SDMEs

$$\Sigma = 2(\rho_{11}^1 + \rho_{33}^1) \quad (6.10)$$

This relation can be used to cross-check the results to some degree. The results are presented in Figure 6.16 and show that there is excellent agreement between the results extracted with the unbinned maximum likelihood fit to the K^+ ϕ -angle distribution (see Section 6.1.3) and the ones extracted via Eq. (2.55). Only the first bin shows a small discrepancy between the two results.

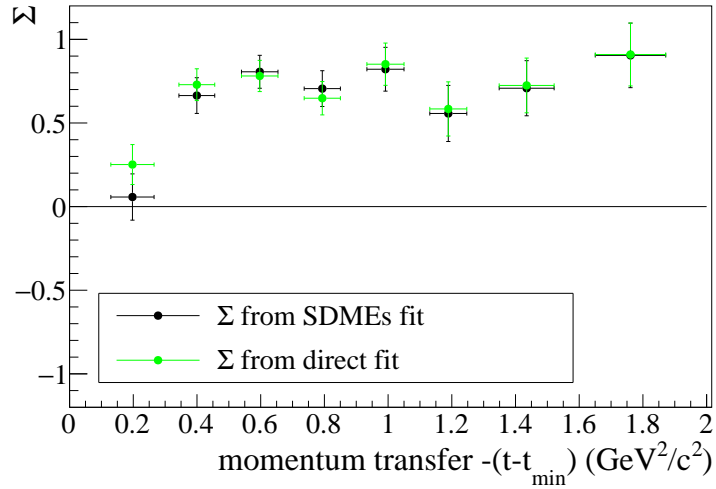


Figure 6.16: Results for the beam asymmetry Σ extracted via Eq. (2.55) (black points) compared to the results from an unbinned maximum likelihood fit using Eq. (6.6) (green points).

The origin of it is not fully understood. It is very important to remember that the direct fit only yields the beam asymmetry Σ when all angles other than ϕ_{K^+} integrate out (see Eq. (2.54)). If this integration is not complete it might cause the beam asymmetry to appear larger. This effect would be expected to be more pronounced at very small $-(t - t_{\min})$ where the acceptance effects introduced through the detector geometry are bigger. Measuring SDMEs accounts for all acceptance effects in the final state and should not be affected by this effect. Therefore, the results from the SDME analysis should be considered more reliable.

6.2.3 Sideband studies

As with the photon beam asymmetry (see Section 6.1.5), a study was carried out to investigate the sideband regions of the $\Lambda(1520)$ peak. It is important to remember that the SDMEs defined in Eq. (2.28) are only meaningful for decays of $J^P = 3/2^- \rightarrow 1/2^+ + 0^-$. Only then does Eq. (2.28) give a formally correct parametrisation of the data, with SDMEs that have a physical meaning. Since Eq. (2.28) has a very complex structure that contains many trigonometric terms, it might

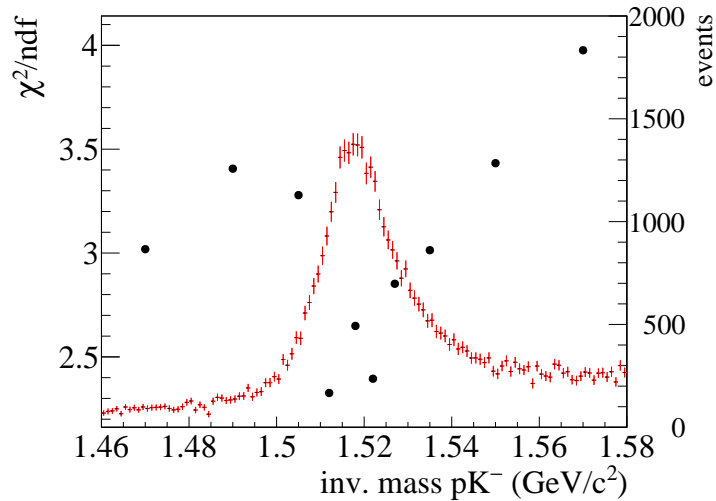


Figure 6.17: Sum of the χ^2/ndf distribution for ϕ_{GJ} and θ_{GJ} for all fits in bins of pK^- invariant mass (black points) and pK^- inv. mass (red).

still result in a fit close to the data for other spin combinations but one would expect to see differences in the fit quality in the sideband compared to the peak.

The SDME fits were repeated without applying the sWeights in ten bins of pK^- invariant mass. As expected, results show clear differences in the quality of the description of the data, and the fits are included in Appendix C.2 for brevity (Figures C.8-C.17). Fit projections in the sideband regions show that the fit procedure did not result in a good description of the data. The angular distributions of events in the $\Lambda(1520)$ peak region on the other hand are very well described by Eq. (2.28). This is also reflected in the χ^2/ndf as calculated for each projection. The sum of the two distributions is shown in Figure 6.17. The χ^2/ndf distribution of projections shows a clear minimum around 1.52 GeV. Only events in the peak region have a spin structure for which Eq. (2.28) is well defined. Those events can therefore be well described by the parametrisation and result in meaningful SDMEs.

The fact that the beam asymmetry Σ from the direct fit using Eq. (6.6) agrees with the results from the SDME fits indicates that the sideband subtraction using sWeights works as intended. To further investigate this extensive MC studies were performed and are reported in the next section.

6.2.4 Validation of results for sPlot and MCMC

In order to validate the results, similar studies to those described in Sections 6.1.2 and 6.1.4, where toy MC samples with known beam asymmetries were analysed, were carried out. For this, a large sample of signal events was generated using an AmpTools [119] based event generator. As background a sample of $\gamma p \rightarrow pK^+K^-$, distributed according to phase space, was produced.

All events were passed through `hdgeant4` to model detector effects (set C, Table 4.3). The angular distribution of the signal events was given by SDMEs specified in Table 6.3 with a degree of polarisation of $P_\gamma = 0.4$ and a run dependent polarisation plane as in real data. The values were chosen such that they reflect the results found in real data.

| | | | | | | | | |
|---------------|---------------|----------------|---------------|---------------|---------------|----------------|---------------|----------------|
| ρ_{11}^0 | ρ_{31}^0 | ρ_{3-1}^0 | ρ_{11}^1 | ρ_{33}^1 | ρ_{31}^1 | ρ_{3-1}^1 | ρ_{31}^2 | ρ_{3-1}^2 |
| 0.26 | -0.06 | 0.23 | 0.2 | 0.1 | 0.04 | 0.2 | 0.04 | 0.01 |

Table 6.3: SDMEs used for signal generation

The four-momentum transfer squared distribution was chosen as $f(t) = t^{0.5}e^{-2.8t}$ to approximate the real data. This resulted in between 900 to 7.5k events per $-(t - t_{\min})$ -bin.

For each of the studies signal and background were added up and the large sample was split into 400 statistically independent smaller samples. These can then be used to perform the parameter extraction many times to create pull distributions, which will ultimately be used to assess the validity of the procedure. For each individual sample the analysis flow of real data was imitated. That means first of all the MC data was split into the same $-(t - t_{\min})$ -bins as real data and an sPlot fit was performed to disentangle signal and background contribution. Then the SDME parameters were estimated with the same MCMC approach described before. The results of the 400 individual samples are then summarised in pull distributions created as

$$\text{pull} = \frac{\text{measured } \rho - \text{true } \rho}{\Delta(\text{measured } \rho)}, \quad (6.11)$$

where $\Delta(\text{measured } \rho)$ denotes the uncertainty on SDME parameter ρ as reported by the MCMC parameter estimation. To summarise the 72 pull distributions each study produced (nine SDME parameters in eight $-(t - t_{\min})$ -bins) only the means and widths will be shown here. Both were extracted via fitting a Gaussian function to the pull distribution and the reported uncertainties on the mean and width are from this fit. In addition, the mean and width of the distribution of differences between fit results and real value is shown.

Analysis of thrown data

In an initial test the thrown (truth) information of signal and background events was used for the analysis. The analysis not being capable of extracting correct results from perfect data would indicate a serious flaw in the procedure.

An example sFit is shown in Figure 6.18. Figure 6.19 shows the projections for the SDME fit to the ϕ_{GJ} and θ_{GJ} distributions. The pull results are summarised in Figures 6.20 to 6.27.

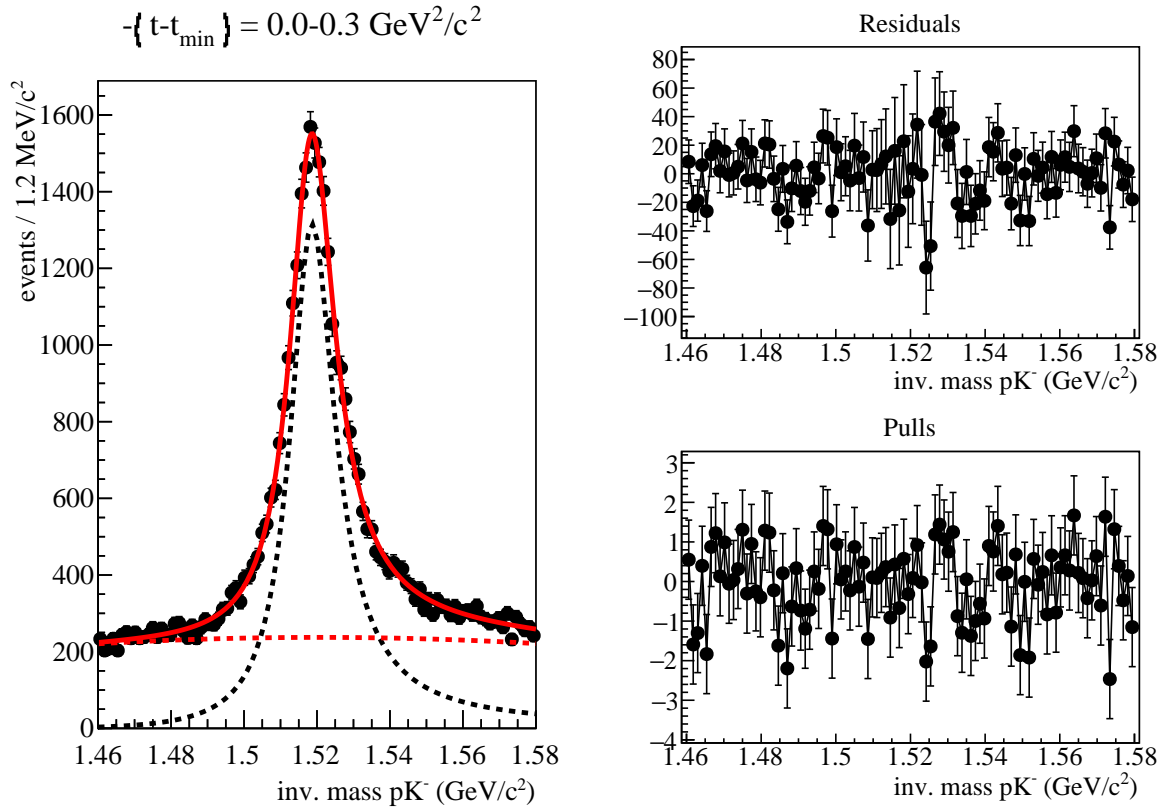


Figure 6.18: Example sFit for one sample of thrown MC. Left: sFit of the pK^- invariant mass. The red dashed line is a Chebychev function used to approximate background. The black dashed line is the Breit-Wigner shape for a $\Lambda(1520)$. The solid red line is the resulting fit to the data. Right: Fit residual on top and pull distribution on bottom.

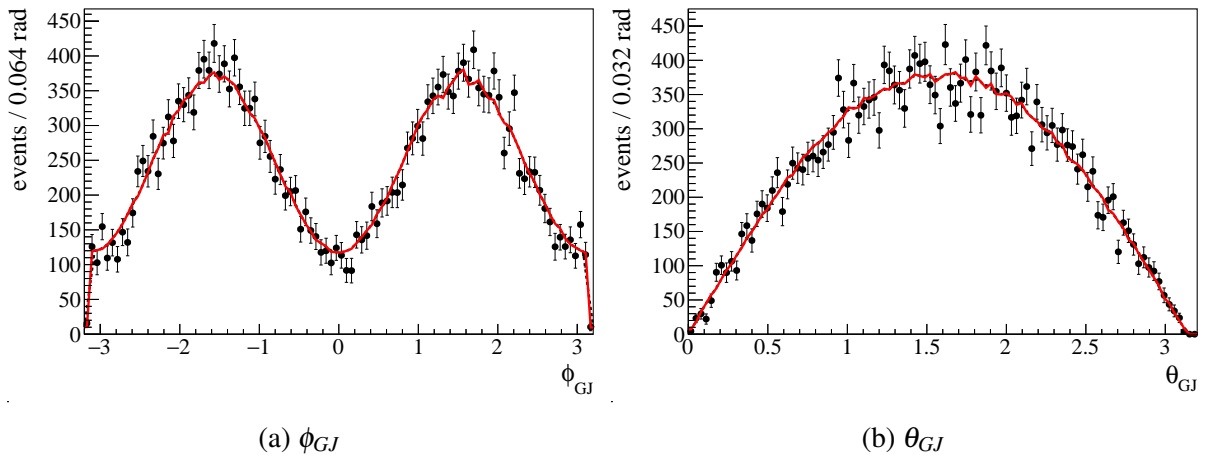


Figure 6.19: Example fits for thrown MC with perfect resolution and acceptance for $-(t - t_{\min}) = 0.0 \text{ GeV}^2/c^2 - 0.3 \text{ GeV}^2/c^2$.

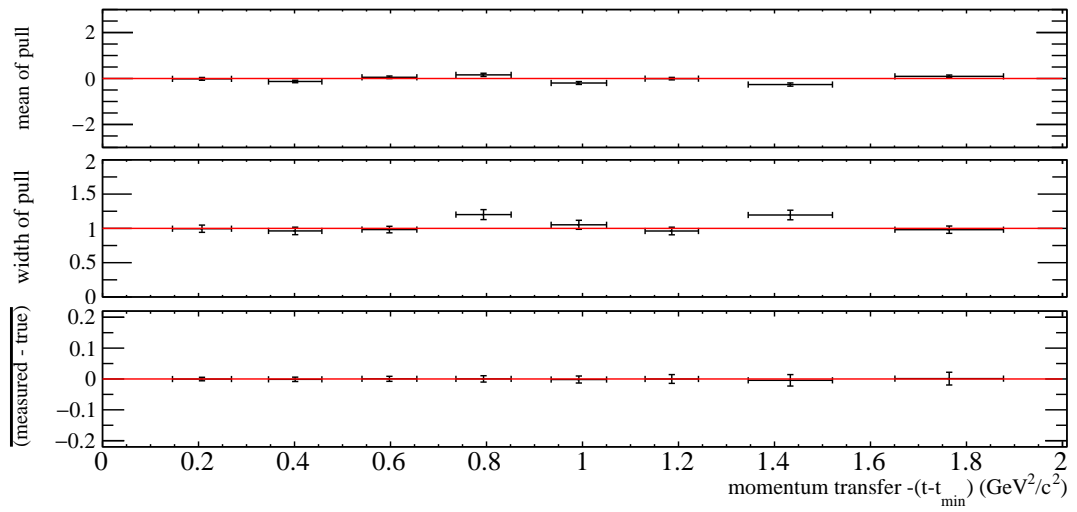


Figure 6.20: Summarised results from thrown data study for ρ_{11}^0 . True value = 0.26.

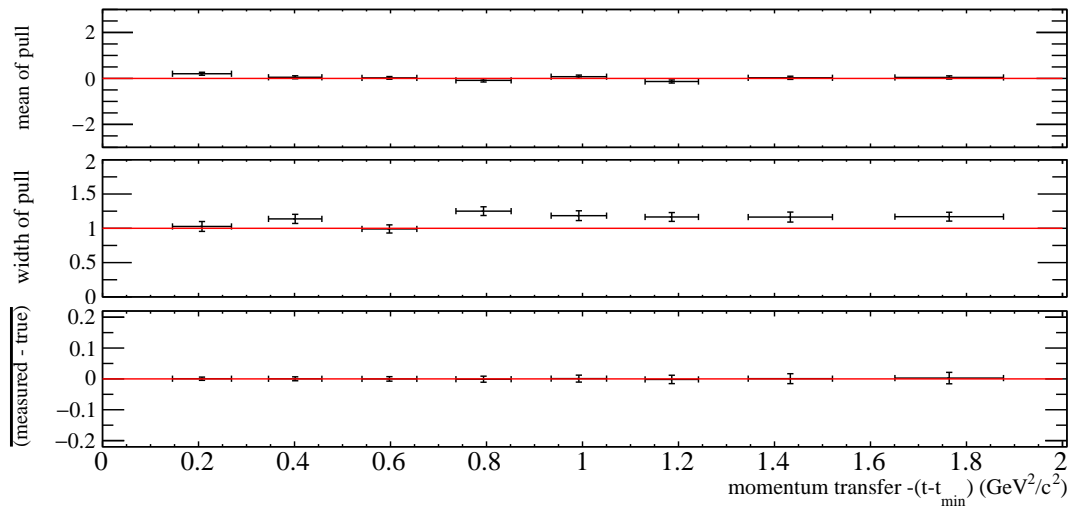


Figure 6.21: Summarised results from thrown data study for ρ_{31}^0 . True value = -0.06.

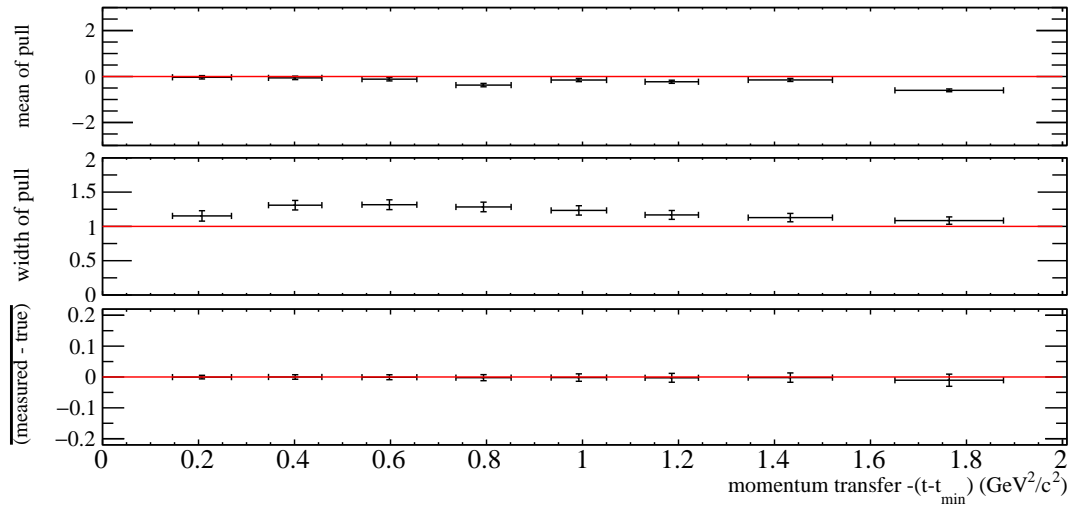


Figure 6.22: Summarised results from thrown data study for ρ_{3-1}^0 . True value = 0.23.

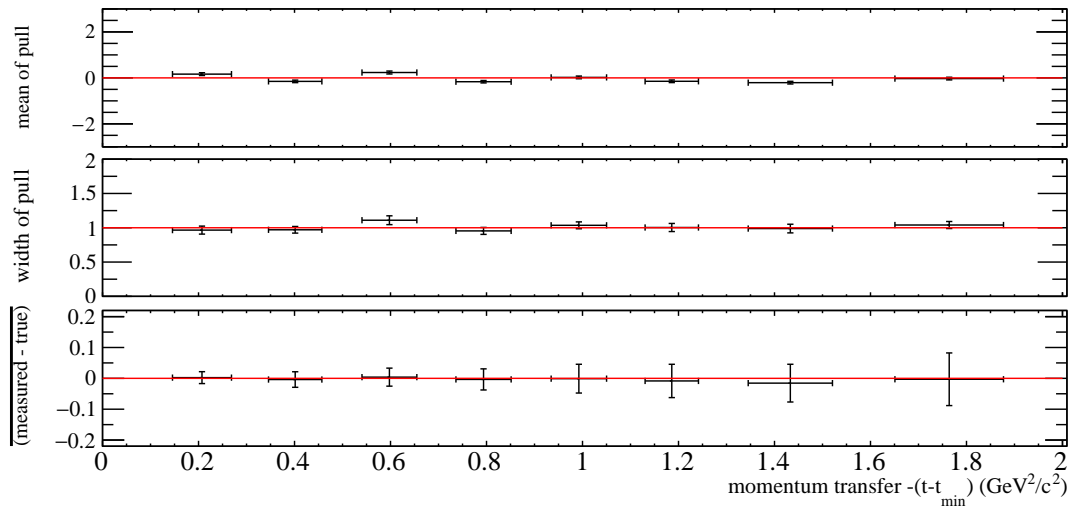


Figure 6.23: Summarised results from thrown data study for ρ_{11}^1 . True value = 0.2.

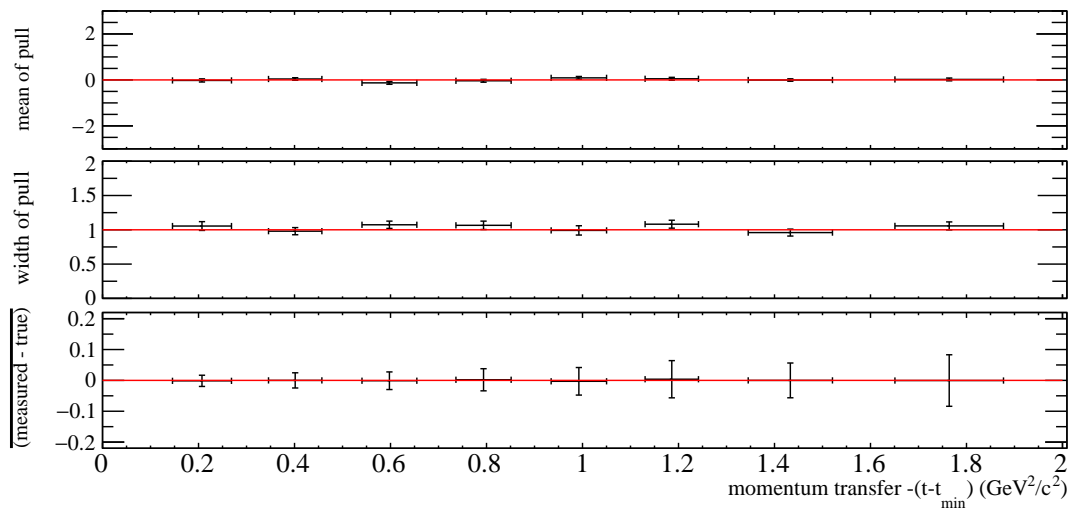


Figure 6.24: Summarised results from thrown data study for ρ_{33}^1 . True value = 0.1.

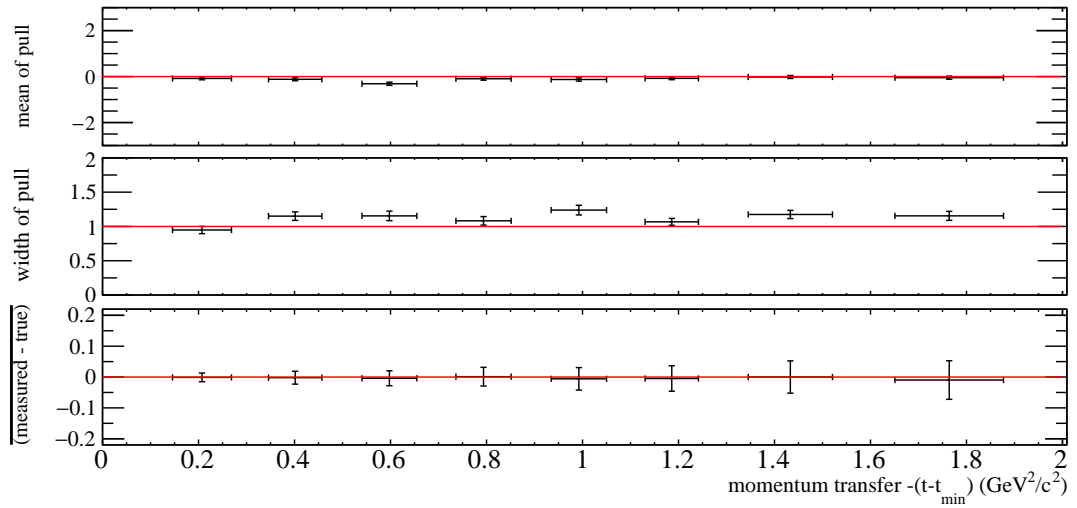


Figure 6.25: Summarised results from thrown data study for ρ_{31}^1 . True value = 0.04.

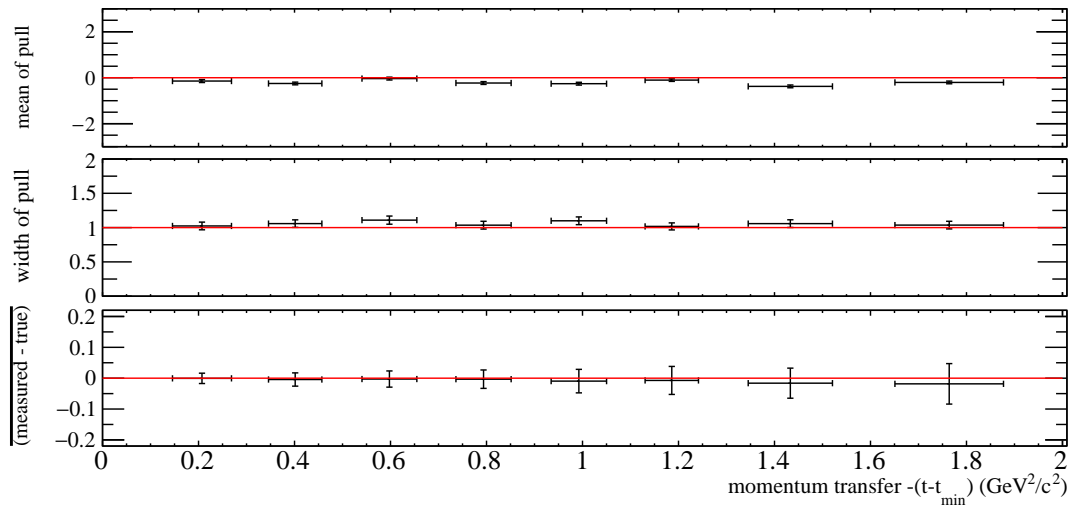


Figure 6.26: Summarised results from thrown data study for ρ_{3-1}^1 . True value = 0.2.

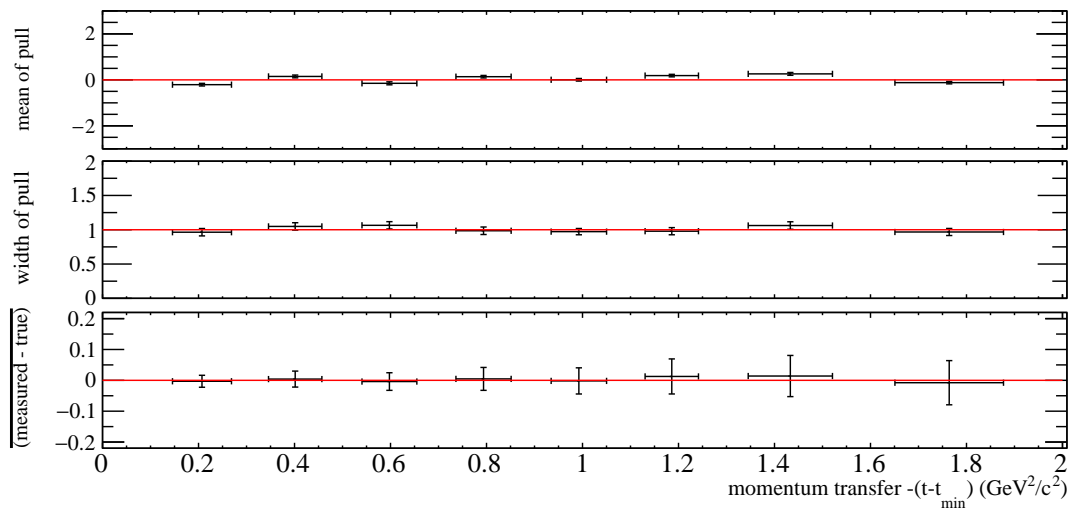


Figure 6.27: Summarised results from thrown data study for ρ_{31}^2 . True value = 0.04.

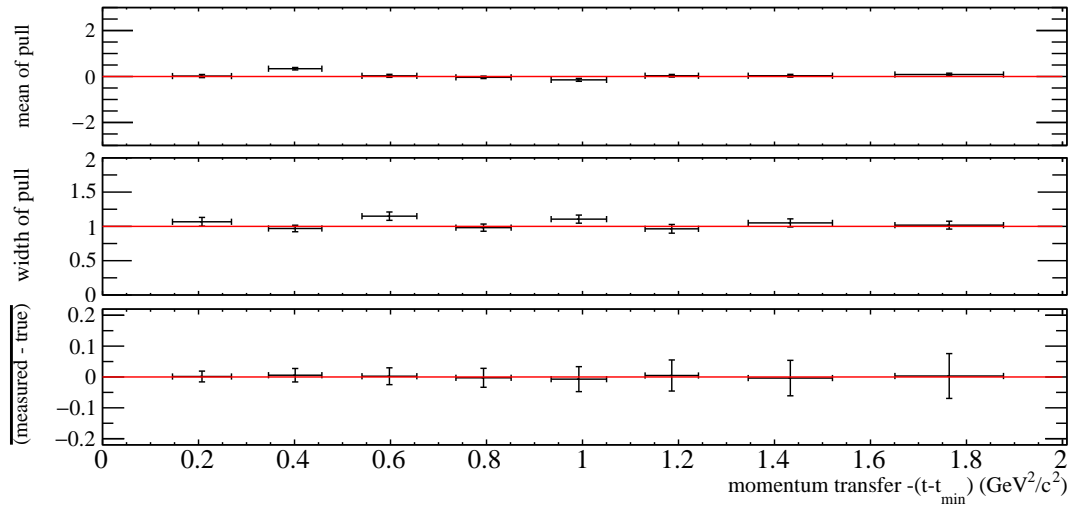


Figure 6.28: Summarised results from thrown data study for ρ_{3-1}^2 . True value = 0.01.

The top plot of each Figure shows the mean values of the pulls as extracted through a Gaussian fit to the pull distribution. The middle plot shows the associated width. The plot at the bottom of each figure shows the mean of the distribution of differences between extracted result and true value, the nominator of the pull. The error bars for mean and width of the pull are the errors reported by the Gaussian fit to the distribution. In the case of the difference the uncertainty is given as the standard deviation of the distribution. The red lines indicate a mean of zero, width of one and difference of zero as one would expect from the pulls for unbiased results with correct error bars. There is excellent agreement between the extracted and true value in all cases as it should be, as by construction the only deviations should be statistical fluctuations. This is generally reflected in the pull distributions, which are as expected in most bins.

To assess the quality of the sPlot procedure one can look at the angular distributions and compare the actual signal put into the simulation with the signal extracted via sWeights. To increase the statistics for this fit, it was done for the whole MC dataset before it was split into 400 independent samples and binned in $-(t - t_{\min})$. The plots can be seen in Figure 6.29. The difference between the real signal and the extracted signal is less than 1%.

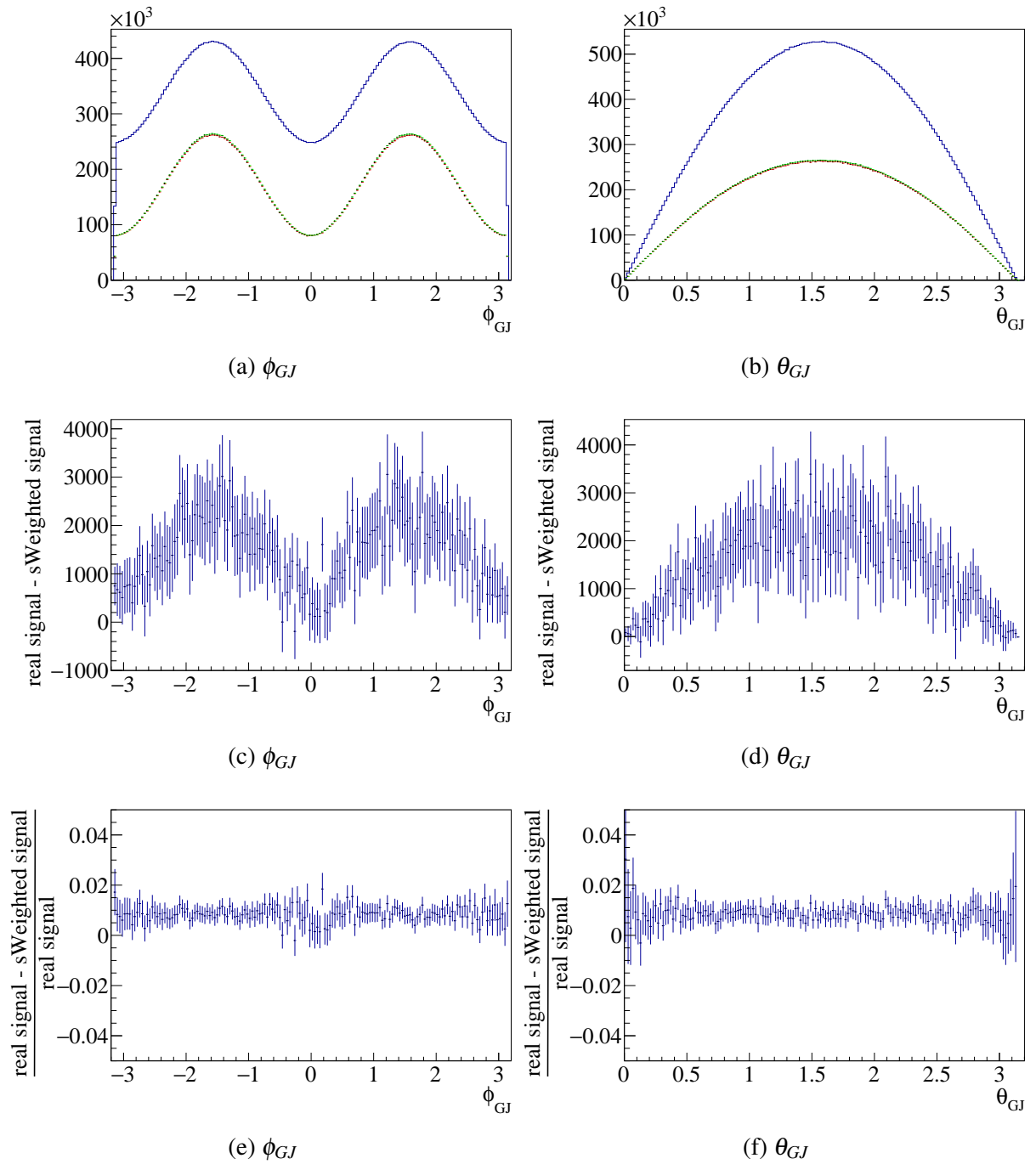


Figure 6.29: Comparison between real MC signal (green) and signal extracted via the sFit (red) in thrown data, both distributions are overlapping. (c) and (d) show the difference between both. The blue histograms in (a) and (b) show the full simulated sample of signal plus background. (e) and (f) show relative differences.

Analysis of full simulation

After it was shown that the analysis procedure works as intended on thrown data, a more realistic check of the SDME extraction using a full simulation of the detector was performed. An example sFit for this setup can be seen in Figure 6.30. An example fit to the ϕ_{GJ} and θ_{GJ} dis-

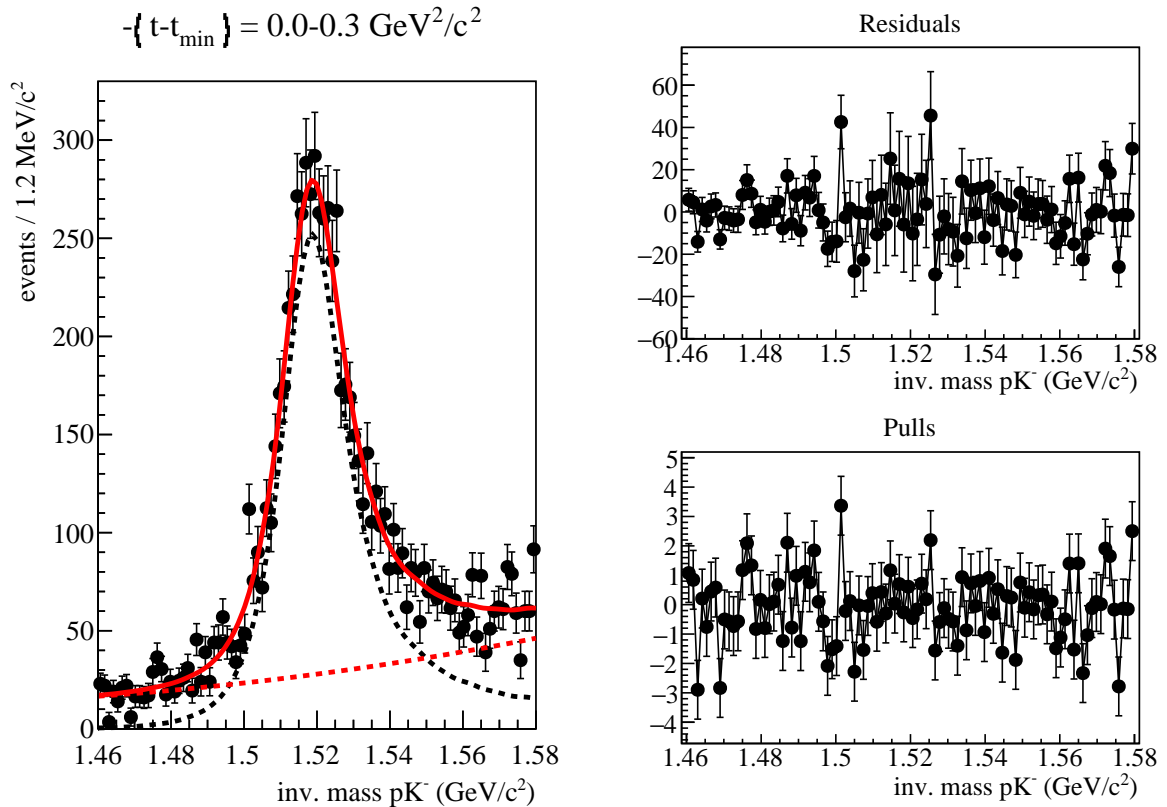


Figure 6.30: Example sFit for one sample of fully simulated MC. Left: sFit of the pK^- invariant mass. The red dashed line is a Chebychev function used to approximate background. The black dashed line is the Breit-Wigner shape for a $\Lambda(1520)$. The solid red line is the resulting fit to the data. Right: Fit residual on top and pull distribution on bottom.

tributions can be seen in Figure 6.31. Figures 6.32 to 6.40 show the extracted means, widths and differences following the same structure as before. The results changed quite significantly, especially for unpolarised SDMEs. They show pull distributions with means not consistent with 0. However, the absolute difference is still generally small.

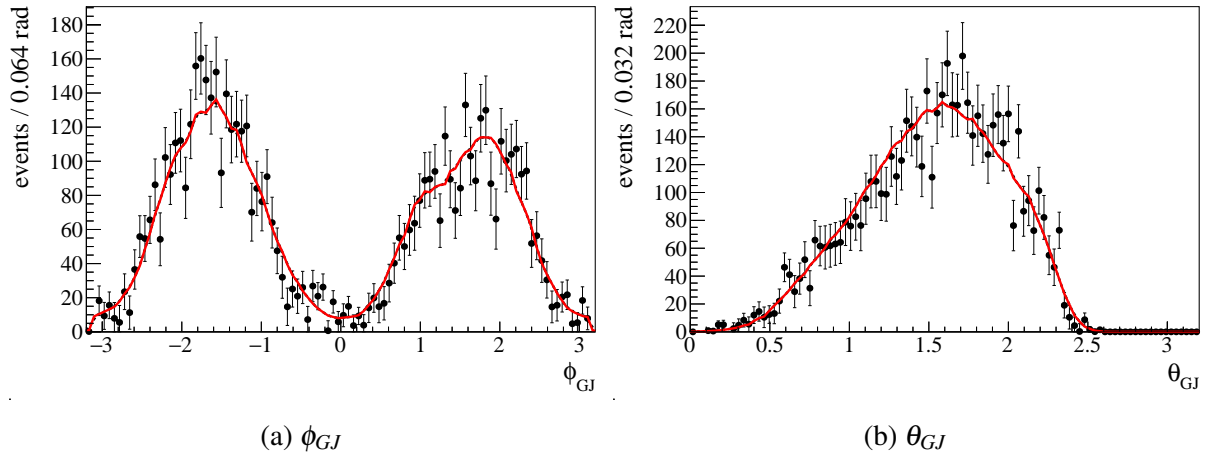


Figure 6.31: Example fits for full MC simulation for $-(t - t_{\min}) = 0.0 \text{ GeV}^2/c^2 - 0.3 \text{ GeV}^2/c^2$.

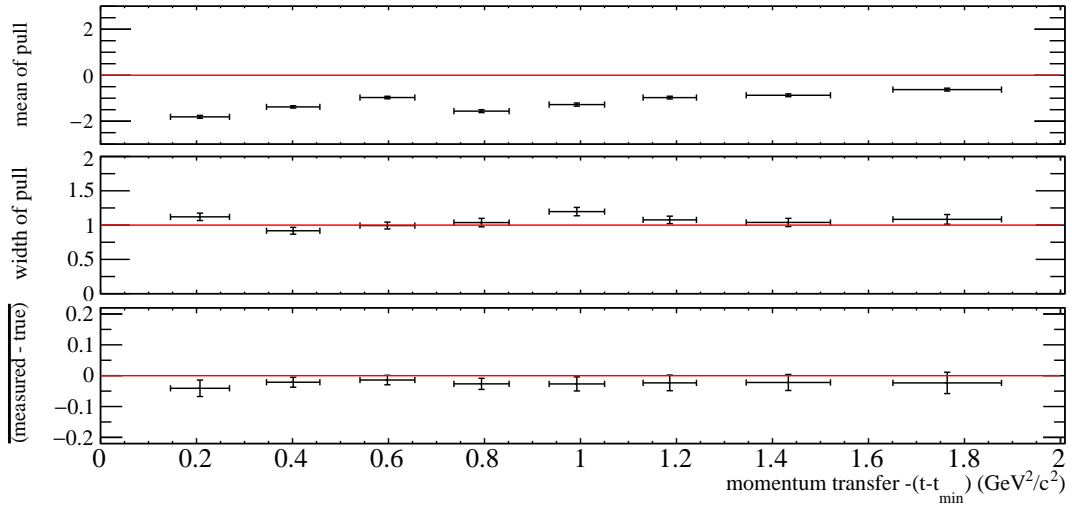


Figure 6.32: Summarised results from study with full simulation for ρ_{11}^0 . True value = 0.26.

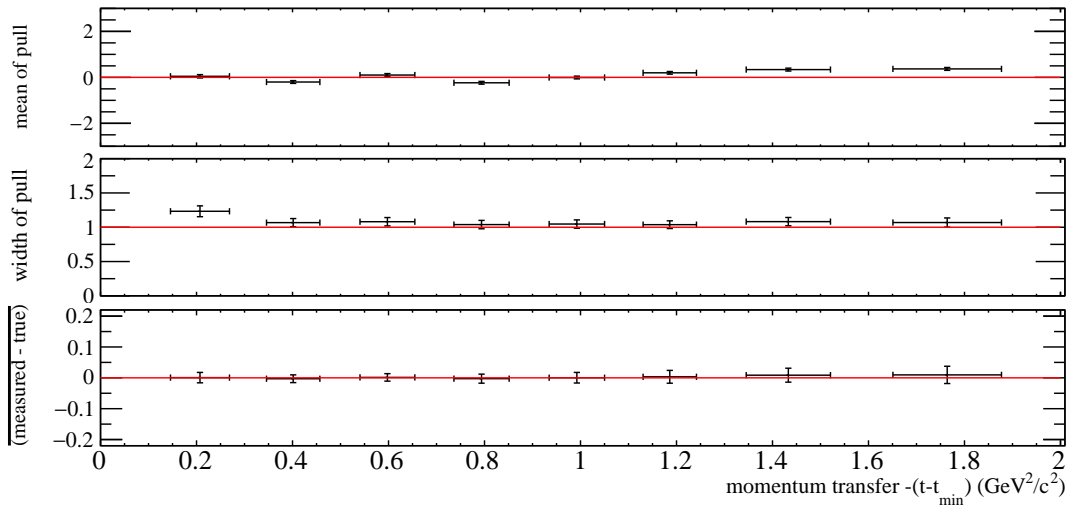


Figure 6.33: Summarised results from study with full simulation for ρ_{31}^0 . True value = -0.06.

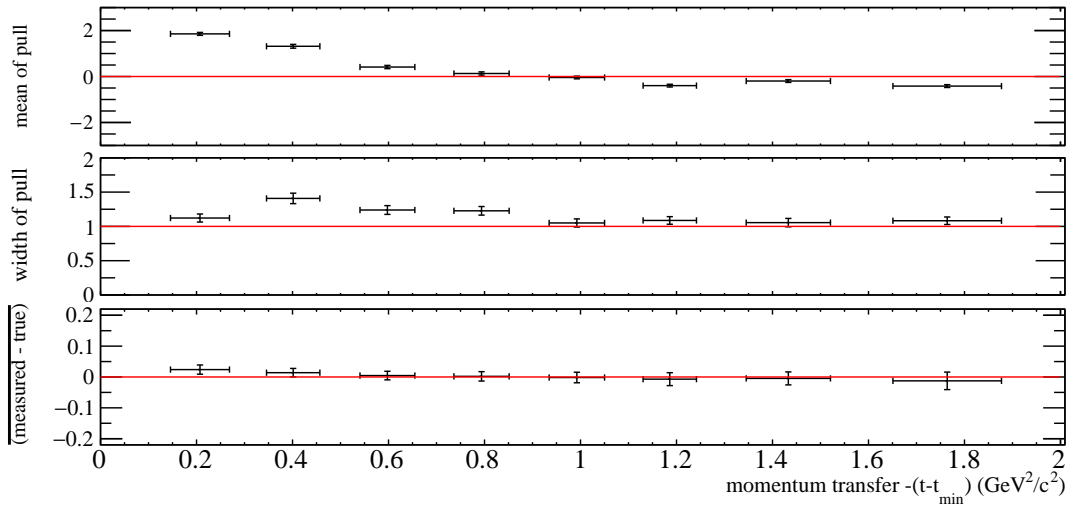


Figure 6.34: Summarised results from study with full simulation for ρ_{3-1}^0 . True value = 0.23.

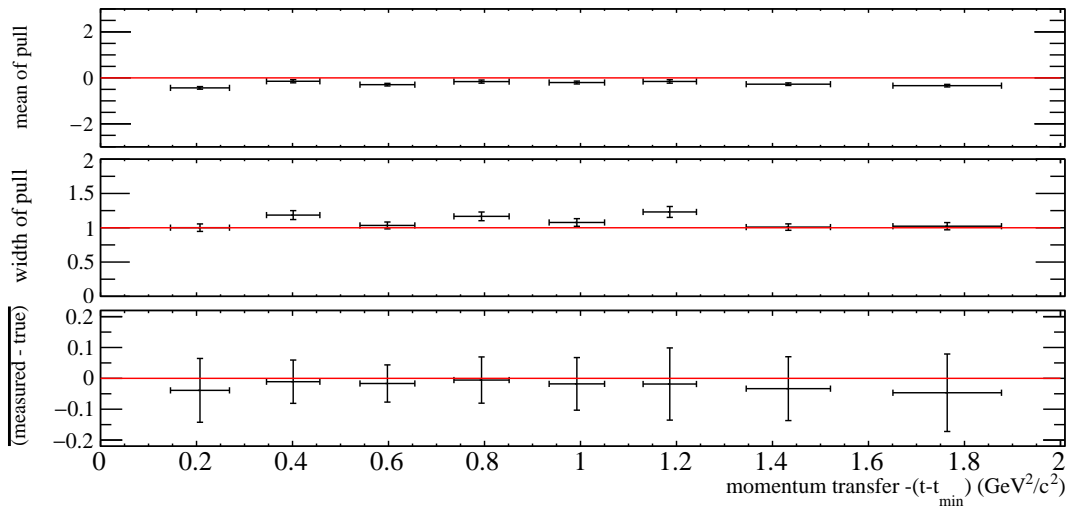


Figure 6.35: Summarised results from study with full simulation for ρ_{11}^1 . True value = 0.2.

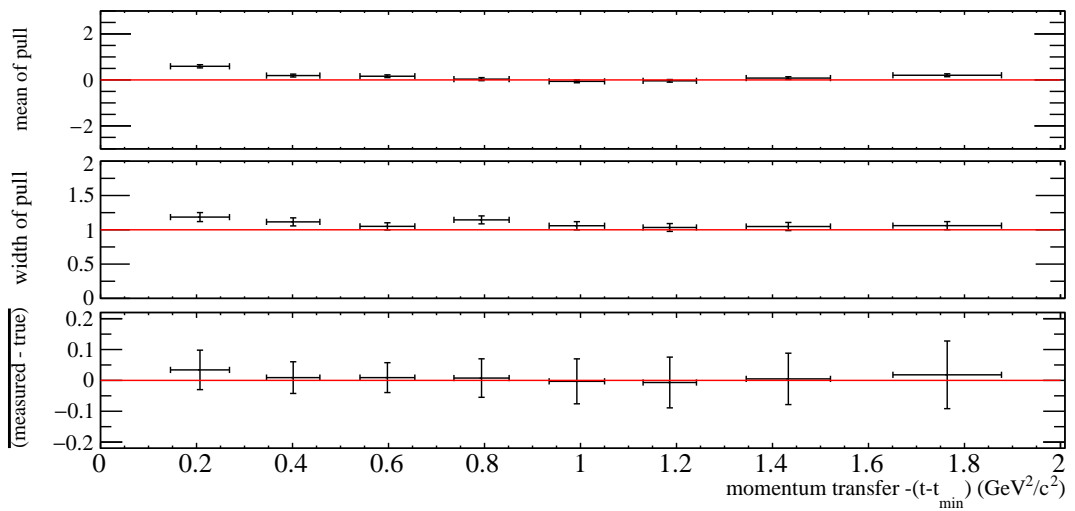


Figure 6.36: Summarised results from study with full simulation for ρ_{33}^1 . True value = 0.1.

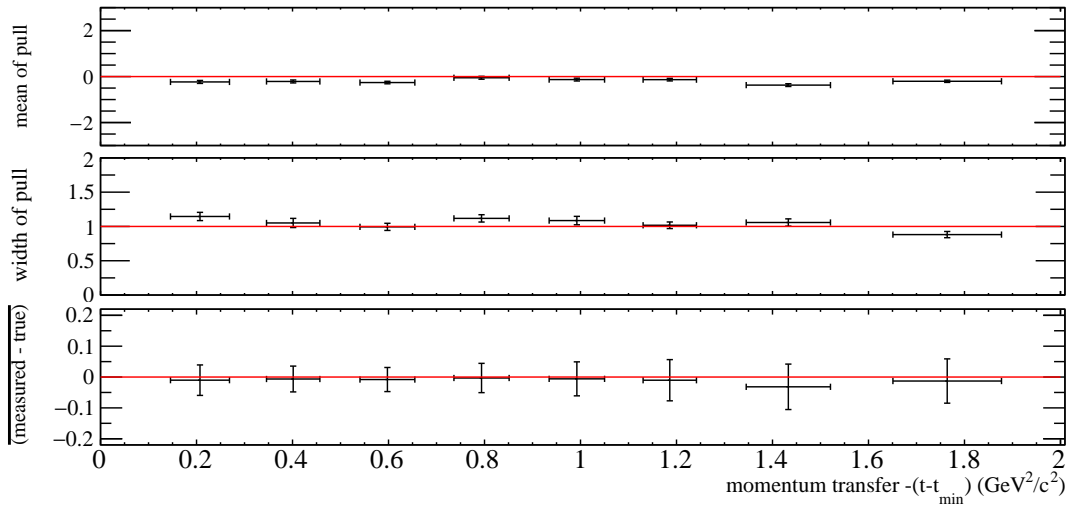


Figure 6.37: Summarised results from study with full simulation for ρ_{31}^1 . True value = 0.04.

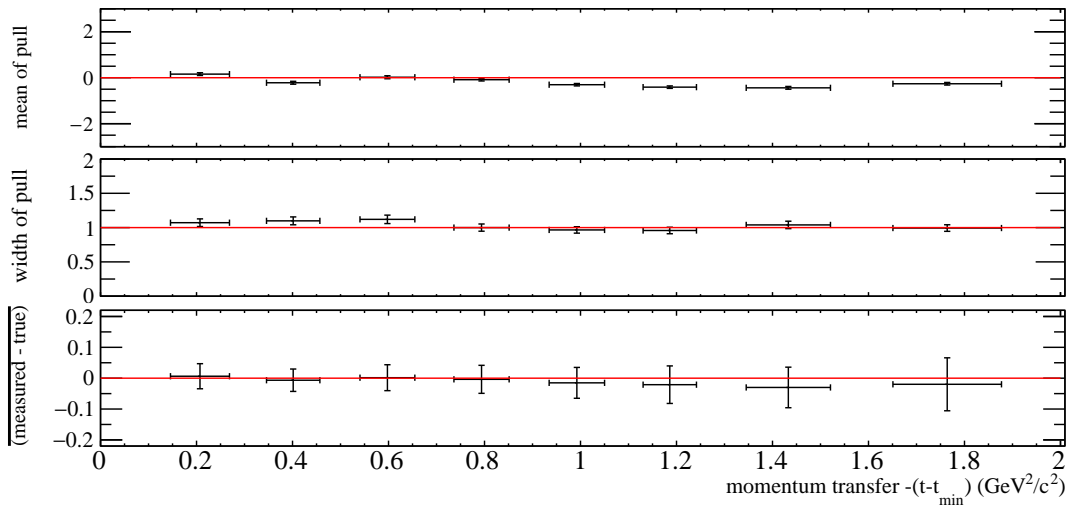


Figure 6.38: Summarised results from study with full simulation for ρ_{3-1}^1 . True value = 0.2.

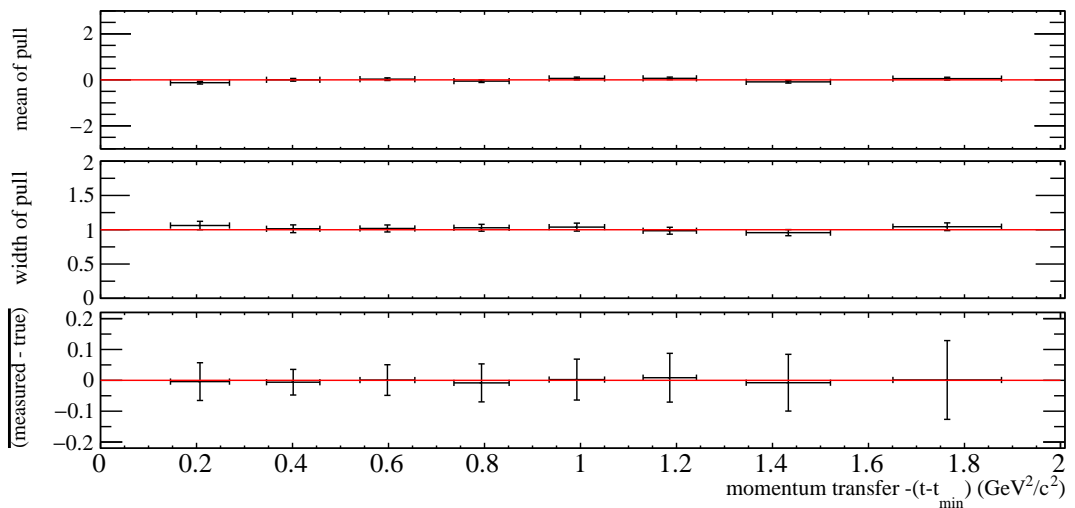


Figure 6.39: Summarised results from study with full simulation for ρ_{31}^2 . True value = 0.04.

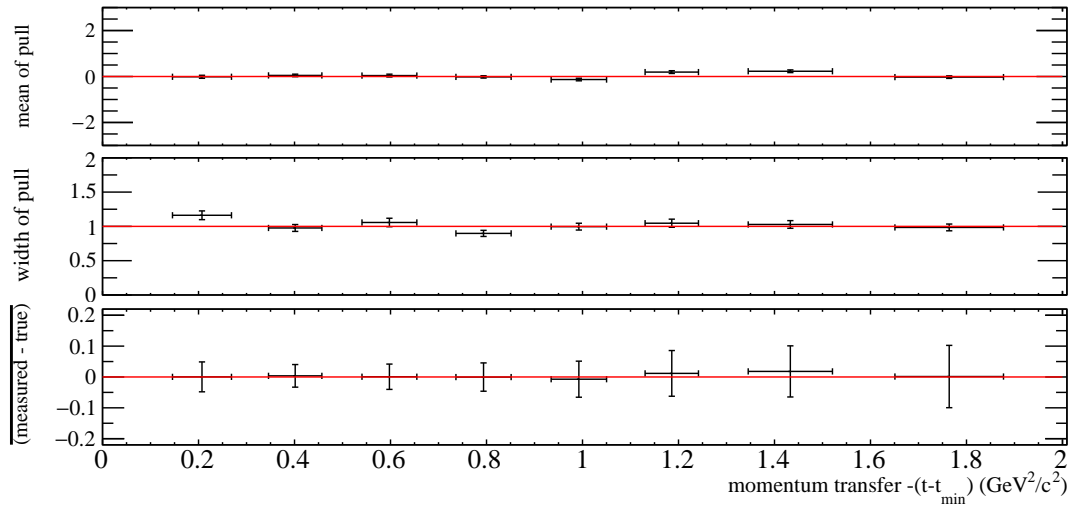


Figure 6.40: Summarised results from study with full simulation for ρ_{3-1}^2 . True value = 0.01.

As before we can also compare the actual signal with the extracted signal. The results are in Figure 6.41. It seems like the sPlot did not manage to capture the full signal distribution. The extracted signal yield is about 4% less than the real signal yield in the MC sample. The missing signal is not uniformly distributed in ϕ_{GJ} and θ_{GJ} . The relative difference shows large deviations in some parts of the angular distributions. It is important to note that the largest relative differences can be observed where the absolute number of events is small. Therefore, the overall effect is not as huge as one might think. The resulting difference might explain why the pulls in some of the bins for some SDMEs are not as expected.

Summary of results of validation studies

The most important studies have been described in detail above. Several more investigations were also made. They are summarised in Table 6.4 and the details are included in Appendix C.3 for brevity. The conclusions from all these studies are summarised below.

The large collection of plots reveal a small systematic effect in the extraction of SDMEs. The most important part of the study is the full simulation (Figs. 6.32-6.40). It is the most realistic

| type of study | summary |
|---|----------------|
| thrown | Section 6.2.4 |
| full simulation | Section 6.2.4 |
| thrown with artificial resolution | Appendix C.3.1 |
| thrown with artificial acceptance | Appendix C.3.2 |
| full simulation without background | Appendix C.3.3 |
| full simulation with small background and no sFit | Appendix C.3.4 |

Table 6.4: Summary of all performed SDME validation studies.

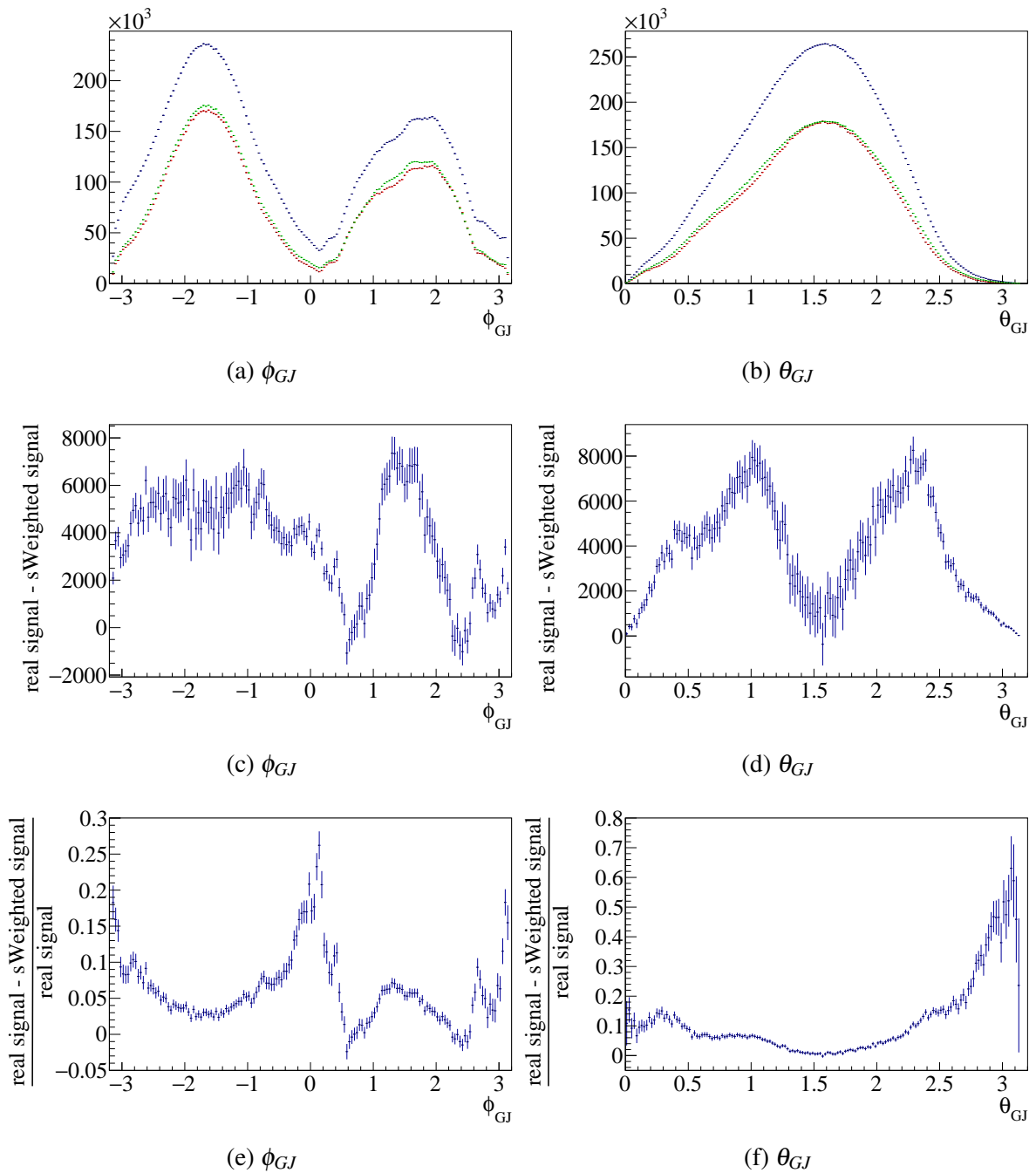


Figure 6.41: Comparison between real MC signal (green) and signal extracted via the sFit (red). (c) and (d) show the difference between both. The blue histogram in (a) and (b) shows the full simulated sample of signal plus background. (e) and (f) show relative differences.

setup, as close to the real data as possible. There one sees that the polarised SDMEs show good behaviour in general. Most of the pulls show a mean of almost 0 and a width of almost 1. The differences are all very close to 0. The behaviour is not as good for the unpolarised SDMEs. In particular, the pulls for ρ_{11}^0 and ρ_{3-1}^0 show large deviations from a standard normal distribution, although the difference in absolute terms is still quite small. To understand the reason behind this problem the other studies have to be looked at carefully. There one can see that neither the case

of the thrown MC sample (Figs 6.20-6.28) nor the thrown sample with an artificial resolution (Figs C.20-C.28) show extreme deviations from a normal distribution in their respective pulls (although ρ_{3-1}^0 seems to be always slightly off). The thrown sample with an artificial acceptance however seems to show an effect (Figs C.32-C.40). The study that used a full detector simulation but had no background in the data samples (Figs. C.42-C.50) revealed good pulls in the majority of SDMEs and bins. In addition, the comparison between the actual signal in the distributions with the sWeight extracted signal shows very small deviations for all samples. The deviations are not uniform in ϕ_{GJ} and θ_{GJ} but have an angular dependence which could bias the fits. This leads to the following conclusions:

- thrown data and thrown data with artificial resolution show good results:
 - the sPlot background subtraction is removing background as expected
 - treatment of weights in likelihood function works well
- full simulation without background shows good results
 - the SDME extraction with MCMC works well
- full simulation with small background but without sFit shows that a very small amount of unsubtracted background in the signal is enough to have noticeable effects on the fit results
- comparisons of decay angle distributions between simulated pure signal and sWeight extracted signal shows small difference
- full simulation with background and thrown data with artificial acceptance shows shifted pulls for unpolarised SDMEs
 - acceptance in combination with background seems to result in a small residual background component that distorts the fit

The deviations that are seen are sensitive to magnitude and angular distribution of the background. Attempting to correct for it would be unreliable and come with its own systematic uncertainties. Therefore, the systematic effects seen in the study are included as a systematic uncertainty on the final results. The studies suggest that the polarised SDMEs are less sensitive to the seen effects than the unpolarised SDMEs. Therefore, only a systematic uncertainty of 0.01 will be added for the former. An uncertainty of 0.02 is added for the latter. These numerical results are based on the averaged differences seen in the studies.

| | set 1 | set 2 | set 3 | set 4 | set 5 |
|----------------|-------|-------|-------|-------|-------|
| ρ_{11}^0 | 0.2 | 0.1 | -0.1 | 0 | 0 |
| ρ_{31}^0 | 0.2 | 0.1 | -0.1 | 0 | 0 |
| ρ_{3-1}^0 | 0.2 | 0.1 | -0.1 | 0 | 0 |
| ρ_{11}^1 | 0.2 | 0.1 | -0.1 | 0.3 | -0.3 |
| ρ_{33}^1 | 0.2 | 0.1 | -0.1 | -0.1 | 0.1 |
| ρ_{31}^1 | 0.2 | 0.1 | -0.1 | 0.3 | -0.3 |
| ρ_{3-1}^1 | 0.2 | 0.1 | -0.1 | 0.3 | -0.3 |
| ρ_{31}^2 | 0.2 | 0.1 | -0.1 | 0.3 | -0.3 |
| ρ_{3-1}^2 | 0.2 | 0.1 | -0.1 | 0.3 | -0.3 |

Table 6.5: Sets of start parameters used for the systematic study of MCMC.

6.2.5 Further systematic studies

Further systematic studies were performed to estimate uncertainties relating to the event selection and photon beam properties. Similar to the studies for the beam asymmetry (see Section 6.1.6) the Barlow test was used as a metric to gain a feeling for the significance of differences in the measurements.

Study of start parameter

First of all it was important to make sure that the extracted results did not depend on the start parameter chosen for the Markov Chain. For that purpose five different sets of start parameters were used in addition to check if the final results changed (see Table 6.5). The extracted SDMEs for all five sets and the baseline setting are shown in Figure 6.42. The agreement between all sets is excellent. To quantify it further the Barlow test was performed. The results are shown in Figure 6.43. No significant systematic deviations are observed. For that reason no systematic uncertainty for the choice of start parameters of the Markov Chain was included in the final results.

Event selection

To test the influences of the event selection the same changes to the cuts as in Section 6.1.6 were checked (see Table 6.1). The results are discussed in the following while the corresponding plots are shown in Appendix C.4.

Invariant mass cut First of all the range of the invariant mass cut for the sPlot fit was varied (Table 6.1, setups 1-6). The results can be seen in Figure C.60. All results seem to agree within

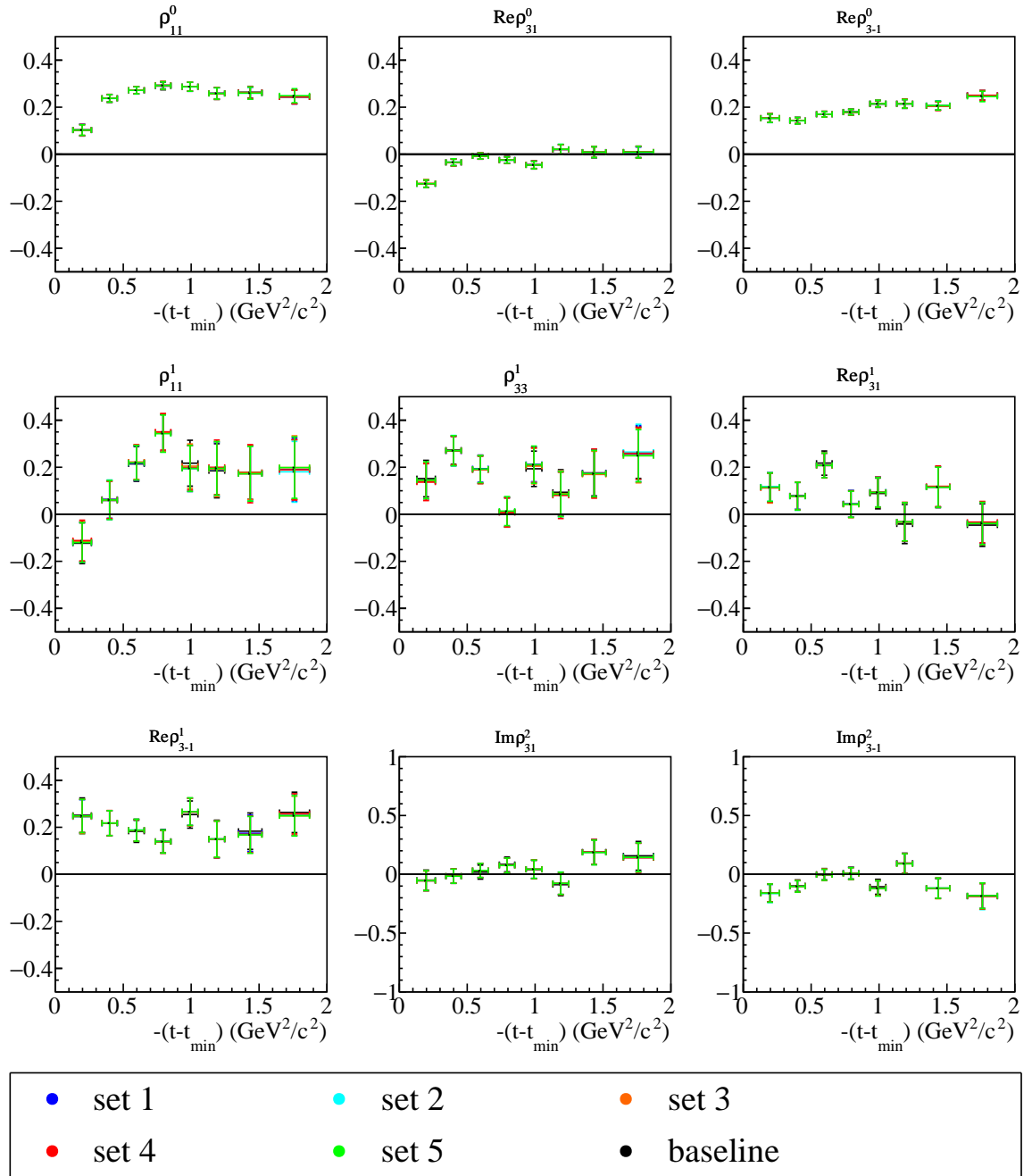


Figure 6.42: Results for the SDMEs for the baseline setting (black points) and five other sets of start parameters for the Markov Chain (see Table 6.5).

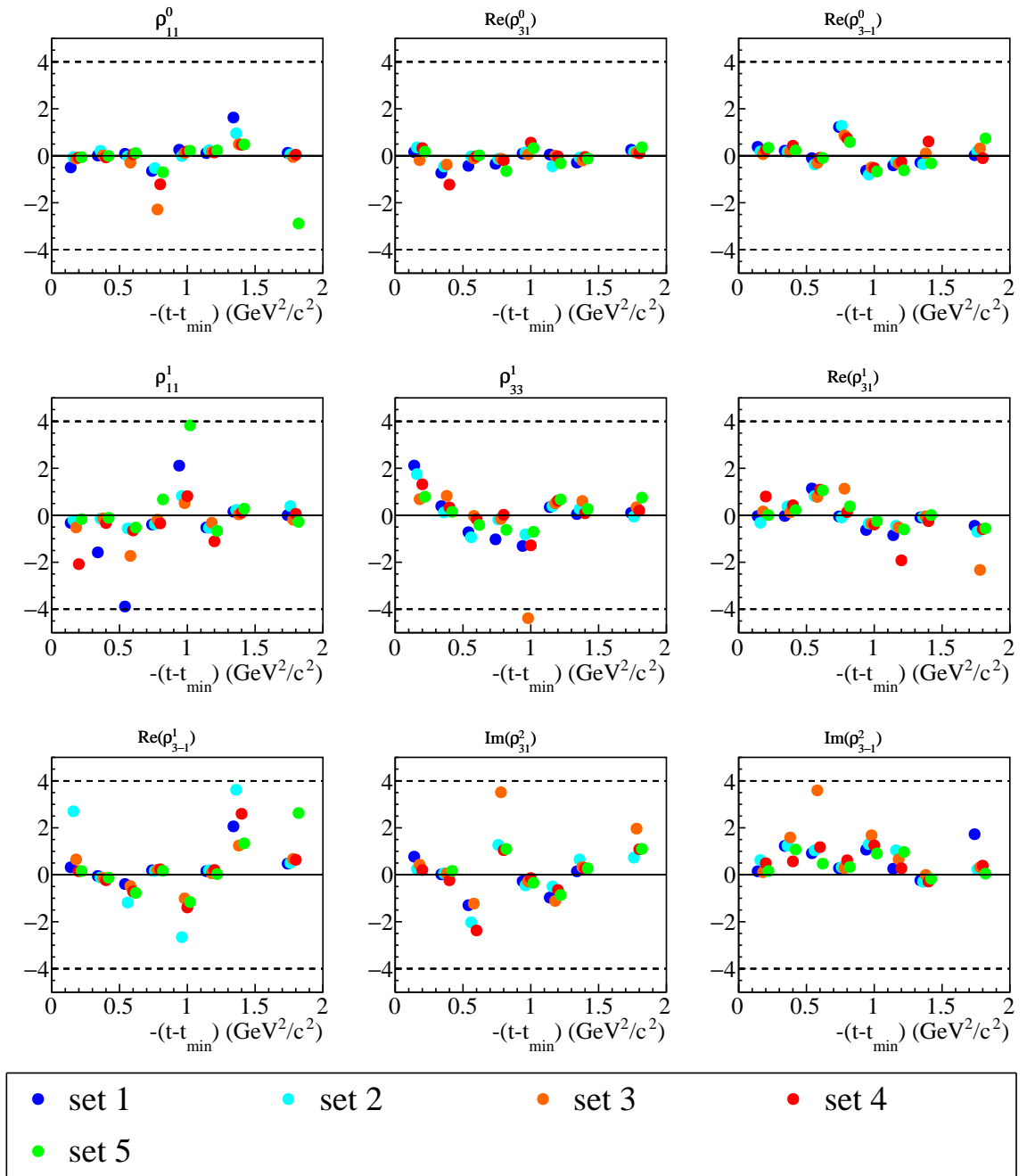


Figure 6.43: The significance as defined in the Barlow test is plotted for each set of start parameters for the Markov Chain (see Table 6.5).

statistics. To quantify if there is a systematic uncertainty introduced by the choice of the fit range the Barlow test was performed. The results are shown in Figure C.61. In general, one can see that almost all points show no significant deviation. There are however a few outliers. An argument is to be made that, similar to the case of the beam asymmetry, one would not expect one bin to show a very strong systematic effect while its neighbours show no effect. While it is possible that systematic effects have a $-(t - t_{\min})$ -dependency one would expect a continuous shift. No such behaviour is seen and therefore it was concluded that no systematic uncertainty needs to be added for the invariant mass cut.

Confidence Level cut The confidence level cut was varied and the whole analysis performed (Table 6.1, setups 7-10). The results are shown in Figure C.62. Again, the Barlow test was performed to quantify a possible systematic effect. The results can be found in Figure C.63. Similar to the previous test, one can see that almost all points are within -4 to 4 . A few outliers can be seen with sometimes extraordinarily high significances. Nevertheless, they seem to be isolated from their neighbours. No significant trend was found for any of the tested settings. Therefore, no systematic uncertainty was added for the choice of CL cut.

Vertex cut To check if there was an effect introduced by the choice of cut on the target cell the cut limits in r and z were varied (Table 6.1, setups 11-14). The results for all SDMEs can be found in Figure C.64. All tested settings seem to agree within error bars. As before, the Barlow test was performed to check quantitatively if there was a systematic effect that needs to be taken into account. The results are shown in Figure C.65. Apart from very few outliers the results suggest that there is no systematic effect that needs to be taken into account. Therefore, no systematic uncertainty was added for the choice of vertex cuts.

PID cut To check the influence of the ΔT cut on the extracted SDMEs the cut limits were varied for all three particles (Table 6.1, setups 15-26). The results are shown in Figures C.66, C.68 and C.70. To check if there is a systematic effect introduced by the choice of the cut limits the Barlow test was performed for all setups. The results can be found in Figures C.67, C.69 and C.71. Taking the same arguments, regarding the outliers, as before into account, no significant systematic shift is observed. Therefore, no additional systematic uncertainty was included for the choice of ΔT cut.

Background shape for sPlot The last check for systematic uncertainties due to the event selection concerned the background shape used to perform the sPlot fit. In addition to the baseline shape (second order Chebychev polynomial), three other Chebychev polynomials (first, third and fourth order) were used to perform the analysis. The results can be seen in Figure C.72.

All results seem to agree within statistics. To test if there is a significant systematic uncertainty related to the background shape the Barlow test was performed. The result is shown in Figure C.73. Apart from two outliers there seems to be no significant systematic effect introduced by the choice of the Chebychev polynomial. No systematic uncertainty was added for the choice of background parametrisation for the sPlot fit.

Beam properties

Degree of polarisation The degree of linear polarisation enters Eq. (2.28) as a scaling factor for the $\rho^{1,2}$. Therefore, the same uncertainty as in the beam asymmetry measurement of 3.5% is added for them.

Offset of polarisation plane To test the influence of the polarisation plane angle used in the fit (Table 4.1), it was increased and decreased by three standard deviations. The results for the baseline and the two varied offsets can be seen in Figure C.74. All results agree within statistics. To quantify if there is a systematic effect present the Barlow test was performed. The results are shown in Figure C.75. No significant systematic changes are observed. Therefore, no systematic uncertainty was added for the uncertainty on the polarisation plane angle.

Combined systematic uncertainty

A summary of all extracted systematic uncertainties can be found in Table 6.6. For the uncertainty on $\Sigma = 2(\rho_{11}^1 + \rho_{33}^1)$ it is assumed that the error from the extraction method is added arithmetically since it comes from the same source for ρ_{11}^1 and ρ_{33}^1 . The error for the degree of polarisation is not added since the error on the overall scaling should stay the same after adding the two SDMEs.

| source | uncertainty ρ^0 | uncertainty $\rho^{1,2}$ | uncertainty $\Sigma = 2(\rho_{11}^1 + \rho_{33}^1)$ |
|------------------------|-------------------------|-----------------------------|--|
| extraction method | 0.02 | 0.01 | 0.02 |
| degree of polarisation | - | 3.5% | 3.5% |

Table 6.6: Numerical results for systematic uncertainties on the SDME extraction.

6.3 Differential cross-section

The differential cross-section as defined in Eq. (2.59) is a valuable addition to the beam asymmetry and spin-density matrix elements. Although its measurement was not in the original scope of this thesis, preliminary results have been obtained.

The key quantities used to extract the cross-section were the photon beam flux and the measurement of the acceptance corrected yield. In addition, the branching ratio and target thickness had to be known. The branching ratio of $\Lambda(1520) \rightarrow N\bar{K}$ is given by the Particle Data Group as $(45 \pm 1)\%$ [15]. Assuming isospin symmetry and fully correlated errors in determining the branching ratios the branching ratio for $\Lambda(1520) \rightarrow pK^-$ was assumed to be $(22.5 \pm 0.5)\%$. The photon beam flux was determined in a separate analysis with the use of the pair spectrometer (see Section 4.2.5) and provided to the collaboration. The target thickness was calculated using the molar mass for LH₂ $M = 2.016 \text{ gmol}^{-1}$, its mass density at a temperature of $T = 20 \text{ K}$ and pressure of $p = 1.31 \text{ bar}$ given as $\rho_m = 71.32 \text{ kgm}^{-3}$ [120], and the analysed length of the target of 27 cm. The number of protons per area in the target was given by

$$\rho = n_t l = 2 \frac{N_A}{M} \rho_m l = 1.142 \text{ b}^{-1} \quad (6.12)$$

where n_t denotes the number density and the factor of two took into account that each LH₂ molecule contains two protons.

6.3.1 Acceptance corrected yield

In order to determine the differential cross-section using Eq. (2.59), the acceptance corrected yield $\frac{Y}{\eta}$ had to be determined.

The yield was measured by performing extended maximum likelihood fits to the pK^- invariant mass distribution in the same manner as the sPlot fits outlined in Section 5.6.8. As statistical uncertainties on the yields are smaller than on SDMEs the data was separated in finer $-(t - t_{\min})$ -bins.

The acceptance η was determined using the hdgeant4 simulation of the detector setup (see Section 4.6; set D, Table 4.3). $\Lambda(1520)$ MC events were generated with a phase-space-like angular decay distribution. After running the generated events through the simulation and performing the same analysis on them as on real data the acceptance could be determined as

$$\eta = \frac{\text{accepted events}}{\text{generated events}} \quad (6.13)$$

In reality the events had an angular distribution that was different from phase-space. This could result in discrepancies with the calculated acceptances. If, for example, the angular distribution was such that real events cluster in a region of phase space that has low acceptance (e.g. an insensitive part of the detector setup) the calculated acceptance would overestimate the real acceptance. A common approach to circumvent this problem is to simulate the reaction with angular and kinematic distributions as close to real data as possible. An alternative approach, which did not rely on detailed knowledge of the pK^- decay distribution before the measurement, was employed for this analysis. Using Eq. (2.17) the number of generated and accepted events was calculated by fitting $W(\theta, \phi, \Phi)$, as given in Eq. (2.28), to the data, as detailed in Section 6.2. The results were then used to sum $W(\theta, \phi, \Phi)$ over all accepted and generated MC events, where the angles are the angles of the MC event. The acceptance was then given as

$$\eta = \frac{\sum_i^{N_{\text{accepted}}} W_i(\theta, \phi, \Phi)}{\sum_i^{N_{\text{generated}}} W_i(\theta, \phi, \Phi)} \quad (6.14)$$

This method made sure that the full angular distributions were properly taken into account when calculating the acceptance. Since this method relied on fitting the angular distributions to get the correct shape and not precise estimates for SDMEs, it was possible to use finer binning than in Section 6.2.

6.3.2 Results

Combining the yield extracted via the extended maximum likelihood fit, Eq. (6.14) and the flux, branching ratio and target thickness, the differential cross-section was calculated using Eq. (2.59) and the results are shown in Figure 6.44. The errors shown are just statistical uncertainties coming from the fit. No systematic studies have been performed for these measurements. Therefore, they are only considered preliminary.

In this chapter it was shown how various different fitting and parameter estimation techniques can be employed to extract physics observables from the data. The beam asymmetry and spin-density matrix elements have been measured. It was shown that they are self consistent and their statistical and systematic uncertainties were extracted. In addition, preliminary results for the differential cross-section were extracted from the data. In the following chapter these results will be summarised and interpreted within a physics context.

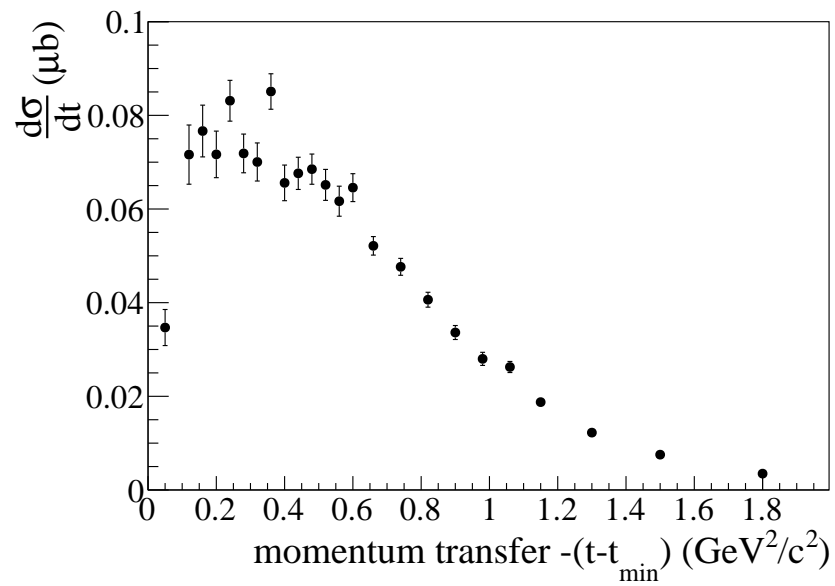


Figure 6.44: Differential cross-section results for $\gamma p \rightarrow K^+ \Lambda(1520)$ between $E_\gamma = 8.2 \text{ GeV} - 8.8 \text{ GeV}$.

Chapter 7

Results and discussion

Chapter 6 focussed on the different fitting and parameter estimation techniques which were used to extract physics observables from the data set, and the studies which were made to quantify systematic uncertainties. Now these results are used to infer information about the production mechanisms involved in $\Lambda(1520)$ photoproduction.

7.1 Beam asymmetry

The final results containing all uncertainties for the beam asymmetry extracted via an unbinned fit to ϕ_{K^+} using Eq. (6.6) are shown in Figure 7.1. The error bars show the statistical uncertainty. The black box around each data point shows the systematic uncertainty, excluding the uncertainty on the degree of beam polarisation, which is shown separately with a blue shaded box for each data point. This is done because the polarisation uncertainty is an overall scaling uncertainty. It is the same for all points and does not vary across the range in $-(t - t_{\min})$ but since the asymmetry varies it appears larger for large asymmetries. The numerical values and associated uncertainties (including the scaling uncertainties) are listed in Table D.1.

As laid out in Section 2.1.2, the beam asymmetry can be measured via a direct fit to ϕ_{K^+} or it can be accessed through a combination of spin-density matrix elements. Fitting ϕ_{K^+} has the advantage that it can be done through a counting asymmetry, which does not require a detector acceptance correction. However, this method relies on the assumption that several quantities integrate to zero and are not affected by detector acceptance. This assumption does not necessarily hold true. The extraction of Σ via the measurement of SDMEs does not rely on these assumptions since the acceptance is corrected for and the full angular distribution is considered. Therefore, the definitive value for Σ is taken from there.

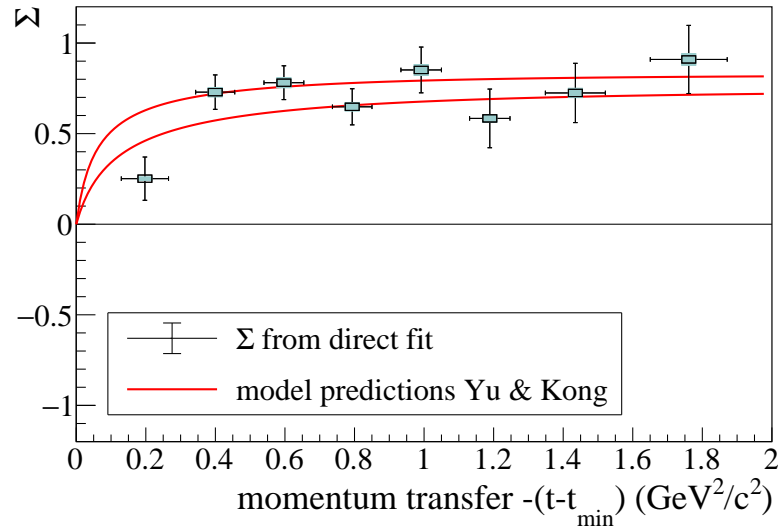


Figure 7.1: Final results for the beam asymmetry Σ extracted via an unbinned maximum likelihood fit to the K^+ ϕ -angle distribution. The error bars contain statistical uncertainties. The black boxes show the systematic uncertainty, excluding the overall scaling uncertainty which is indicated by the blue boxes. The red lines are model predictions from Yu and Kong based on [35]. The model parameters were fixed using two separate sets of data from different experiments. The spread in the predictions represents an uncertainty coming from those data sets.

7.2 Spin-density matrix elements

The final results containing the statistical and systematic uncertainties for the extraction of SDMEs are plotted in Figure 7.2 and Figure 7.3. As before, the error bars show the statistical uncertainty. The black box around each data point shows the systematic uncertainty, excluding the uncertainty on the degree of beam polarisation, which acts as a scaling for the polarised SDMEs. Its uncertainty is indicated by a blue box for each data point. As noted before in Section 6.2, the agreement between Σ for the two different extraction methods is excellent.

The numerical values for all SDMEs and their associated uncertainties are listed in Tables D.2 to D.10. The final results for $\Sigma = 2(\rho_{11}^1 + \rho_{33}^1)$ and their associated uncertainties are listed in Table D.11.

7.3 Interpretation of angular decay distributions

Yu and Kong made predictions for all nine SDMEs (priv. communication based on [35]). They used a Regge framework in which they included the $K(494)$, $K^*(892)$ and $K_2^*(1430)$. They used existing (differential) cross-section and photon beam asymmetry data from various experiments [43–46, 48, 49] to fix the signs and magnitudes of the coupling constants and claim that the role of K^* exchange is very small while the K_2^* dominates at high energies. When using the available

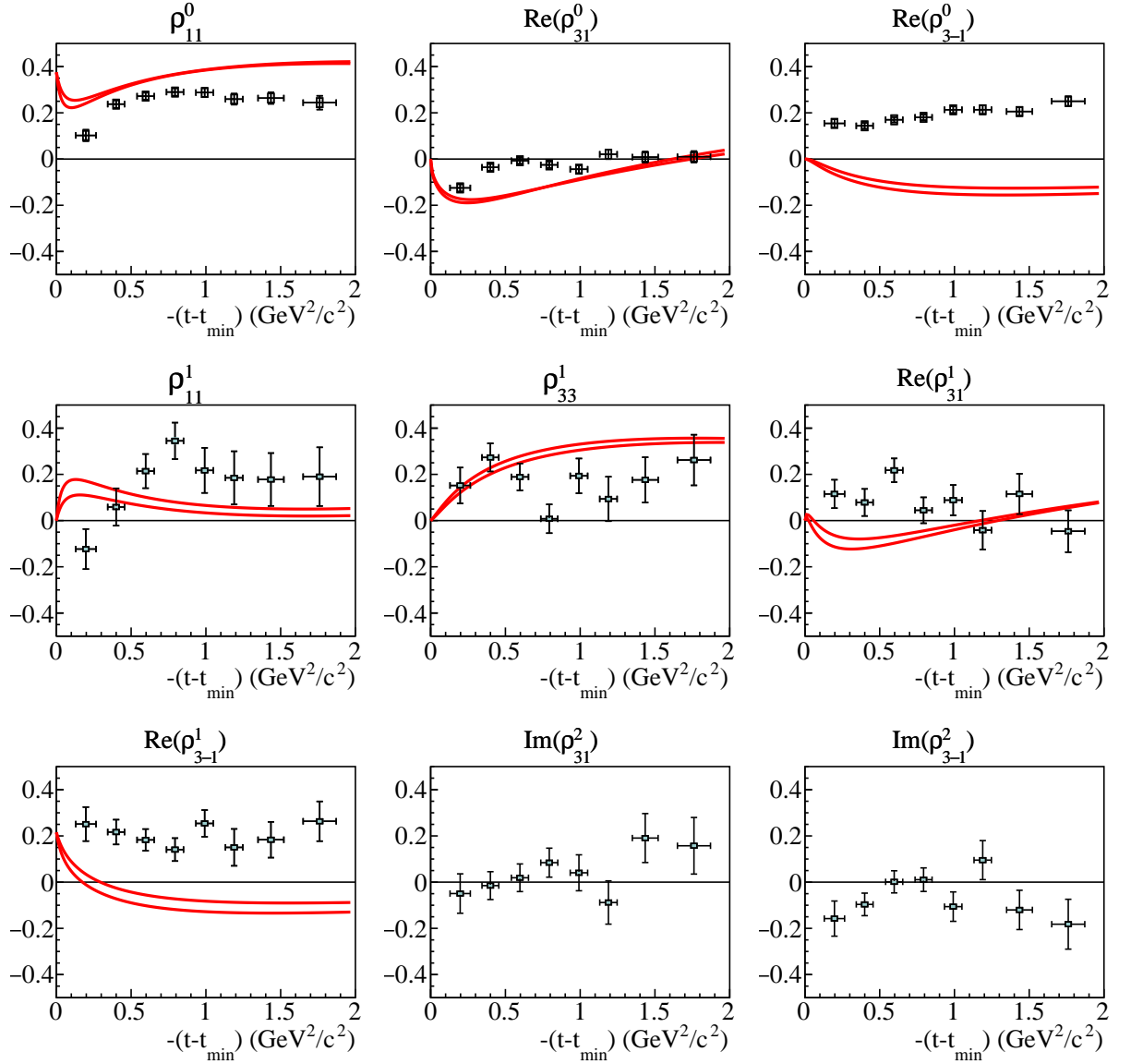


Figure 7.2: Final results plot for all SDMEs in eight bins of $-(t - t_{\min})$. The error bars contain statistical uncertainties. The black boxes show the systematic uncertainty, excluding the overall scaling uncertainty which is indicated by the blue boxes (only polarised SDMEs). The red lines are model predictions from Yu and Kong based on [35]. The model parameters were fixed using two separate sets of data from different experiments. The spread in the predictions represents an uncertainty coming from those data sets.

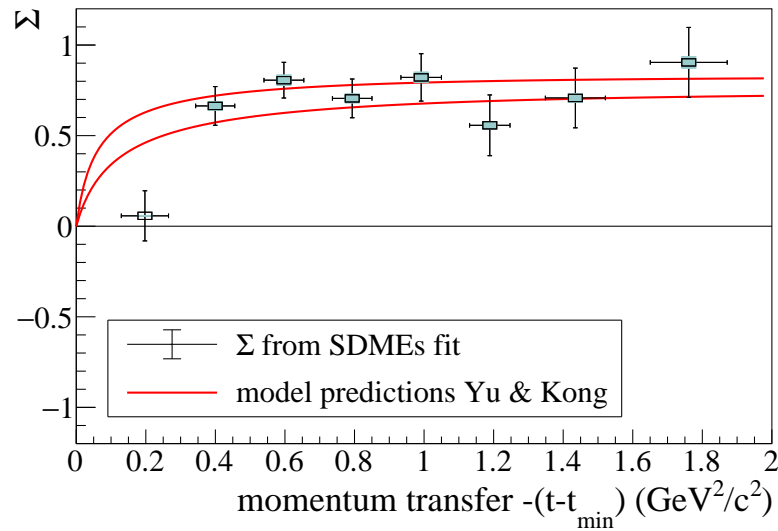


Figure 7.3: Final results for the beam asymmetry $\Sigma = 2(\rho_{11}^1 + \rho_{33}^1)$. The error bars contain statistical uncertainties. The black boxes show the systematic uncertainty, excluding the overall scaling uncertainty, which is indicated by the blue boxes. The red lines are model predictions from Yu and Kong based on [35]. The model parameters were fixed using two separate sets of data from different experiments. The spread in the predictions represents an uncertainty coming from those data sets.

data they split it up in two sets which they fitted separately. For that reason they provided two curves for all observables. It is fair to treat the spread as a systematic uncertainty stemming from the uncertainty on the data used to fix model parameters.

Figures 7.1, 7.2 and 7.3 show a comparison of the results obtained in this analysis with the predictions by Yu and Kong. The agreement in the beam asymmetry is very good. The sign as well as the magnitude seems to agree well for most of the $-(t - t_{\min})$ -range, but there is a discrepancy at very low $-(t - t_{\min})$, where the extracted beam asymmetry Σ is significantly smaller than the prediction. The situation in the SDMEs is more complex. Some, like e.g. ρ_{11}^0 or ρ_{33}^1 show fair agreement. Others like $\text{Re}(\rho_{3-1}^0)$ seems to have the correct shape and amplitude but the wrong sign. With the information provided it is not straight forward to assess the reason for the deviations between model and data. One should keep in mind, though, that there were no previous SDME measurements at high photon beam energies and none at all for polarised SDMEs with which to constrain the model. Therefore, differences are not unexpected. Most of the data used to fix the model was taken at much lower energies where very different production mechanisms dominate. Only SLAC [43] provided some data at $E_\gamma = 11 \text{ GeV}$. The new data can now be used to refine some of the model assumptions. This should lead to better agreement of the model with data in the future.

In Section 2.1.1 it was shown how certain combinations of SDMEs can be related to combinations of purely (un)natural amplitudes (see Eqs. (2.43)-(2.46)). Natural amplitudes indicate exchanges of a vector (e.g. $K^*(892)$) or a tensor (e.g. $K_2^*(1430)$) meson. Unnatural exchanges

are exchanges of a pseudoscalar (e.g. $K(492)$) or axial-vector (e.g. $K_1(1270)$) meson. Figure 7.4 shows the measured distributions of these combinations. The numerical results including statistical and systematic uncertainties propagated through from the SDME measurements can be found in Tables D.12-D.19. One can see that over most of the $-(t - t_{\min})$ -range the natural amplitudes dominate. At small $-(t - t_{\min})$ a non-zero unnatural contribution seems to be present. This is in line with what has been seen in the beam asymmetry. Σ rises from small values to an asymmetry of about 0.7 and then stays roughly constant.

Although the natural amplitudes seem to dominate over the unnatural amplitudes, the data shows that they are not all the same. Combinations of SDMEs at low $-(t - t_{\min})$ show differences between $(|N_0|^2 + |N_1|^2)$ and $(|N_{-1}|^2 + |N_2|^2)$, in particular the former vanishing at low $-(t - t_{\min})$. $\text{Re}(N_{-1}N_0^* - N_2N_1^*)$ and $\text{Re}(N_{-1}N_1^* + N_2N_0^*)$ are different across the whole $-(t - t_{\min})$ -range. This is very interesting and might help to disentangle the contributions from the different amplitudes. The combinations of unnatural amplitudes, though, seem to be more or less consistent over the whole range.

7.4 Differential cross-section

As mentioned before, the differential cross-section results are to be considered preliminary. This means that important checks for systematic uncertainties have not yet been performed. The flux is an overall scaling factor that affects all bins the same way. Therefore, it is very important to fully understand the photon beam flux and its uncertainties. At the time of submission studies for that purpose are ongoing within the collaboration.

The acceptance correction that has been performed relied heavily on MC simulations. While the detector geometry, which heavily influenced the angular distributions was modelled well, other aspects that influence the overall normalisation, such as the trigger emulation, are still under study.

As laid out in Chapter 3, there are published results for the differential cross-section at lower and higher photon beam energies. Barber *et al.* (LAMP2) [44] compared their results to the SLAC data [43] by assuming that the cross-section scales with $1/E_\gamma^2$. Figure 7.5 shows a comparison of the results of this work with the previous data scaled by the photon beam energies squared. In their paper Barber *et al.* cite the branching ratio for $\Lambda(1520) \rightarrow pK^-$ as 46.2%. This is a factor two too high. It is not clear if they made a mistake by not taking the isospin symmetry into account or if they quoted the wrong number in their publication. If they used the wrong branching ratio for the calculation of the differential cross-section, then all their results are a factor two too low. For that reason Figure 7.5 also shows their results scaled up by two (brown points). In addition to the data, two red lines coming from the same model predicting SDMEs

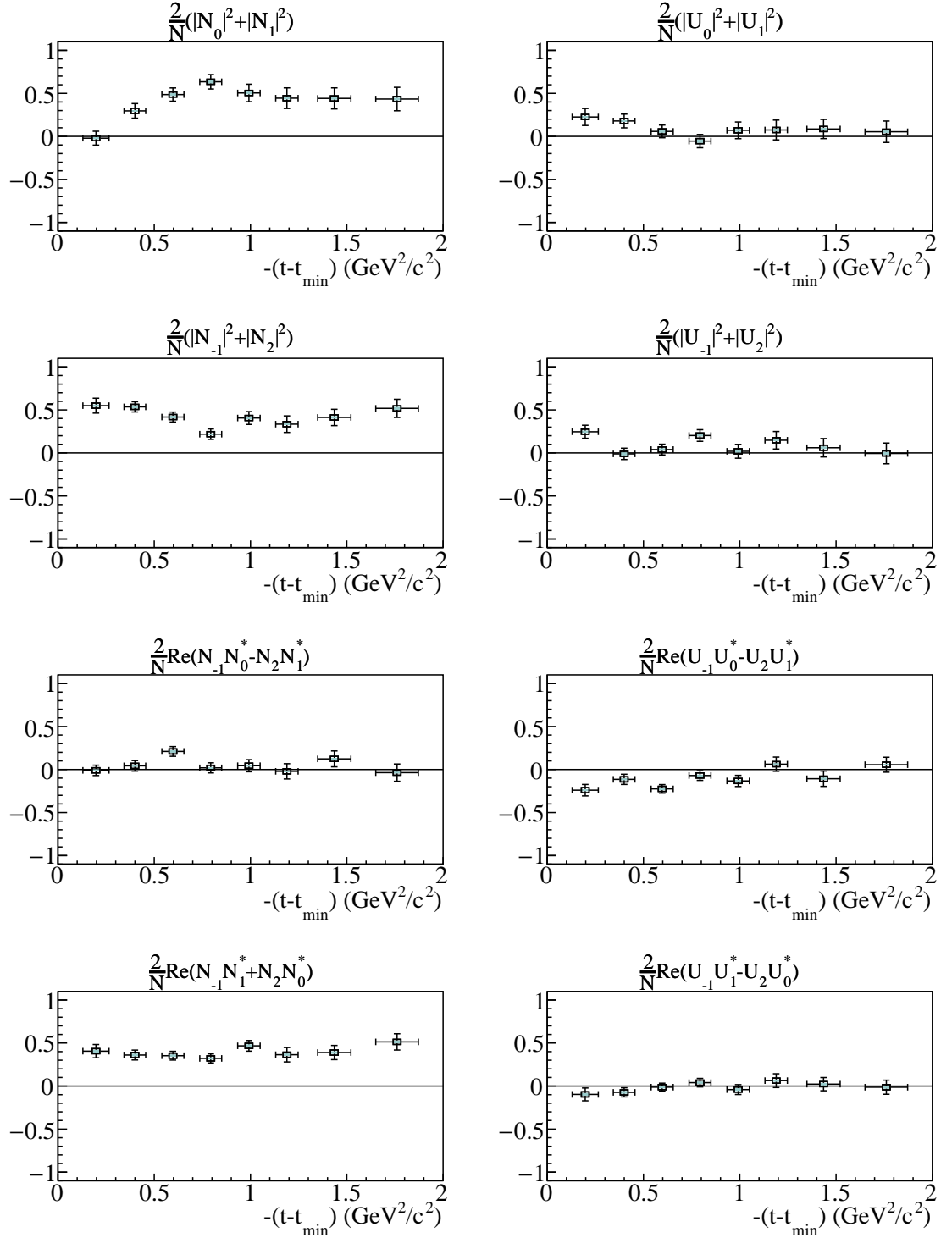


Figure 7.4: Various combinations of natural and unnatural amplitudes as calculated from the SDMEs (see Eqs. (2.43)-(2.46)).

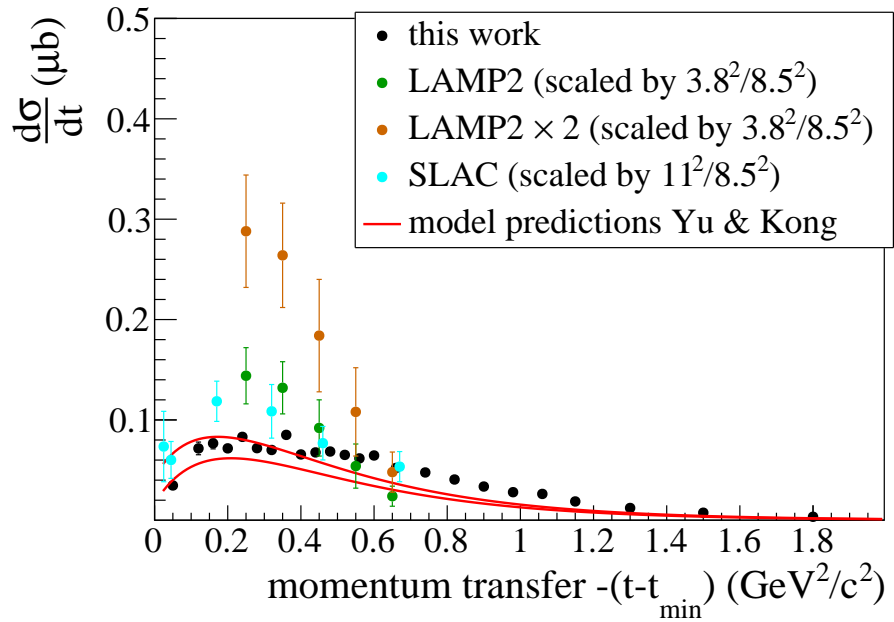


Figure 7.5: Differential cross-section results compared previous measurements by LAMP2 [44] and SLAC [43], and model predictions by Yu and Kong (priv. communication based on [35]). The previous data was scaled assuming that the cross-section scales with $1/E_\gamma^2$. The model parameters were fixed using two separate sets of data from different experiments. The spread in the predictions represents an uncertainty coming from those data sets.

are shown (priv. communication based on [35]). Comparing the results one can see that they are roughly in agreement with the previous measurements by SLAC and the model predictions. The scaled up LAMP2 results are a factor three higher than the results from this work and the SLAC results. It is not clear at the moment, if this is due to an experimental issue or if the assumption that the cross-section scales with $1/E_\gamma^2$ is not valid over such a wide range in energy. It would not be surprising if the shape of the differential cross-section changes with photon beam energy as it is dependent on the production process. The photon beam energy used in this work is much closer to the SLAC experiment than the LAMP2 experiment so better agreement is expected here.

7.5 Conclusion

The results from the beam asymmetry as well as SDME combinations indicate dominance of natural over unnatural production processes in the production of the $\Lambda(1520)$ hyperon in photoproduction at 8.8 GeV. This is in agreement with Yu and Kong's prediction of a dominating (natural) K_2^* exchange for this reaction. The simple interpretation given based on 2.1.1 nicely shows the importance of natural amplitudes but it does not yet allow differentiation between different types of natural exchanges. These results are currently being prepared for publication.

They will hopefully trigger interest on theory side to further study this reaction with a selection of reaction models.

The differences between model predictions and data, visible at low momentum transfer $-(t - t_{\min})$, reinforce the need for high quality data in the region. Unfortunately, it is also the region with low statistics and small acceptance (see Figure 5.26). In order to improve the data quality more data is required.

Additional data would also enable the analysis of very large momentum transfer $-(t - t_{\min})$, which corresponds to u -channel exchanges (see Figure 2.1c). This alternative production mechanism is weaker due to the vector meson nature of the photon beam, which favours meson exchanges over hyperon exchanges, and therefore harder to measure. It would be an interesting study to complete the picture of $\Lambda(1520)$ photoproduction.

A first look at differential cross-sections in this reaction showed that the results roughly agreed with previous measurements. There are, however, still discrepancies that need to be addressed as well as systematic studies that have to be performed in the future, before the results can be published.

The results obtained in this thesis are the first measurements of polarised spin-density matrix elements in $\Lambda(1520)$ photoproduction. They are also the first measurement of unpolarised spin-density matrix elements at high photon energies. Hence, they will provide valuable information for production mechanisms in the GlueX energy range. This will ultimately help with GlueX's main physics mission, to establish the existence of exotic hybrid mesons and to map out their spectrum.

Appendix A

Derivation: Fit function for the fractional beam asymmetry

Using Eqs. (2.50) and

$$N \propto \sigma \times F \quad (\text{A.1})$$

one can derive the following fit function for the beam asymmetry [108]:

$$\begin{aligned}
 \frac{N_{\perp} - N_{\parallel}}{N_{\perp} + N_{\parallel}} &= \frac{F_{\perp} [1 - \Sigma P_{\perp} \cos(2\phi - 180^{\circ})] - F_{\parallel} [1 - \Sigma P_{\parallel} \cos(2\phi)]}{F_{\perp} [1 - \Sigma P_{\perp} \cos(2\phi - 180^{\circ})] + F_{\parallel} [1 - \Sigma P_{\parallel} \cos(2\phi)]} \\
 &= \frac{A [1 + \Sigma P_{\perp} \cos(2\phi)] - [1 - \Sigma P_{\parallel} \cos(2\phi)]}{A [1 + \Sigma P_{\perp} \cos(2\phi)] + [1 - \Sigma P_{\parallel} \cos(2\phi)]} \\
 &= \frac{A - 1 + \Sigma (AP_{\perp} + P_{\parallel}) \cos(2\phi)}{A + 1 + \Sigma (AP_{\perp} - P_{\parallel}) \cos(2\phi)} \\
 &= \frac{A - 1 + \frac{AP_{\perp} + P_{\parallel}}{P_{\perp} + P_{\parallel}} 2C \cos(2\phi)}{A + 1 + \frac{AP_{\perp} - P_{\parallel}}{P_{\perp} + P_{\parallel}} 2C \cos(2\phi)} \\
 \implies \frac{N_{\perp} - N_{\parallel}}{N_{\perp} + N_{\parallel}} &= \frac{A - 1 + \frac{AB+1}{B+1} 2C \cos(2(\phi - D))}{A + 1 + \frac{AB-1}{B+1} 2C \cos(2(\phi - D))} \quad (\text{A.2})
 \end{aligned}$$

with $A = \frac{F_{\perp}}{F_{\parallel}}$, $B = \frac{P_{\perp}}{P_{\parallel}}$, $C = \Sigma \frac{P_{\perp} + P_{\parallel}}{2}$ and $D = \phi_{\text{off}}$, where $N_{\perp/\parallel}$ denotes the number of events in a certain region of ϕ , $F_{\perp/\parallel}$ denotes the photon flux, $P_{\perp/\parallel}$ the photon polarization and ϕ_{off} is a term correcting for a slight misalignment between the two settings.

Appendix B

Additional plots from SDME extraction

The performance of the MCMC parameter estimation used in Section 6.2 can be assessed by plotting the *timeline* and *corner plots* for each of the eight $-(t - t_{\min})$ -bins. They are shown in Figures B.1-B.16. The timeline plots show the evolution of each matrix element with respect to the steps taken by the Markov chain. The first 100 steps are discarded from the chain (*burn-in*). One can see that all chains found stable solutions for all parameters. The corner plots show the correlation between the matrix elements by plotting one against another for each step in the chain.

Figures B.17-B.24 show the results weighted flat MC sample (red line) overlaid over the data (black points). If the MCMC parameter estimation works well, one would expect to see good agreement between the line and the data. This is the case in all bins.

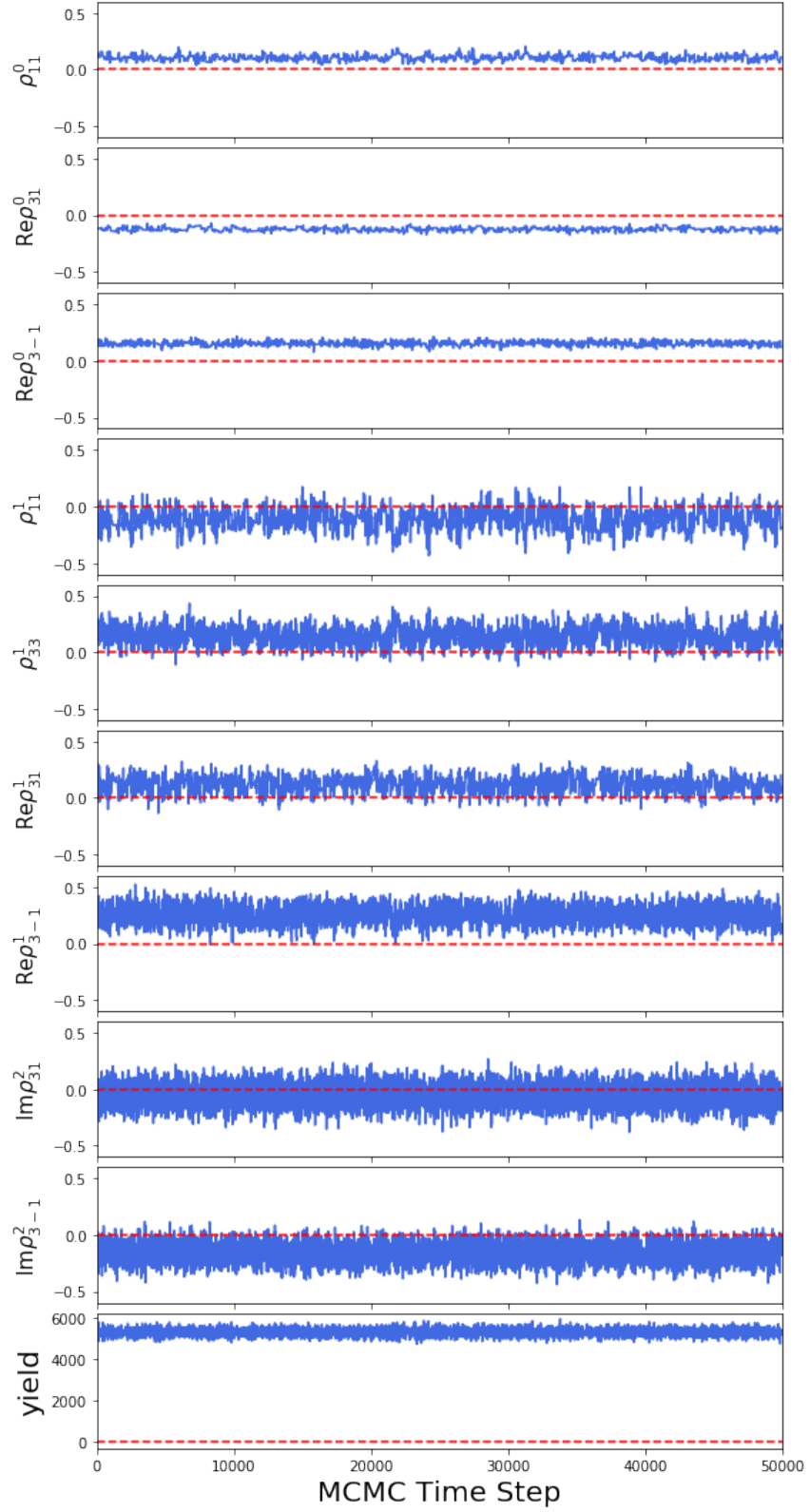


Figure B.1: SDME timeline plot for $-(t - t_{\min}) = 0 \text{ GeV}^2/c^2 - 0.3 \text{ GeV}^2/c^2$.

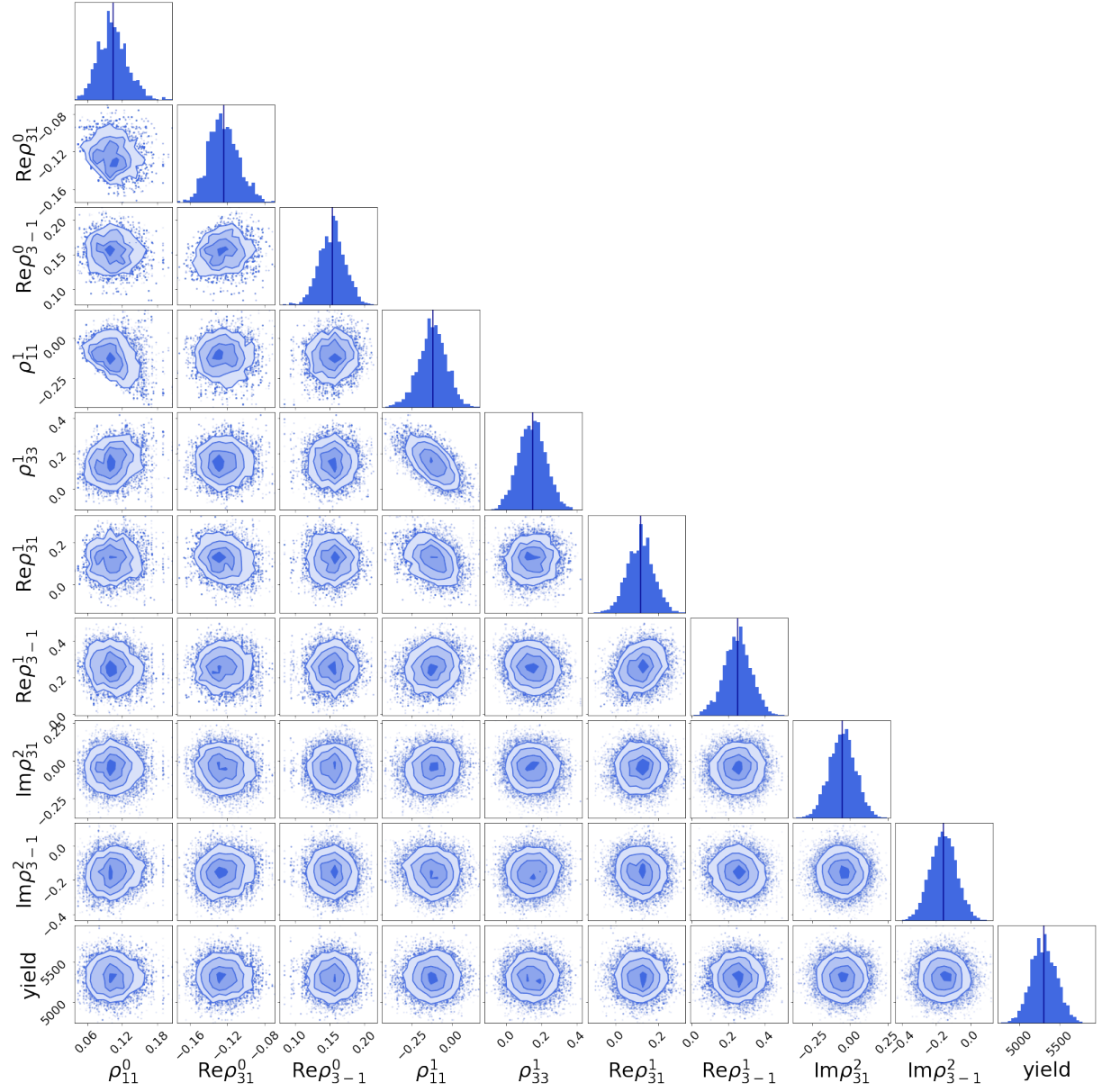


Figure B.2: SDME corner plot for $-(t - t_{\min}) = 0 \text{ GeV}^2/c^2 - 0.3 \text{ GeV}^2/c^2$. The vertical blue line in the 1D distribution indicates the mean.

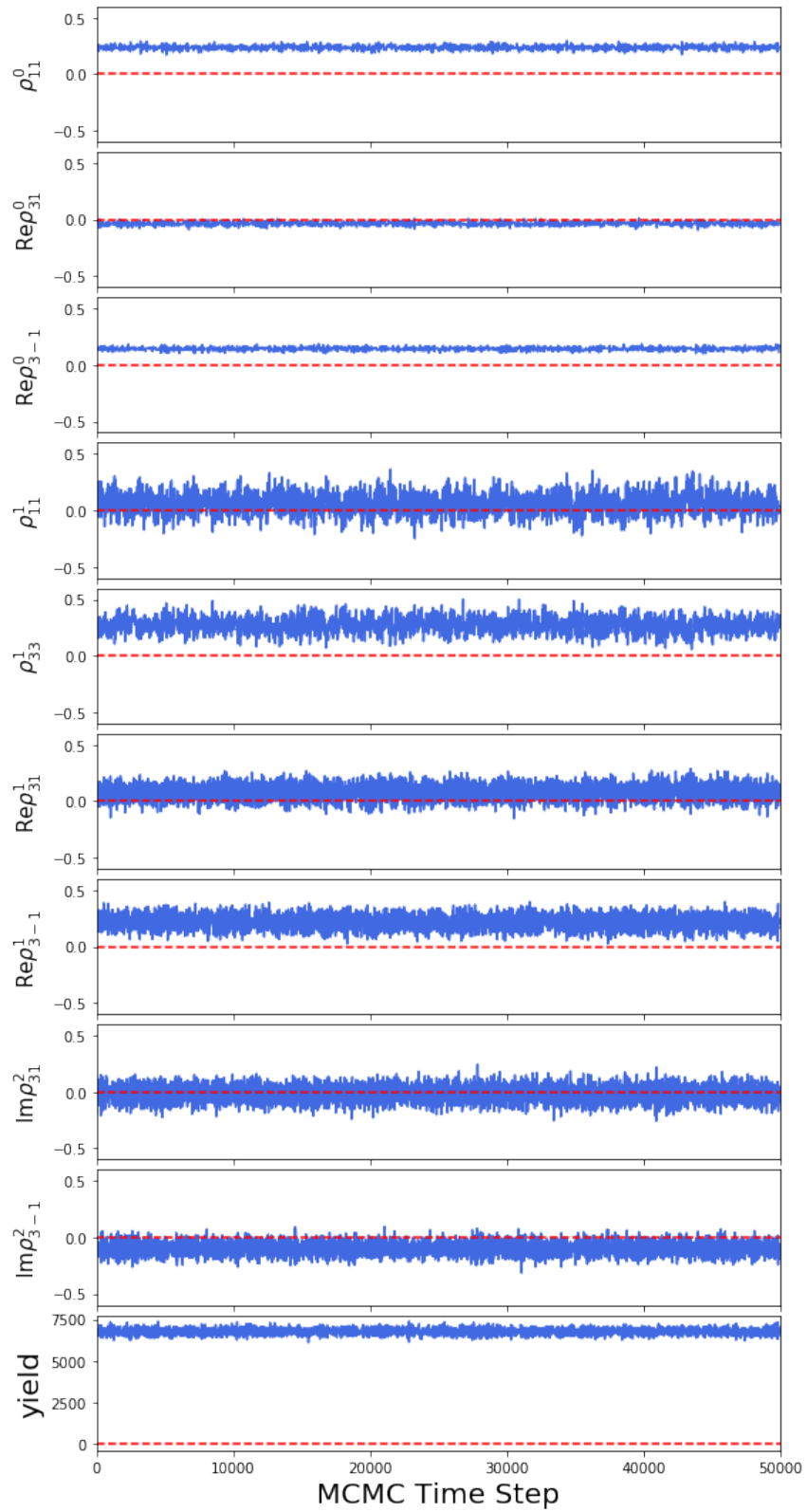


Figure B.3: SDME timeline plot for $-(t - t_{\min}) = 0.3 \text{ GeV}^2/c^2 - 0.5 \text{ GeV}^2/c^2$.

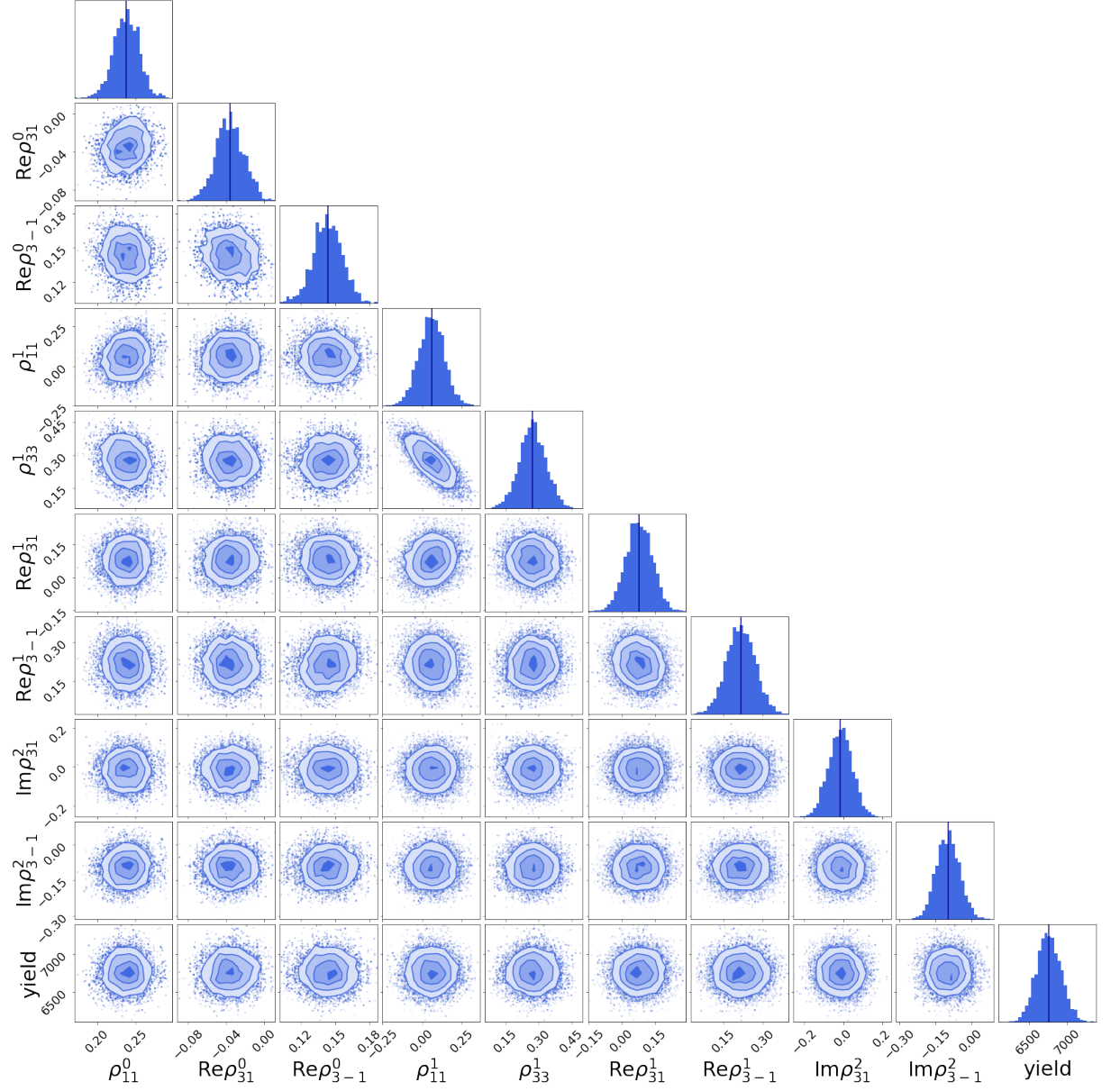


Figure B.4: SDME corner plot for $-(t - t_{\min}) = 0.3 \text{ GeV}^2/c^2 - 0.5 \text{ GeV}^2/c^2$. The vertical blue line in the 1D distribution indicates the mean.

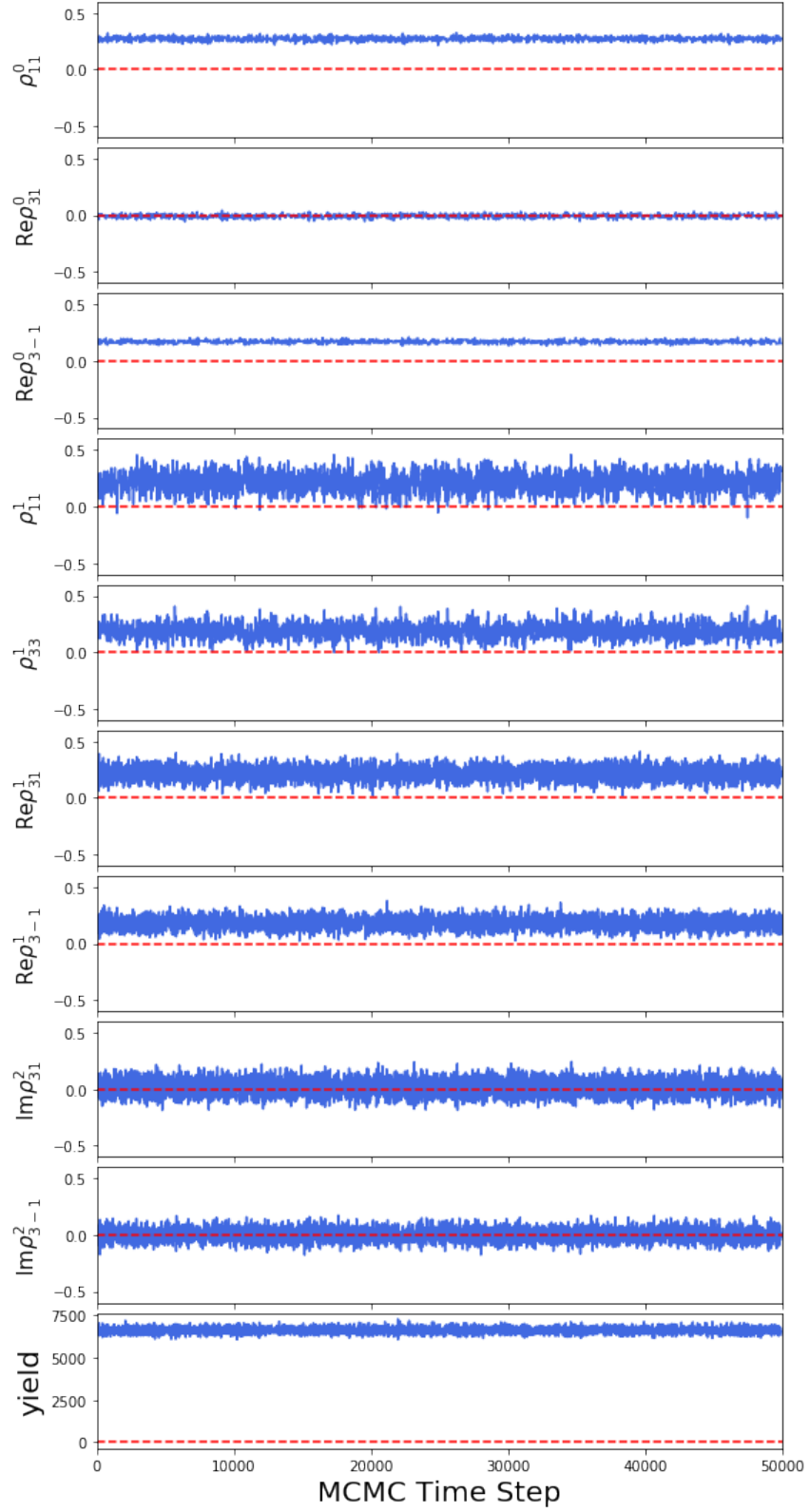


Figure B.5: SDME timeline plot for $-(t - t_{\min}) = 0.5 \text{ GeV}^2/c^2 - 0.7 \text{ GeV}^2/c^2$.

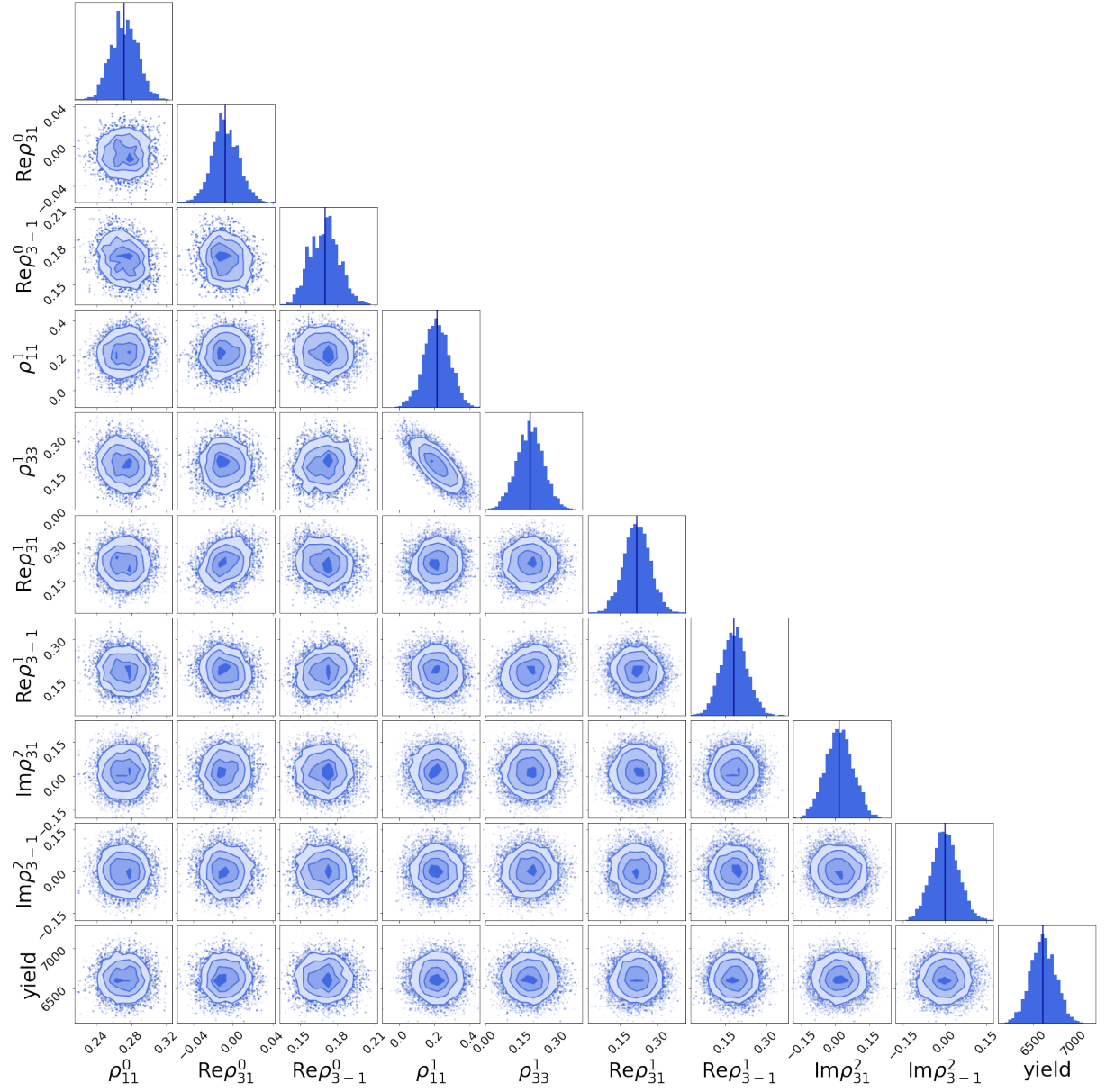


Figure B.6: SDME corner plot for $-(t - t_{\min}) = 0.5 \text{ GeV}^2/c^2 - 0.7 \text{ GeV}^2/c^2$. The vertical blue line in the 1D distribution indicates the mean.

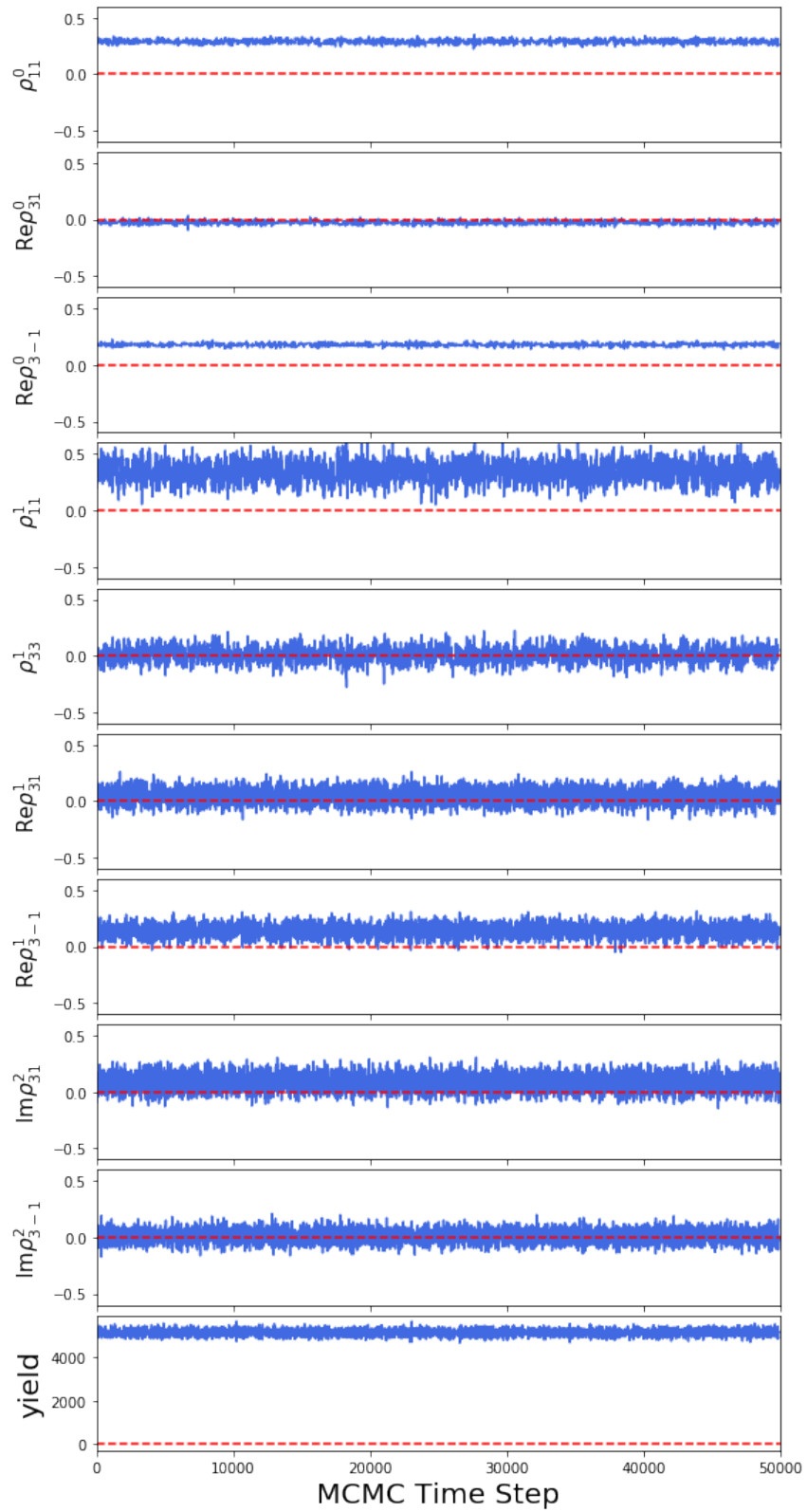


Figure B.7: SDME timeline plot for $-(t - t_{\min}) = 0.7 \text{ GeV}^2/c^2 - 0.9 \text{ GeV}^2/c^2$.

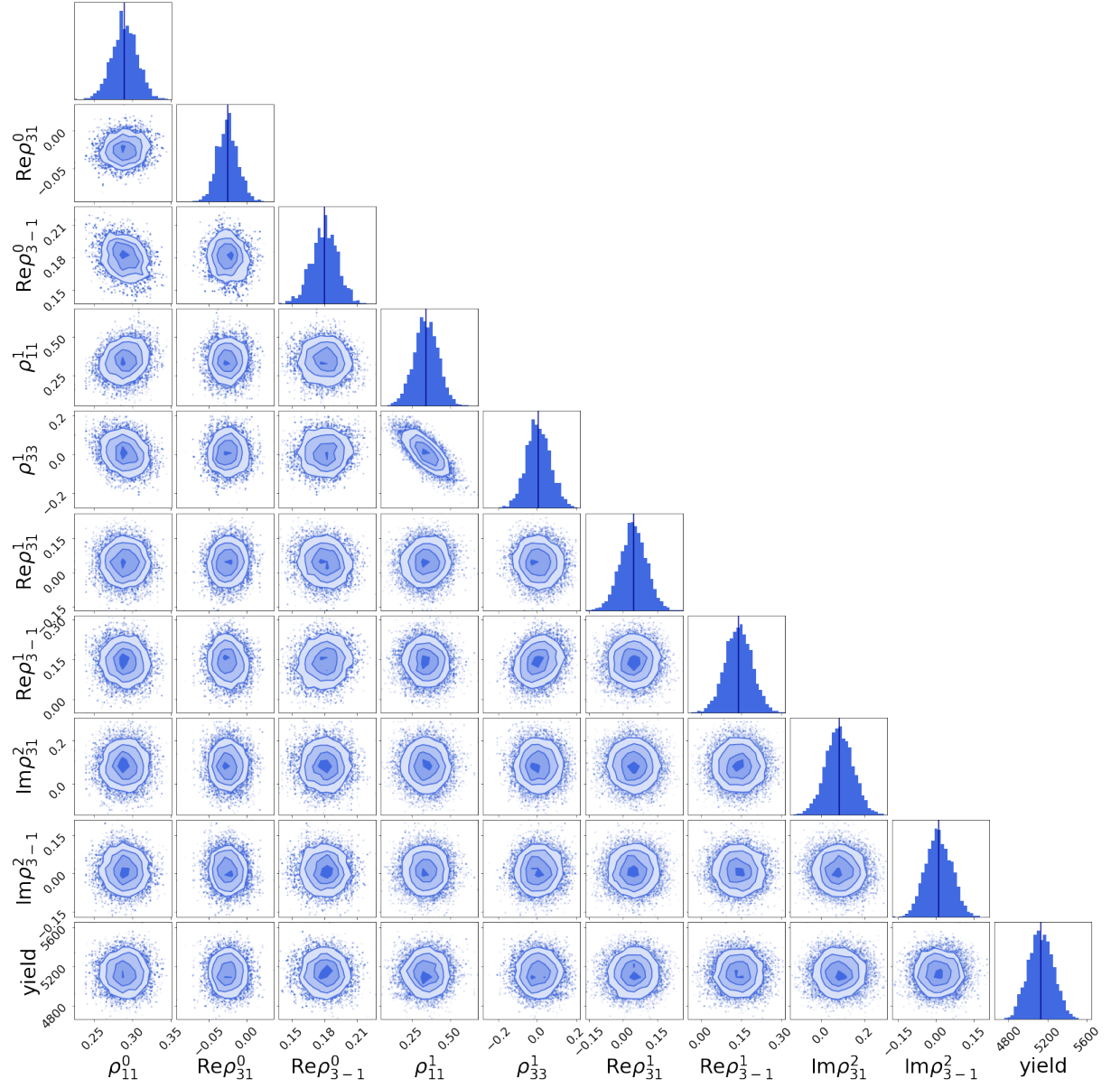


Figure B.8: SDME corner plot for $-(t - t_{\min}) = 0.7\text{GeV}^2/c^2 - 0.9\text{GeV}^2/c^2$. The vertical blue line in the 1D distribution indicates the mean.

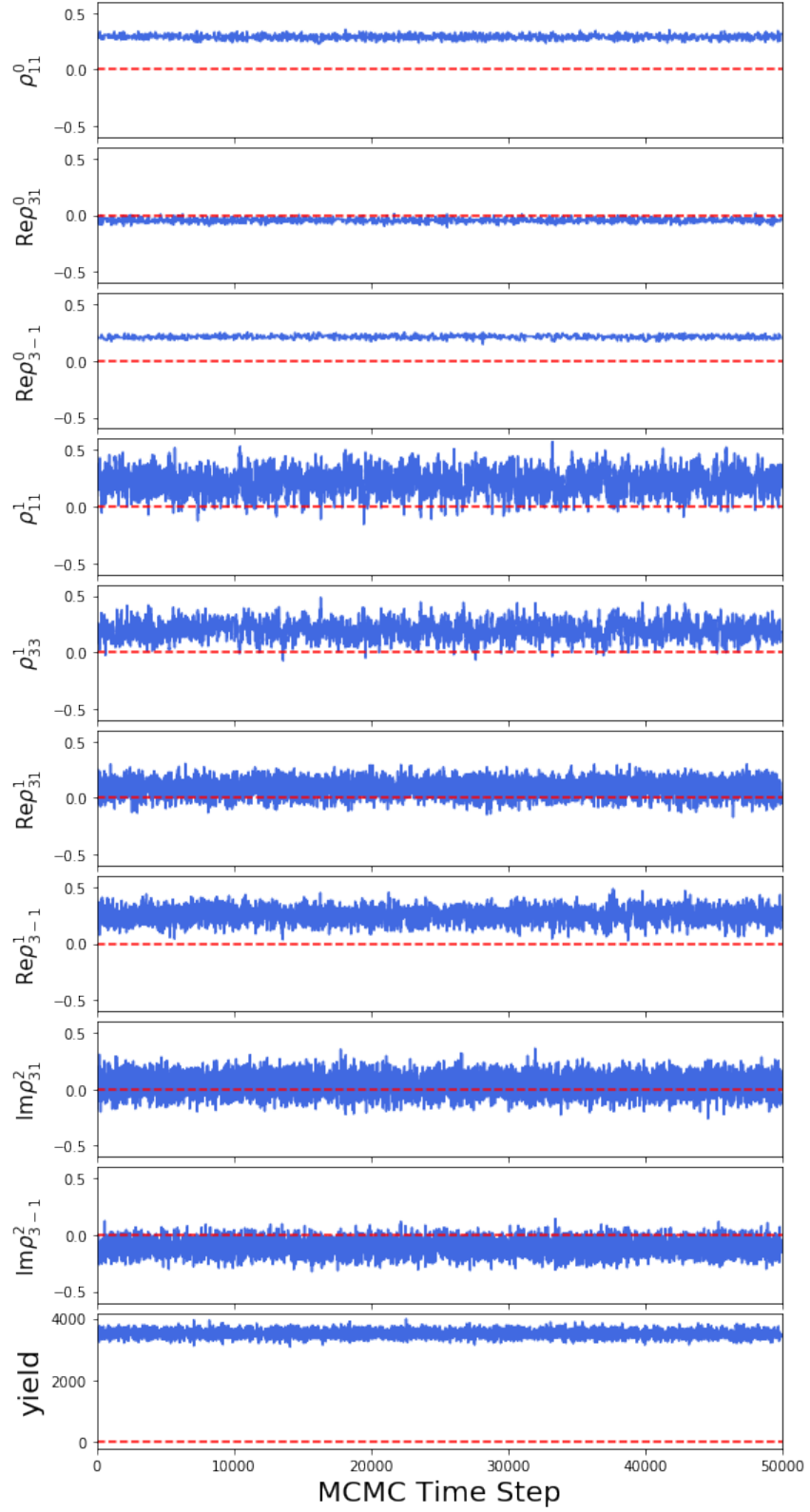


Figure B.9: SDME timeline plot for $-(t - t_{\min}) = 0.9 \text{ GeV}^2/c^2 - 1.1 \text{ GeV}^2/c^2$.

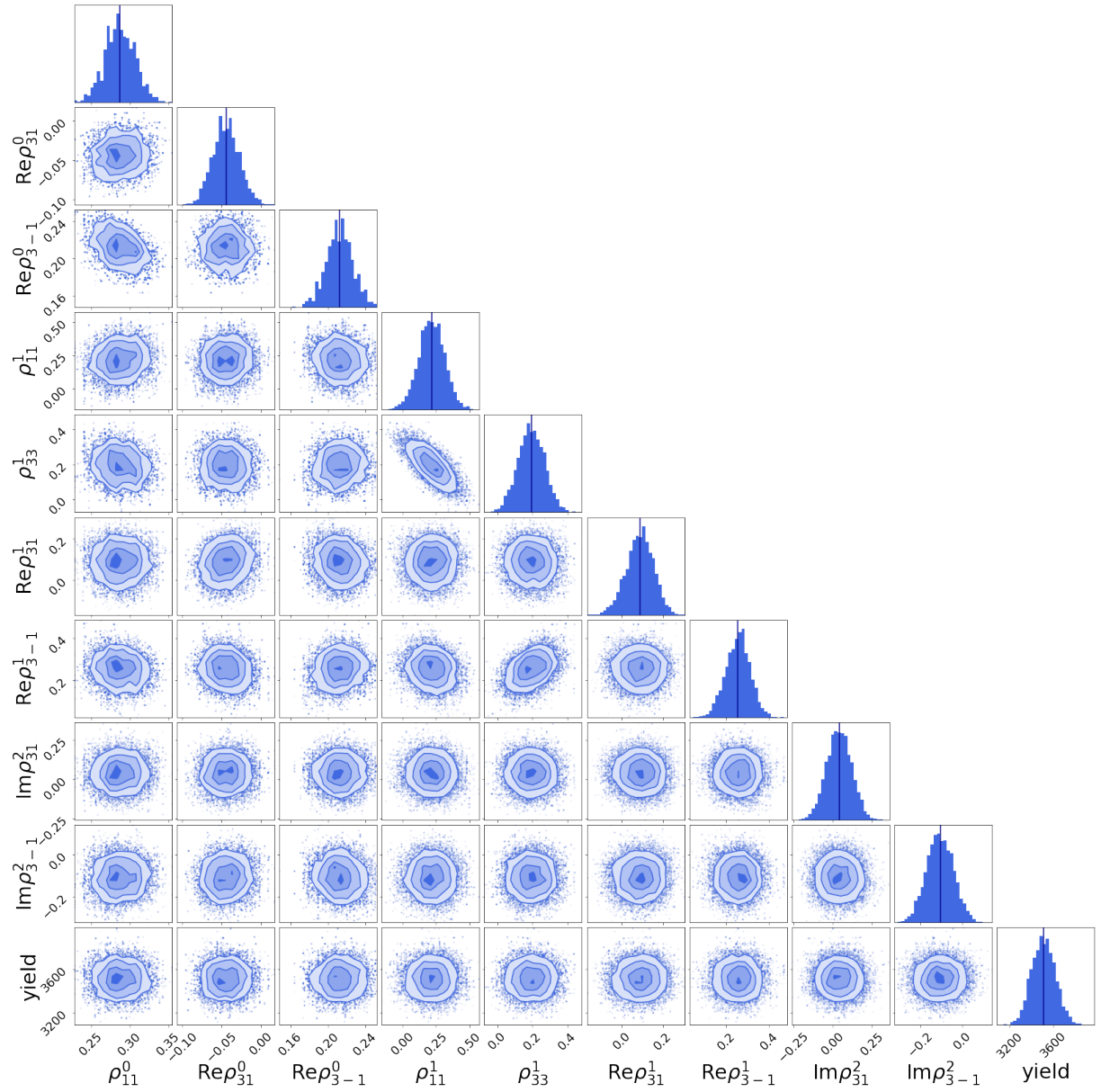


Figure B.10: SDME corner plot for $-(t - t_{\min}) = 0.9 \text{ GeV}^2/c^2 - 1.1 \text{ GeV}^2/c^2$. The vertical blue line in the 1D distribution indicates the mean.

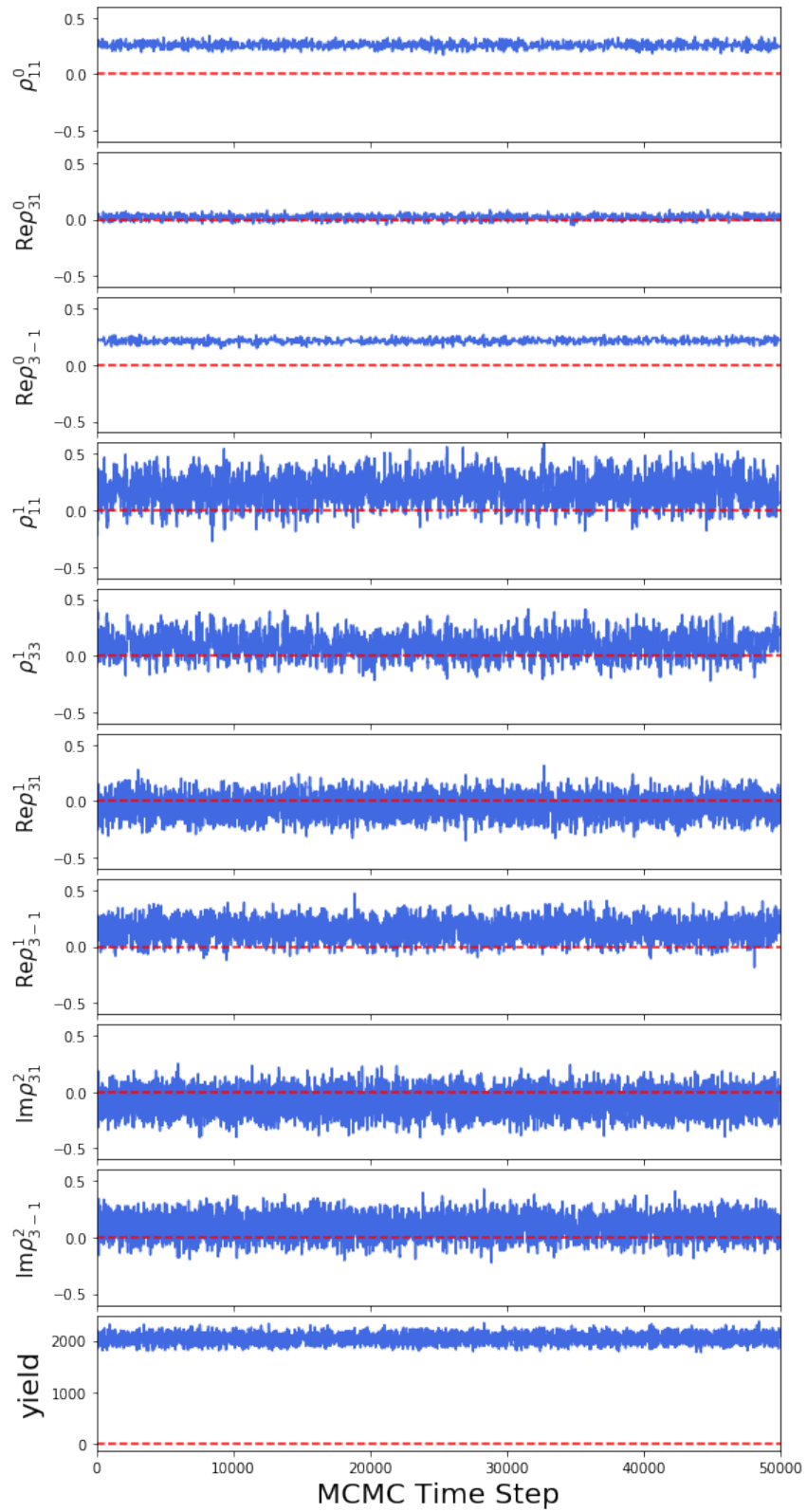


Figure B.11: SDME timeline plot for $-(t - t_{\min}) = 1.1 \text{ GeV}^2/c^2 - 1.3 \text{ GeV}^2/c^2$.

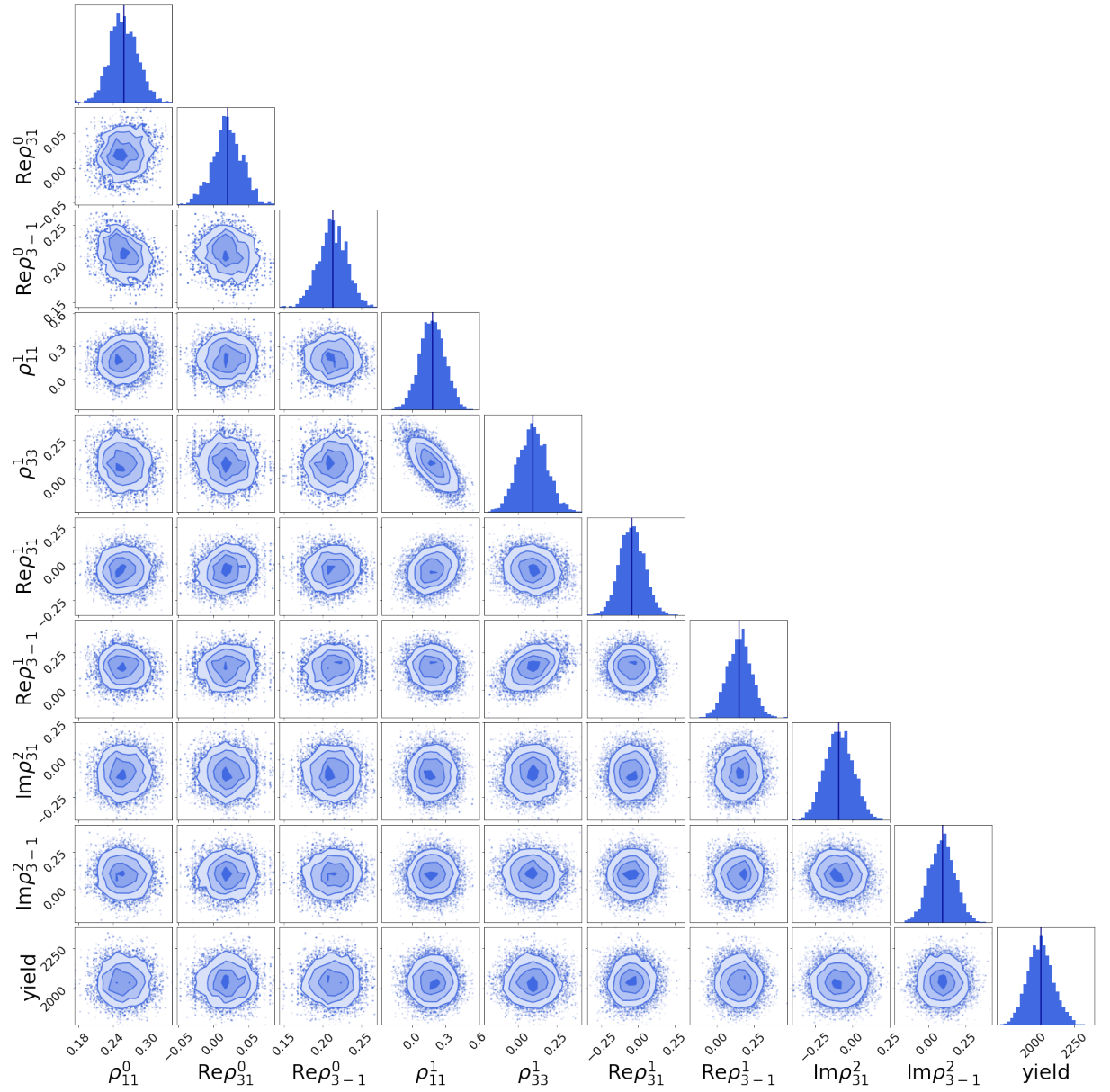


Figure B.12: SDME corner plot for $-(t - t_{\min}) = 1.1 \text{ GeV}^2/c^2 - 1.3 \text{ GeV}^2/c^2$. The vertical blue line in the 1D distribution indicates the mean.

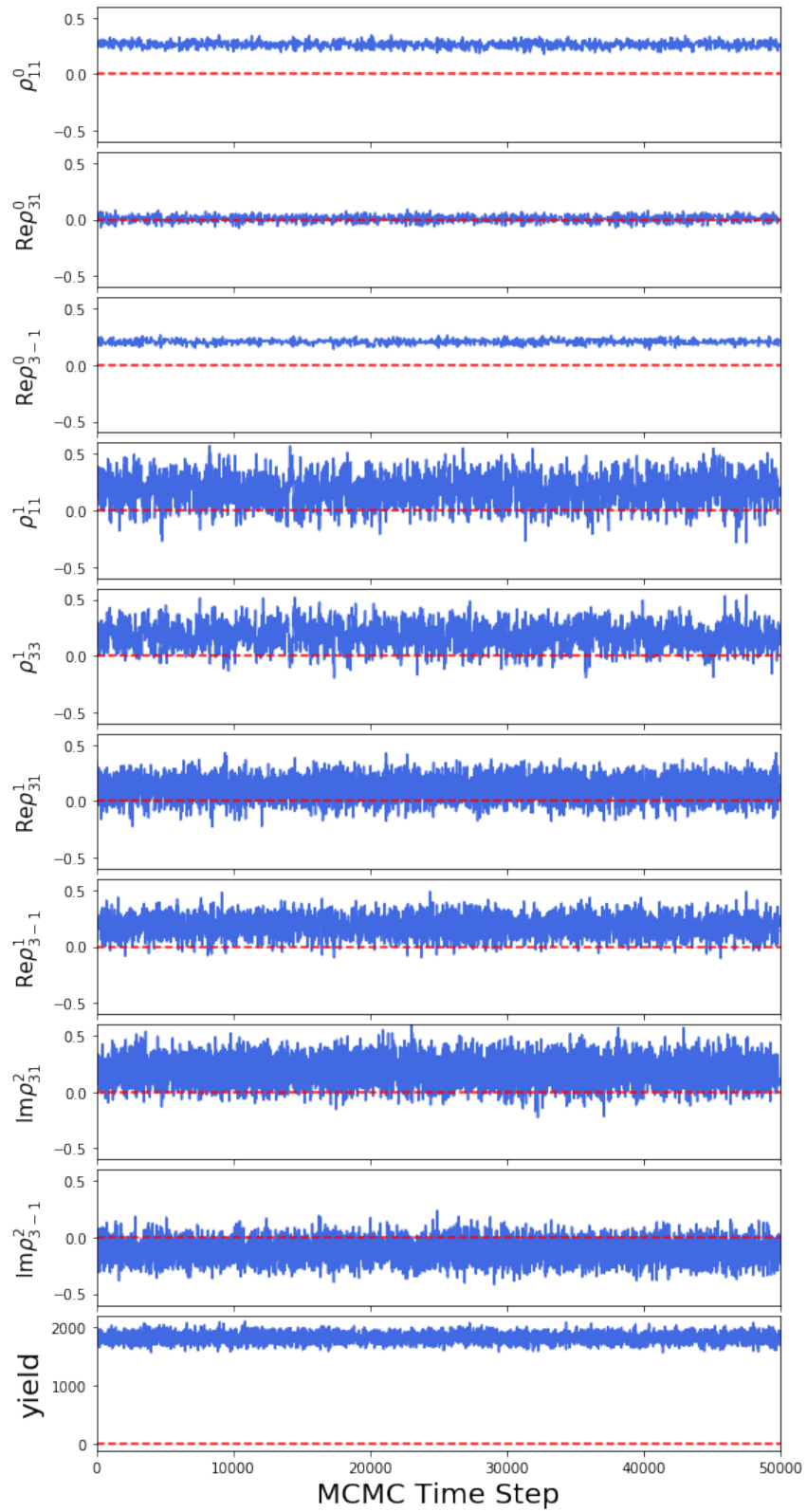


Figure B.13: SDME timeline plot for $-(t - t_{\min}) = 1.3 \text{ GeV}^2/c^2 - 1.6 \text{ GeV}^2/c^2$.

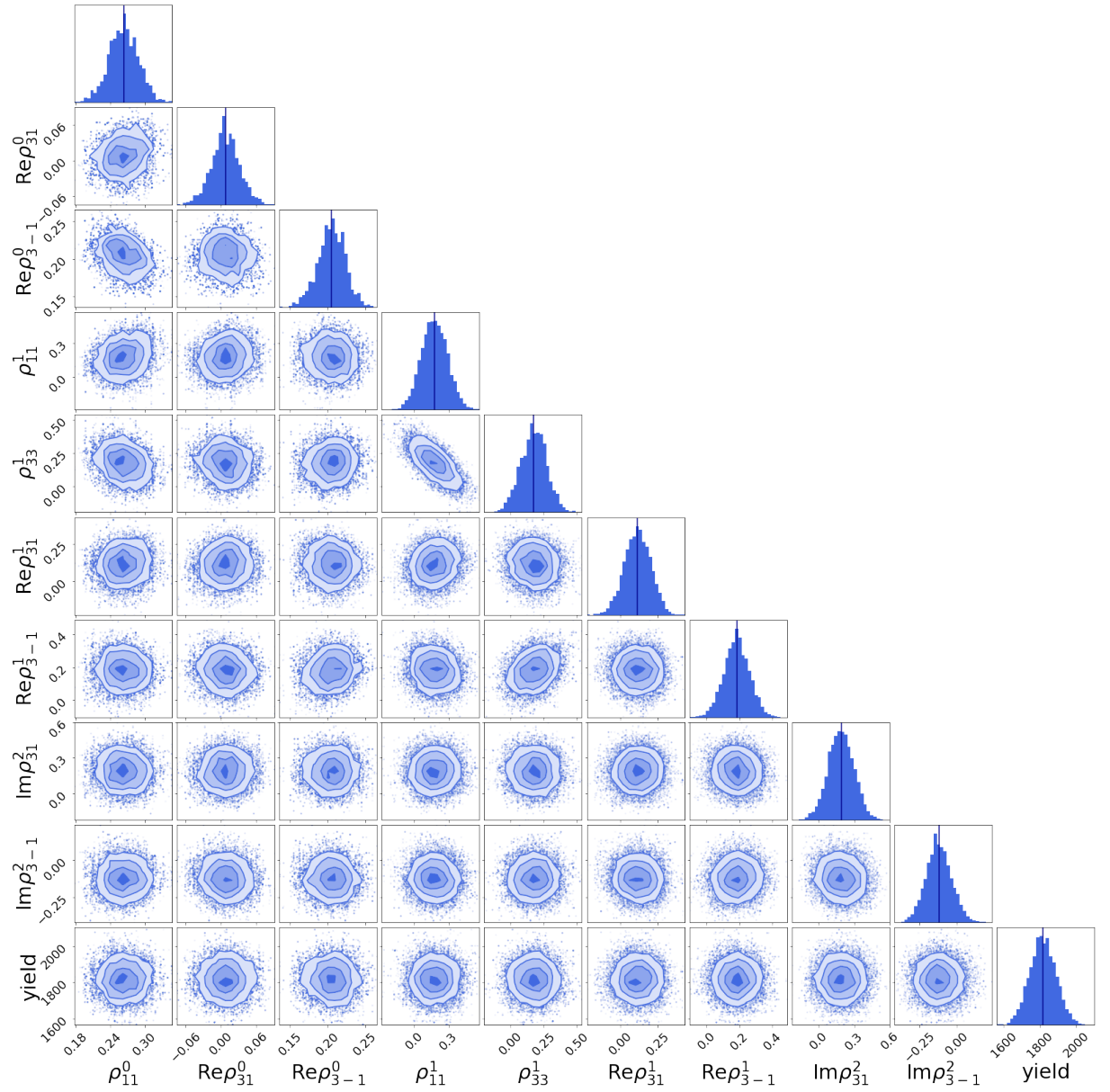


Figure B.14: SDME corner plot for $-(t - t_{\min}) = 1.3 \text{ GeV}^2/c^2 - 1.6 \text{ GeV}^2/c^2$. The vertical blue line in the 1D distribution indicates the mean.

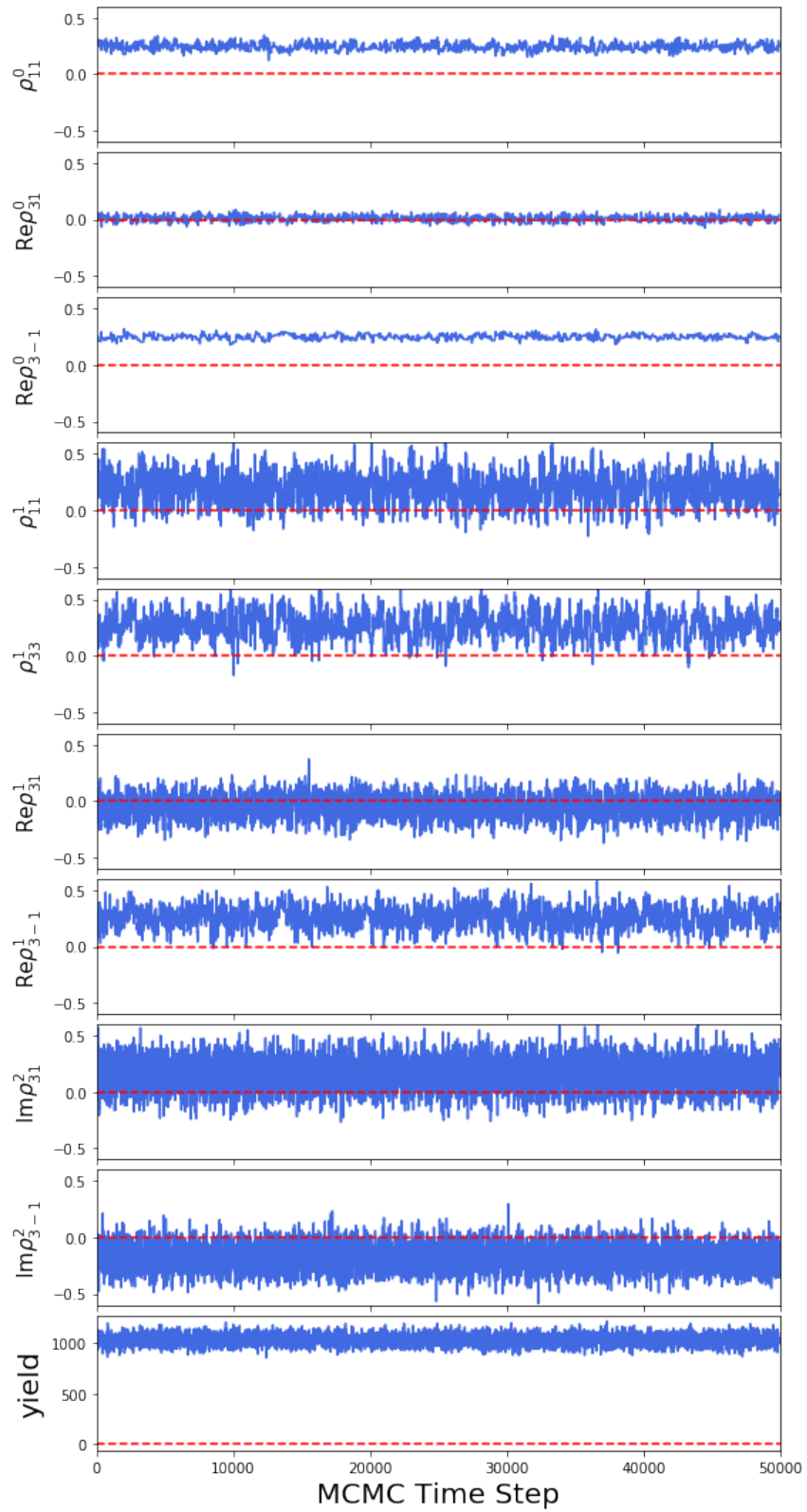


Figure B.15: SDME timeline plot for $-(t - t_{\min}) = 1.6 \text{ GeV}^2/c^2 - 2.0 \text{ GeV}^2/c^2$.

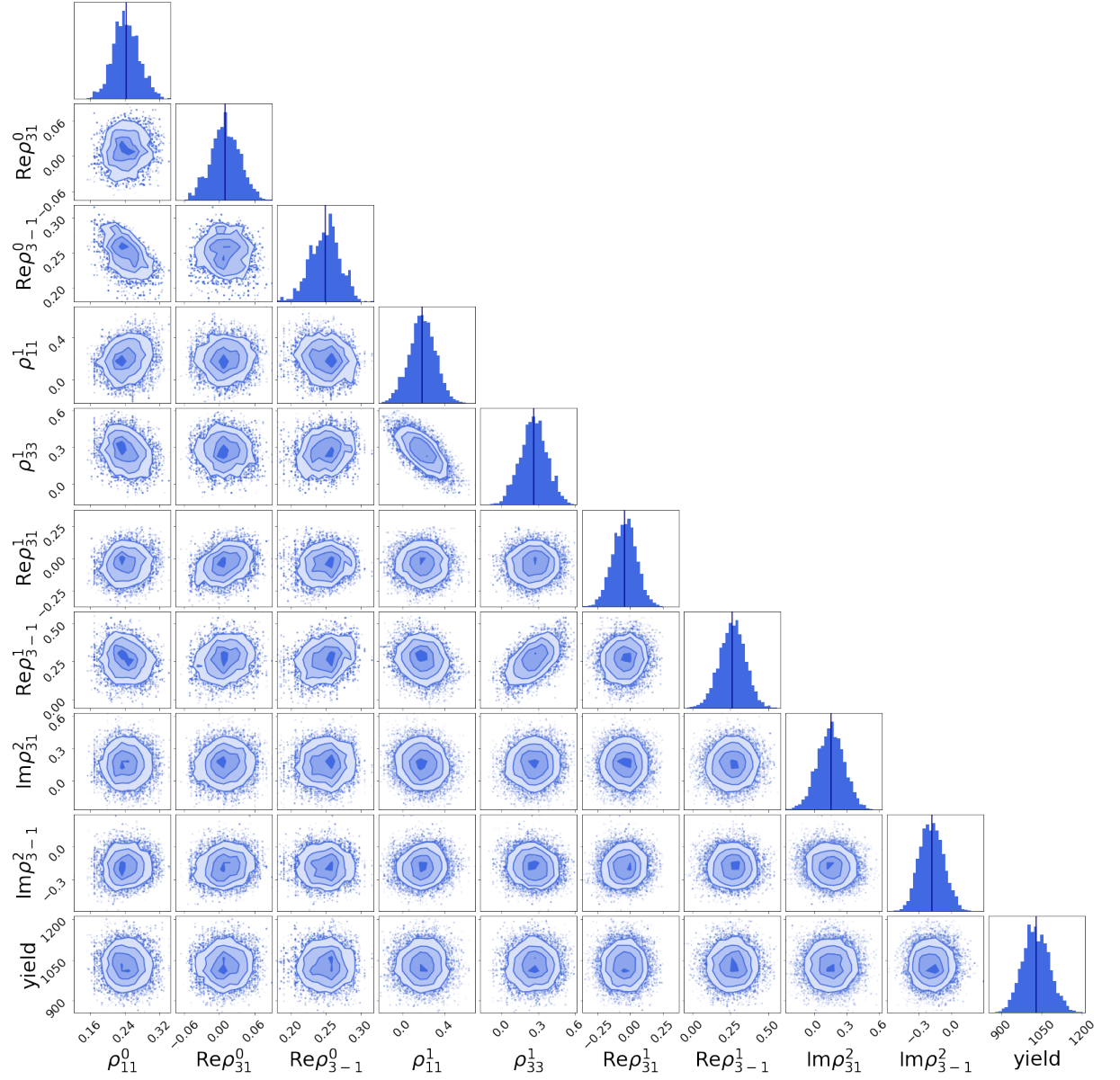


Figure B.16: SDME corner plot for $-(t - t_{\min}) = 1.6 \text{ GeV}^2/c^2 - 2.0 \text{ GeV}^2/c^2$. The vertical blue line in the 1D distribution indicates the mean.

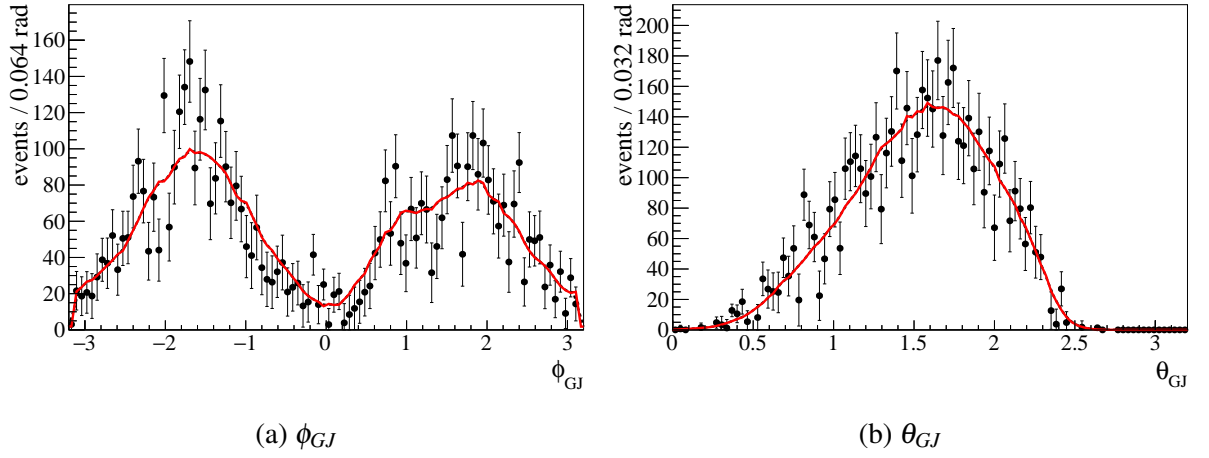


Figure B.17: Projections of sPlot subtracted data (black points) and acceptance weighted fit results (red lines) for $-(t - t_{\min}) = 0 \text{ GeV}^2/c^2 - 0.3 \text{ GeV}^2/c^2$.

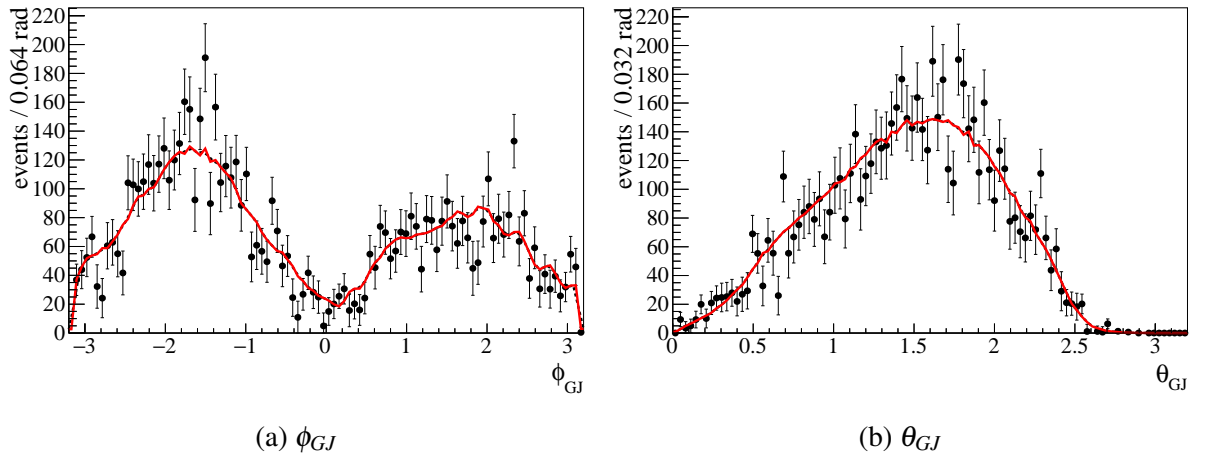


Figure B.18: Projections of sPlot subtracted data (black points) and acceptance weighted fit results (red lines) for $-(t - t_{\min}) = 0.3 \text{ GeV}^2/c^2 - 0.5 \text{ GeV}^2/c^2$.

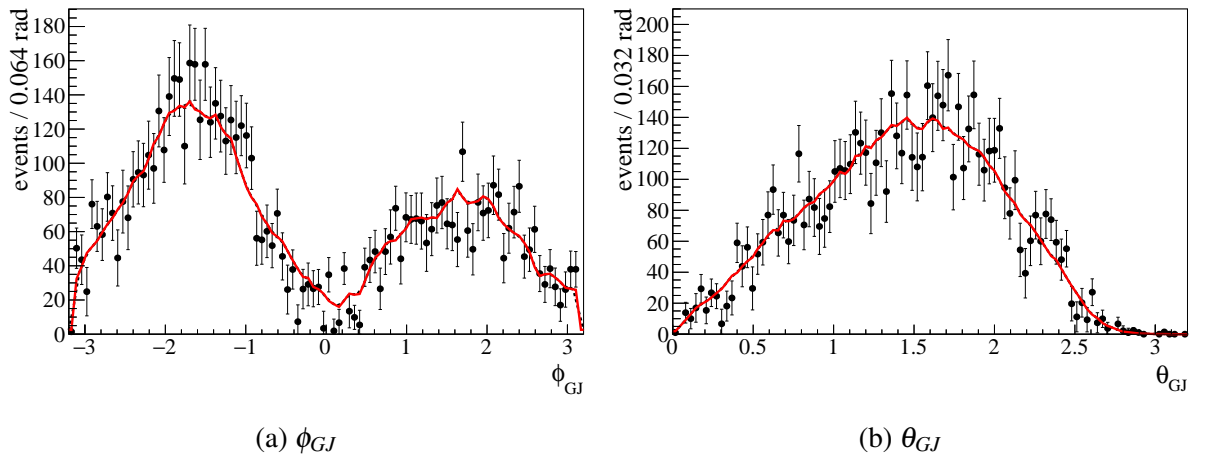


Figure B.19: Projections of sPlot subtracted data (black points) and acceptance weighted fit results (red lines) for $-(t - t_{\min}) = 0.5 \text{ GeV}^2/c^2 - 0.7 \text{ GeV}^2/c^2$.

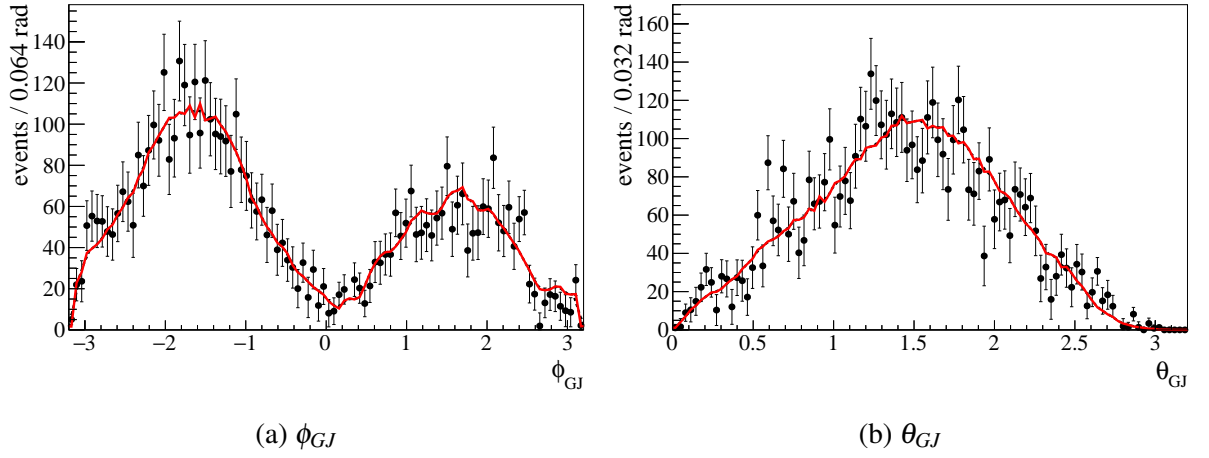


Figure B.20: Projections of sPlot subtracted data (black points) and acceptance weighted fit results (red lines) for $-(t - t_{\min}) = 0.7 \text{ GeV}^2/c^2 - 0.9 \text{ GeV}^2/c^2$.

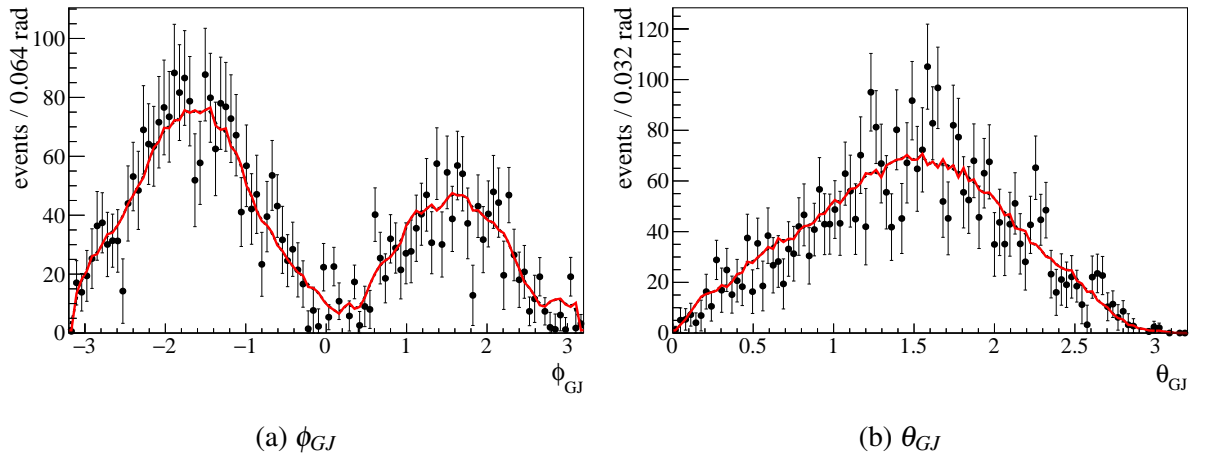


Figure B.21: Projections of sPlot subtracted data (black points) and acceptance weighted fit results (red lines) for $-(t - t_{\min}) = 0.9 \text{ GeV}^2/c^2 - 1.1 \text{ GeV}^2/c^2$.

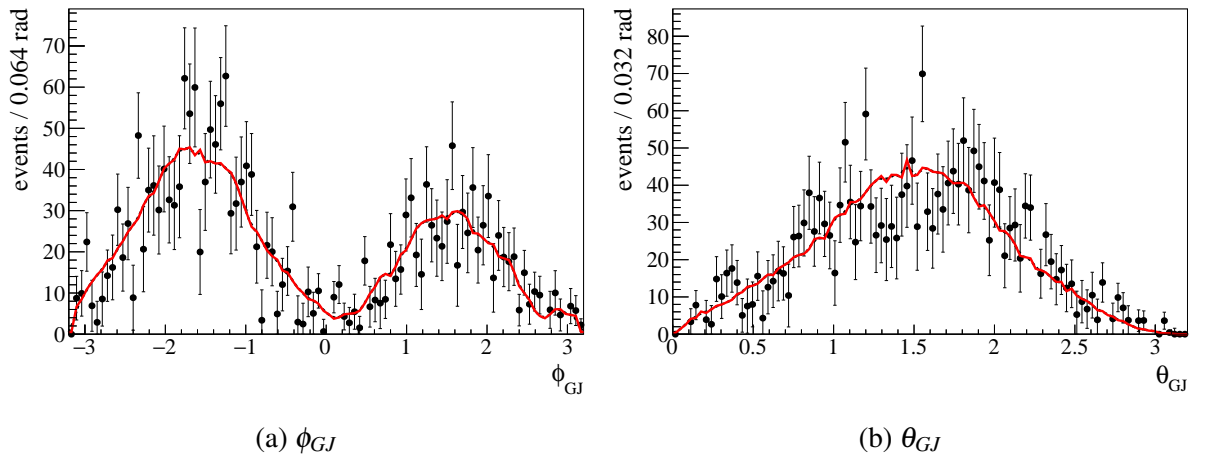


Figure B.22: Projections of sPlot subtracted data (black points) and acceptance weighted fit results (red lines) for $-(t - t_{\min}) = 1.1 \text{ GeV}^2/c^2 - 1.3 \text{ GeV}^2/c^2$.

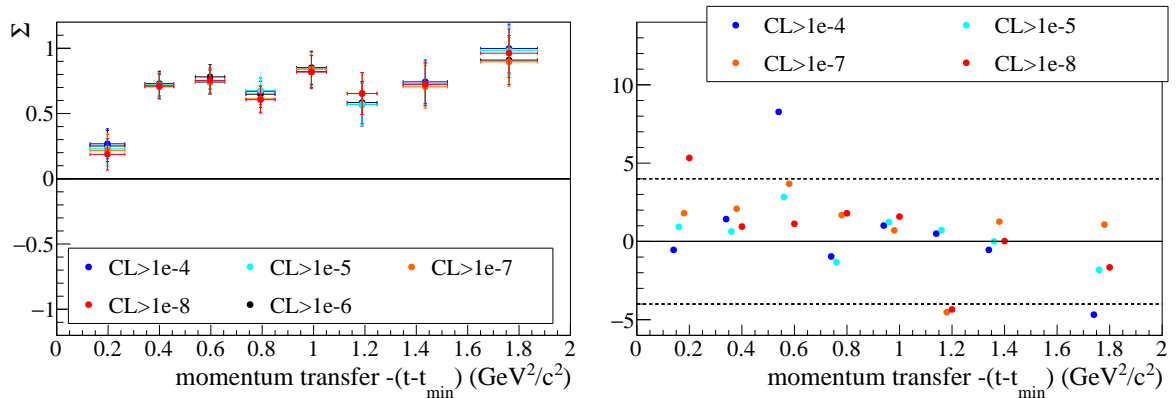
Appendix C

Additional plots of systematic studies

As part of the systematic studies performed in Chapter 6 many tests have been performed. In the following the plots which were not shown earlier, for brevity, are presented.

C.1 Event selection studies beam asymmetry

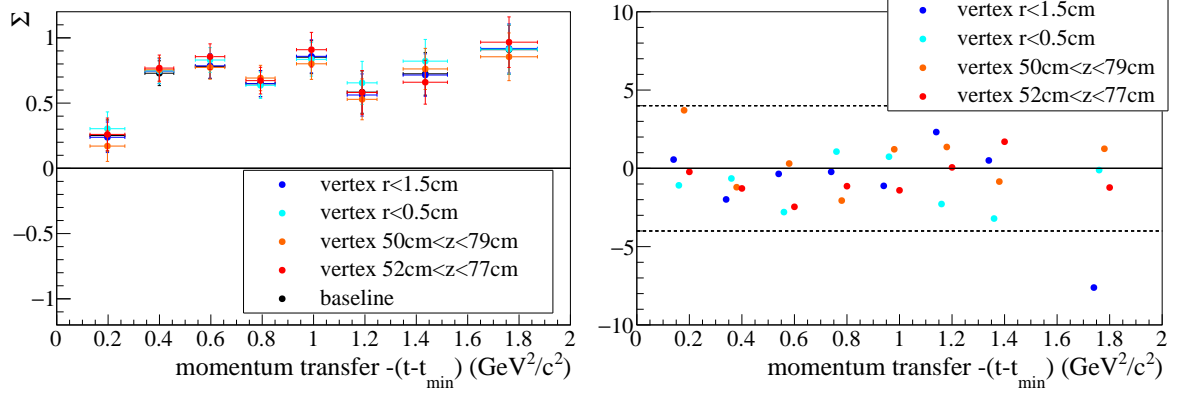
Figures C.1 to C.7 were created as part of the studies performed in Section 6.1.6 (see also Table 6.1).



(a) Results for the beam asymmetry Σ for the baseline setting (black points) and four variations.

(b) The significance as defined in the Barlow test is plotted for each bin and each variation.

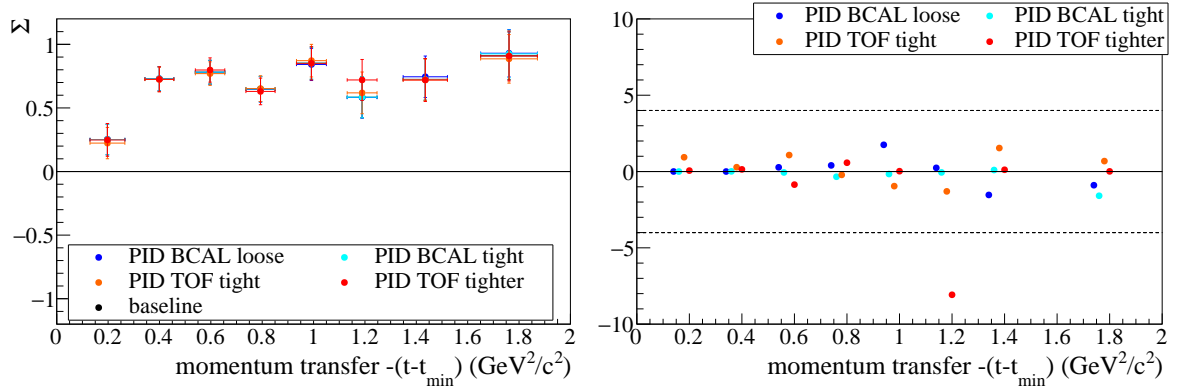
Figure C.1: Results for the CL cut study (see Table 6.1 setups 7-10).



(a) Results for the beam asymmetry Σ for the baseline setting (black points) and four variations.

(b) The significance as defined in the Barlow test is plotted for each bin and each variation.

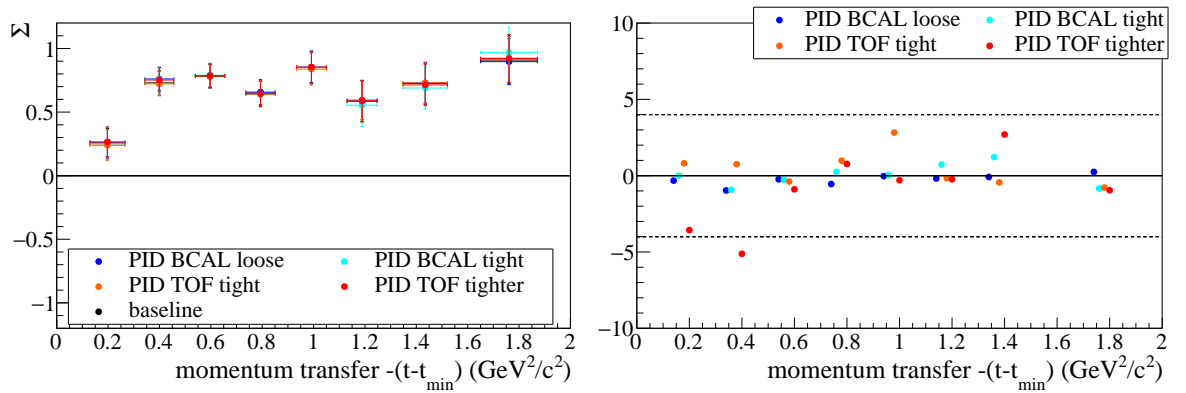
Figure C.2: Results for the vertex cut study (see Table 6.1 setups 11-14).



(a) Results for the beam asymmetry Σ for the baseline setting (black points) and four variations.

(b) The significance as defined in the Barlow test is plotted for each bin and each variation.

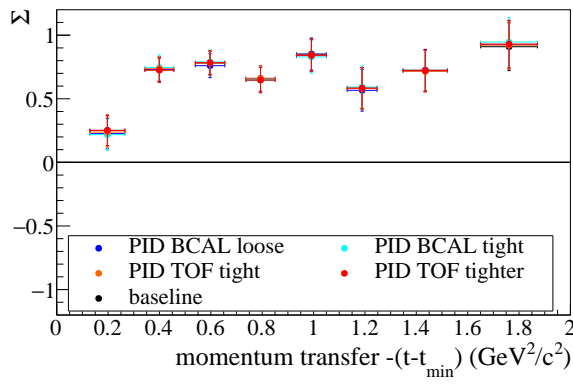
Figure C.3: Results for the K^+ ΔT PID cut study (see Table 6.1 setups 15-18).



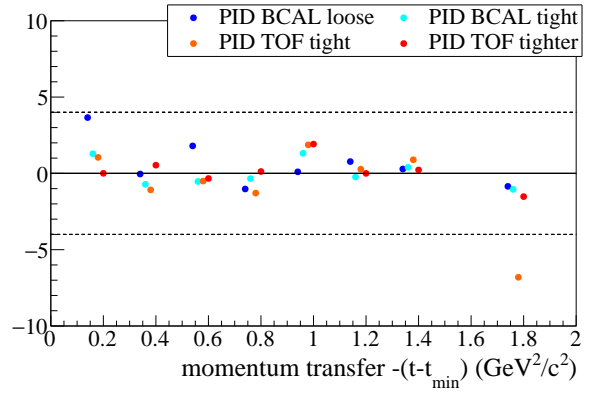
(a) Results for the beam asymmetry Σ for the baseline setting (black points) and four variations.

(b) The significance as defined in the Barlow test is plotted for each bin and each variation.

Figure C.4: Results for the K^- ΔT PID cut study (see Table 6.1 setups 19-22).

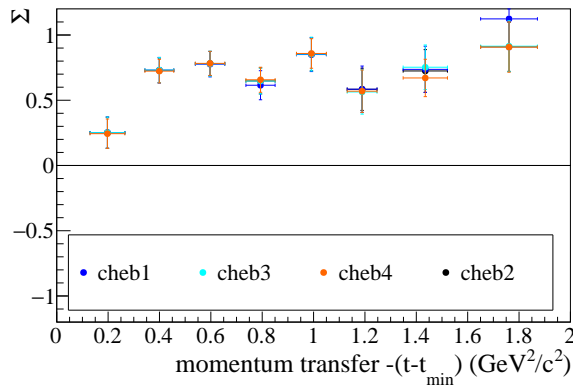


(a) Results for the beam asymmetry Σ for the baseline setting (black points) and four variations.

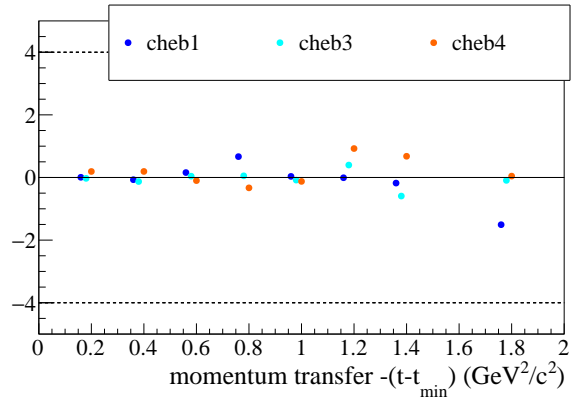


(b) The significance as defined in the Barlow test is plotted for each bin and each variation.

Figure C.5: Results for the $p \Delta T$ PID cut study (see Table 6.1 setups 23-26).

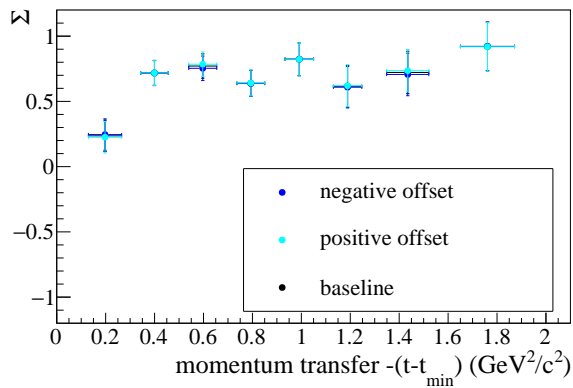


(a) Results for the beam asymmetry Σ for the baseline setting (black points) and three variations.

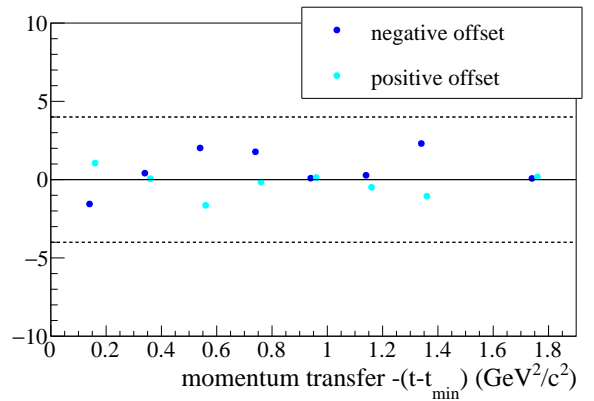


(b) The significance as defined in the Barlow test is plotted for each bin and each variation.

Figure C.6: Results for the background shape study.



(a) Results for the beam asymmetry Σ for the baseline setting (black points) and two variations.



(b) The significance as defined in the Barlow test is plotted for each bin and each variation.

Figure C.7: Results for the polarisation plane offset study.

C.2 Sideband studies spin-density matrix elements

In Section 6.2.3 the sideband of the $\Lambda(1520)$ in the pK^- invariant mass spectrum is investigated. Figures C.8 to C.17 show the fit results for all 10 bins.

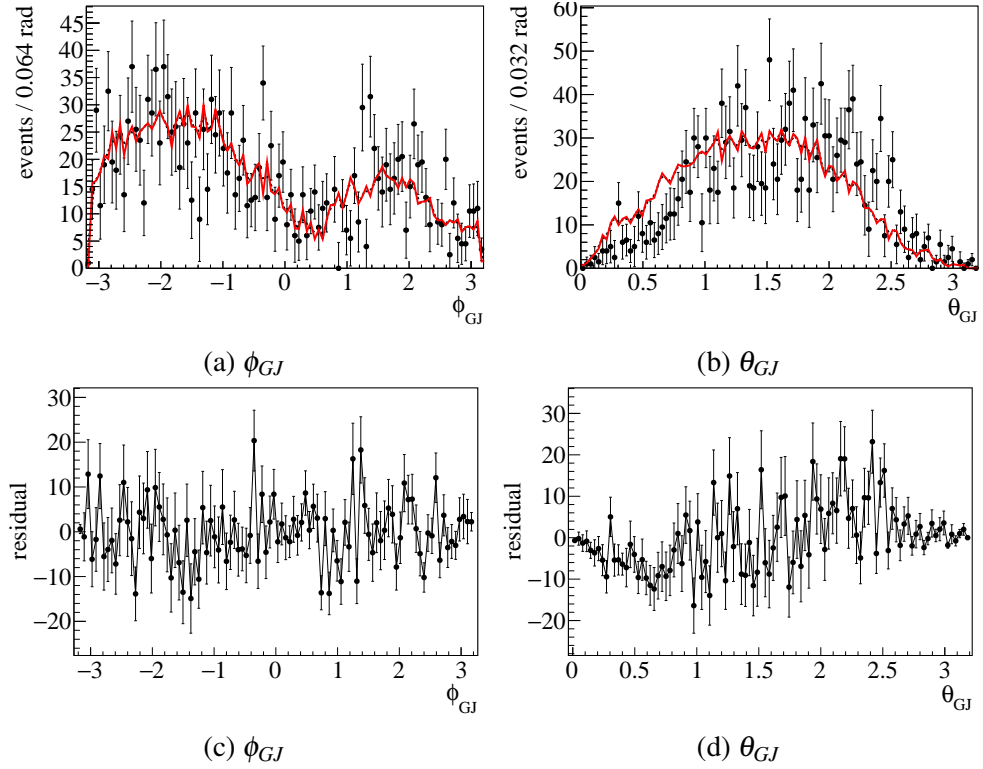


Figure C.8: Resulting fit projections and their residuals from MCMC for pK^- inv. mass range $1.46 \text{ GeV}/c^2 - 1.48 \text{ GeV}/c^2$.

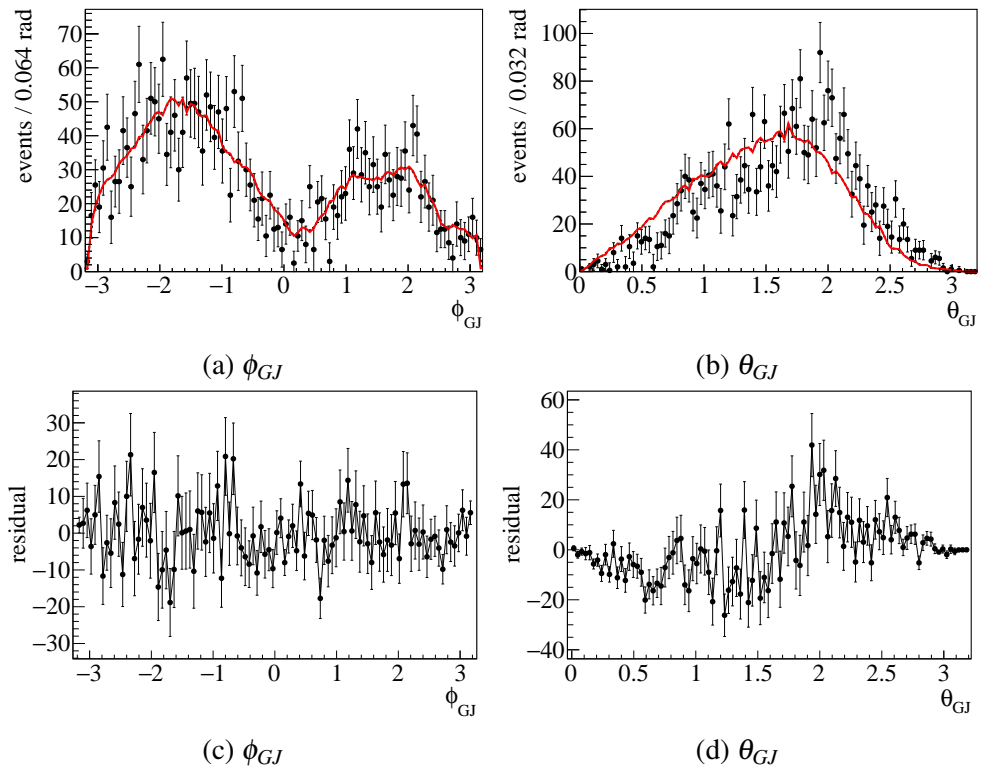


Figure C.9: Resulting fit projections and their residuals from MCMC for pK^- inv. mass range $1.48\text{ GeV}/c^2 - 1.50\text{ GeV}/c^2$.

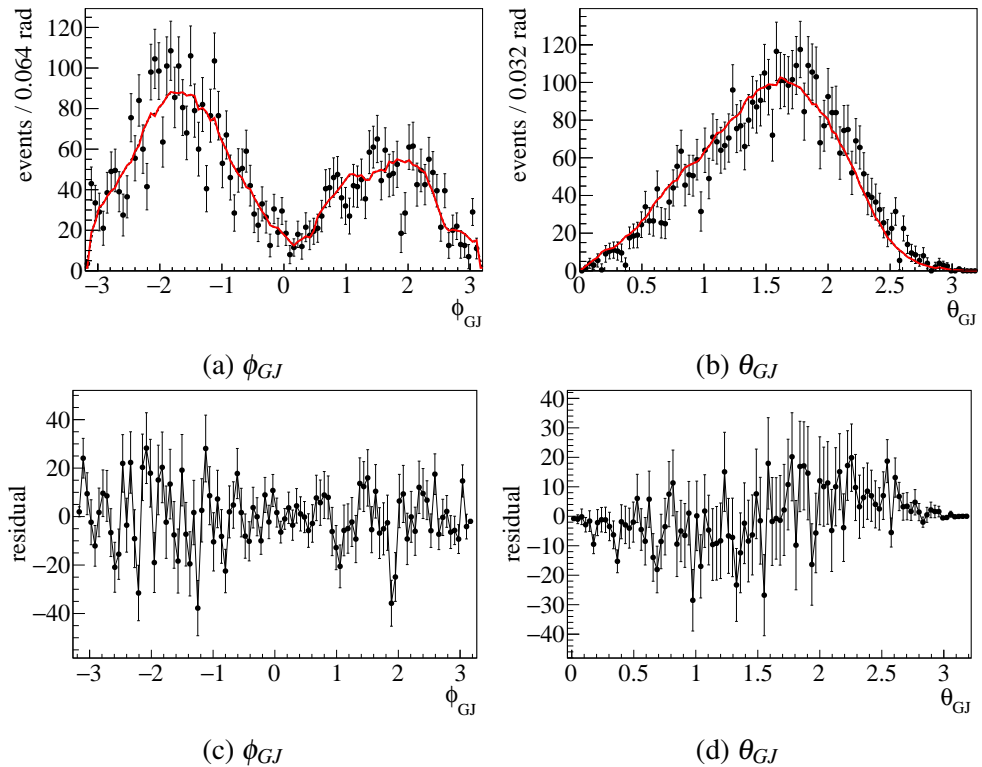


Figure C.10: Resulting fit projections and their residuals from MCMC for pK^- inv. mass range $1.50\text{ GeV}/c^2 - 1.51\text{ GeV}/c^2$.

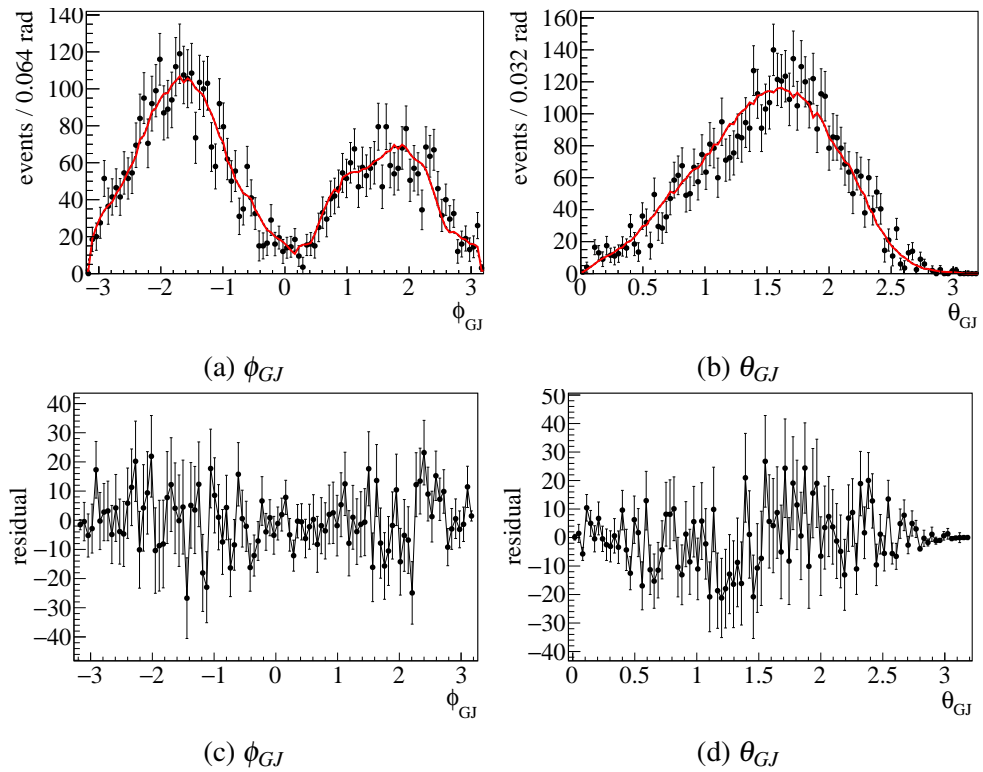


Figure C.11: Resulting fit projections and their residuals from MCMC for pK^- inv. mass range $1.510\text{GeV}/c^2 - 1.515\text{GeV}/c^2$.

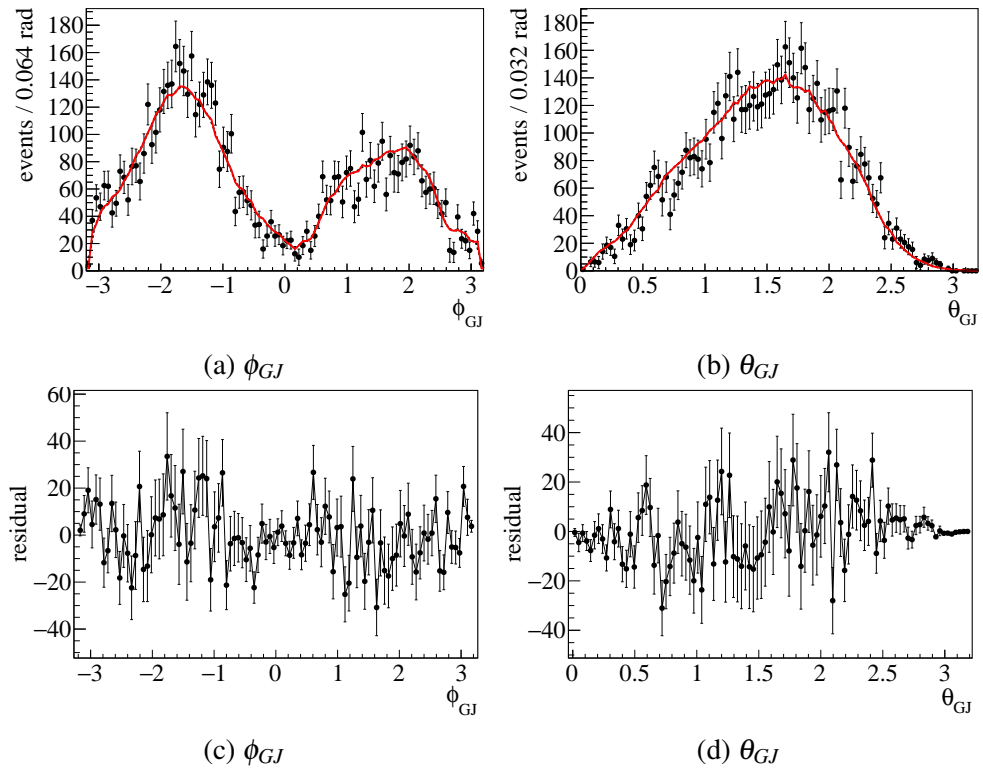


Figure C.12: Resulting fit projections and their residuals from MCMC for pK^- inv. mass range $1.515\text{GeV}/c^2 - 1.520\text{GeV}/c^2$.

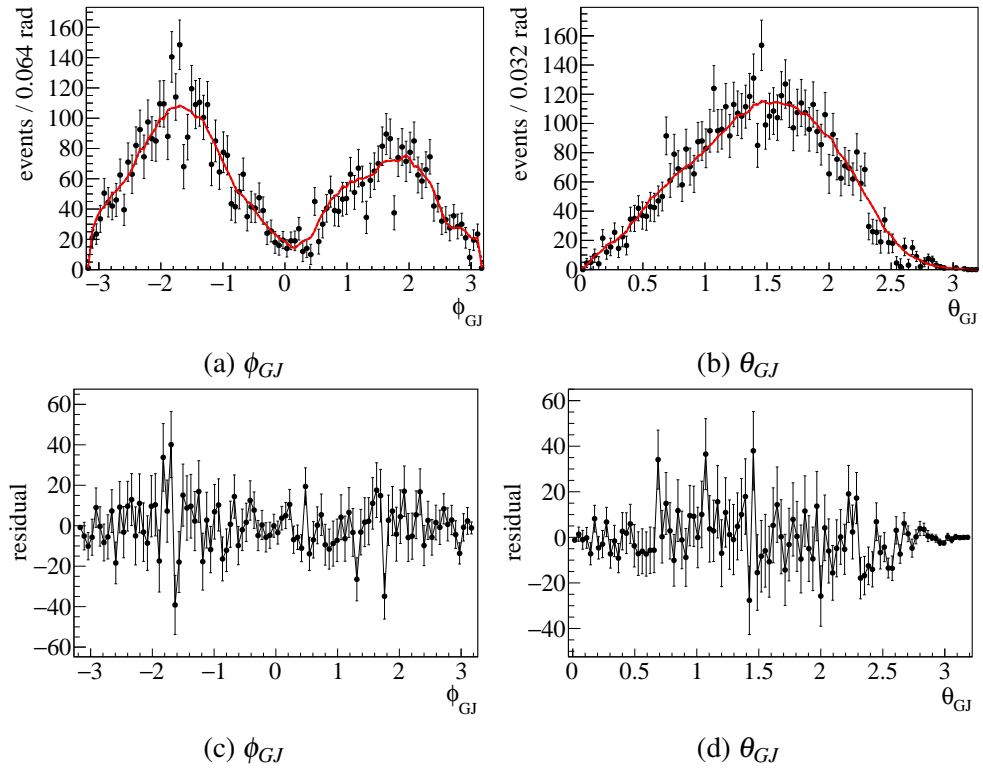


Figure C.13: Resulting fit projections and their residuals from MCMC for pK^- inv. mass range $1.520\text{GeV}/c^2 - 1.525\text{GeV}/c^2$.

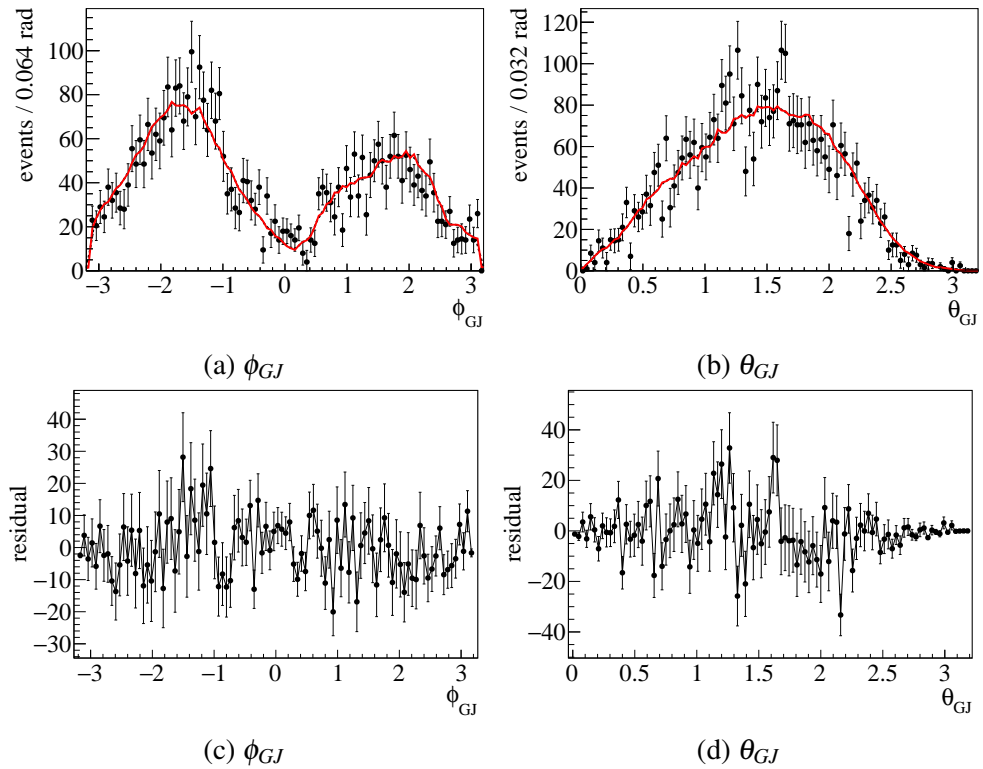


Figure C.14: Resulting fit projections and their residuals from MCMC for pK^- inv. mass range $1.525\text{GeV}/c^2 - 1.530\text{GeV}/c^2$.

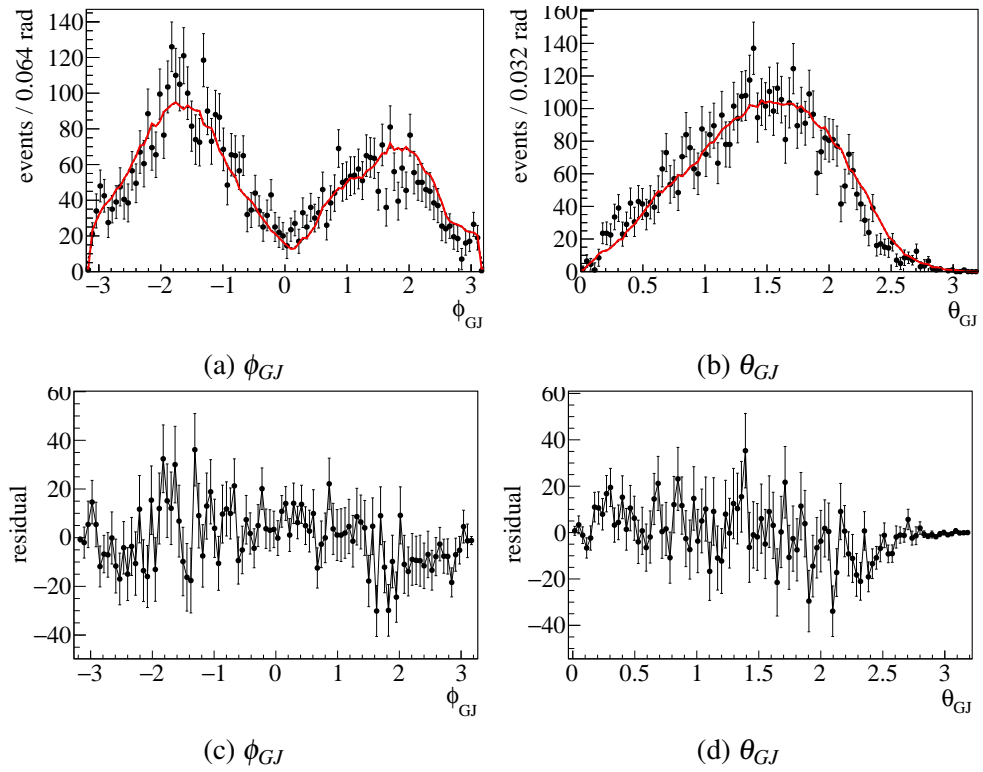


Figure C.15: Resulting fit projections and their residuals from MCMC for pK^- inv. mass range $1.53\text{ GeV}/c^2 - 1.54\text{ GeV}/c^2$.

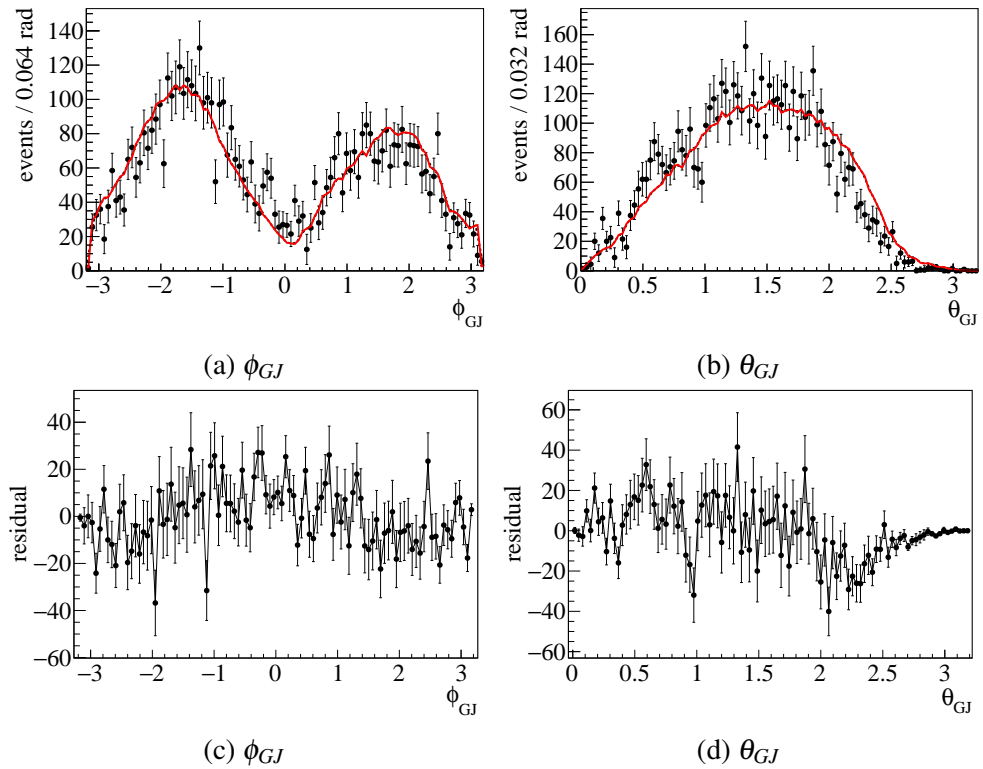


Figure C.16: Resulting fit projections and their residuals from MCMC for pK^- inv. mass range $1.54\text{ GeV}/c^2 - 1.56\text{ GeV}/c^2$.

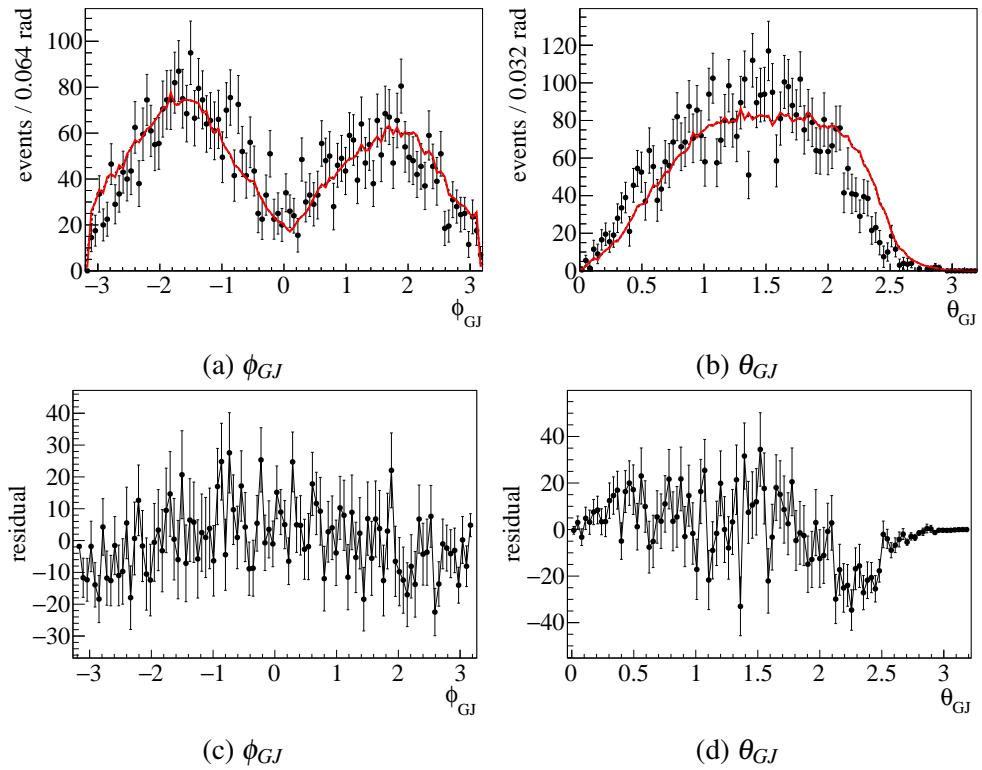


Figure C.17: Resulting fit projections and their residuals from MCMC for pK^- inv. mass range $1.56\text{ GeV}/c^2 - 1.58\text{ GeV}/c^2$.

C.3 SDME result validation studies

During the validation for the SDME parameter estimation in Section 6.2.4 extensive studies have been performed to understand the discrepancy seen. The results that were only summarised in the main body of this work are shown in the following in more detail.

C.3.1 Analysis of thrown data with artificial resolution

To investigate this issue the thrown sample is used as before but this time the angular information is smeared out by a Gaussian to simulate non-perfect resolution. For that the ϕ_{K^+} angle, which is used to determine the production plane, is smeared out with a Gaussian with a width of 0.01 and ϕ_{GJ} and θ_{GJ} are smeared out with a Gaussian with width 0.02. An example sFit can be seen in Figure C.18. Figure C.19 shows an example fit of the ϕ_{GJ} and θ_{GJ} distributions. The means and widths extracted from the pull distributions and the absolute differences can be seen in Figures C.20 to C.28. They seem to be very much in agreement with what was seen for the thrown sample without artificial resolution. As before we can also compare the actual signal with the extracted signal. The results are in Figure C.29. They look very similar to the results obtained from the thrown fit without artificial resolution.

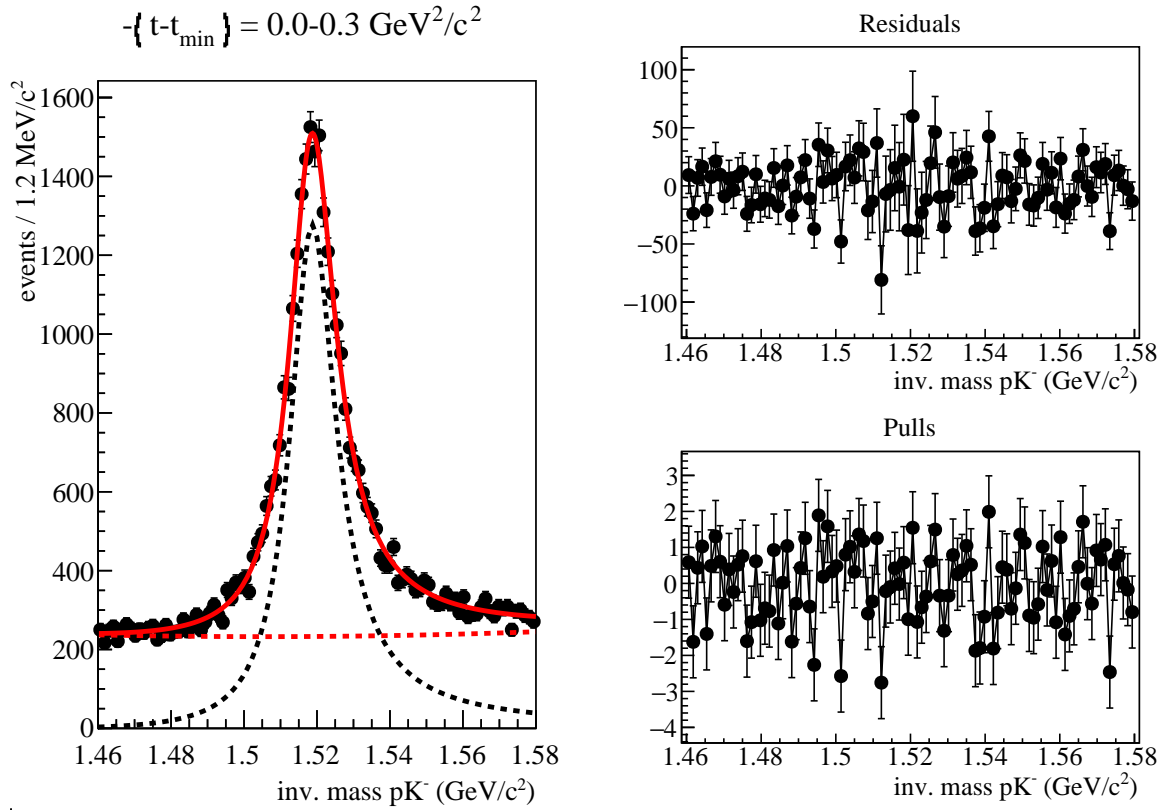


Figure C.18: Example sFit for one sample of thrown MC with an artificial resolution. Left: sFit of the pK^- invariant mass. The red dashed line is a Chebychev function used to approximate background. The black dashed line is the Breit-Wigner shape for a $\Lambda(1520)$. The solid red line is the resulting fit to the data. Right: Fit residual on top and pull distribution on bottom.

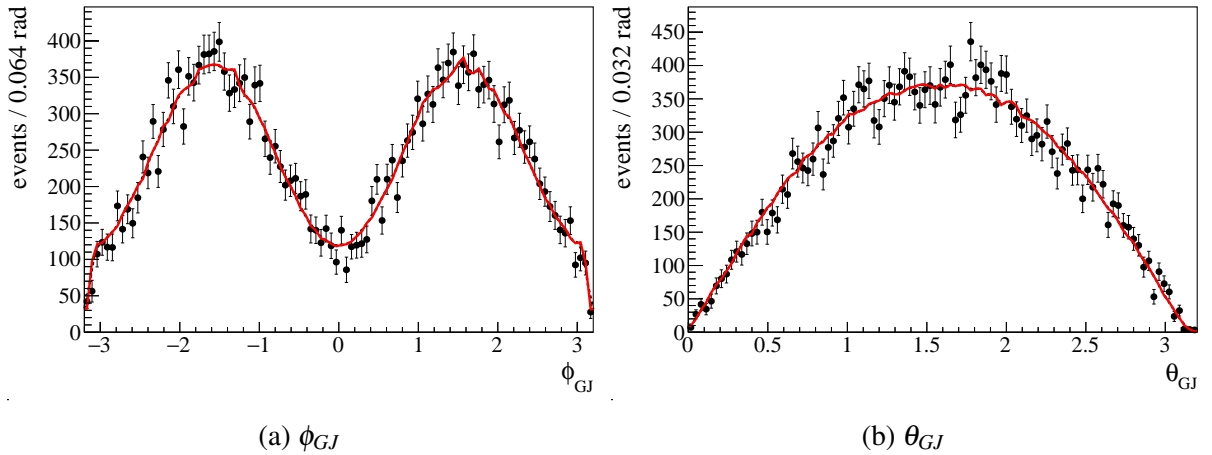


Figure C.19: Example fits for thrown MC with artificial resolution for $-(t-t_{\min}) = 0.0 \text{ GeV}^2/c^2 - 0.3 \text{ GeV}^2/c^2$.

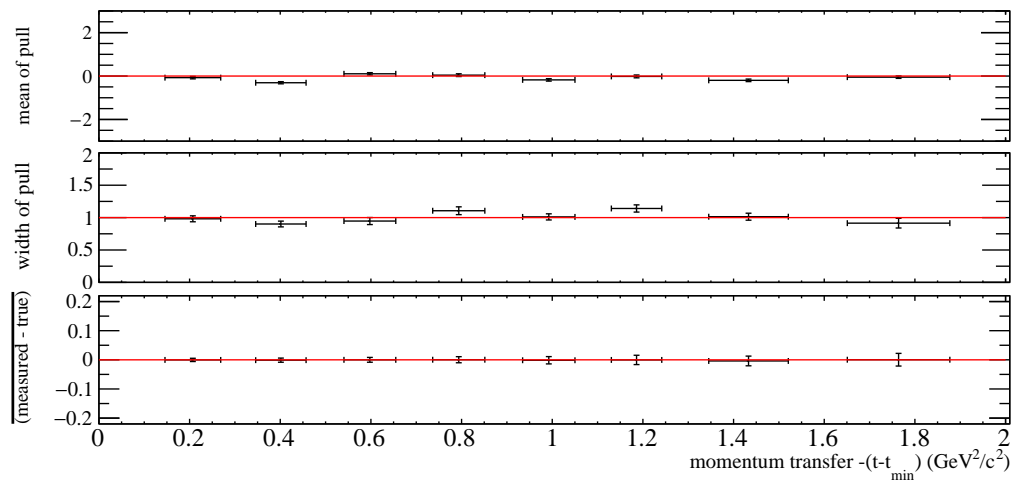


Figure C.20: Summarised results from thrown data study with artificial resolution for ρ_{11}^0 . True value = 0.26

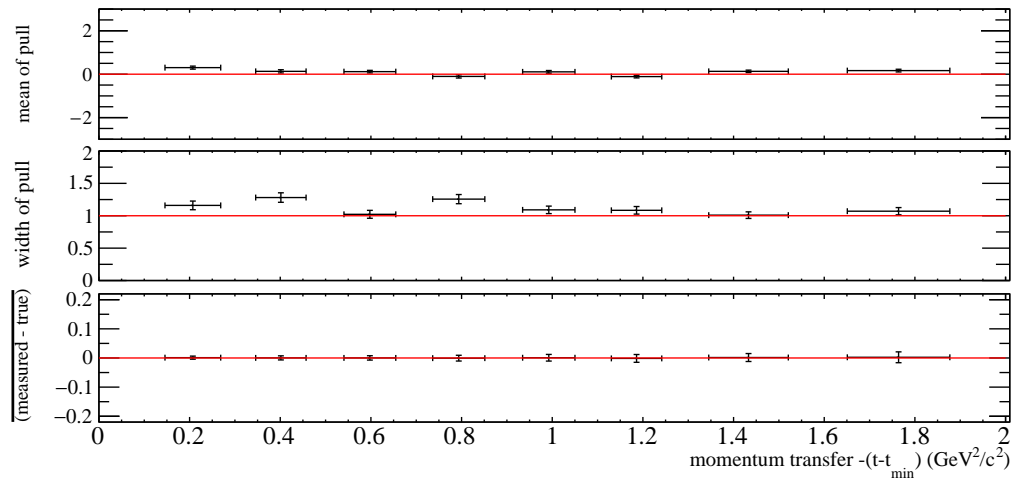


Figure C.21: Summarised results from thrown data study with artificial resolution for ρ_{31}^0 . True value = -0.06.

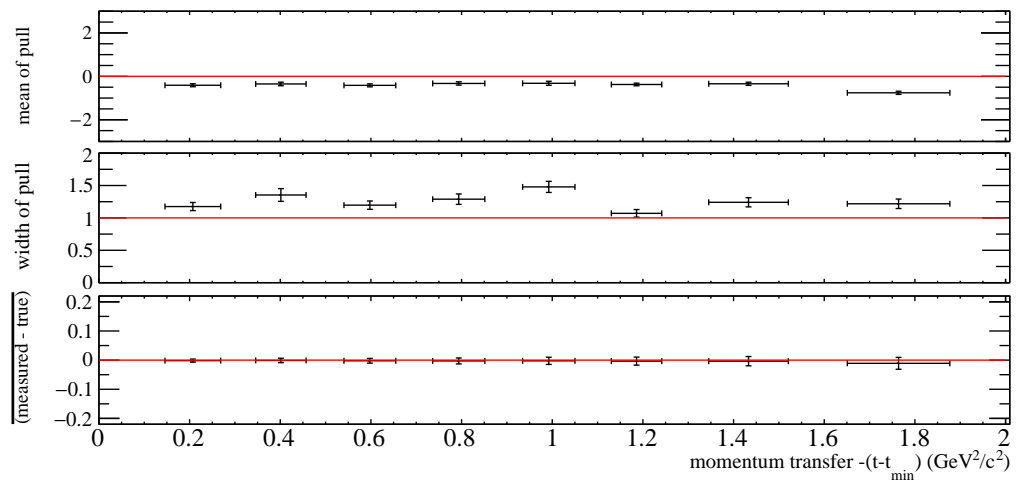


Figure C.22: Summarised results from thrown data study with artificial resolution for ρ_{3-1}^0 . True value = 0.23.

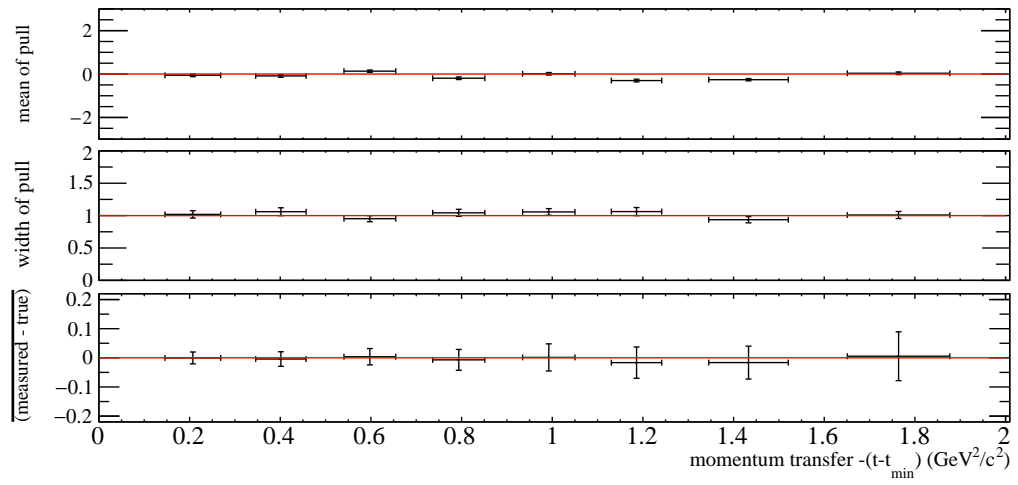


Figure C.23: Summarised results from thrown data study with artificial resolution for ρ_{11}^1 . True value = 0.2.

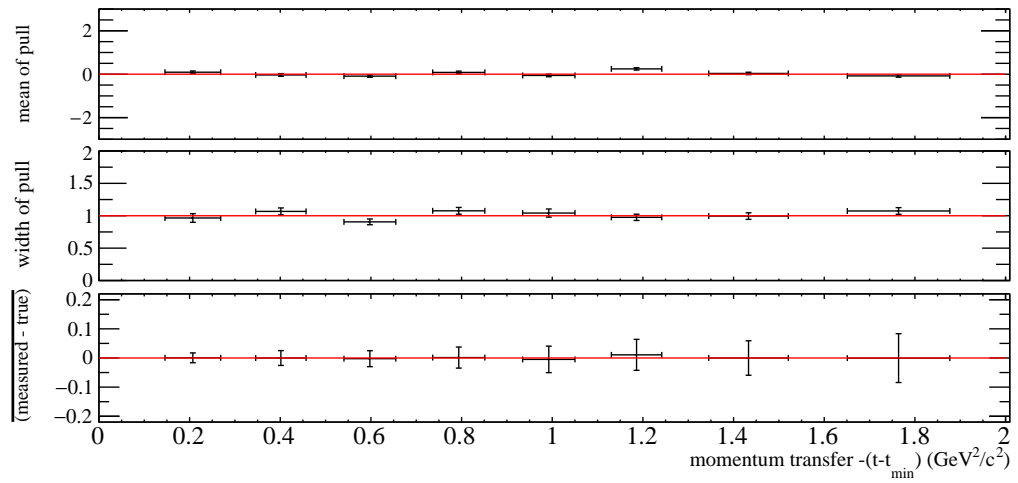


Figure C.24: Summarised results from thrown data study with artificial resolution for ρ_{33}^1 . True value = 0.1.

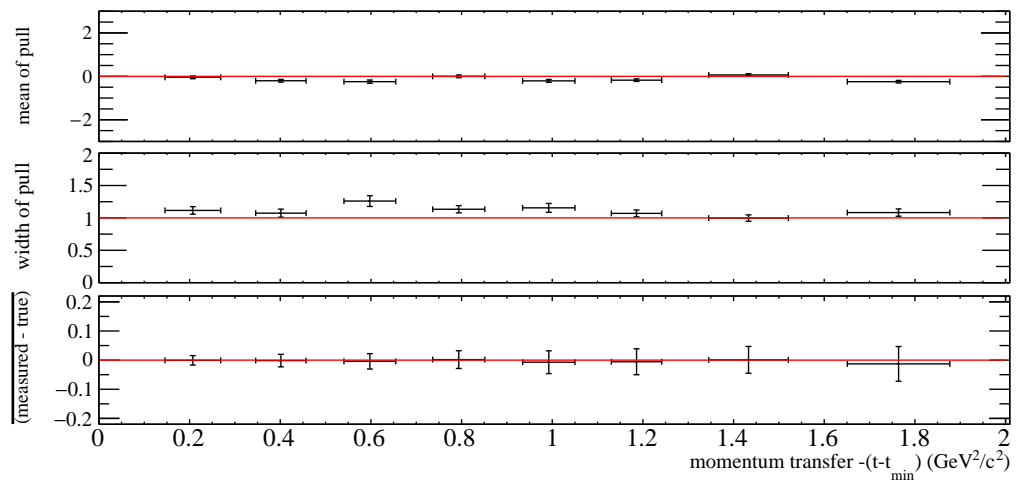


Figure C.25: Summarised results from thrown data study with artificial resolution for ρ_{31}^1 . True value = 0.04.

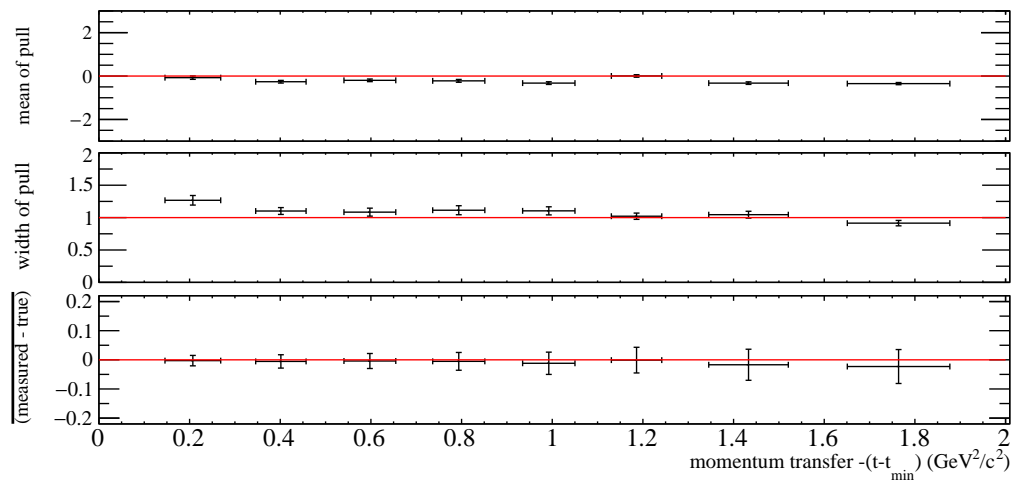


Figure C.26: Summarised results from thrown data study with artificial resolution for ρ_{3-1}^1 . True value = 0.2.

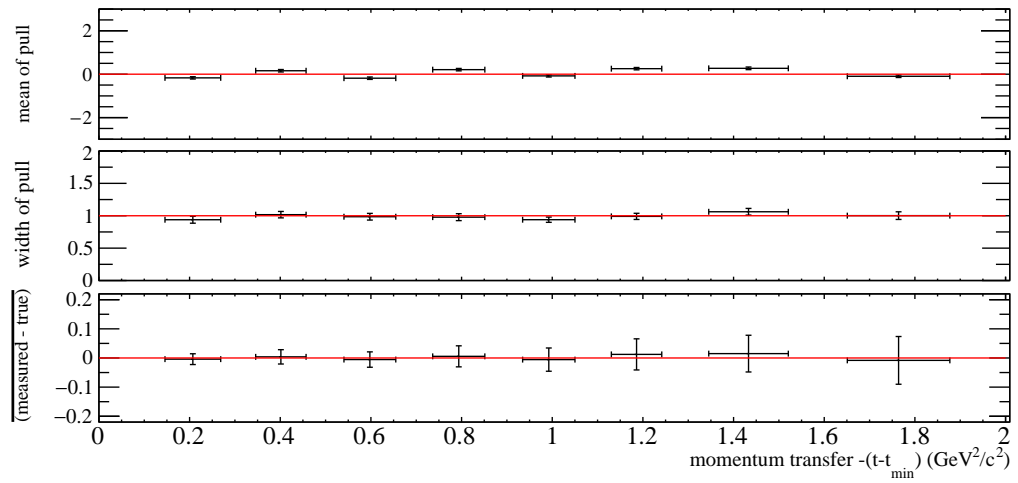


Figure C.27: Summarised results from thrown data study with artificial resolution for ρ_{31}^2 . True value = 0.04.

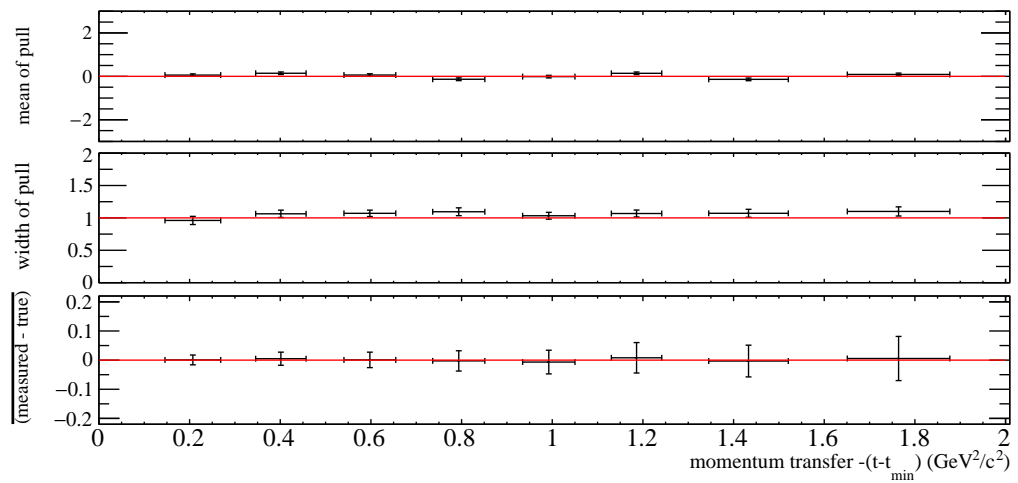


Figure C.28: Summarised results from thrown data study with artificial resolution for ρ_{3-1}^2 . True value = 0.01.

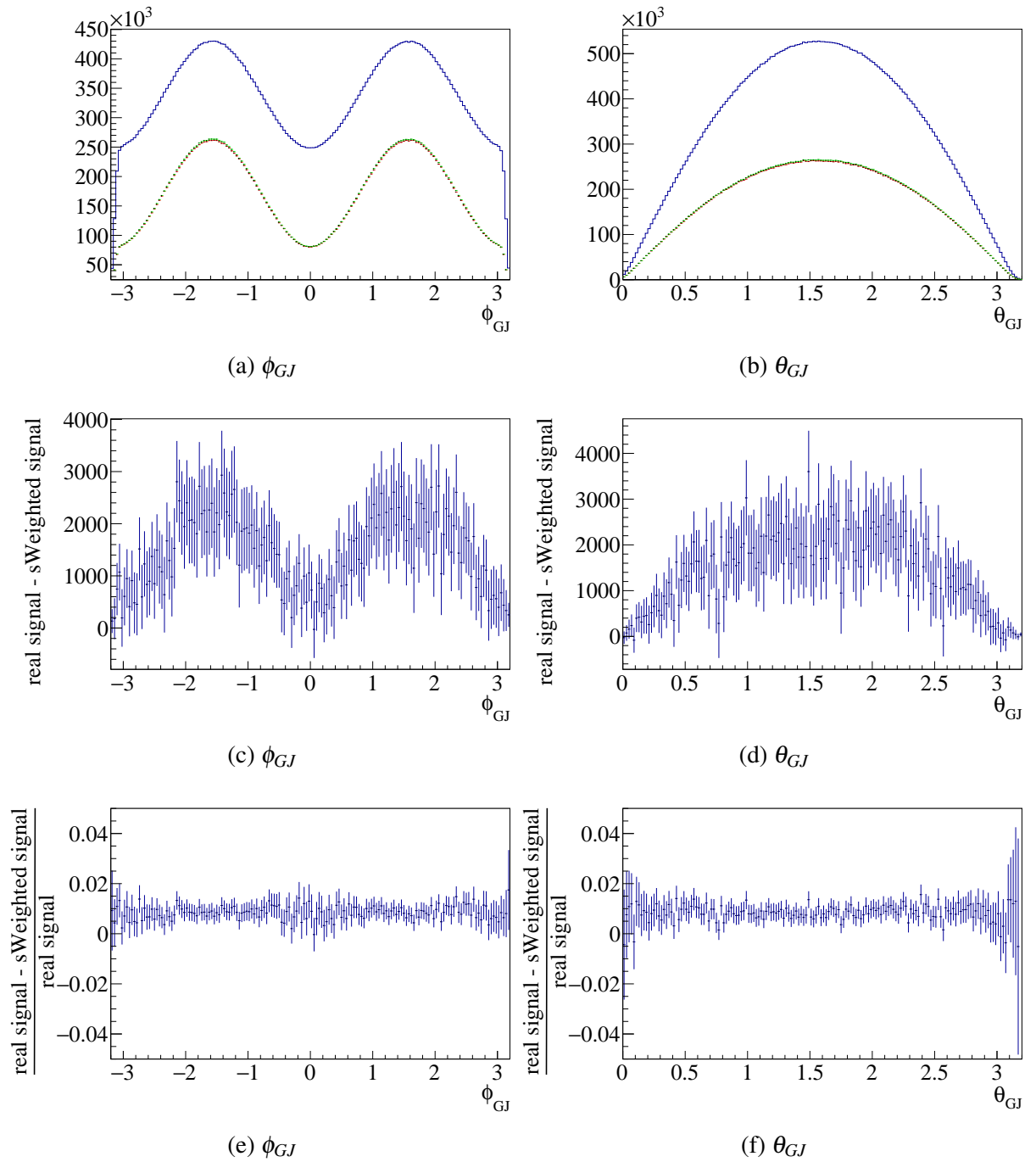


Figure C.29: Comparison between real MC signal (green) and signal extracted via the sFit (red), both distributions are overlapping. (c) and (d) show the difference between both. The blue histograms in (a) and (b) show the the full simulated sample of signal plus background. (e) and (f) show relative differences.

C.3.2 Analysis of thrown data with artificial acceptance

To further investigate the issue, the thrown sample is used again but this time an artificial acceptance is introduced by placing cuts on some of the angular variables. For all three final state particles a cut of $\theta < 2^\circ$ and $15^\circ < \theta < 18^\circ$ is placed as well as an 80% inefficiency imposed on events with the theta angle of the K^- in the Gottfried-Jackson frame of $\theta_{GJ}^{K^-} > 2.5$ rad. An example sFit can be seen in Figure C.30. Figure C.31 shows an example fit of the ϕ_{GJ} and

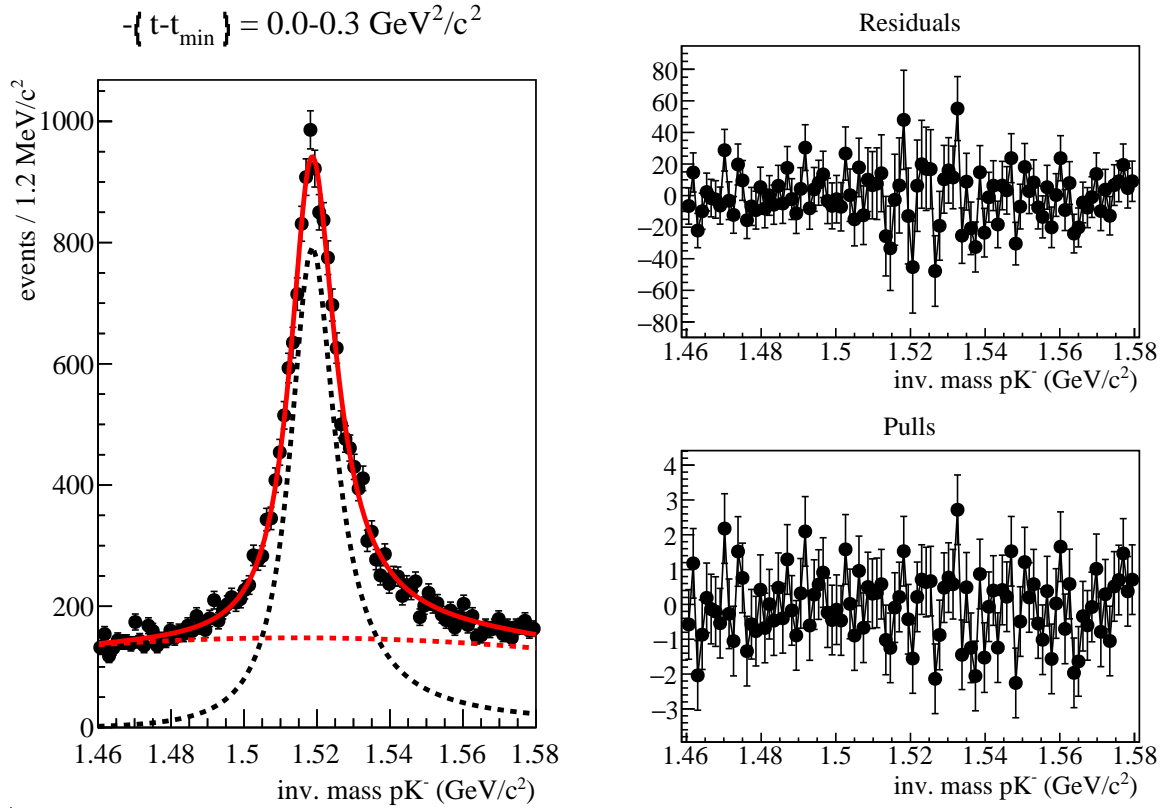


Figure C.30: Example sFit for one sample of thrown MC with an artificial acceptance. Left: sFit of the pK^- invariant mass. The red dashed line is a Chebychev function used to approximate background. The black dashed line is the Breit-Wigner shape for a $\Lambda(1520)$. The solid red line is the resulting fit to the data. Right: Fit residual on top and pull distribution on bottom.

θ_{GJ} distributions. The means and widths extracted from the pull distributions and the absolute differences can be seen in Figures C.32 to C.40. Similar to the full simulation the unpolarised SDMEs seem to be affected by the introduced acceptance. The pulls for them are significantly different from a normal distribution. As before we can also compare the actual signal with the extracted signal. The results are in Figure C.41. One can see a structure appearing in the ϕ_{GJ} distribution that has strong peaks. These could potentially disturb the fit results. It is important to note that the biggest relative deviations appear where the number of events is fairly small.

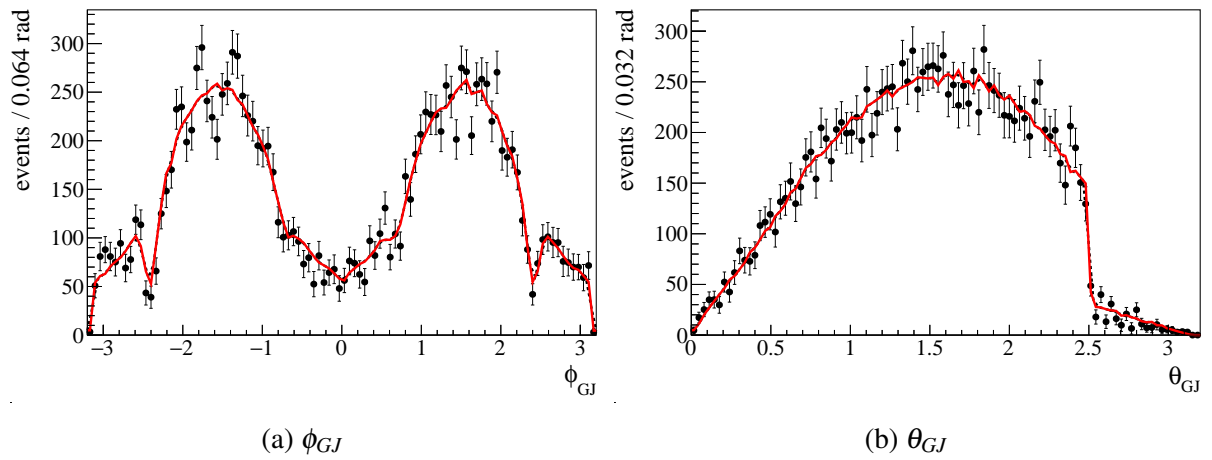


Figure C.31: Example fits for thrown MC with artificial acceptance for $-(t - t_{\min}) = 0.0\text{GeV}^2/c^2 - 0.3\text{GeV}^2/c^2$.

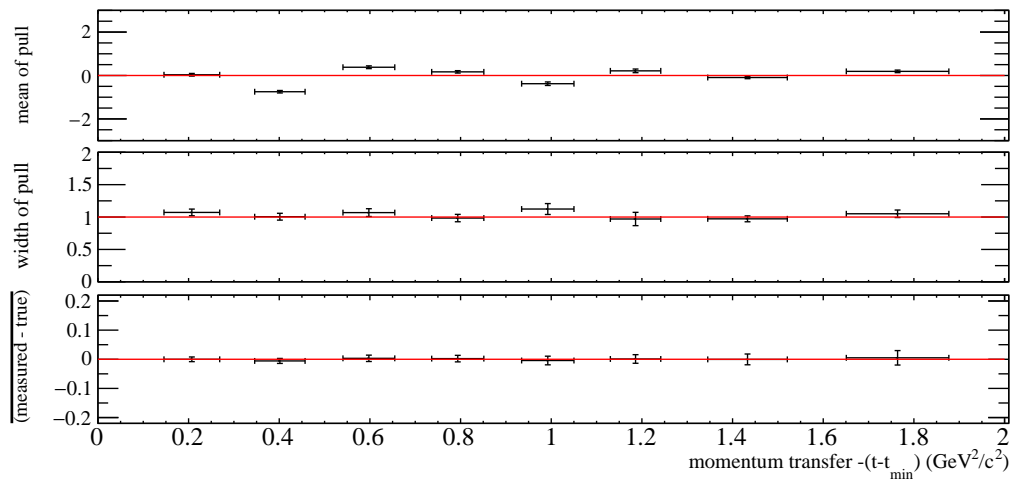


Figure C.32: Summarised results from thrown data study with artificial acceptance for ρ_{11}^0 . True value = 0.26.

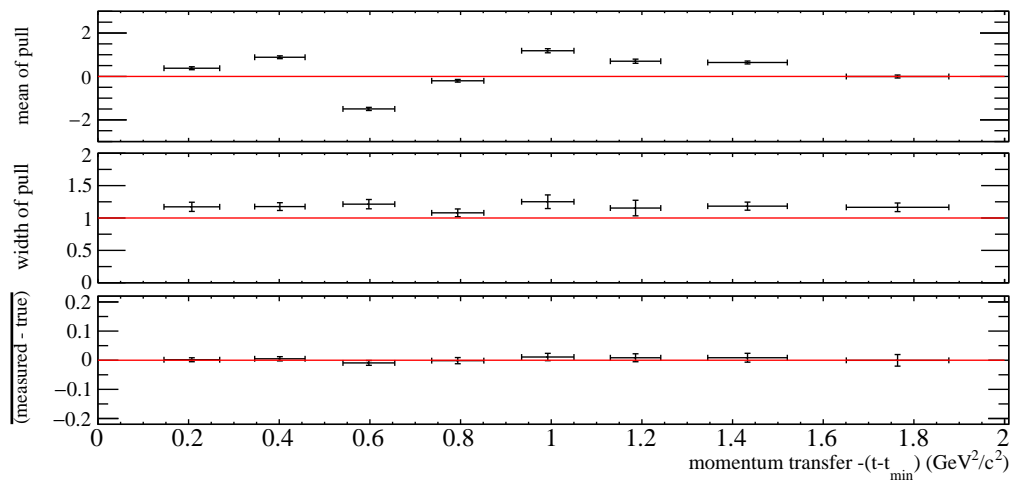


Figure C.33: Summarised results from thrown data study with artificial acceptance for ρ_{31}^0 . True value = -0.06.

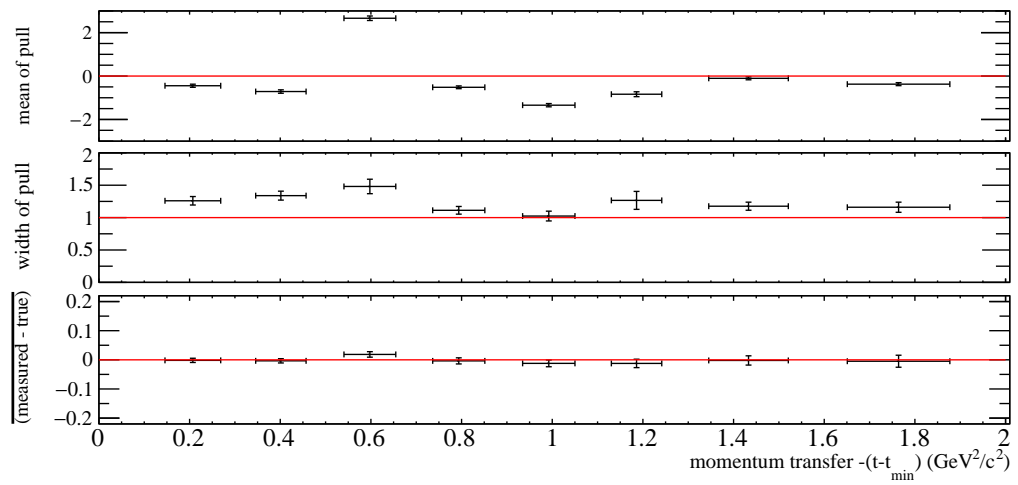


Figure C.34: Summarised results from thrown data study with artificial acceptance for ρ_{3-1}^0 . True value = 0.23.

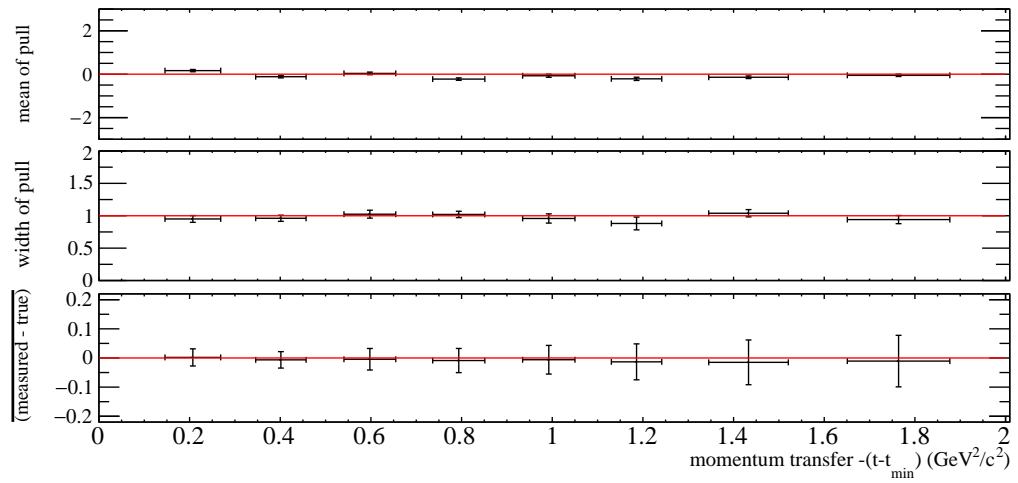


Figure C.35: Summarised results from thrown data study with artificial acceptance for ρ_{11}^1 . True value = 0.2.

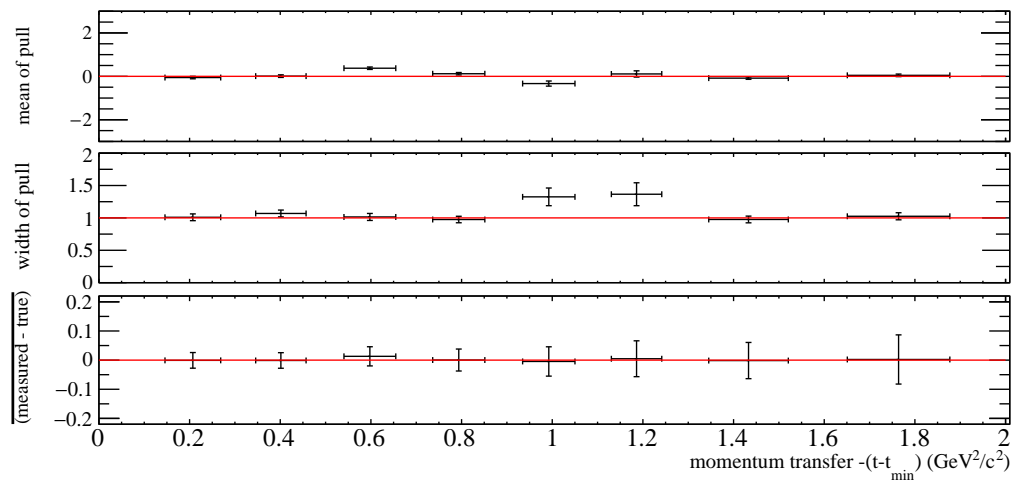


Figure C.36: Summarised results from thrown data study with artificial acceptance for ρ_{33}^1 . True value = 0.1.

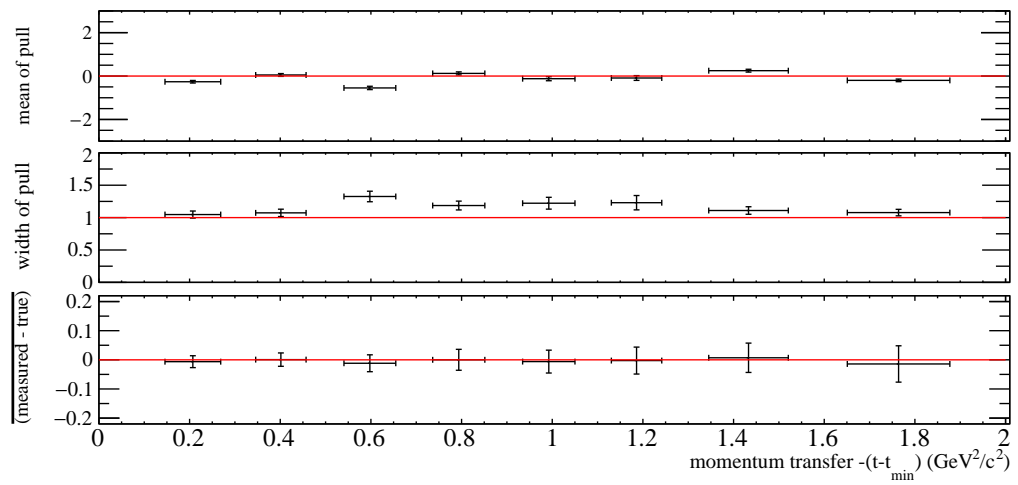


Figure C.37: Summarised results from thrown data study with artificial acceptance for ρ_{31}^1 . True value = 0.04.

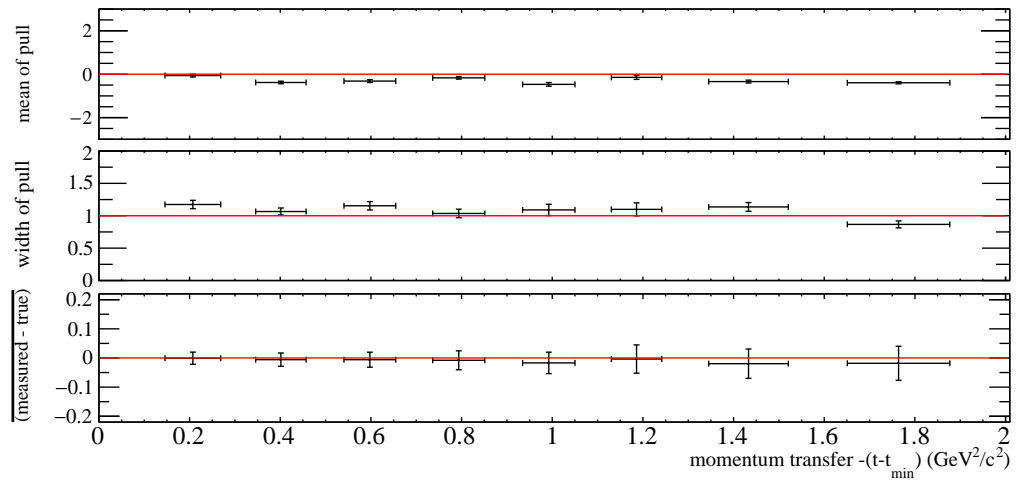


Figure C.38: Summarised results from thrown data study with artificial acceptance for ρ_{3-1}^1 . True value = 0.2.

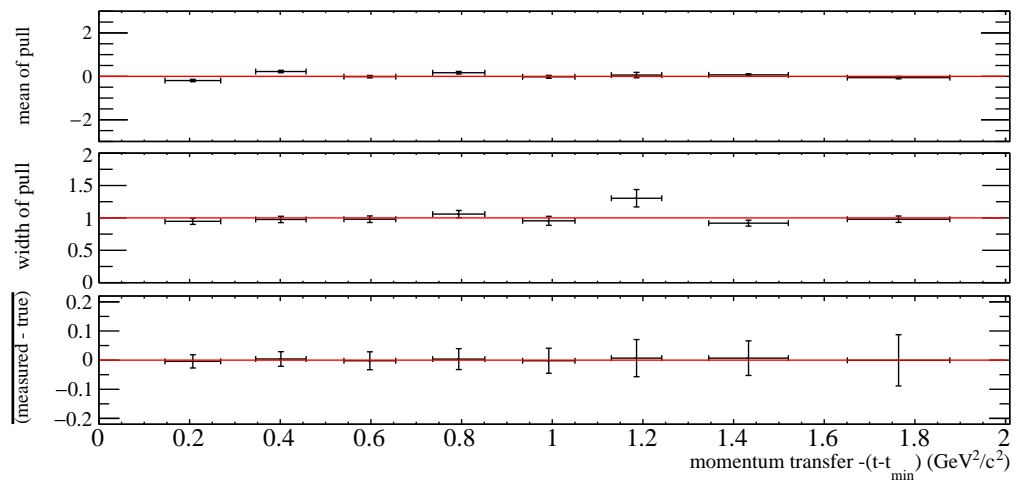


Figure C.39: Summarised results from thrown data study with artificial acceptance for ρ_{31}^2 . True value = 0.04.

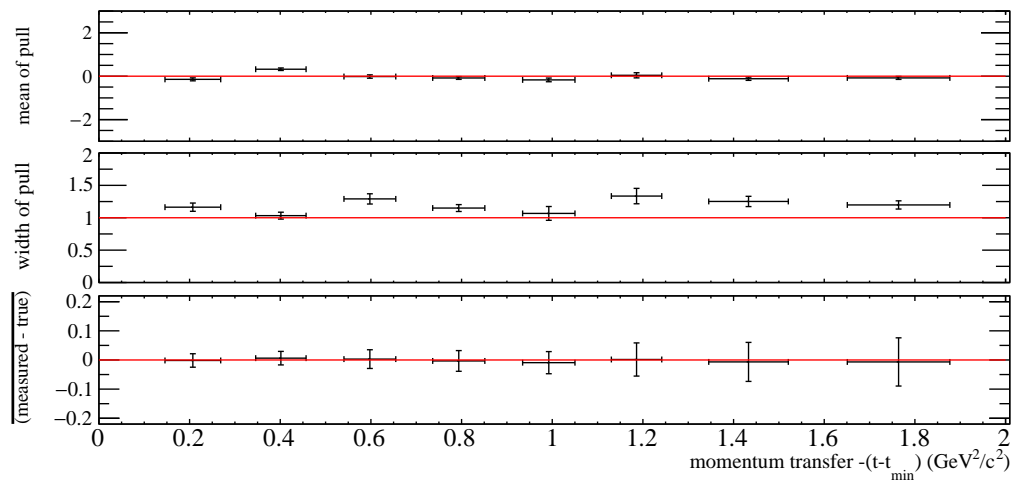


Figure C.40: Summarised results from thrown data study with artificial acceptance for ρ_{3-1}^2 . True value = 0.01.

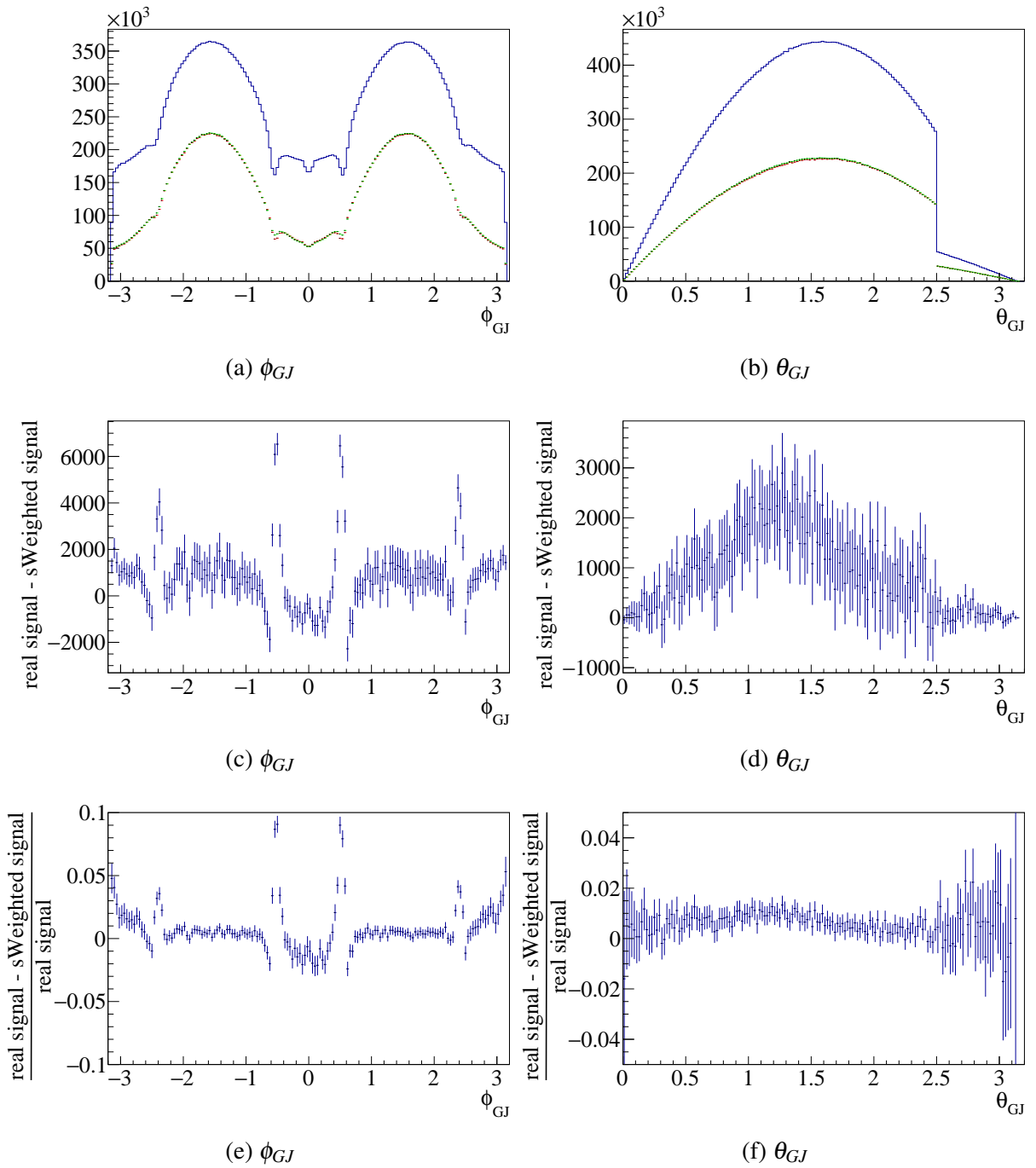


Figure C.41: Comparison between real MC signal (green) and signal extracted via the sFit (red), both distributions are overlapping. (c) and (d) show the difference between both. The blue histograms in (a) and (b) show the the full simulated sample of signal plus background. (e) and (f) show relative differences.

C.3.3 Analysis of full simulation without background

As a further test the fits are repeated for the samples with the full hdgeant4 simulation but without background added on. Therefore, an sFit to separate signal from background is not necessary and the fits to extract the SDMEs can be performed directly. The means and widths as extracted from the pull distributions as well as the absolute differences can be seen in Figures C.42 to C.50.

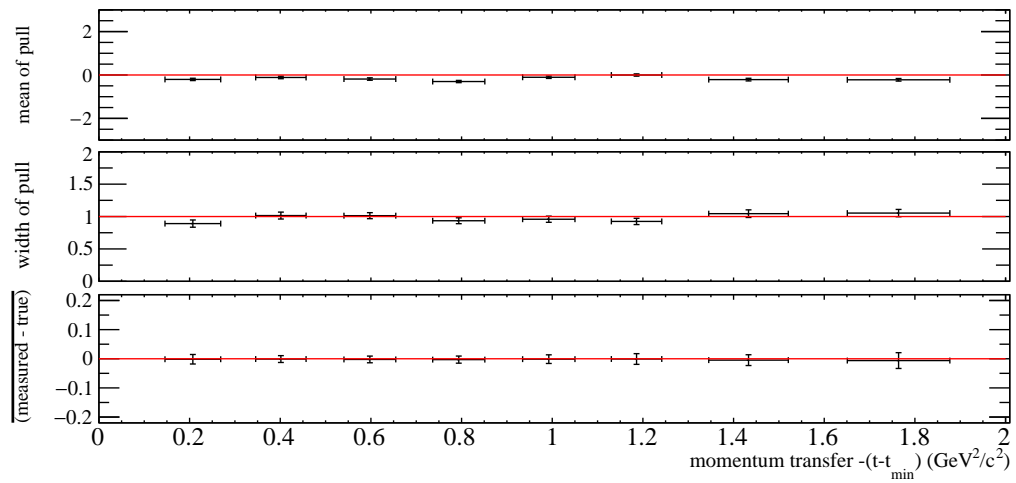


Figure C.42: Summarised results from study with full simulation without background for ρ_{11}^0 . True value = 0.26.

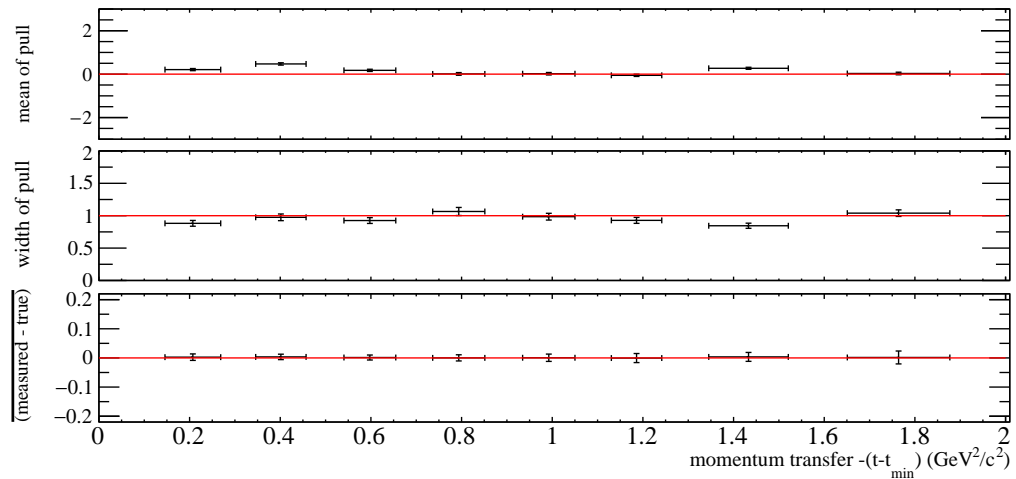


Figure C.43: Summarised results from study with full simulation without background for ρ_{31}^0 . True value = -0.06.

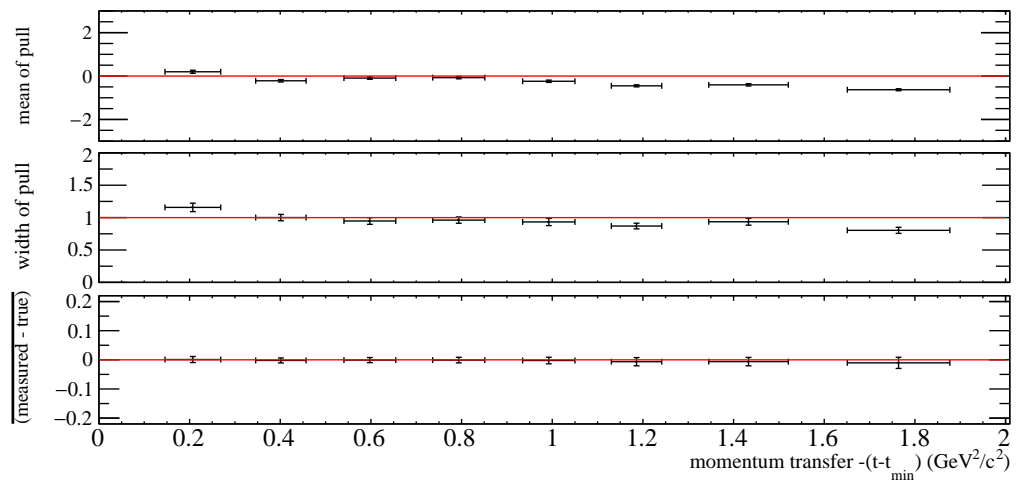


Figure C.44: Summarised results from study with full simulation without background for ρ_{3-1}^0 . True value = 0.23.

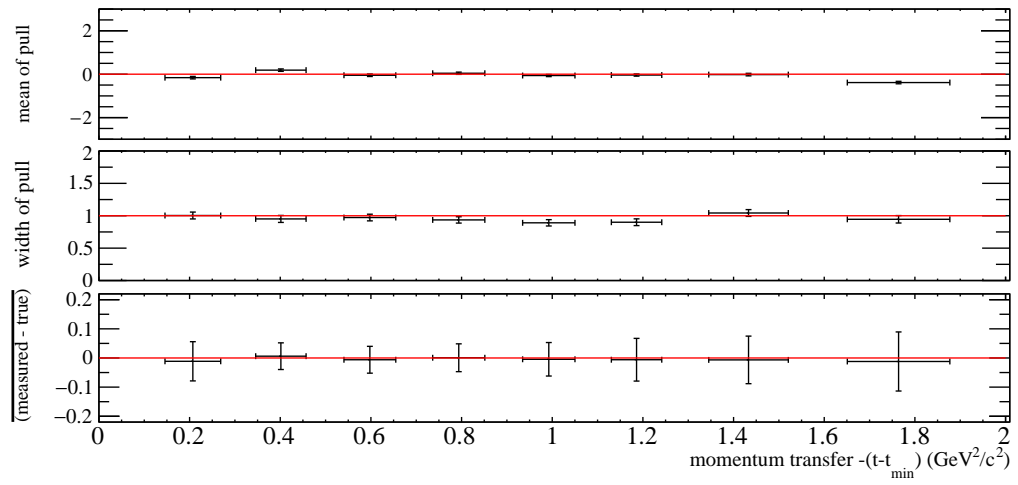


Figure C.45: Summarised results from study with full simulation without background for ρ_{11}^1 . True value = 0.2.

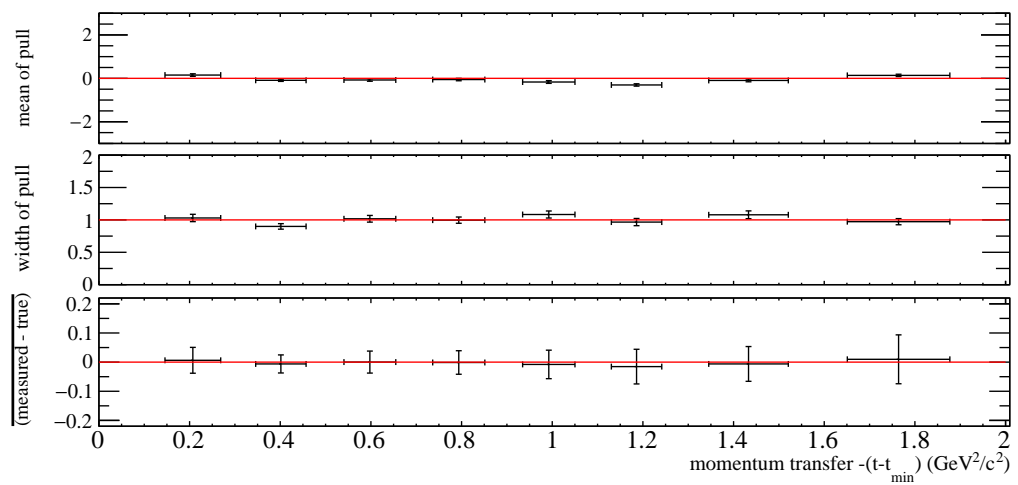


Figure C.46: Summarised results from study with full simulation without background for ρ_{33}^1 . True value = 0.1.

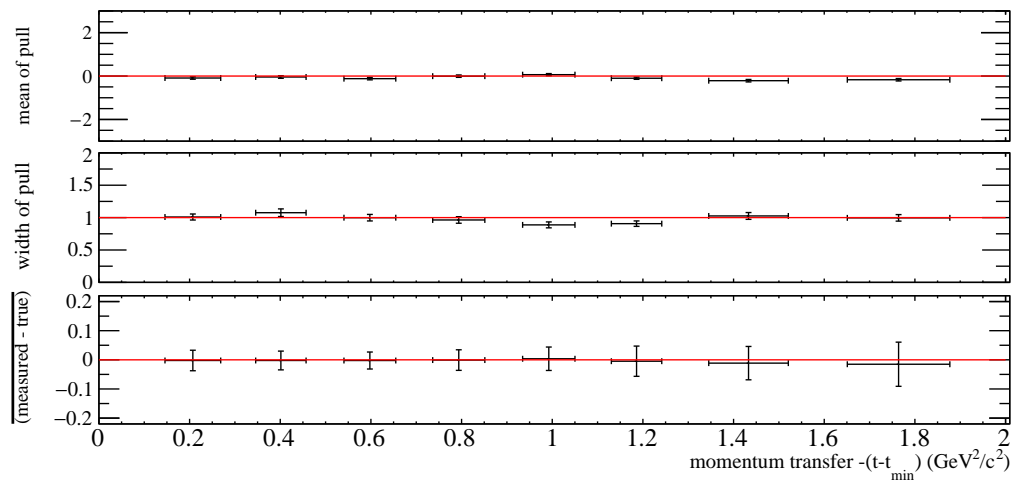


Figure C.47: Summarised results from study with full simulation without background for ρ_{31}^1 . True value = 0.04.

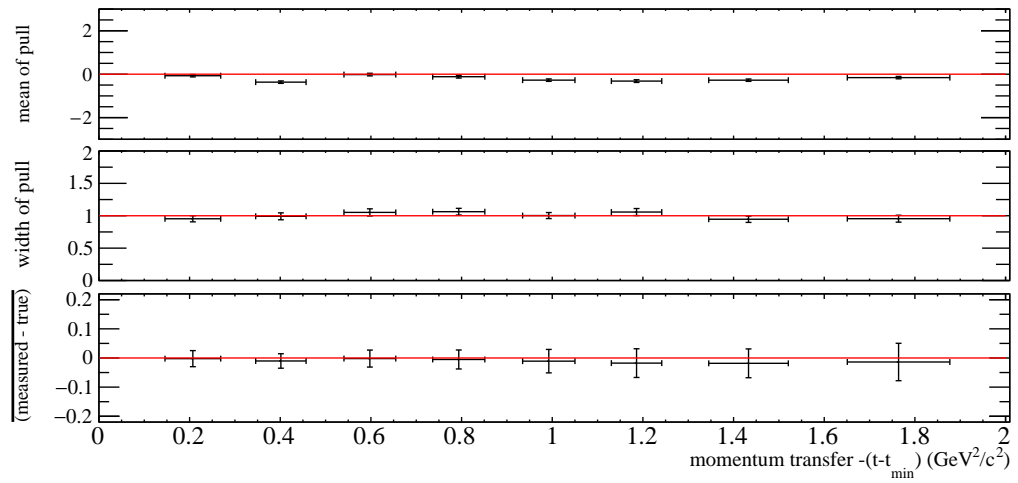


Figure C.48: Summarised results from study with full simulation without background for ρ_{3-1}^1 . True value = 0.2.

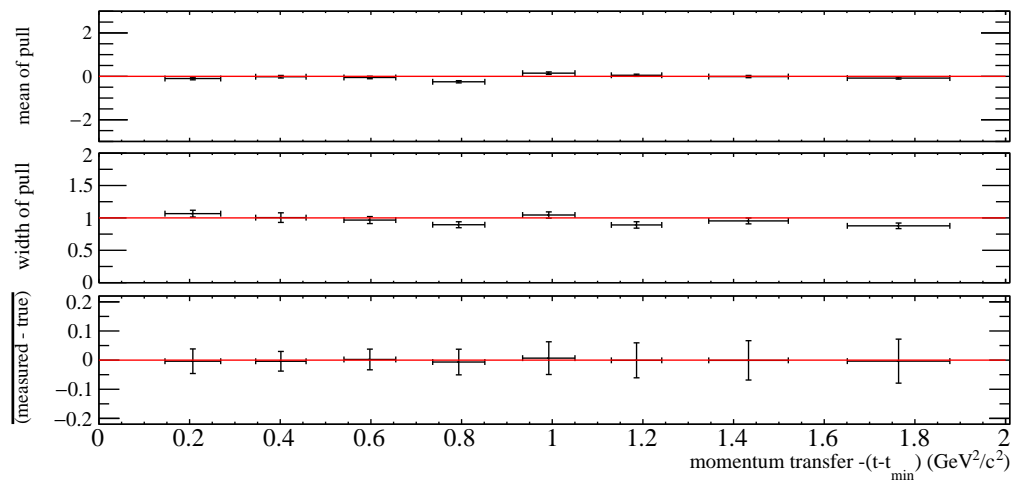


Figure C.49: Summarised results from study with full simulation without background for ρ_{31}^2 . True value = 0.04.

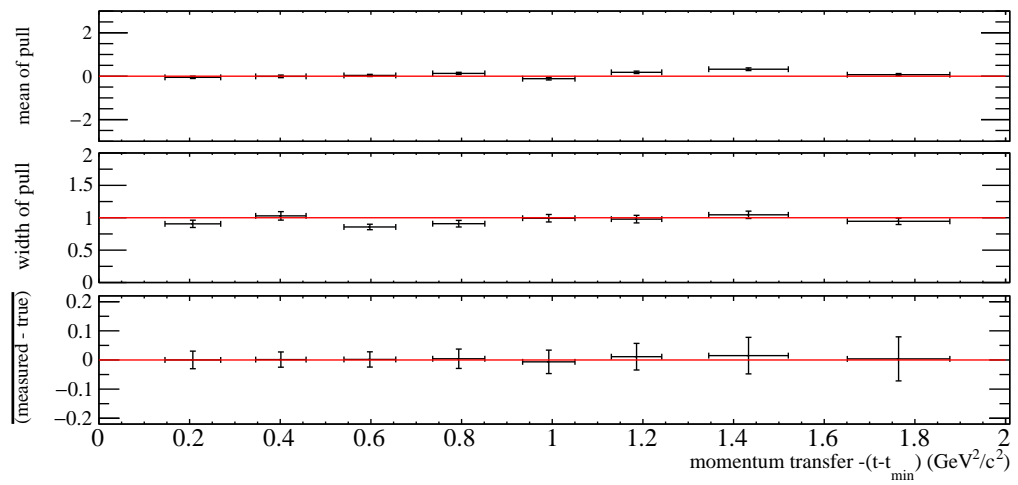


Figure C.50: Summarised results from study with full simulation without background for ρ_{3-1}^2 . True value = 0.01.

C.3.4 Analysis of full simulation with small amount of background and no sFit

As a last test the fits are repeated for the samples with the full hdgeant4 simulation with a small amount of background but without an sFit. This simulates the effect of residual background after the sWeights are applied. It tests the hypothesis that a small amount of residual background in the signal sample can cause the SDME fits to be bad. The means and widths as extracted from the pull distributions, and the absolute differences can be seen in Figures C.51 to C.59.

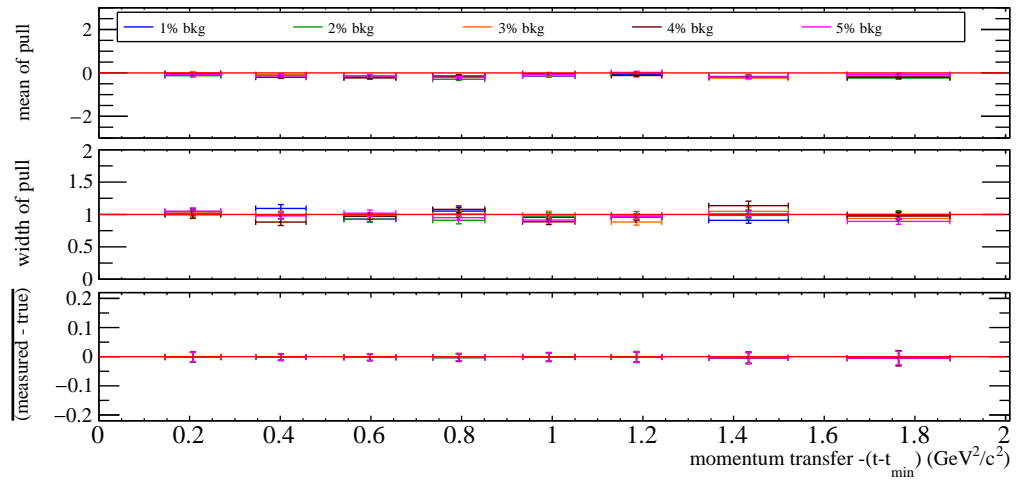


Figure C.51: Summarised results from study with full simulation with small background and no sFit for ρ_{11}^0 . True value = 0.26.

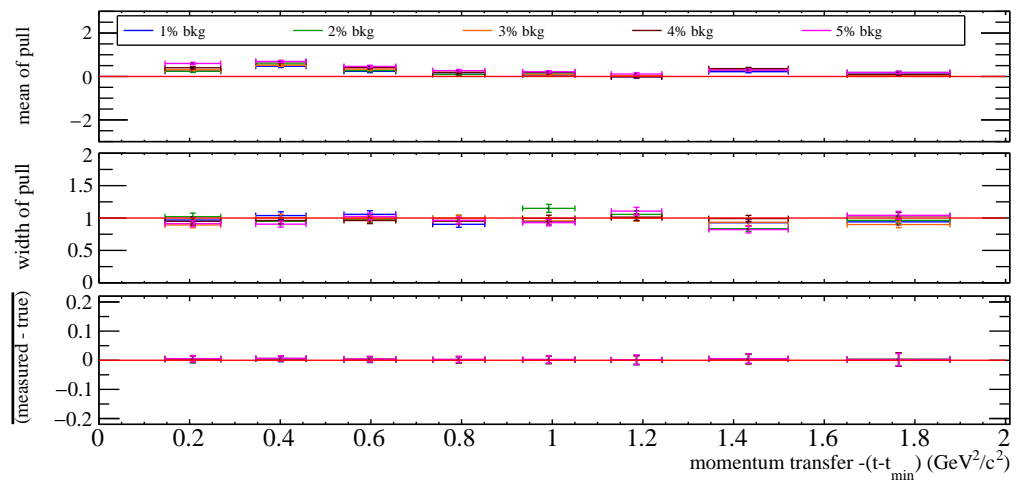


Figure C.52: Summarised results from study with full simulation with small background and no sFit for ρ_{31}^0 . True value = -0.06.

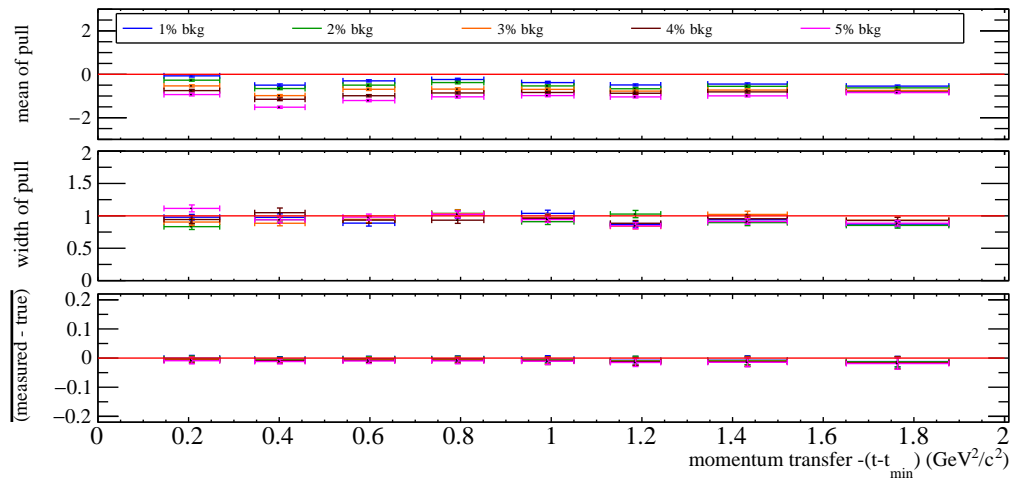


Figure C.53: Summarised results from study with full simulation with small background and no sFit for ρ_{3-1}^0 . True value = 0.23.

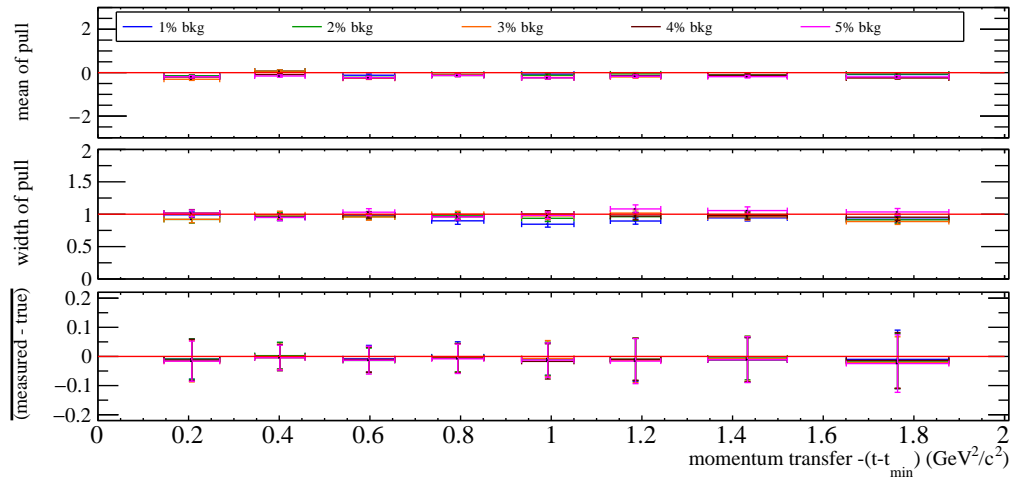


Figure C.54: Summarised results from study with full simulation with small background and no sFit for ρ_{11}^1 . True value = 0.2.

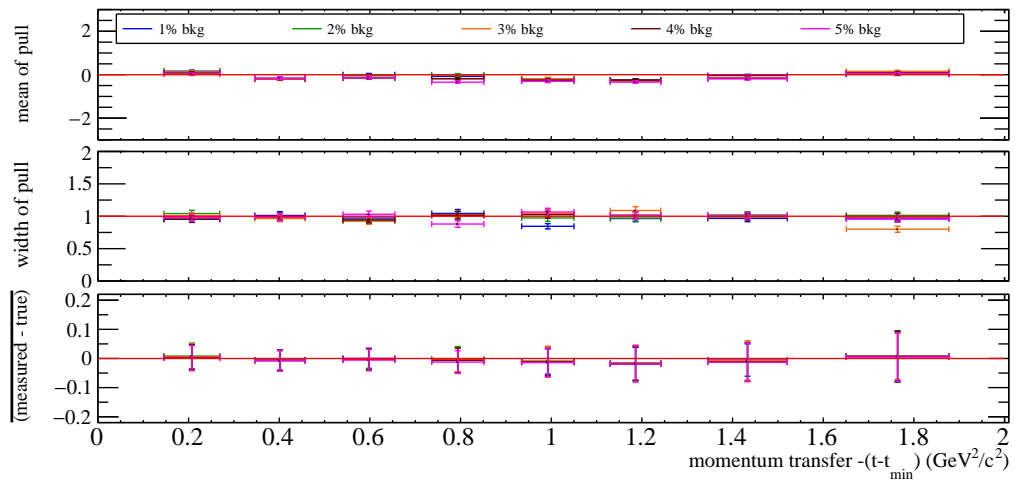


Figure C.55: Summarised results from study with full simulation with small background and no sFit for ρ_{33}^1 . True value = 0.1.

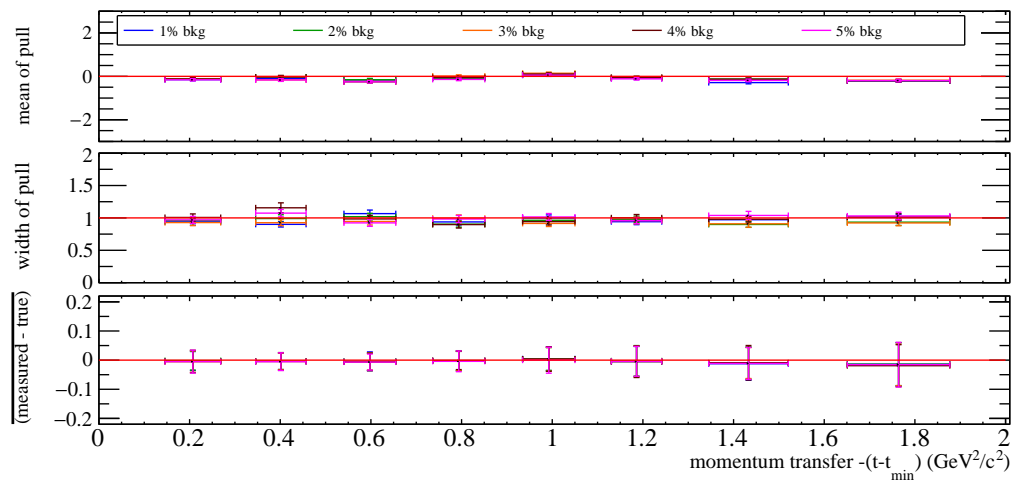


Figure C.56: Summarised results from study with full simulation with small background and no sFit for ρ_{31}^1 . True value = 0.04.

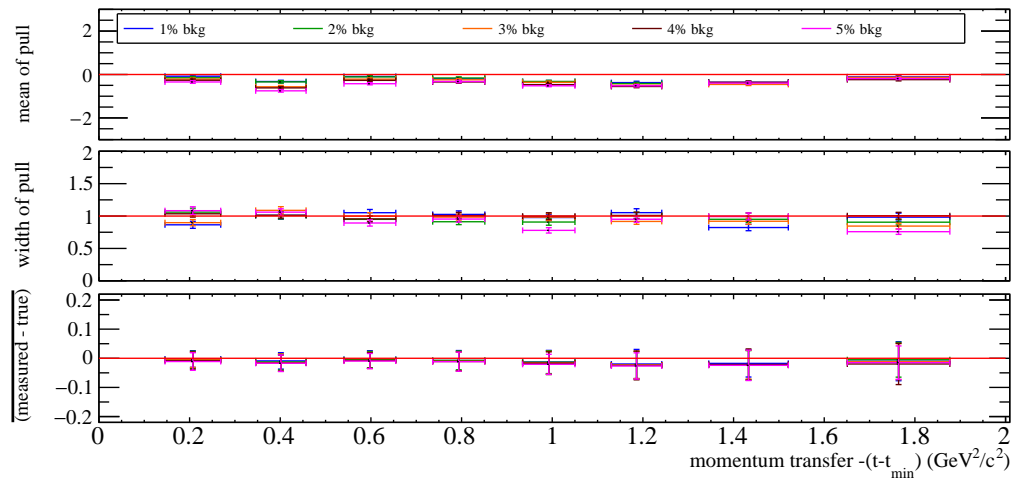


Figure C.57: Summarised results from study with full simulation with small background and no sFit for ρ_{3-1}^1 . True value = 0.2.

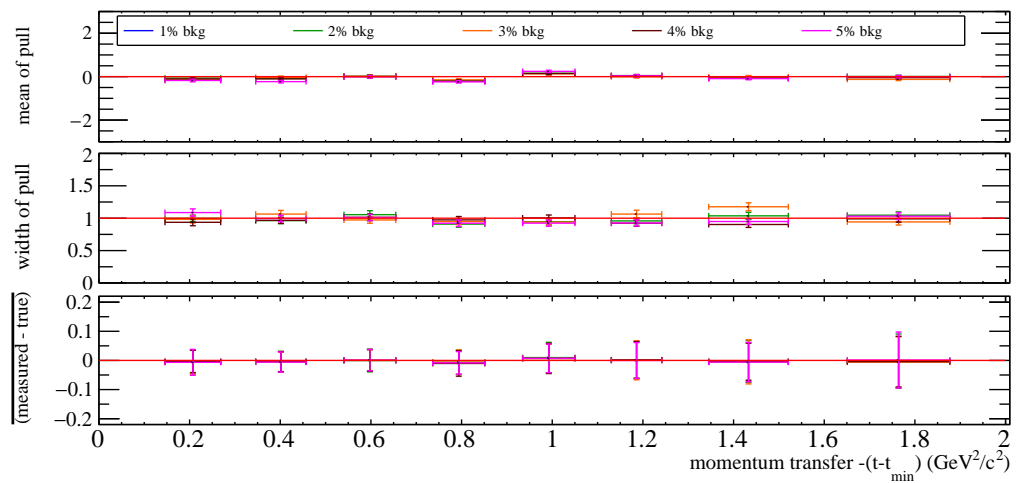


Figure C.58: Summarised results from study with full simulation with small background and no sFit for ρ_{31}^2 . True value = 0.04.

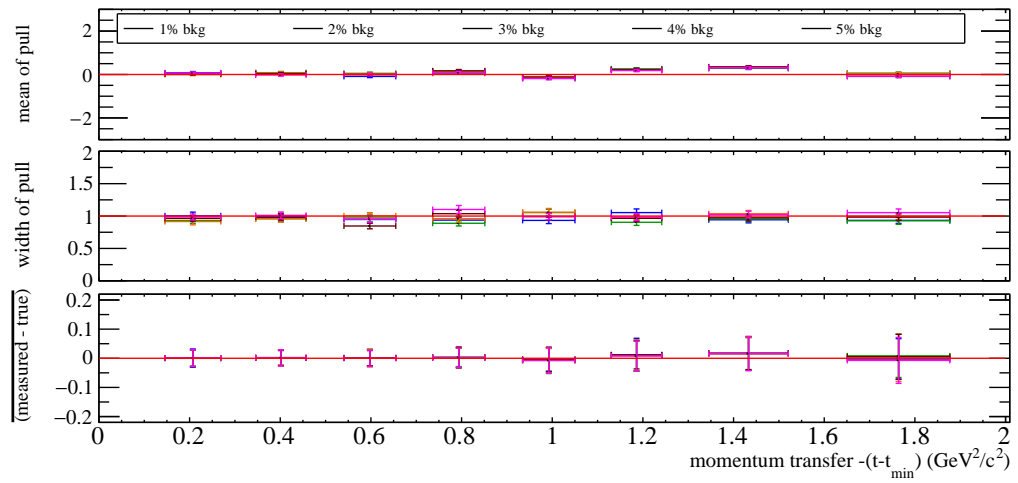


Figure C.59: Summarised results from study with full simulation with small background and no sFit for ρ_{3-1}^2 . True value = 0.01.

C.4 Event selection studies spin-density matrix elements

Figures C.60 to C.75 were created as part of the studies performed in Section 6.2.5 (see also Table 6.1).

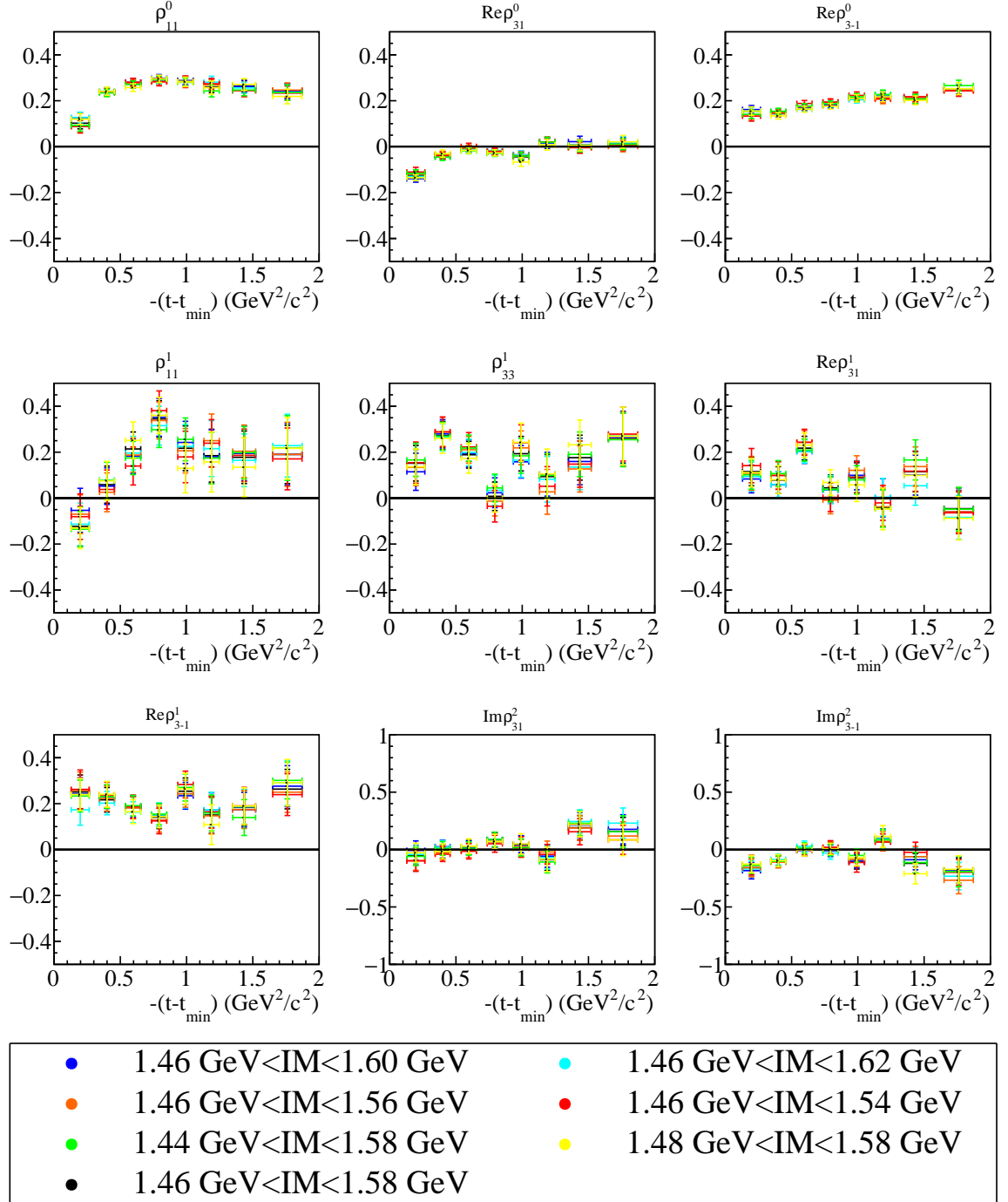


Figure C.60: Results for the SDMEs for the baseline setting (black points) and six variations (see Table 6.1 setups 1-6).

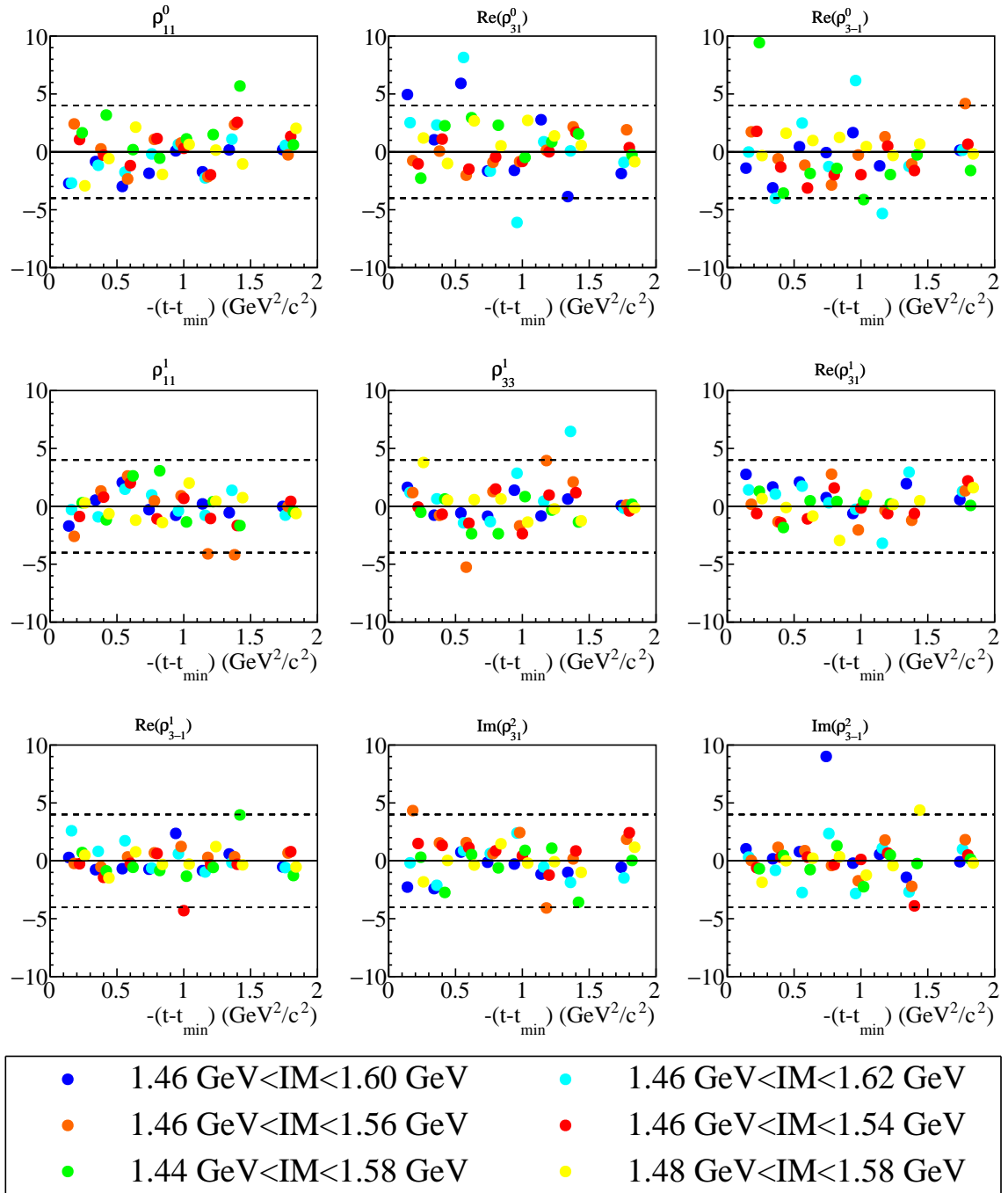


Figure C.61: The significance as defined in the Barlow test is plotted for six invariant mass cut variations (see Table 6.1 setups 1-6).

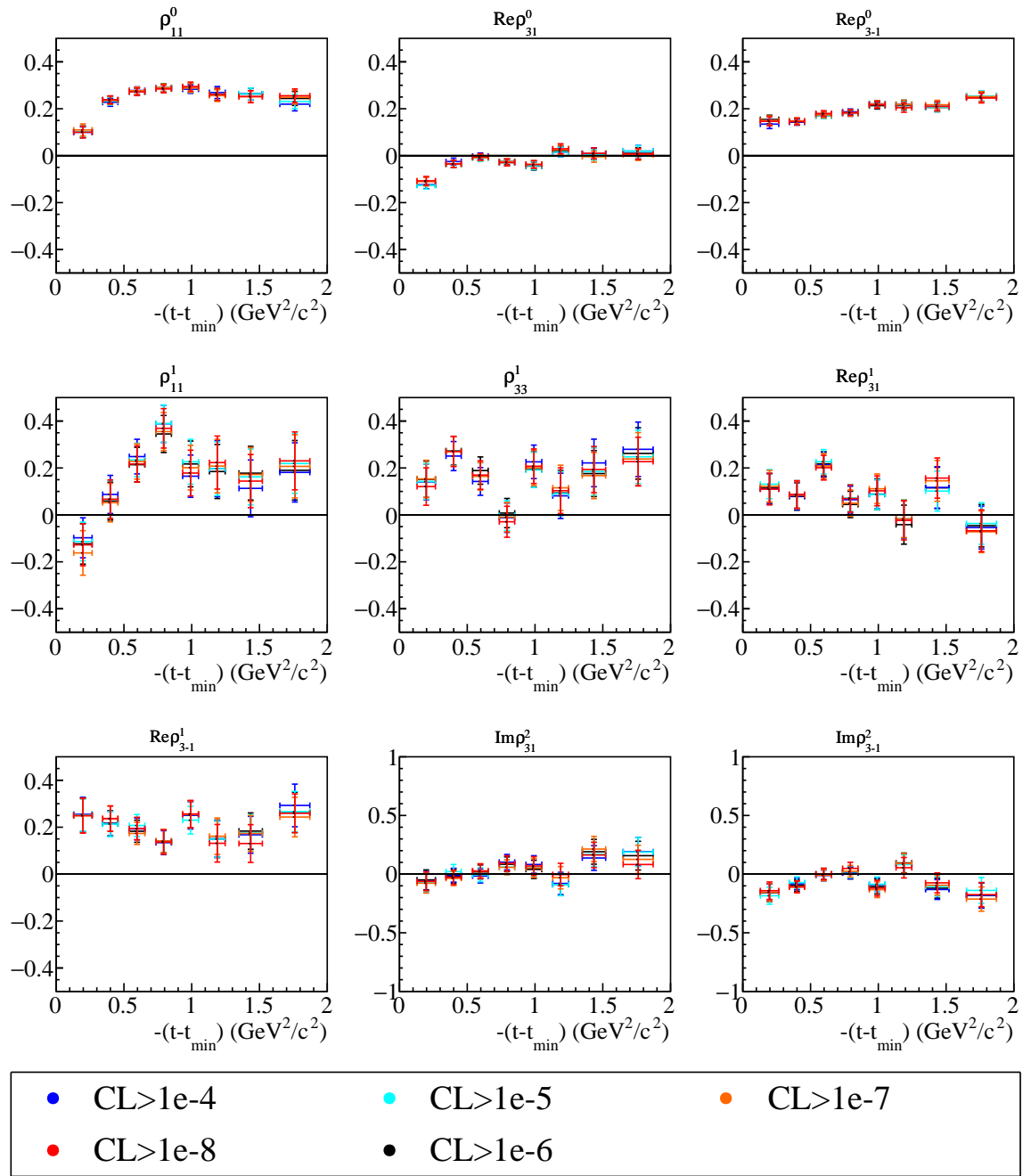


Figure C.62: Results for the SDMEs for the baseline setting (black points) and four variations (see Table 6.1 setups 7-10).

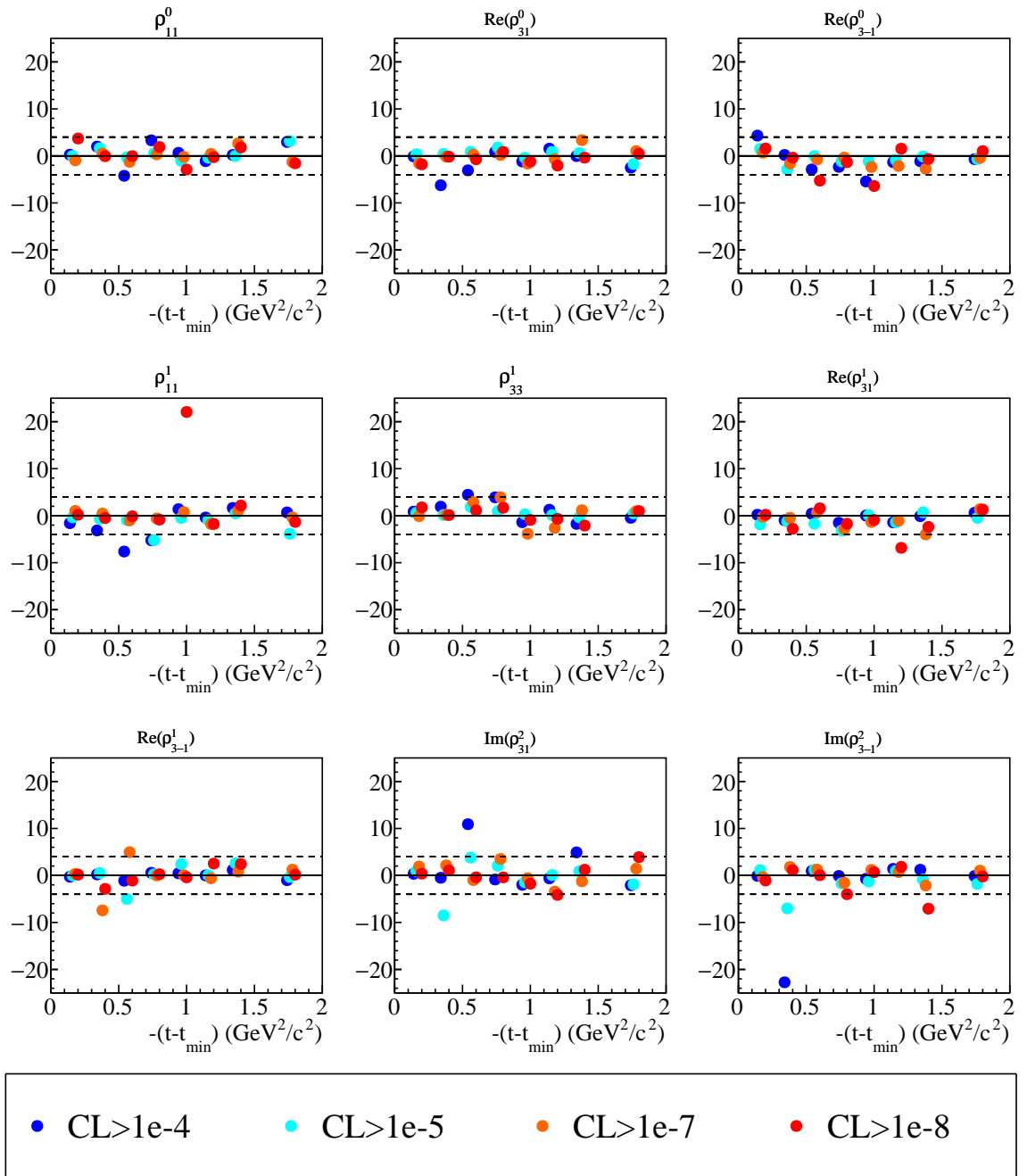


Figure C.63: The significance as defined in the Barlow test is plotted for four CL cut variations (see Table 6.1 setups 7-10).

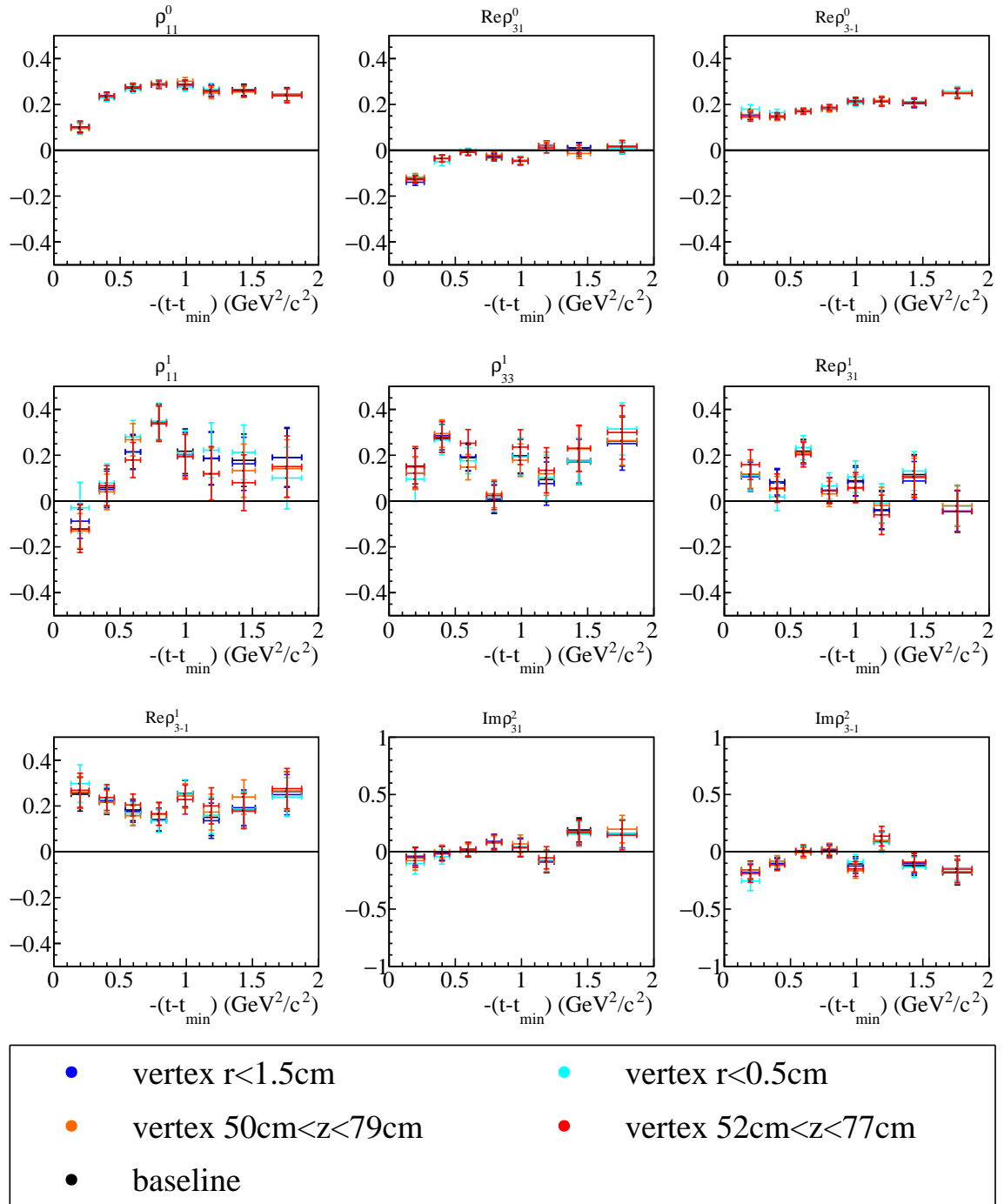


Figure C.64: Results for the SDMEs for the baseline setting (black points) and four variations (see Table 6.1 setups 11-14).

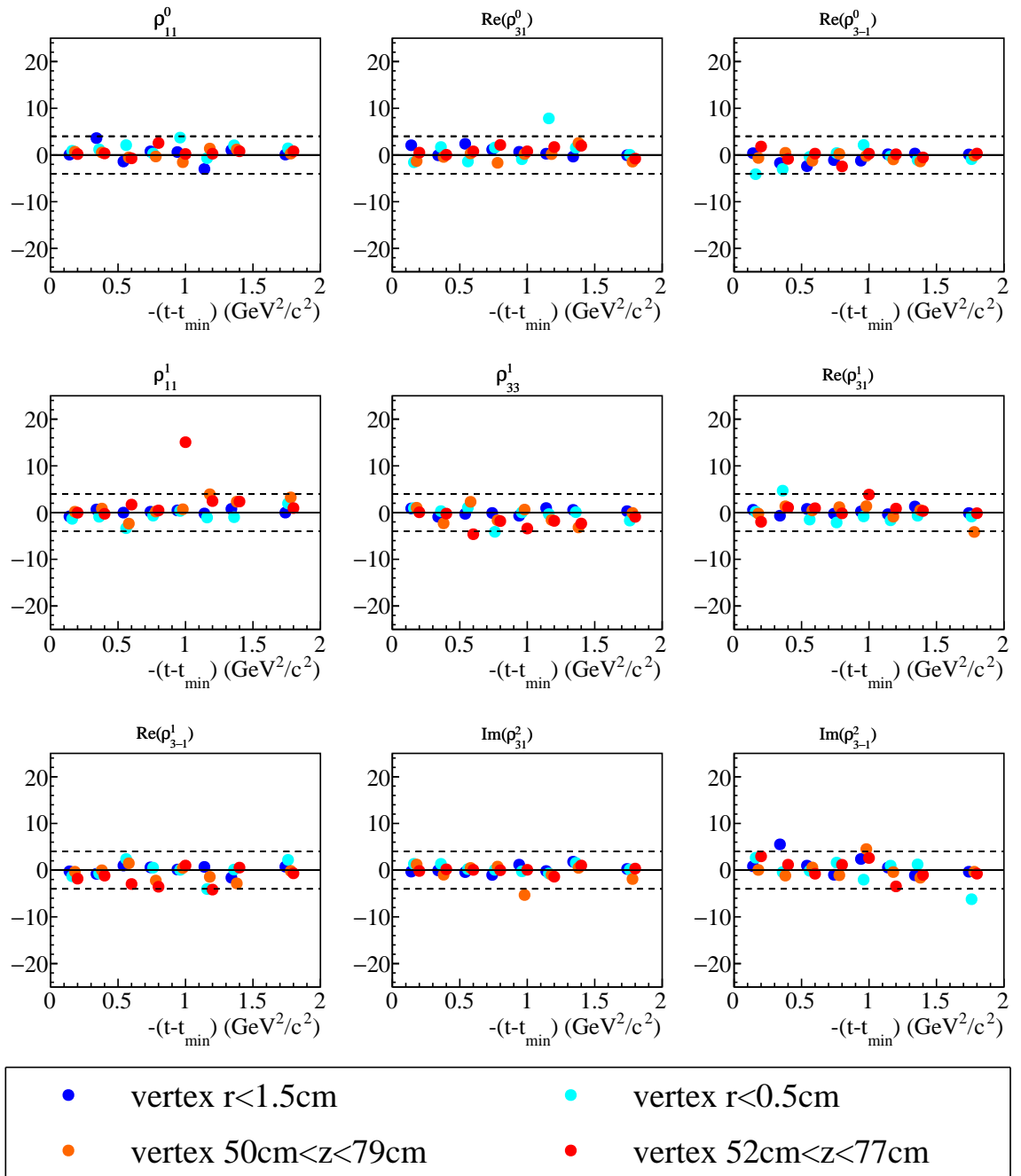


Figure C.65: The significance as defined in the Barlow test is plotted for four vertex cut variations (see Table 6.1 setups 11-14).

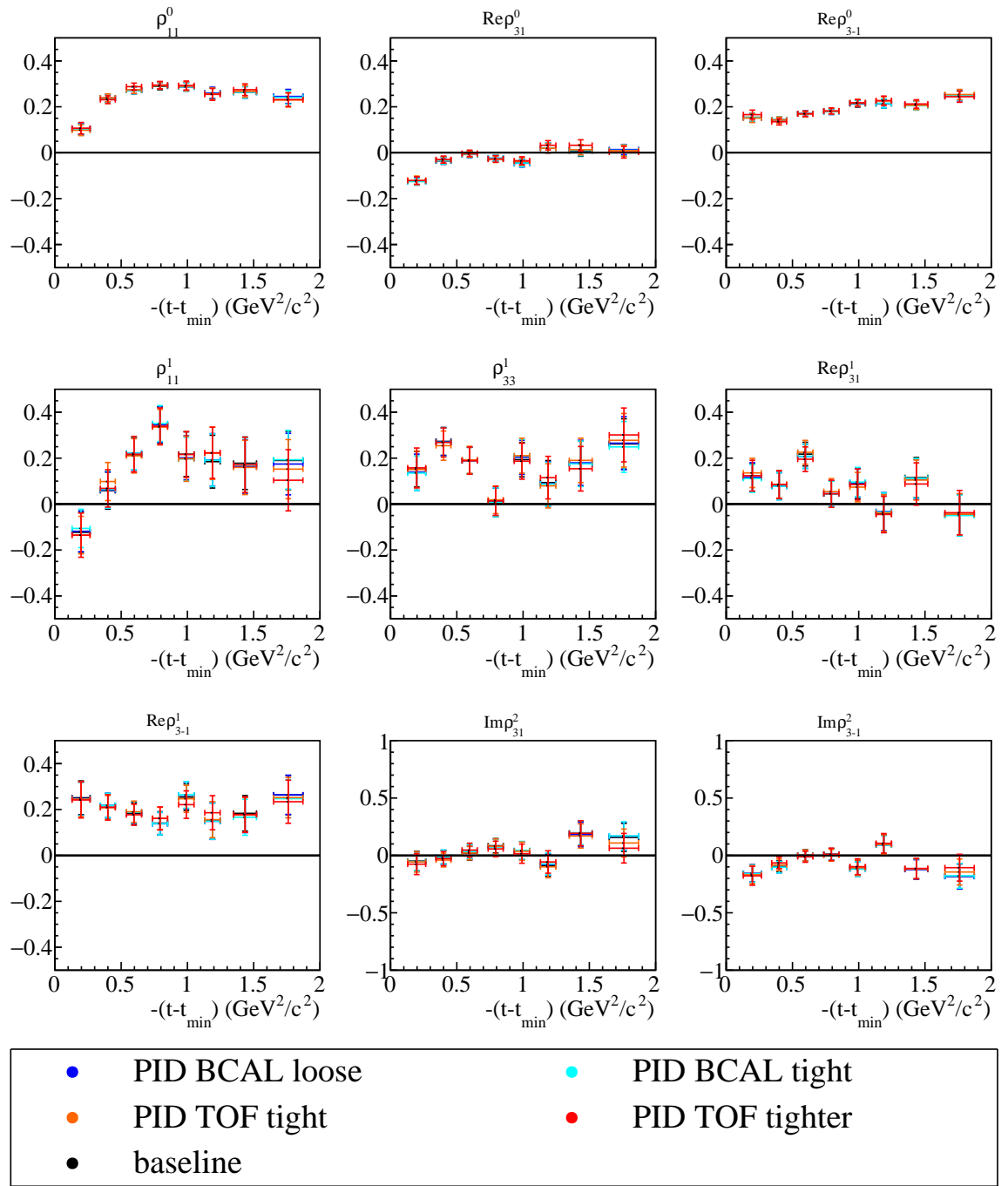


Figure C.66: Results for the SDMEs for the baseline setting (black points) and four variations of K^+ PID cuts (see Table 6.1 setups 15-18).

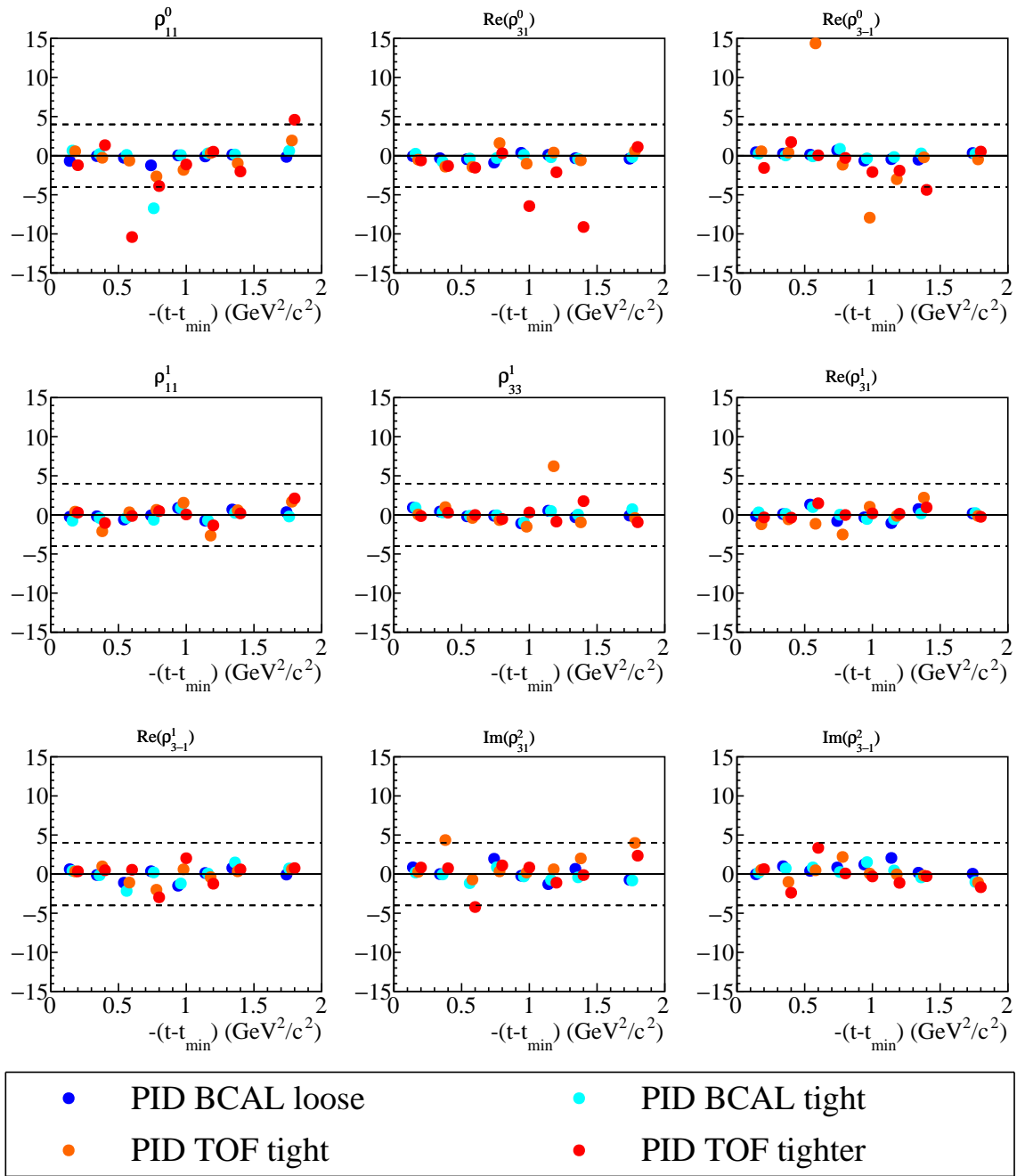


Figure C.67: The significance as defined in the Barlow test is plotted for four variations of K^+ PID cuts (see Table 6.1 setups 15-18).

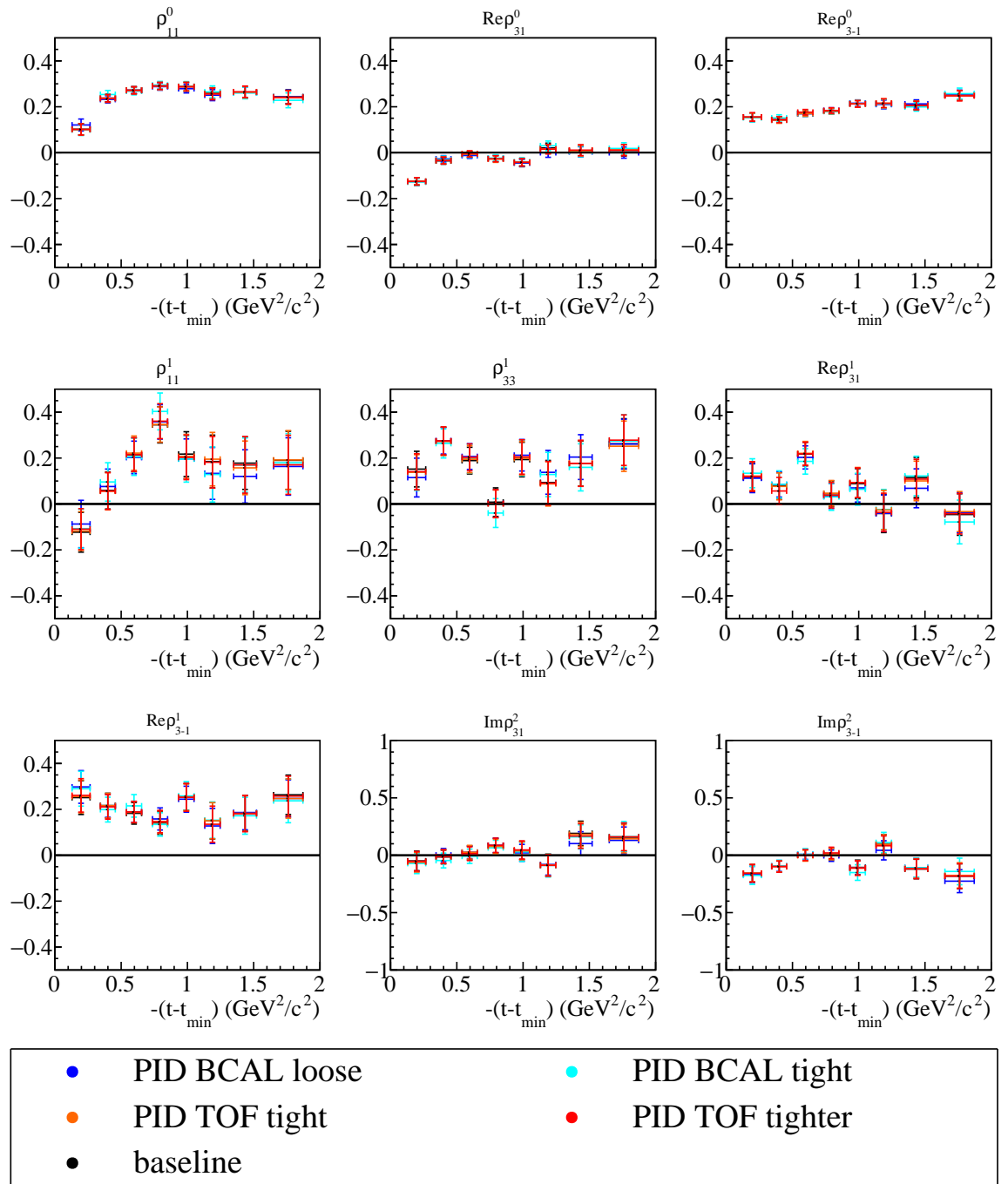


Figure C.68: Results for the SDMEs for the baseline setting (black points) and four variations of K^- PID cuts (see Table 6.1 setups 19-22).

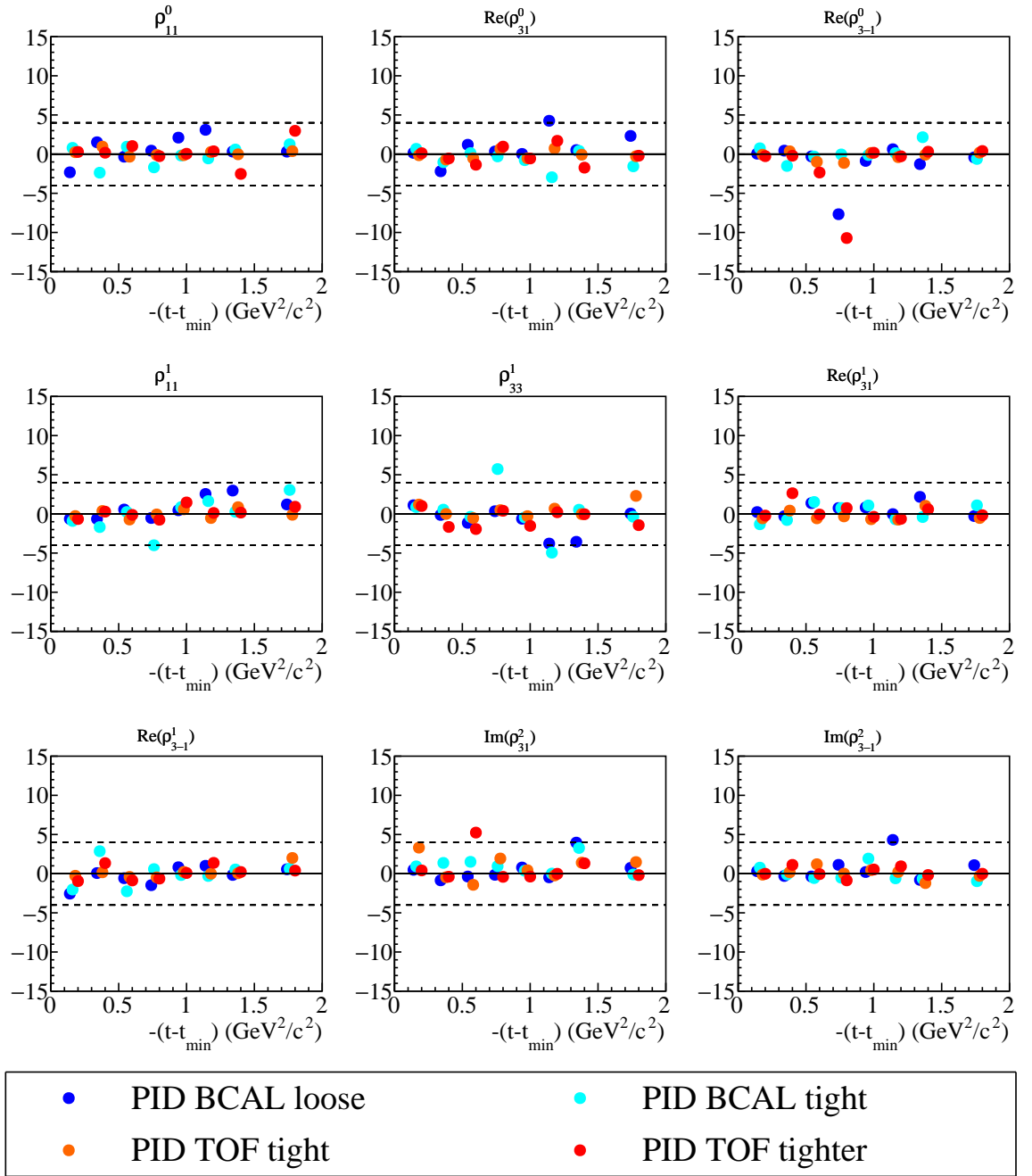


Figure C.69: The significance as defined in the Barlow test is plotted for four variations of K^- PID cuts (see Table 6.1 setups 19-22).

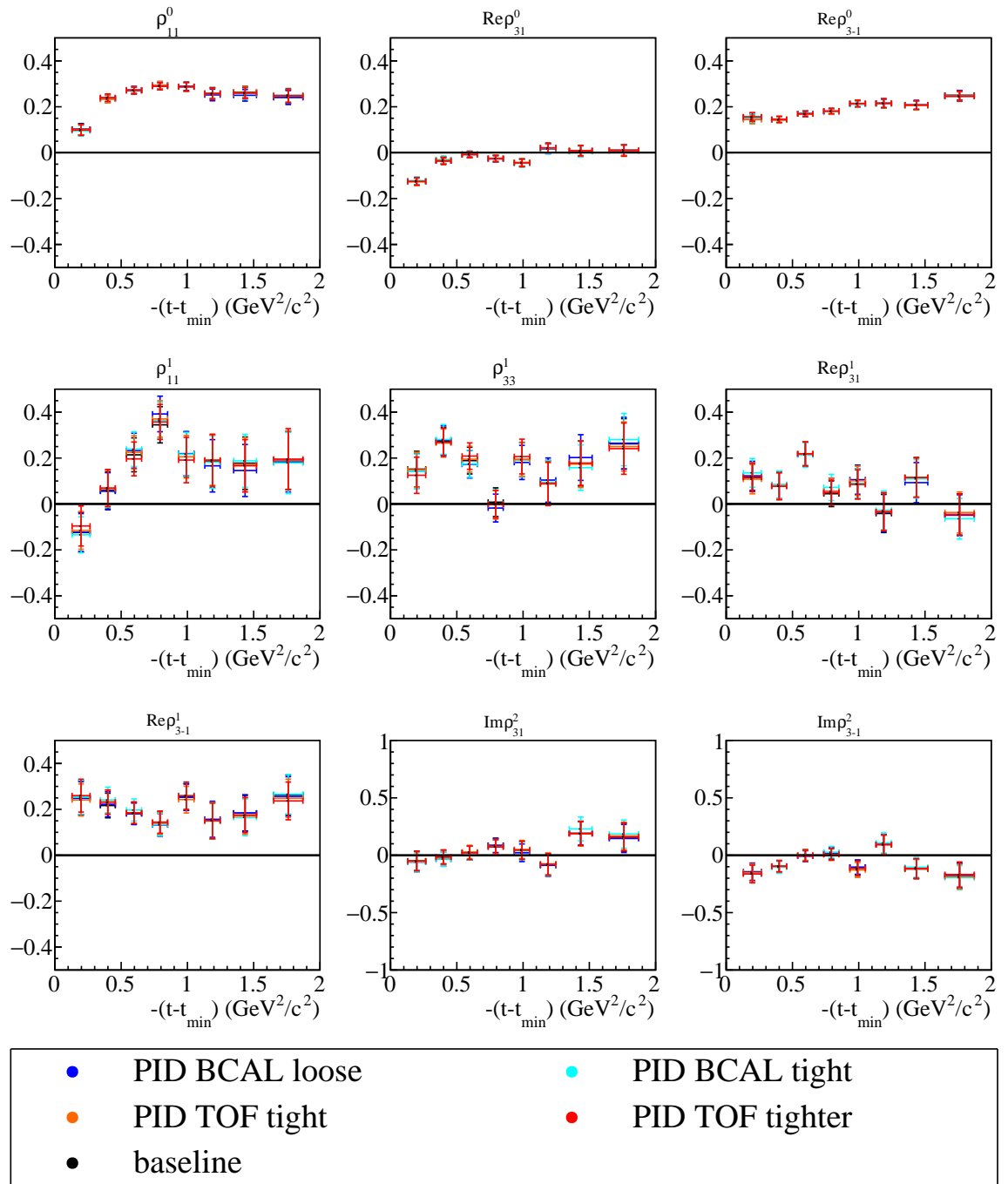


Figure C.70: Results for the SDMEs for the baseline setting (black points) and four variations of p PID cuts (see Table 6.1 setups 23-26).

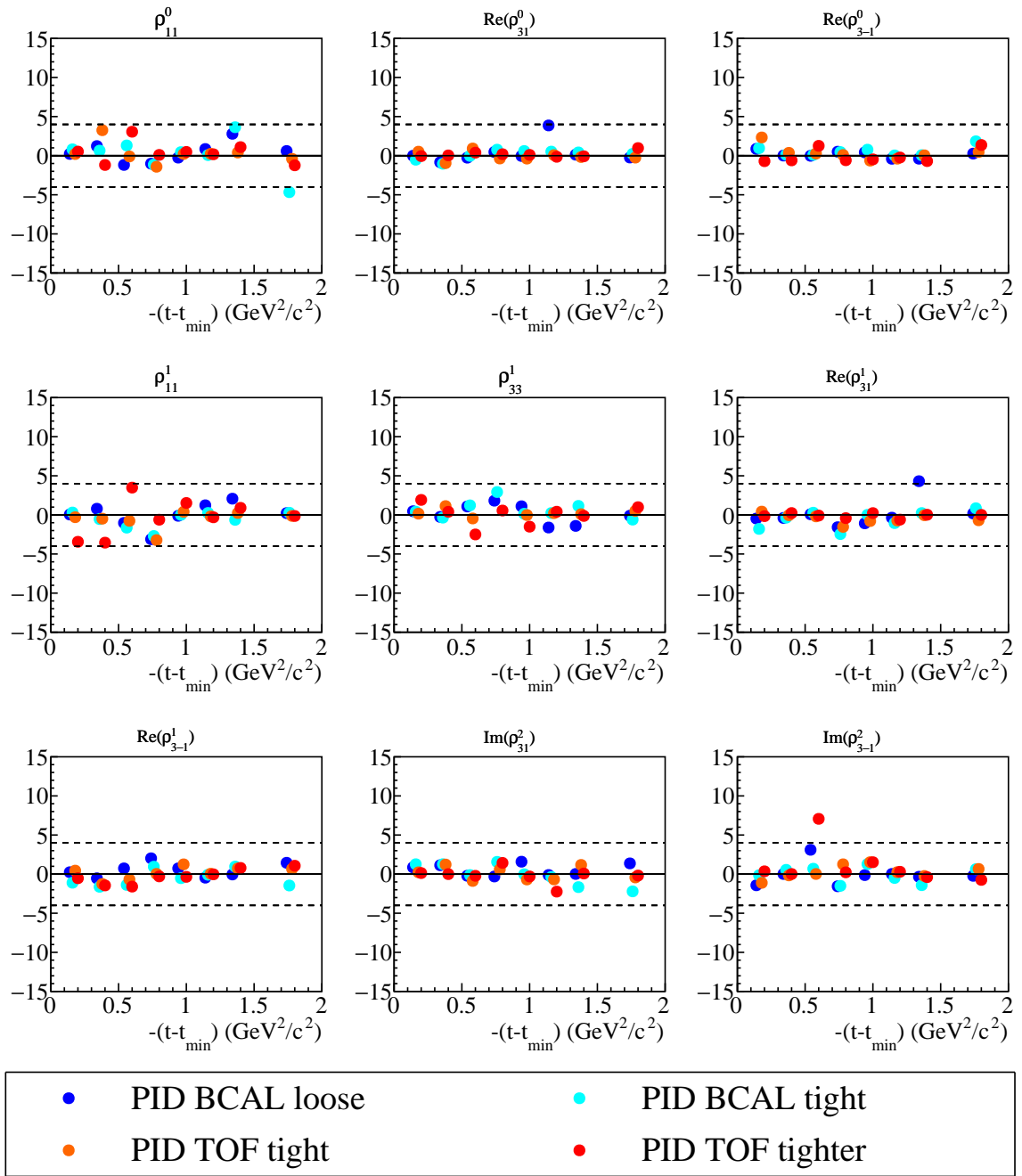


Figure C.71: The significance as defined in the Barlow test is plotted for four variations of p PID cuts (see Table 6.1 setups 23-26).

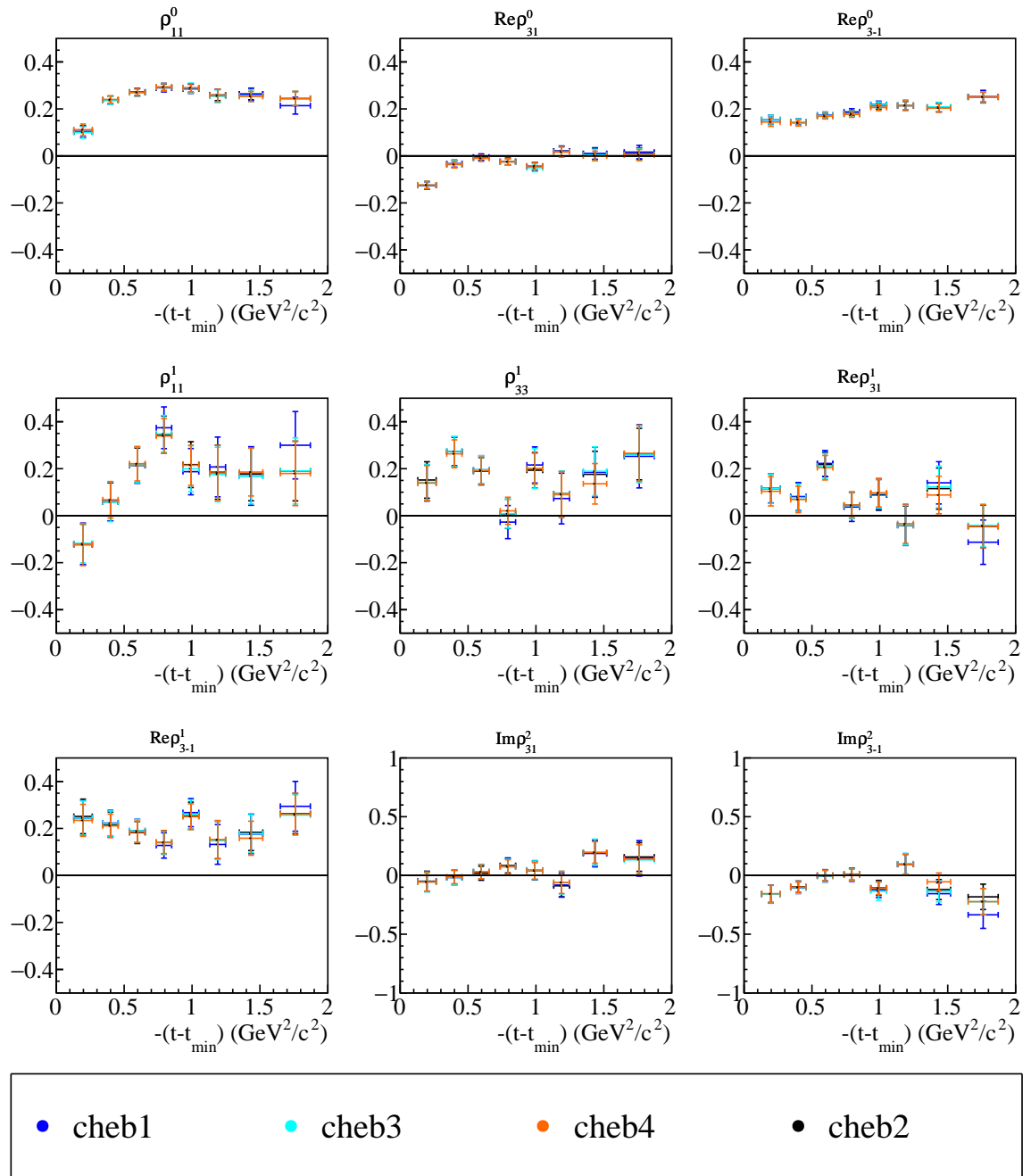


Figure C.72: Results for the SDMEs for the baseline setting (black points) and three variations of background shape.

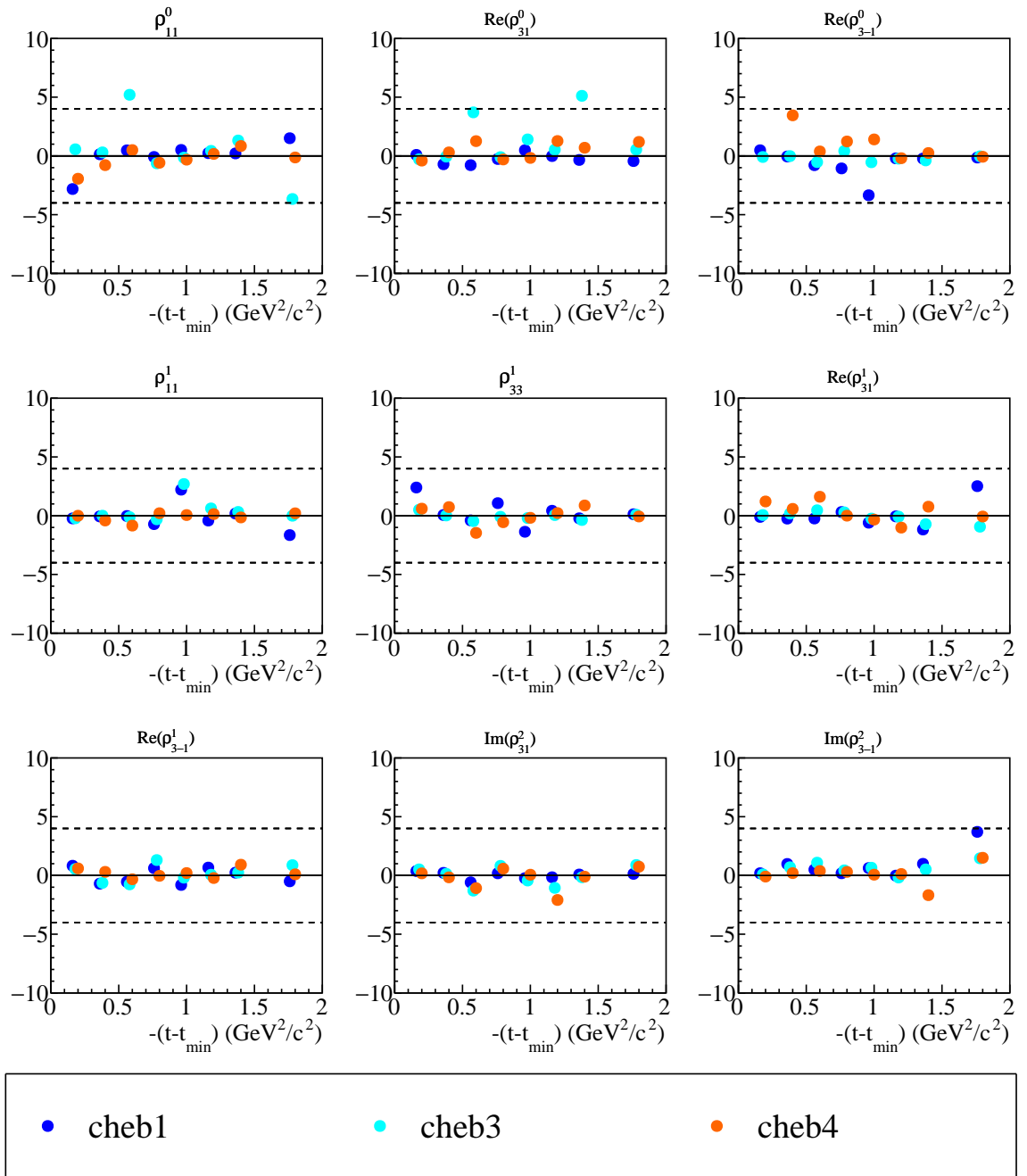


Figure C.73: The significance as defined in the Barlow test is plotted for three different variations of the background shape.

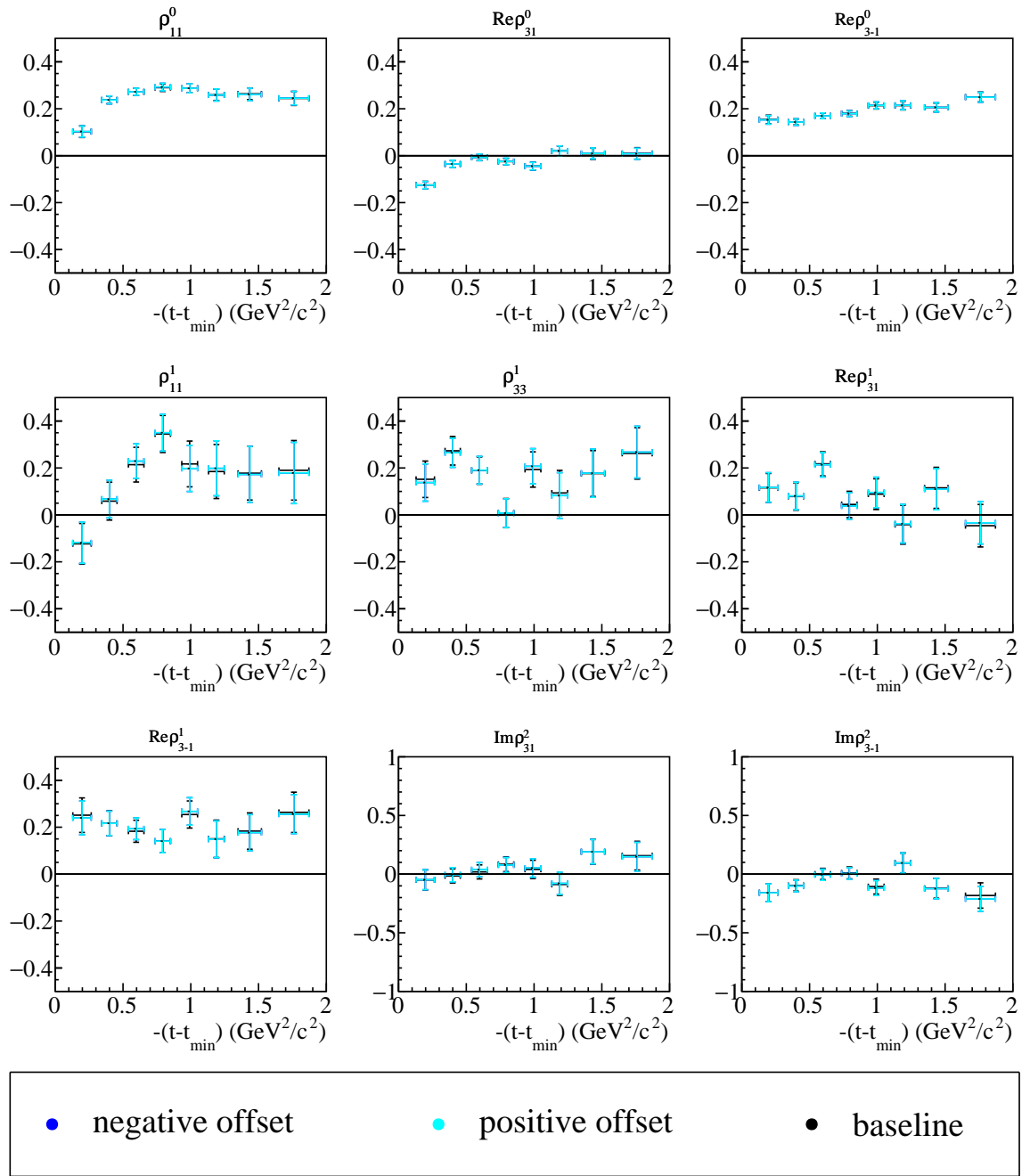


Figure C.74: Results for the SDMEs for the baseline setting (black points) and two variations of the polarisation plane angle.

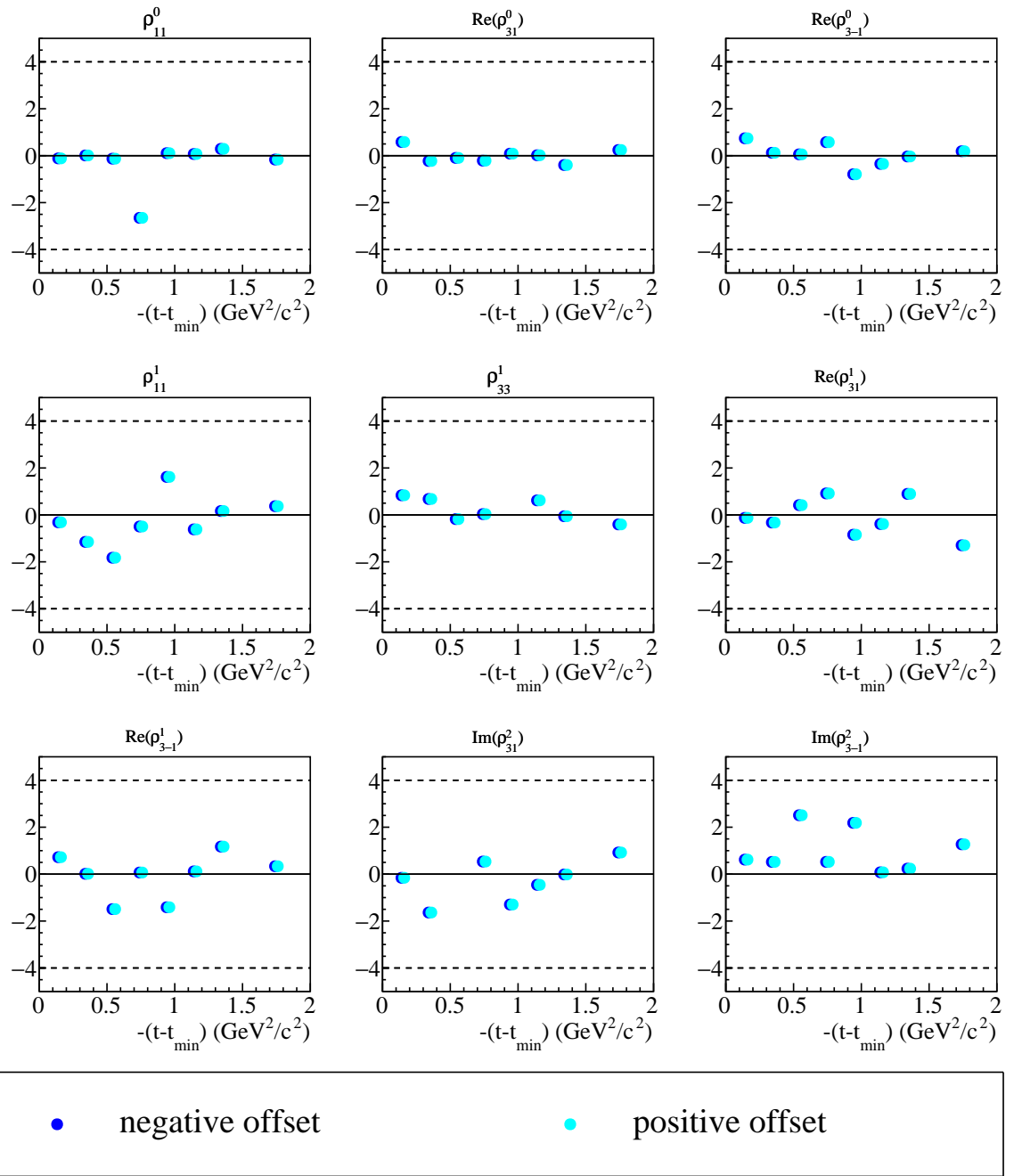


Figure C.75: The significance as defined in the Barlow test is plotted for two variations of the polarisation plane angle.

Appendix D

Numerical results

In the following all numerical values of the final results obtained in this work are listed for reference.

Beam asymmetry from direct fit

| $-(t - t_{\min})$ in GeV^2/c^2 | Σ | stat. uncertainty | sys. uncertainty |
|---|----------|-------------------|------------------|
| 0.197 ± 0.069 | 0.251 | 0.120 | 0.022 |
| 0.400 ± 0.056 | 0.729 | 0.095 | 0.032 |
| 0.597 ± 0.057 | 0.781 | 0.093 | 0.034 |
| 0.793 ± 0.057 | 0.648 | 0.100 | 0.030 |
| 0.992 ± 0.058 | 0.852 | 0.126 | 0.036 |
| 1.189 ± 0.058 | 0.584 | 0.162 | 0.029 |
| 1.435 ± 0.086 | 0.725 | 0.164 | 0.032 |
| 1.761 ± 0.111 | 0.909 | 0.188 | 0.038 |

Table D.1: Final results for beam asymmetry Σ extracted via an unbinned maximum likelihood fit.

Spin-density matrix elements

| $-(t - t_{\min})$ in GeV^2/c^2 | ρ_{11}^0 | stat. uncertainty | sys. uncertainty |
|---|---------------|-------------------|------------------|
| 0.197 ± 0.069 | 0.102 | 0.025 | 0.02 |
| 0.400 ± 0.056 | 0.238 | 0.016 | 0.02 |
| 0.597 ± 0.057 | 0.272 | 0.015 | 0.02 |
| 0.793 ± 0.057 | 0.290 | 0.016 | 0.02 |
| 0.992 ± 0.058 | 0.288 | 0.019 | 0.02 |
| 1.189 ± 0.058 | 0.259 | 0.024 | 0.02 |
| 1.435 ± 0.086 | 0.264 | 0.025 | 0.02 |
| 1.761 ± 0.111 | 0.244 | 0.030 | 0.02 |

Table D.2: Final results for ρ_{11}^0 .

| $-(t - t_{\min})$ in GeV^2/c^2 | ρ_{31}^0 | stat. uncertainty | sys. uncertainty |
|---|---------------|-------------------|------------------|
| 0.197 ± 0.069 | -0.125 | 0.016 | 0.02 |
| 0.400 ± 0.056 | -0.036 | 0.015 | 0.02 |
| 0.597 ± 0.057 | -0.007 | 0.013 | 0.02 |
| 0.793 ± 0.057 | -0.025 | 0.013 | 0.02 |
| 0.992 ± 0.058 | -0.044 | 0.017 | 0.02 |
| 1.189 ± 0.058 | 0.021 | 0.021 | 0.02 |
| 1.435 ± 0.086 | 0.008 | 0.024 | 0.02 |
| 1.761 ± 0.111 | 0.010 | 0.024 | 0.02 |

Table D.3: Final results for ρ_{31}^0 .

| $-(t - t_{\min})$ in GeV^2/c^2 | ρ_{3-1}^0 | stat. uncertainty | sys. uncertainty |
|---|----------------|-------------------|------------------|
| 0.197 ± 0.069 | 0.154 | 0.018 | 0.02 |
| 0.400 ± 0.056 | 0.144 | 0.013 | 0.02 |
| 0.597 ± 0.057 | 0.170 | 0.012 | 0.02 |
| 0.793 ± 0.057 | 0.180 | 0.012 | 0.02 |
| 0.992 ± 0.058 | 0.213 | 0.014 | 0.02 |
| 1.189 ± 0.058 | 0.214 | 0.018 | 0.02 |
| 1.435 ± 0.086 | 0.206 | 0.019 | 0.02 |
| 1.761 ± 0.111 | 0.250 | 0.021 | 0.02 |

Table D.4: Final results for ρ_{3-1}^0 .

| $-(t - t_{\min})$ in GeV^2/c^2 | ρ_{11}^1 | stat. uncertainty | sys. uncertainty |
|---|---------------|-------------------|------------------|
| 0.197 ± 0.069 | -0.123 | 0.088 | 0.011 |
| 0.400 ± 0.056 | 0.059 | 0.081 | 0.010 |
| 0.597 ± 0.057 | 0.214 | 0.074 | 0.012 |
| 0.793 ± 0.057 | 0.345 | 0.079 | 0.016 |
| 0.992 ± 0.058 | 0.217 | 0.098 | 0.013 |
| 1.189 ± 0.058 | 0.185 | 0.115 | 0.012 |
| 1.435 ± 0.086 | 0.178 | 0.114 | 0.012 |
| 1.761 ± 0.111 | 0.190 | 0.127 | 0.012 |

Table D.5: Final results for ρ_{11}^1 .

| $-(t - t_{\min})$ in GeV^2/c^2 | ρ_{33}^1 | stat. uncertainty | sys. uncertainty |
|---|---------------|-------------------|------------------|
| 0.197 ± 0.069 | 0.152 | 0.078 | 0.011 |
| 0.400 ± 0.056 | 0.273 | 0.061 | 0.014 |
| 0.597 ± 0.057 | 0.189 | 0.058 | 0.012 |
| 0.793 ± 0.057 | 0.008 | 0.062 | 0.010 |
| 0.992 ± 0.058 | 0.193 | 0.075 | 0.012 |
| 1.189 ± 0.058 | 0.094 | 0.096 | 0.011 |
| 1.435 ± 0.086 | 0.176 | 0.098 | 0.012 |
| 1.761 ± 0.111 | 0.262 | 0.110 | 0.014 |

Table D.6: Final results for ρ_{33}^1 .

| $-(t - t_{\min})$ in GeV^2/c^2 | ρ_{31}^1 | stat. uncertainty | sys. uncertainty |
|---|---------------|-------------------|------------------|
| 0.197 ± 0.069 | 0.115 | 0.061 | 0.011 |
| 0.400 ± 0.056 | 0.078 | 0.059 | 0.010 |
| 0.597 ± 0.057 | 0.218 | 0.051 | 0.013 |
| 0.793 ± 0.057 | 0.045 | 0.056 | 0.010 |
| 0.992 ± 0.058 | 0.088 | 0.065 | 0.010 |
| 1.189 ± 0.058 | -0.041 | 0.083 | 0.010 |
| 1.435 ± 0.086 | 0.115 | 0.087 | 0.011 |
| 1.761 ± 0.111 | -0.046 | 0.090 | 0.010 |

Table D.7: Final results for ρ_{31}^1 .

| $-(t - t_{\min})$ in GeV^2/c^2 | ρ_{3-1}^1 | stat. uncertainty | sys. uncertainty |
|---|----------------|-------------------|------------------|
| 0.197 ± 0.069 | 0.251 | 0.074 | 0.013 |
| 0.400 ± 0.056 | 0.217 | 0.054 | 0.013 |
| 0.597 ± 0.057 | 0.183 | 0.047 | 0.012 |
| 0.793 ± 0.057 | 0.141 | 0.050 | 0.011 |
| 0.992 ± 0.058 | 0.254 | 0.058 | 0.013 |
| 1.189 ± 0.058 | 0.150 | 0.080 | 0.011 |
| 1.435 ± 0.086 | 0.183 | 0.077 | 0.012 |
| 1.761 ± 0.111 | 0.263 | 0.086 | 0.014 |

Table D.8: Final results for ρ_{3-1}^1 .

| $-(t - t_{\min})$ in GeV^2/c^2 | ρ_{31}^2 | stat. uncertainty | sys. uncertainty |
|---|---------------|-------------------|------------------|
| 0.197 ± 0.069 | -0.049 | 0.085 | 0.010 |
| 0.400 ± 0.056 | -0.015 | 0.060 | 0.010 |
| 0.597 ± 0.057 | 0.019 | 0.060 | 0.010 |
| 0.793 ± 0.057 | 0.084 | 0.063 | 0.010 |
| 0.992 ± 0.058 | 0.040 | 0.078 | 0.010 |
| 1.189 ± 0.058 | -0.088 | 0.094 | 0.010 |
| 1.435 ± 0.086 | 0.180 | 0.106 | 0.012 |
| 1.761 ± 0.111 | 0.157 | 0.122 | 0.011 |

Table D.9: Final results for ρ_{31}^2 .

| $-(t - t_{\min})$ in GeV^2/c^2 | ρ_{3-1}^2 | stat. uncertainty | sys. uncertainty |
|---|----------------|-------------------|------------------|
| 0.197 ± 0.069 | -0.158 | 0.076 | 0.011 |
| 0.400 ± 0.056 | -0.096 | 0.049 | 0.011 |
| 0.597 ± 0.057 | -0.001 | 0.048 | 0.010 |
| 0.793 ± 0.057 | 0.011 | 0.051 | 0.010 |
| 0.992 ± 0.058 | -0.106 | 0.064 | 0.011 |
| 1.189 ± 0.058 | 0.095 | 0.084 | 0.011 |
| 1.435 ± 0.086 | -0.120 | 0.085 | 0.011 |
| 1.761 ± 0.111 | -0.182 | 0.108 | 0.012 |

Table D.10: Final results for ρ_{3-1}^2 .

| $-(t - t_{\min})$ in GeV^2/c^2 | $2(\rho_{11}^1 + \rho_{33}^1)$ | stat. uncertainty | sys. uncertainty |
|---|--------------------------------|-------------------|------------------|
| 0.197 ± 0.069 | 0.057 | 0.138 | 0.020 |
| 0.400 ± 0.056 | 0.664 | 0.107 | 0.031 |
| 0.597 ± 0.057 | 0.806 | 0.098 | 0.035 |
| 0.793 ± 0.057 | 0.706 | 0.107 | 0.032 |
| 0.992 ± 0.058 | 0.821 | 0.131 | 0.035 |
| 1.189 ± 0.058 | 0.557 | 0.168 | 0.028 |
| 1.435 ± 0.086 | 0.708 | 0.165 | 0.032 |
| 1.761 ± 0.111 | 0.904 | 0.193 | 0.037 |

Table D.11: Final results for $\Sigma = 2(\rho_{11}^1 + \rho_{33}^1)$.

| $-(t - t_{\min})$ in GeV^2/c^2 | $\frac{2}{N} (N_0 ^2 + N_1 ^2)$ | stat. uncertainty | sys. uncertainty |
|---|-----------------------------------|-------------------|------------------|
| 0.197 ± 0.069 | -0.021 | 0.081 | 0.030 |
| 0.400 ± 0.056 | 0.296 | 0.085 | 0.030 |
| 0.597 ± 0.057 | 0.486 | 0.077 | 0.031 |
| 0.793 ± 0.057 | 0.635 | 0.084 | 0.032 |
| 0.992 ± 0.058 | 0.505 | 0.102 | 0.031 |
| 1.189 ± 0.058 | 0.444 | 0.120 | 0.031 |
| 1.435 ± 0.086 | 0.441 | 0.123 | 0.031 |
| 1.761 ± 0.111 | 0.434 | 0.136 | 0.031 |

Table D.12: Final results for $\frac{2}{N} (|N_0|^2 + |N_1|^2)$.

| $-(t - t_{\min})$ in GeV^2/c^2 | $\frac{2}{N} (U_0 ^2 + U_1 ^2)$ | stat. uncertainty | sys. uncertainty |
|---|-----------------------------------|-------------------|------------------|
| 0.197 ± 0.069 | 0.225 | 0.099 | 0.030 |
| 0.400 ± 0.056 | 0.179 | 0.080 | 0.030 |
| 0.597 ± 0.057 | 0.058 | 0.074 | 0.031 |
| 0.793 ± 0.057 | -0.055 | 0.077 | 0.032 |
| 0.992 ± 0.058 | 0.070 | 0.097 | 0.031 |
| 1.189 ± 0.058 | 0.074 | 0.115 | 0.031 |
| 1.435 ± 0.086 | 0.086 | 0.111 | 0.031 |
| 1.761 ± 0.111 | 0.054 | 0.124 | 0.031 |

Table D.13: Final results for $\frac{2}{N} (|U_0|^2 + |U_1|^2)$.

| $-(t - t_{\min})$ in GeV^2/c^2 | $\frac{2}{N} (N_{-1} ^2 + N_2 ^2)$ | stat. uncertainty | sys. uncertainty |
|---|--------------------------------------|-------------------|------------------|
| 0.197 ± 0.069 | 0.550 | 0.087 | 0.030 |
| 0.400 ± 0.056 | 0.536 | 0.060 | 0.031 |
| 0.597 ± 0.057 | 0.417 | 0.058 | 0.031 |
| 0.793 ± 0.057 | 0.218 | 0.061 | 0.030 |
| 0.992 ± 0.058 | 0.406 | 0.075 | 0.031 |
| 1.189 ± 0.058 | 0.334 | 0.096 | 0.030 |
| 1.435 ± 0.086 | 0.412 | 0.095 | 0.031 |
| 1.761 ± 0.111 | 0.518 | 0.106 | 0.031 |

Table D.14: Final results for $\frac{2}{N} (|N_{-1}|^2 + |N_2|^2)$.

| $-(t - t_{\min})$ in GeV^2/c^2 | $\frac{2}{N} (U_{-1} ^2 + U_2 ^2)$ | stat. uncertainty | sys. uncertainty |
|---|--------------------------------------|-------------------|------------------|
| 0.197 ± 0.069 | 0.246 | 0.076 | 0.030 |
| 0.400 ± 0.056 | -0.011 | 0.066 | 0.031 |
| 0.597 ± 0.057 | 0.039 | 0.062 | 0.031 |
| 0.793 ± 0.057 | 0.202 | 0.068 | 0.030 |
| 0.992 ± 0.058 | 0.019 | 0.080 | 0.031 |
| 1.189 ± 0.058 | 0.147 | 0.102 | 0.030 |
| 1.435 ± 0.086 | 0.060 | 0.107 | 0.031 |
| 1.761 ± 0.111 | -0.006 | 0.121 | 0.031 |

Table D.15: Final results for $\frac{2}{N} (|U_{-1}|^2 + |U_2|^2)$.

| $-(t - t_{\min})$ in GeV^2/c^2 | $\frac{2}{N} \text{Re} (N_{-1}N_0^* - N_2N_1^*)$ | stat. uncertainty | sys. uncertainty |
|---|--|-------------------|------------------|
| 0.197 ± 0.069 | -0.010 | 0.060 | 0.030 |
| 0.400 ± 0.056 | 0.043 | 0.061 | 0.030 |
| 0.597 ± 0.057 | 0.210 | 0.057 | 0.031 |
| 0.793 ± 0.057 | 0.019 | 0.059 | 0.030 |
| 0.992 ± 0.058 | 0.044 | 0.070 | 0.030 |
| 1.189 ± 0.058 | -0.021 | 0.089 | 0.030 |
| 1.435 ± 0.086 | 0.124 | 0.092 | 0.030 |
| 1.761 ± 0.111 | -0.036 | 0.100 | 0.030 |

Table D.16: Final results for $\frac{2}{N} \text{Re} (N_{-1}N_0^* - N_2N_1^*)$.

| $-(t - t_{\min})$ in GeV^2/c^2 | $\frac{2}{N}\text{Re}(U_{-1}U_0^* - U_2U_1^*)$ | stat. uncertainty | sys. uncertainty |
|---|--|-------------------|------------------|
| 0.197 ± 0.069 | -0.240 | 0.065 | 0.030 |
| 0.400 ± 0.056 | -0.114 | 0.059 | 0.030 |
| 0.597 ± 0.057 | -0.225 | 0.050 | 0.031 |
| 0.793 ± 0.057 | -0.070 | 0.057 | 0.030 |
| 0.992 ± 0.058 | -0.133 | 0.065 | 0.030 |
| 1.189 ± 0.058 | 0.062 | 0.083 | 0.030 |
| 1.435 ± 0.086 | -0.107 | 0.089 | 0.030 |
| 1.761 ± 0.111 | 0.056 | 0.087 | 0.030 |

Table D.17: Final results for $\frac{2}{N}\text{Re}(U_{-1}U_0^* - U_2U_1^*)$.

| $-(t - t_{\min})$ in GeV^2/c^2 | $\frac{2}{N}\text{Re}(N_{-1}N_1^* + N_2N_0^*)$ | stat. uncertainty | sys. uncertainty |
|---|--|-------------------|------------------|
| 0.197 ± 0.069 | 0.405 | 0.077 | 0.031 |
| 0.400 ± 0.056 | 0.360 | 0.057 | 0.031 |
| 0.597 ± 0.057 | 0.353 | 0.051 | 0.031 |
| 0.793 ± 0.057 | 0.321 | 0.053 | 0.030 |
| 0.992 ± 0.058 | 0.467 | 0.062 | 0.031 |
| 1.189 ± 0.058 | 0.364 | 0.084 | 0.030 |
| 1.435 ± 0.086 | 0.389 | 0.082 | 0.031 |
| 1.761 ± 0.111 | 0.513 | 0.095 | 0.031 |

Table D.18: Final results for $\frac{2}{N}\text{Re}(N_{-1}N_1^* + N_2N_0^*)$.

| $-(t - t_{\min})$ in GeV^2/c^2 | $\frac{2}{N}\text{Re}(U_{-1}U_1^* + U_2U_0^*)$ | stat. uncertainty | sys. uncertainty |
|---|--|-------------------|------------------|
| 0.197 ± 0.069 | -0.097 | 0.075 | 0.031 |
| 0.400 ± 0.056 | -0.073 | 0.053 | 0.031 |
| 0.597 ± 0.057 | -0.013 | 0.046 | 0.031 |
| 0.793 ± 0.057 | 0.039 | 0.050 | 0.030 |
| 0.992 ± 0.058 | -0.041 | 0.057 | 0.031 |
| 1.189 ± 0.058 | 0.063 | 0.080 | 0.030 |
| 1.435 ± 0.086 | 0.022 | 0.077 | 0.031 |
| 1.761 ± 0.111 | -0.013 | 0.082 | 0.031 |

Table D.19: Final results for $\frac{2}{N}\text{Re}(U_{-1}U_1^* + U_2U_0^*)$.

Appendix E

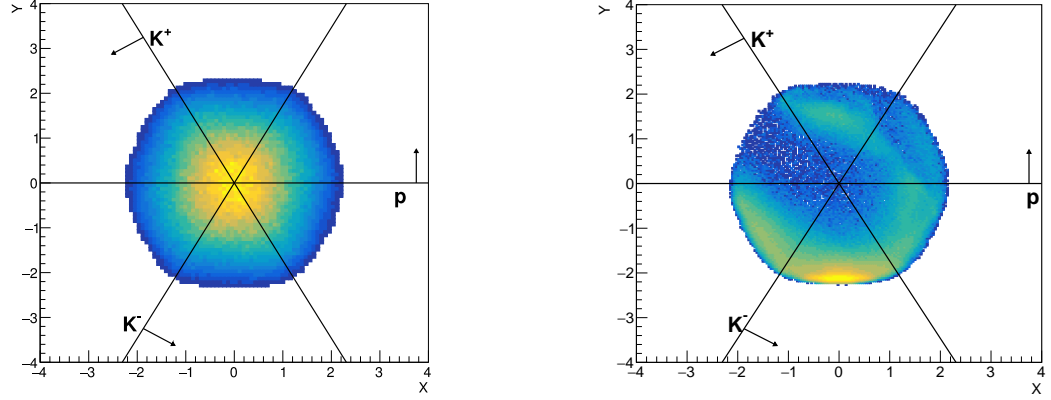
Longitudinal phase space analysis

The possibility to perform a longitudinal phase space analysis to improve the event selection was studied extensively and eventually resulted in a publication [121]. In the following the concept of longitudinal phase space analysis will be briefly introduced and the findings of the study will be summarised. For that, the general structure of the publication will be followed and some parts will be adopted.

Introduction

Many hadron spectroscopy analyses require the identification of a specific reaction. For that it is not enough to simply identify all final state particles correctly. It can happen that the same final state arises from two very different reactions. The reaction of interest for this work is $\gamma p \rightarrow K^+ \Lambda(1520) \rightarrow K^+ K^- p$. The same final state can also arise from $\gamma p \rightarrow \phi(1020) p \rightarrow K^+ K^- p$. In fact it is entirely possible that the kinematics of the reactions cause those two states to overlap in a Dalitz plot. In that case a simple cut in the invariant mass spectrum of $K^+ K^-$ to reduce the $\phi(1020)$ background might cause a large loss of good $\Lambda(1520)$ events. It is therefore desirable to come up with a better way to isolate a certain reaction. In 2015 the JPAC collaboration investigated $K^+ K^-$ photoproduction in the double-Regge exchange limit and found that certain phase space cuts could be applied to enhance that contribution [122]. A similar approach could help with the stated problem.

The idea of longitudinal phase space (LPS) plots was introduced by L. van Hove in 1969 ([123–125]). The method assumes that at high enough centre-of-mass energies the reaction kinematics can be completely described in terms of their longitudinal momenta. Therefore, the dimensionality of the phase space reduces and the kinematics of a three particle final state can



(a) Monte Carlo data without any intermediate resonances. Taken from [121].

(b) Real data with event selection described in Chapter 5.

Figure E.1: Two van Hove plots showing the distribution with and without any intermediate resonances.

be visualised in a two dimensional plane by defining the polar coordinates q and ω through

$$q_1 = \sqrt{\frac{2}{3}}q \sin(\omega) \quad (\text{E.1})$$

$$q_2 = \sqrt{\frac{2}{3}}q \sin(\omega + \frac{2}{3}\pi) \quad (\text{E.2})$$

$$q_3 = \sqrt{\frac{2}{3}}q \sin(\omega + \frac{4}{3}\pi) \quad (\text{E.3})$$

$$q = (q_1^2 + q_2^2 + q_3^2)^{\frac{1}{2}} \quad (\text{E.4})$$

where q_i denotes the longitudinal momentum component of the i -th particle in the centre-of-mass frame. Figure E.1 shows two van Hove plots for the K^+K^-p final state, once phase space Monte Carlo data without any intermediate resonances (Figure E.1a) and once real data, taken during the Spring 2017 beam time (Figure E.1b). To plot the data the coordinates X and Y were defined by

$$X = q \cos(\omega) \quad (\text{E.5})$$

$$Y = q \sin(\omega) \quad (\text{E.6})$$

One can identify six sectors on the van Hove plot, indicated by the black lines, corresponding to the direction of the final state particle in the centre-of-mass frame, indicated by the labelled arrows. Assuming t -channel production with small momentum transfer, which is expected to be the dominant process at high energies, one would expect the K^+K^- pair to go forward in case of an intermediate meson and the K^-p to go backward in case of an intermediate baryon. As indicated by the arrows the bottom middle sector is the one where both kaons go forward and

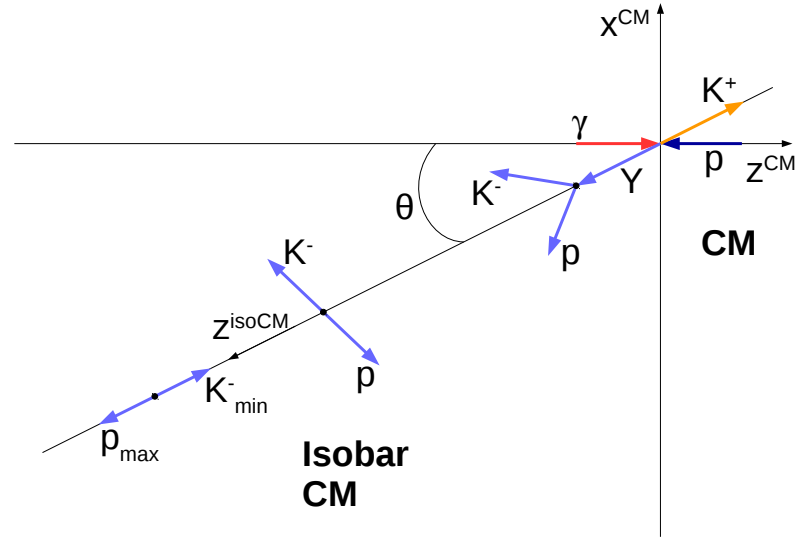


Figure E.2: Coordinate systems used to calculate the mass-dependent cut limits in longitudinal phase space. p_{\max} and K_{\min}^- show the case of a reaction with minimal K^- and maximal p momentum in the CM frame. Taken from [121].

the proton goes backward. Therefore, this is where one would expect to see meson production. Analogously one would expect to find baryon production in the bottom left sector. Indeed, looking at the real data (Figure E.1b) one can see that those two sectors are populated the most.

Mass-dependent cuts in longitudinal phase space

A simple cut along the sector boundaries would enhance the relative contribution of one reaction over the other. If one is interested only in one particular resonance (e.g. a baryon) one could remove a large fraction of the other resonances (e.g. mesons) decaying into the same final state. This works well for light resonances which are produced at very small momentum transfer but heavier resonances leak into neighbouring sectors. A simple cut would cause a potentially large loss of good events. Therefore, it would be desirable to have a reliable method to determine cut limits depending on the mass of the intermediate resonance.

One way of defining mass-dependent cut limits is to answer the question: “Could two particles in the final state have formed an isobar solely considering their kinematics?” In the following the solution is given for the case of the three particle final state arising from the reaction $\gamma p \rightarrow K^+ Y \rightarrow K^+ K^- p$, a more general derivation of the necessary quantities can be found in [121].

The two reference frames needed are depicted in Figure E.2. The overall centre-of-mass frame (CM) is defined such that z^{CM} is along the incoming beam axis, y^{CM} is perpendicular to z^{CM} and the outgoing isobar Y ($\hat{p}_Y \times \hat{p}_\gamma$) and $x^{\text{CM}} = y^{\text{CM}} \times z^{\text{CM}}$. The isobar CM frame (isoCM) is defined such that z^{isoCM} is in direction of the isobar in the CM frame, $y^{\text{isoCM}} = \hat{p}_\gamma^{\text{isoCM}} \times z^{\text{isoCM}}$

and $x^{\text{isoCM}} = y^{\text{isoCM}} \times z^{\text{isoCM}}$. In the isoCM frame the K^- and p are back to back with a fixed momentum given by

$$P = \frac{\left[\left(M_Y^2 - (m_p + m_{K^-})^2 \right) \left(M_Y^2 - (m_p - m_{K^-})^2 \right) \right]^{1/2}}{2M_Y} \quad (\text{E.7})$$

where M_Y is the invariant mass of the isobar. For a particle's four-momentum (p^x, p^y, p^z, E)

$$p_{K^-/p}^{\text{isoCM}} = \left(0, 0, \pm P, \sqrt{P^2 + m_{K^-/p}^2} \right) \quad (\text{E.8})$$

in the isoCM frame, boosting back to the overall CM frame yields the maximal/minimal momentum it can have in this frame (see Figure E.2). To easily evaluate the mass-dependent longitudinal phase space cut the van Hove angle ω is replaced with

$$\rho = \arctan \left(\frac{p_{K^-}^{z,CM}}{p_p^{z,CM}} \right) \quad (\text{E.9})$$

where $p^{z,CM}$ indicates that, as in the van Hove plot, only the longitudinal momentum components are used to evaluate the angle. Using the four-momentum vectors as defined in Eq. (E.7) and boosted back into the CM frame lower and upper cut limits for ρ can be defined as

$$\rho_{\text{low}} = \arctan \left(\frac{p_{K^-}^{z,CM, \text{min}}}{p_p^{z,CM, \text{max}}} \right) \quad (\text{E.10})$$

$$\rho_{\text{up}} = \arctan \left(\frac{p_{K^-}^{z,CM, \text{max}}}{p_p^{z,CM, \text{min}}} \right) \quad (\text{E.11})$$

Figure E.3 shows the new cut limits in the coordinate system used to evaluate them. Reactions with a ρ that fulfils the condition

$$\rho_{\text{low}} < \rho < \rho_{\text{up}} \quad (\text{E.12})$$

could have formed an isobar with momentum (anti-)parallel to the beam axis. It is very important to note that the cut limits defined in Eq. (E.10) and Eq. (E.11) are dependent on the isobar mass. For large isobar masses the decay can occupy a large fraction of the available phase space and hence the cut results in less rejection of background. As in the van Hove plot, all relations hold only strictly true in the case of infinite longitudinal momentum (i.e. vanishing transverse momentum) for which the angle θ , as defined in Figure E.2, is zero. For large longitudinal momenta, as in high energy photoproduction with small momentum transfer, the condition is approximately fulfilled. For large momentum transfer the cut will remove more events with the isobar of interest and become less effective.

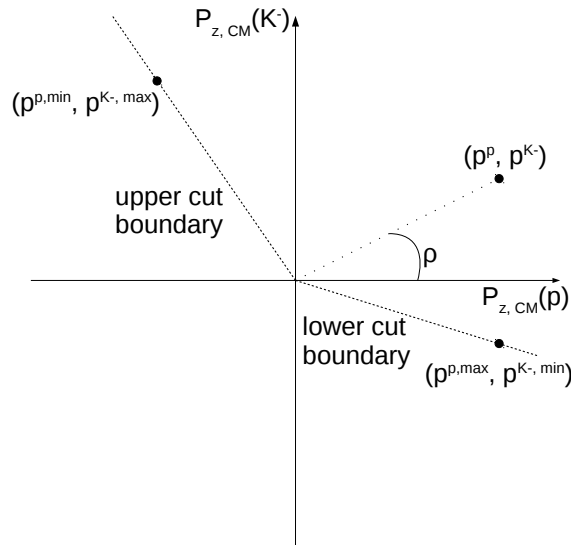


Figure E.3: Coordinate system used to evaluate mass-dependent cut limits in longitudinal phase space. Taken from [121].

Comparison

Now that new cut limits were defined that take the isobar mass into account, studies were performed to test and compare the performance of old and new method. For those studies a signal and a background sample of toy Monte Carlo data was produced. The signal reaction used in the study was $\gamma p \rightarrow K^+ Y(2200) \rightarrow K^+ K^- p$, where $Y(2200)$ denotes a hyperon with an invariant mass of 2.2 GeV, width of 50 MeV and a production t-slope of $t_1 = 1.5 \text{ GeV}^2$. As background a spectrum of mesons decaying into the same final state was produced with invariant masses between 1.0 GeV and 1.8 GeV, widths of 50 MeV and a production t-slope of $t_2 = 3.0 \text{ GeV}^2$. For both samples a mono-energetic photon beam of $E_\gamma = 9 \text{ GeV}$ was used. A cut of $\pm 0.2 \text{ GeV}$ around the pK^- invariant mass of 2.2 GeV was placed, as one might do to study the $Y(2200)$. After those two samples were prepared four different scenarios were carefully studied:

1. no cut
2. baryon sector cut:
apply a cut on ω such that only events in the bottom left sector of the van Hove plot are preserved
3. baryon isobar cut:
apply the mass-dependent cut on ρ to keep events where the K^- and p could have formed a resonance

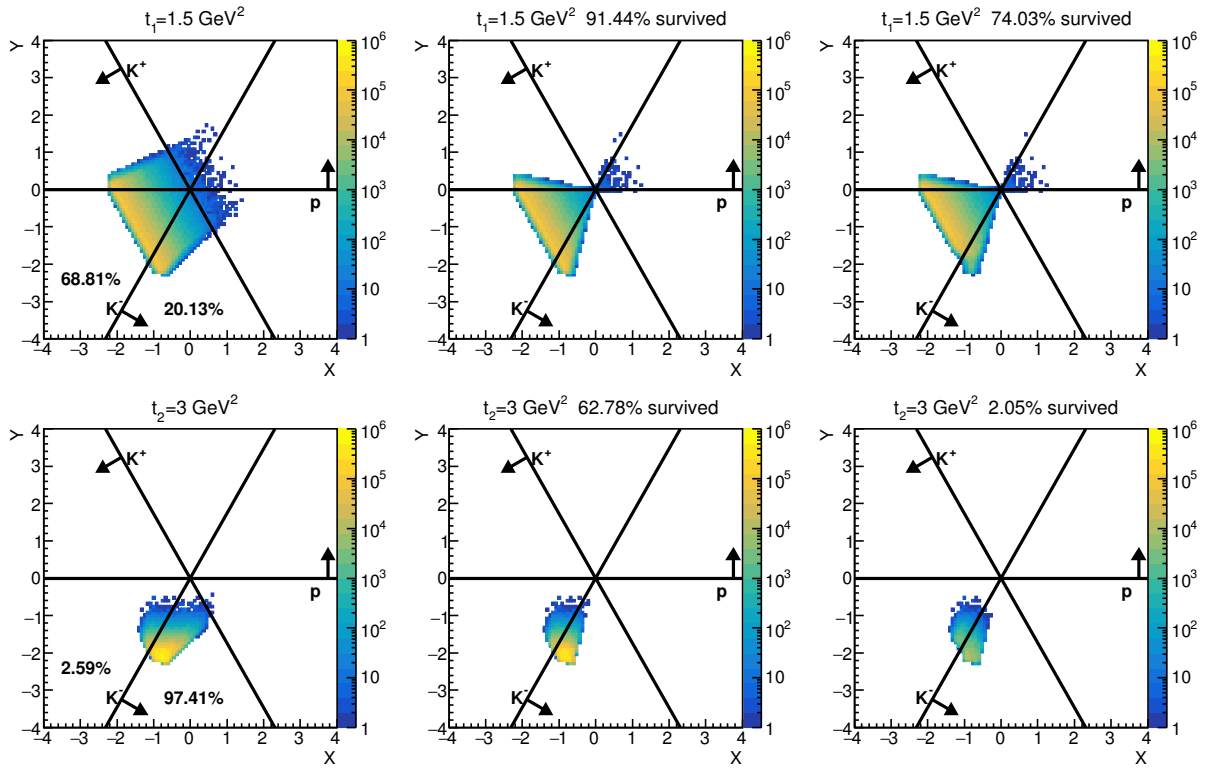


Figure E.4: Van Hove plots for signal (top) and background (bottom) for all four tested scenarios. The no-cut-scenario is depicted on the left. The sector cut is indicated by the black lines and the percentages show the relative number of events in the sector. The plots in the middle show the effect on the baryon isobar cut and the plots on the right the effect of the BNM cut. The relative amount of events surviving the cut is stated in the titles. Taken from [121].

4. baryon-not-meson isobar (BNM) cut:

same as 'baryon isobar cut' and in addition remove events that passed the mass-dependent cut for a K^+K^- isobar hypothesis, as long as the invariant mass of the K^+K^- pair is below 2 GeV

The purpose of the K^+K^- invariant mass constraint in the last case is to make sure that only the part of phase space gets vetoed that realistically can contain meson resonances. The effect of all four scenarios on the van Hove plots for signal and background can be seen in Figure E.4. The top row shows plots for the signal sample while the bottom row shows the same plots for the background sample. On the left one can see what the van Hove plot looks like without any cuts applied. The baryon isobar appears as a very broad band that is located mainly in the bottom left sector, as expected. Here one can clearly see that heavy particles will leak into neighbouring sectors due to the large amount of phase space their decay can cover. If one were to place a baryon sector cut one would keep 68.81% signal while allowing in 2.59% of the background. The plots in the middle show the effect of the baryon isobar cut. In this case 91.44% of the signal are preserved while 62.78% of the background pass the cut. This shows that a much larger fraction of the signal is preserved since events leaking into neighbouring sectors are kept

but this comes at the cost of much more background being allowed. The plots on the right show the last scenario, the BNM cut. Now the amount of signal is slightly reduced again to 74.03% but the amount of background is greatly suppressed and only 2.05% of the generated background sample survives. From this numbers one concludes that the isobar cut preserves the most signal but the BNM is most efficient at reducing background. On top of that it outperforms the sector cut at preserving signal and hence shows by far the best signal-to-background ratio. Figure E.5 shows the effect of the cuts on Dalitz plots. Figure E.5a shows the Dalitz plot without any cut

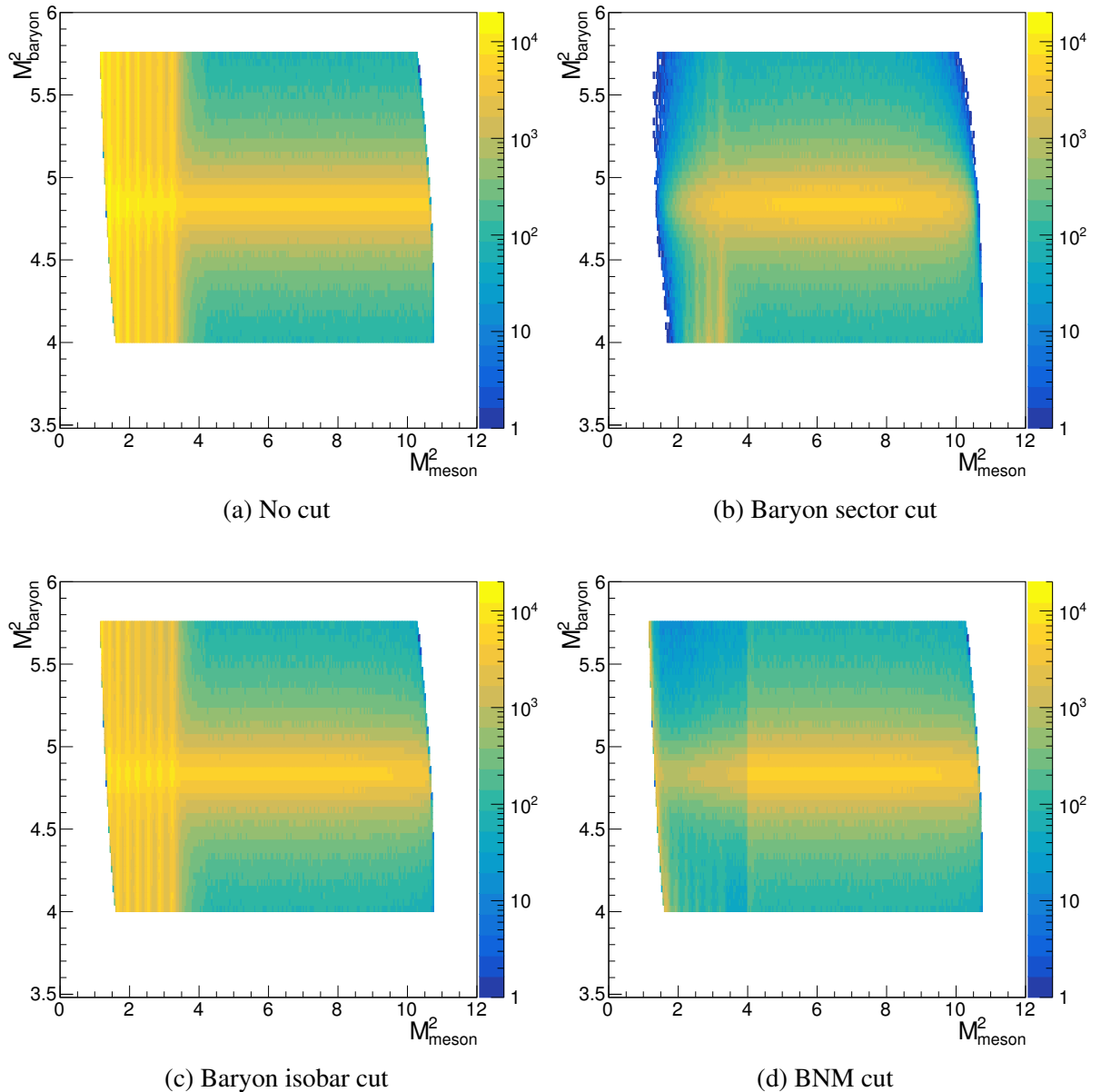


Figure E.5: Dalitz plots for all four discussed scenarios. All taken from [121].

applied. The broad horizontal band is the $Y(2200)$ hyperon. There is a fairly large overlap with the vertical bands stemming from the background meson spectrum. Cutting on the baryon sector (Figure E.5b) removes a large part of the background but especially the heavier mesons survive

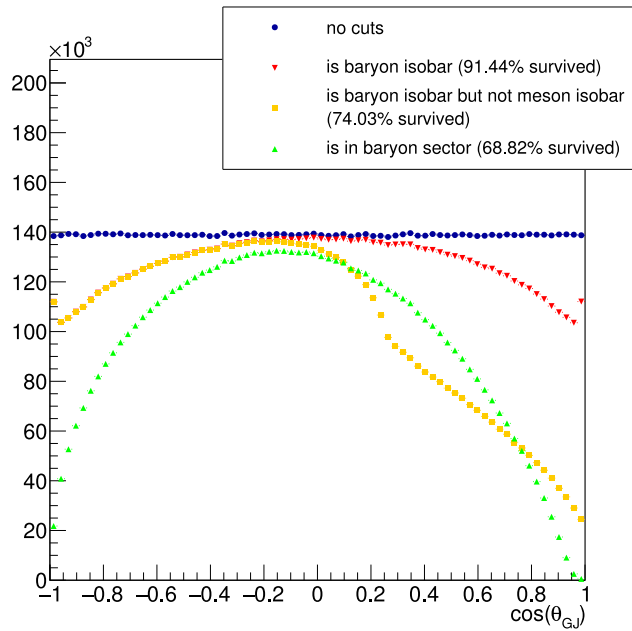


Figure E.6: $\cos(\theta_{GJ})$ distribution for the K^- for all four studied scenarios. Taken from [121].

this cut. Figure E.5d shows the effect of the BNM cut. Now a larger part of the heavier mesons gets cut away.

It is not only interesting to see how much signal and background is removed by the cuts but also what they do to angular distributions of final state particles. After all this is what many physics analyses rely on in the end. To investigate this, the signal $\cos(\theta_{GJ})$ distribution of the K^- was studied for all four cases. The θ_{GJ} is the theta angle in the Gottfried-Jackson frame, also referred to as t-channel helicity frame [31]. The results can be seen in Figure E.6. Since the events were generated without any specific angular distribution the $\cos(\theta_{GJ})$ distribution is flat for the 'no cut' case (blue). Therefore, all deviations from a flat distribution can be accounted to acceptance effects due to the applied cuts. The red points show the distribution after the isobar cut was applied. One can see that good events were mainly lost towards $\cos(\theta_{GJ}) = 1$. The effect of the baryon sector cut is shown in green. Here it becomes apparent that most signal events were lost towards $\cos(\theta_{GJ}) = \pm 1$ and this is also precisely were the BNM cut (yellow) regained events from. The consequences of that can be seen later.

Moment extraction using mass-dependent cuts

It has been shown that the BNM cut outperforms the other cuts in terms of signal-to-background ratio. In order to establish if the acceptance effects introduced by this cut prevent a reliable extraction of physics information from the remaining events, a second study on toy Monte Carlo data was performed.

For this purpose 300 independent toy Monte Carlo samples were generated. Each sample contained 10,000 events of the signal reaction with an angular distribution in the Gottfried-Jackson frame according to moments of spherical harmonics $\langle Y_{LM} \rangle$ with $L_{\max} = 4$ and $M_{\max} = 2$, where the K^- was chosen to evaluate the angles. The spherical harmonics are given by

$$f(\phi, \theta) = \sum_{L=0, M=0}^{L_{\max}, M_{\max}} \langle Y_{LM} \rangle \cos(M\phi) \times \sqrt{\frac{2L+1}{4\pi} \frac{(L-M)!}{(L+M)!}} P_{LM}(\cos\theta) \quad (\text{E.13})$$

where $P_{LM}(\cos\theta)$ denotes the associated Legendre polynomials. Spherical harmonics are a common parametrisation of angular decay distributions. For this study the spherical harmonic moments were arbitrarily chosen to be

$$\begin{aligned} \langle Y_{11} \rangle &= 0.3 \\ \langle Y_{20} \rangle &= -0.2 \\ \langle Y_{41} \rangle &= -0.2 \\ \langle Y_{42} \rangle &= 0.1 \end{aligned}$$

After generating the samples the different cuts were applied and an unbinned extended maximum likelihood fit [110] was performed to extract the spherical harmonic moments. The acceptance effects were corrected for by calculating the normalisation integrals through summing phase space Monte Carlo events which had identical cuts applied. All fits were done using the HASPECT framework [126] which is build on RooFit [105].

In order to assess the goodness of the extracted moments, pull distributions were used. They are a commonly used tool in such studies. A pull can be calculated as

$$\text{pull} = \frac{\text{measured value} - \text{true value}}{\text{error on measured value}} \quad (\text{E.14})$$

This has been done for each fit parameter for each of the 300 samples and then the pulls have been histogrammed. For unbiased fit results with Gaussian errors one would expect a normal distribution with a mean of 0 and a width of 1. The results for means and widths for all moments for the four studied scenarios can be found in Figure E.7. Within statistical fluctuations all results agree with a mean of 1 and a width of 0. This shows that all applied cuts preserved enough acceptance to reliably extract information from the angular distributions. In order to assess the precision of the extracted results, the spread of extracted values was examined. To do that all results were histogrammed and fitted with a Gaussian distribution. The results for the non-zero moments can be found in Figure E.8. The mean is plotted as dot with the error stem-

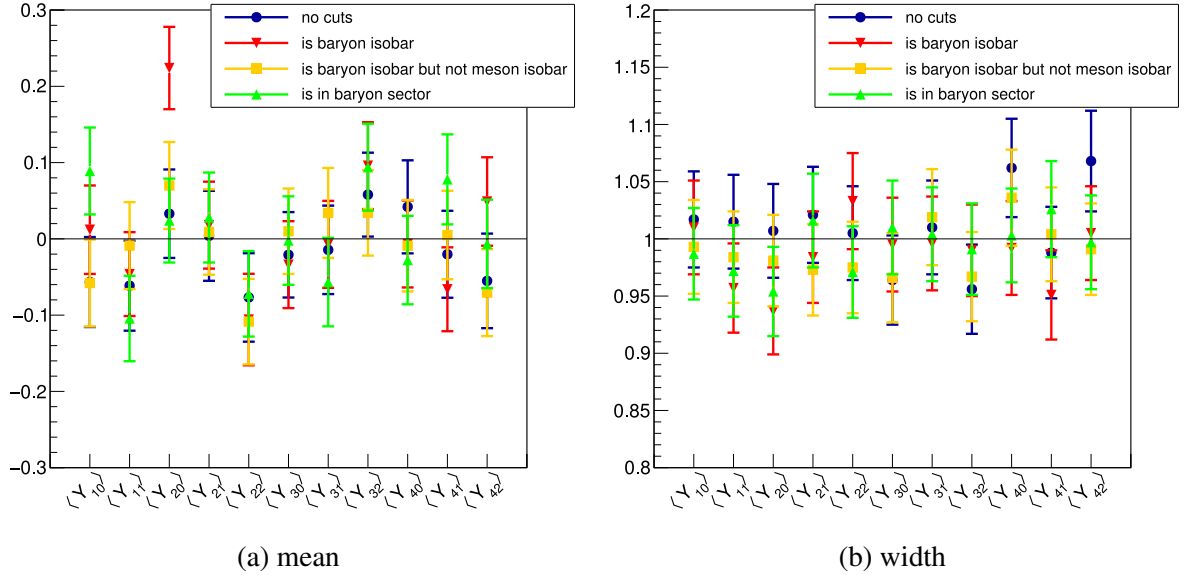


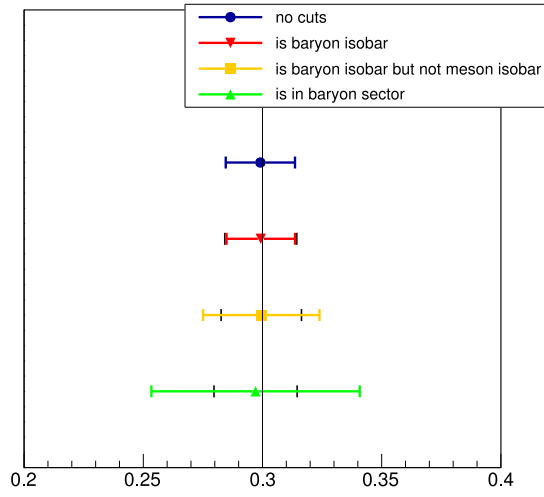
Figure E.7: Means and widths of the pull distributions for all spherical harmonic moments for the four studied scenarios. Both taken from [121].

ming from the width of the Gaussian distribution. The black lines indicate the true value. As already apparent from the pull distributions all results agree with the true value within their statistical uncertainty. Interesting are the errors, which reflect the precision of moment extraction. Since the cuts leave the samples with different number of events one would naturally expect the ranking in precision that can be seen in the result plots. Therefore, the black error bars were included that indicate the expected errors that come from counting statistics and grow with \sqrt{N} . Now it becomes apparent that the BNM cut (yellow) causes a slight worsening of the precision in moment extraction. In all cases the sample with the baryon sector cut applied (green) has by far the least precise results. This can possibly be explained by the extremely low acceptance at $\cos(\theta_{GJ}) = \pm 1$ in that case.

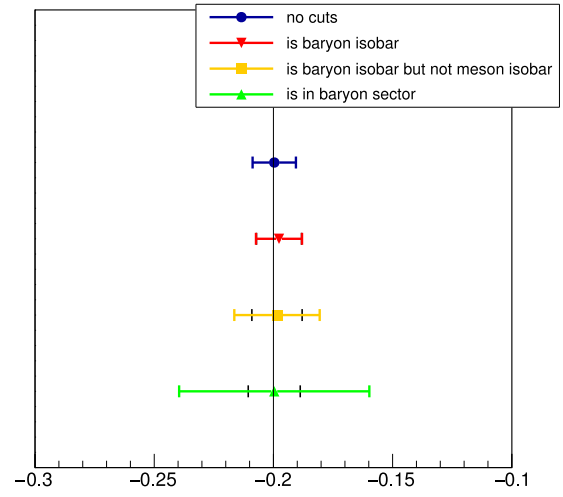
Summary of findings

The studies have shown that cuts in longitudinal phase space can be a powerful tool to improve the signal-to-background ratio for reactions with large longitudinal momenta. The combination of a mass-dependent baryon isobar cut with a meson anti-cut proved to be the most efficient and greatly outperformed the conventional cut on a sector in a van Hove plot alone. Furthermore, it was shown that information from the angular decay distribution can be extracted in all four scenarios but again the BNM cut outperformed the conventional cut on a sector.

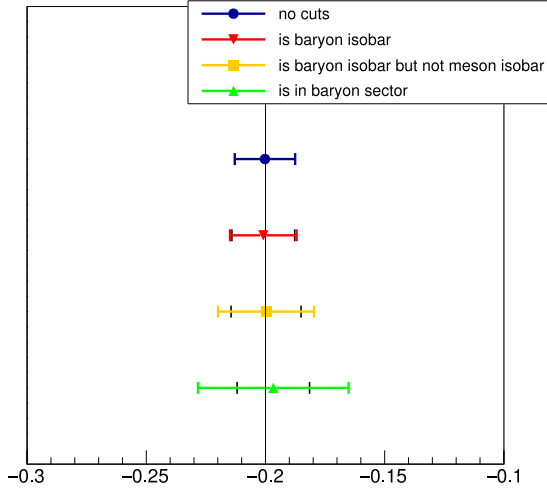
It is important to note that these studies were performed for one heavy baryon decaying into a specific final state. It is expected that the results (especially numerical values) will change for



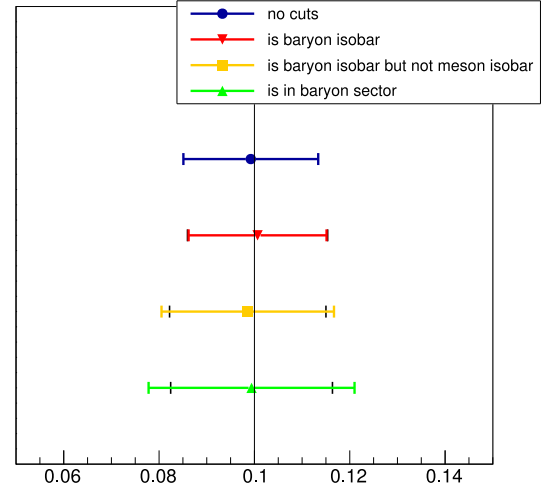
(a) $\langle Y_{11} \rangle$



(b) $\langle Y_{20} \rangle$



(c) $\langle Y_{41} \rangle$



(d) $\langle Y_{42} \rangle$

Figure E.8: Mean value and width of the four non-zero moments for all four studied scenarios. All taken from [121]

different resonances and final states. Therefore, it is highly recommended to repeat these studies for each individual reaction one wants to study with this method.

These studies were all extremely instructive and concluded in a publication. Unfortunately, it also became clear that the effect on the main analysis of this thesis was negligible due to the fact that the main meson background from the $\phi(1020)$ and the $\Lambda(1520)$ are sufficiently separated on a Dalitz plot. Therefore, this technique was not applied. Nevertheless, it might be a very powerful tool to investigate higher mass hyperons in this final state in future analyses.

Bibliography

- [1] P. Pauli. *Investigation of the Absolute Normalisation of the Helicity Dependent Cross-Sections $\sigma^{1/2}$ and $\sigma^{3/2}$* . Master thesis, University of Bonn, 2016.
- [2] S. Bethke. The 2009 world average of α_s . *The European Physical Journal C*, 64(4):689–703, 2009. doi:10.1140/epjc/s10052-009-1173-1.
- [3] D. J. Gross and F. Wilczek. Ultraviolet Behavior of Non-Abelian Gauge Theories. *Physical Review Letters*, 30(26):1343–1346, 1973. doi:10.1103/PhysRevLett.30.1343.
- [4] D. J. Gross and F. Wilczek. Asymptotically Free Gauge Theories. I. *Physical Review D*, 8(10):3633–3652, 1973. doi:10.1103/PhysRevD.8.3633.
- [5] D. H. Politzer. Reliable Perturbative Results for Strong Interactions? *Physical Review Letters*, 30(26):1346–1349, 1973. doi:10.1103/PhysRevLett.30.1346.
- [6] D. H. Politzer. Asymptotic freedom: An approach to strong interactions. *Physics Reports*, 14(4):129–180, 1974. doi:10.1016/0370-1573(74)90014-3.
- [7] E. Rutherford. Collision of α particles with light atoms. IV. An anomalous effect in nitrogen. *Philosophical Magazine*, 90(sup1):31–37, 2010. doi:10.1080/14786431003659230.
- [8] J. Chadwick. Possible Existence of a Neutron. *Nature*, 129(3252):312–312, 1932. doi:10.1038/129312a0.
- [9] J. Chadwick. The Existence of a Neutron. *Proceedings of the Royal Society A: Mathematical, Physical and Engineering Sciences*, 136(830):692–708, 1932. doi:10.1098/rspa.1932.0112.
- [10] M. Gell-Mann. The Eightfold Way: A Theory of Strong Interaction Symmetry. Technical report, 1961. doi:10.2172/4008239.
- [11] M. Gell-Mann. Symmetries of Baryons and Mesons. *Physical Review*, 125(3):1067–1084, 1962. doi:10.1103/PhysRev.125.1067.

- [12] M. Gell-Mann. A schematic model of baryons and mesons. *Physics Letters*, 8(3):214–215, 1964. doi:[https://doi.org/10.1016/S0031-9163\(64\)92001-3](https://doi.org/10.1016/S0031-9163(64)92001-3).
- [13] G. Zweig. An SU_3 model for strong interaction symmetry and its breaking, 1964. url <http://cds.cern.ch/record/570209>.
- [14] S.-K. Choi, et al. Observation of a Narrow Charmoniumlike State in Exclusive $B^\pm \rightarrow K^\pm \pi^+ \pi^- J/\Psi$ Decays. *Physical Review Letters*, 91(26):262001, 2003. doi:10.1103/PhysRevLett.91.262001.
- [15] M. Tanabashi, et al. Review of Particle Physics. *Physical Review D*, 98(3):030001, 2018. doi:10.1103/PhysRevD.98.030001.
- [16] A. Ali, J. S. Lange, and S. Stone. Exotics: Heavy Pentaquarks and Tetraquarks. *Progress in Particle and Nuclear Physics*, 97:123–198, 2017. doi:10.1016/j.pnpnp.2017.08.003.
- [17] F.-K. Guo, et al. Hadronic molecules. *Reviews of Modern Physics*, 90(1):015004, 2017. doi:10.1103/RevModPhys.90.015004.
- [18] S. L. Olsen, T. Skwarnicki, and D. Zieminska. Nonstandard heavy mesons and baryons: Experimental evidence. *Reviews of Modern Physics*, 90(1):015003, 2018. doi:10.1103/RevModPhys.90.015003.
- [19] N. Brambilla, et al. QCD and strongly coupled gauge theories: challenges and perspectives. *The European Physical Journal C*, 74(10):2981, 2014. doi:10.1140/epjc/s10052-014-2981-5.
- [20] T. Aaltonen, et al. Precision Measurement of the $X(3872)$ Mass in $J/\psi \pi^+ \pi^-$ Decays. *Physical Review Letters*, 103(15):152001, 2009. doi:10.1103/PhysRevLett.103.152001.
- [21] A. Tomaradze, S. Dobbs, T. Xiao, and Kamal K. Seth. Precision Measurement of the Mass of the D^{*0} Meson and the Binding Energy of the $X(3872)$ Meson as a $D^0 \overline{D}^{*0}$ Molecule. *Physical Review D*, 91(1):011102, 2015. doi:10.1103/PhysRevD.91.011102.
- [22] D. Alde, et al. Evidence for a 1^{-+} exotic meson. *Physics Letters B*, 205(2):397–400, 1988. doi:[https://doi.org/10.1016/0370-2693\(88\)91686-3](https://doi.org/10.1016/0370-2693(88)91686-3).
- [23] G. S. Adams, et al. Observation of a New $J^{PC} = 1^{-+}$ Exotic State in the Reaction $\pi^- p \rightarrow \pi^+ \pi^- \pi^- p$ at 18 GeV/c. *Physical Review Letters*, 81(26):5760–5763, 1998. doi:10.1103/PhysRevLett.81.5760.
- [24] G. S. Adams, et al. Confirmation of the 1^+ meson exotics in the $\eta \pi^0$ system. *Physics Letters B*, 657(1):27–31, 2007. doi:<https://doi.org/10.1016/j.physletb.2007.07.068>.

- [25] M. G. Alekseev, et al. Observation of a $J^{PC} = 1^{-+}$ exotic resonance in diffractive dissociation of 190 GeV/c π^{-} into $\pi^{-}\pi^{-}\pi^{+}$. *Physical Review Letters*, 104(24):241803, 2010. doi:10.1103/PhysRevLett.104.241803.
- [26] M. Aghasyan, et al. Light isovector resonances in $\pi^{-}p \rightarrow \pi^{-}\pi^{-}\pi^{+}p$ at 190 GeV/c. *Physical Review D*, 98(9):092003, 2018. doi:10.1103/PhysRevD.98.092003.
- [27] M. Ferro-Luzzi, R. D. Tripp, and M. B. Watson. Excited Hyperon of Mass 1520 Mev. *Physical Review Letters*, 8(1):28–31, 1962. doi:10.1103/PhysRevLett.8.28.
- [28] B. Povh, F. Zersche, K. Rith, C. Scholz, and W. Rodejohann. *Particles and Nuclei*. Springer Berlin Heidelberg, 2006. doi:10.1007/3-540-36684-9.
- [29] U. Fano. Description of States in Quantum Mechanics by Density Matrix and Operator Techniques. *Reviews of Modern Physics*, 29(1):74–93, 1957. doi:10.1103/RevModPhys.29.74.
- [30] K. Schilling, P. Seyboth, and G. Wolf. On the analysis of vector-meson production by polarized photons. *Nuclear Physics B*, 15(2):397–412, 1970. doi:10.1016/0550-3213(70)90070-2.
- [31] K. Gottfried and J. D. Jackson. On the connection between production mechanism and decay of resonances at high energies. *Il Nuovo Cimento*, 33(2):309–330, 1964. doi:10.1007/BF02750195.
- [32] M. Thomson. *Modern Particle Physics*. Cambridge University Press, 2013. doi:10.1017/CBO9781139525367.
- [33] M. Jacob and G. C. Wick. On the general theory of collisions for particles with spin. *Annals of Physics*, 1959. doi:10.1016/0003-4916(59)90051-X.
- [34] S.-U. Chung. Spin Formalisms. Technical Report BNL-QGS-02-0900, CERN 71-8, BNL, 2014. url <http://suchung.web.cern.ch/spinfml.pdf>.
- [35] B. G. Yu and K. J. Kong. Photoproduction of $\gamma p \rightarrow K + \Lambda^{*}(1520)$ and decay of $\Lambda^{*}(1520) \rightarrow K^{-}p$ in the Reggeized framework. *Physical Review C*, 96(2):025208, 2017. doi:10.1103/PhysRevC.96.025208.
- [36] M. E. Rose. *Elementary Theory of Angular Momentum*. John Wiley & Sons, Inc., New York, 1957.
- [37] G. Otter. Present Experimental Status of Helicity Conservation in Diffractive Processes. *Acte Physica Polonica*, B(3):809–844, 1972. url <http://www.actaphys.uj.edu.pl/fulltext?series=Reg&vol=3&page=809>.

- [38] W. I. Levine. *Measurement of spin density matrix elements in the reaction $\gamma p \rightarrow K^+ \Lambda(1520)$ using CLAS at Jefferson Lab*. PhD thesis, Carnegie Mellon University, 2016.
- [39] V. Mathieu. $\gamma p \rightarrow K^+ \Lambda(1520)$ SDME at GlueX. Technical Report, priv. communication, Complutense University of Madrid, Madrid, 2019.
- [40] I.S. Barker, A. Donnachie, and J.K. Storrow. Complete experiments in pseudoscalar photoproduction. *Nuclear Physics B*, 95(2):347–356, 1975. doi:10.1016/0550-3213(75)90049-8.
- [41] D. Mack. Potential Bias in "Direct" Sigma Asymmetry Measurements with Decaying Recoil Baryon. Technical Report GlueX-doc-4308-v3, Jefferson Lab, 2020.
- [42] M. B. Watson, M. Ferro-Luzzi, and R. D. Tripp. Analysis of Y_0^* (1520) and Determination of the Σ Parity. *Physical Review*, 131(5):2248–2281, 1963. doi:10.1103/PhysRev.131.2248.
- [43] A. M. Boyarski, et al. Photoproduction of K^+ -hyperon from hydrogen and deuterium at 11 GeV. *Physics Letters B*, 34(6):547–550, 1971. doi:http://dx.doi.org/10.1016/0370-2693(71)90677-0.
- [44] D. P. Barber, et al. Strangeness exchange in the photoproduction of $K^+ \Lambda(1520)$ between 2.8 and 4.8 GeV. *Zeitschrift für Physik C Particles and Fields*, 7(1):17–20, 1980. doi:10.1007/BF01577315.
- [45] N. Muramatsu, et al. Near-threshold photoproduction of $\Lambda(1520)$ from protons and deuterons. *Physical Review Letters*, 103(1):012001, 2009. doi:10.1103/PhysRevLett.103.012001.
- [46] H. Kohri, et al. Near-Threshold $\Lambda(1520)$ Production by the $\vec{\gamma} p \rightarrow K^+ \Lambda(1520)$ Reaction at Forward K^+ Angles. *Physical Review Letters*, 104(17):172001, 2010. doi:10.1103/PhysRevLett.104.172001.
- [47] A. Lleres, et al. Polarization observable measurements for $\gamma p \rightarrow K^+ \Lambda$ and $\gamma p \rightarrow K^+ \Sigma$ for energies up to 1.5 GeV. *The European Physical Journal A*, 31(1):79–93, 2007. doi:10.1140/epja/i2006-10167-8.
- [48] F. W. Wieland, et al. Study of the reaction $\gamma p \rightarrow K^+ \Lambda(1520)$ at photon energies up to 2.65 GeV. *The European Physical Journal A*, 47(1520):1–11, 2011. doi:10.1140/epja/i2011-11047-x.
- [49] K. Moriya, et al. Differential photoproduction cross sections of the $\Sigma^0(1385)$, $\Lambda(1405)$, and $\Lambda(1520)$. *Physical Review C*, 88(4):45201, 2013. doi:10.1103/PhysRevC.88.045201.

- [50] J. He and X.-R. Chen. Roles of nucleon resonances in $\Lambda(1520)$ photoproduction off the proton. *Physical Review C*, 86(3):035204, 2012. doi:10.1103/PhysRevC.86.035204.
- [51] S.-I. Nam and C.-W. Kao. $\Lambda(1520)$ photoproduction off the proton target with Regge contributions. *Physical Review C*, 81:55206, 2010. doi:10.1103/PhysRevC.81.055206.
- [52] Z. Zhao. *Photoproduction of the $\Lambda^*(1520)$ Hyperon off Protons and Neutrons in Deuterium*. PhD thesis, University of South Carolina, 2010.
- [53] S.-I. Nam, A. Hosaka, and H.-C. Kim. $\Lambda(1520, 3/2^-)$ -photoproduction reaction via $\gamma N \rightarrow K\Lambda^*(1520)$. *Physical Review D*, 71(11):114012, 2005. doi:10.1103/PhysRevD.71.114012.
- [54] J. He. Theoretical study of the $\Lambda(1520)$ photoproduction off proton target based on the new CLAS data. *Nuclear Physics A*, (927):24–35, 2014. doi:10.1016/j.nuclphysa.2014.03.008.
- [55] H. Al Ghouli, et al. First results from the GlueX experiment. *AIP Conference Proceedings*, 1735(1):20001, 2016. doi:10.1063/1.4949369.
- [56] M. Spata. 12 GeV CEBAF Initial Operational Experience and Challenges. In *Proc. 9th International Particle Accelerator Conference (IPAC'18), Vancouver, BC, Canada, April 29-May 4, 2018*, pages 1771–1775, Geneva, Switzerland, 2018. JACoW Publishing. doi:10.18429/JACoW-IPAC2018-WEYGBD1.
- [57] Jefferson Lab. CEBAF at 12 GeV Schematic. <https://www.flickr.com/photos/jeffersonlab/12599705145>, last access 03/06/2020.
- [58] R. Suleiman, et al. High current polarized electron source. In *AIP Conference Proceedings*, volume 1970. American Institute of Physics Inc., 2018. doi:10.1063/1.5040226.
- [59] T. Plawski, et al. CEBAF Photo Gun RF System. In *Proc. 29th Linear Accelerator Conference (LINAC'18), Beijing, China, 16-21 September 2018*, pages 236–238, Geneva, Switzerland, 2018. JACoW Publishing. doi:10.18429/JACoW-LINAC2018-MOPO115.
- [60] A. Freyberger. Commissioning and Operation of 12 GeV CEBAF. In *Proc. 6th International Particle Accelerator Conference (IPAC 2015), Richmond, VA, USA, May 3-8, 2015*, page MOXGB2, 2015. doi:10.18429/JACoW-IPAC2015-MOXGB2.
- [61] C. E. Reece. Continuous wave superconducting radio frequency electron linac for nuclear physics research. *Physical Review Accelerators and Beams*, 19(12):124801, 2016. doi:10.1103/PhysRevAccelBeams.19.124801.

- [62] Y. Qiang. Physics Program at Jefferson Lab Hall-D. *5th Workshop on Hadron Physics in China and Opportunities in US*, (GlueX-doc-2282), 2013.
- [63] H. Bethe and W. Heitler. On the Stopping of Fast Particles and on the Creation of Positive Electrons. *Proceedings of the Royal Society A: Mathematical, Physical and Engineering Sciences*, 146(856):83–112, 1934. doi:10.1098/rspa.1934.0140.
- [64] R. Jones. Hall D Coherent Bremsstrahlung Rate Calculator. <http://zeus.phys.uconn.edu/halld/cobrems/ratetool.cgi>, last access 3/6/2020, 2012.
- [65] U. Timm. Coherent Bremsstrahlung of Electrons in Crystals. *Fortschritte der Physik*, 17(12):765–808, 1969. doi:10.1002/prop.19690171202.
- [66] GlueX Collaboration. Crystal Radiator Goniometer. https://halldweb.jlab.org/wiki/index.php/Crystal_Radiator_Goniometer, last access 3/6/2020.
- [67] F. A. Natter, P. Grabmayr, T. Hehl, R. O. Owens, and S. Wunderlich. Monte Carlo simulation and analytical calculation of coherent bremsstrahlung and its polarisation. *Nuclear Instruments and Methods in Physics Research, Section B: Beam Interactions with Materials and Atoms*, 211(4):465–486, 2003. doi:10.1016/S0168-583X(03)01420-4.
- [68] S. Adhikari, et al. The GlueX Beamline and Detector. 2020, arXiv:2005.14272.
- [69] A. E. Barnes. *Development of the Tagger Microscope & Analysis of Spin Density Matrix Elements in $\gamma p \rightarrow \phi p$ for the GlueX Experiment*. PhD thesis, University of Connecticut, 2017.
- [70] M. Dugger, et al. Design and construction of a high-energy photon polarimeter. *Nuclear Instruments and Methods in Physics Research Section A: Accelerators, Spectrometers, Detectors and Associated Equipment*, 867(June):115–127, 2017. doi:10.1016/j.nima.2017.05.026.
- [71] M. Dugger, N. Sparks, and B.G. Ritchie. Photon beam polarization by analysis of data from the Hall D Triplet Polarimeter. Technical Report GlueX-doc-3181-v2, 2017.
- [72] F. Barbosa, et al. Pair spectrometer hodoscope for Hall D at Jefferson Lab. *Nuclear Instruments and Methods in Physics Research Section A: Accelerators, Spectrometers, Detectors and Associated Equipment*, 795:376–380, 2015. doi:10.1016/j.nima.2015.06.012.
- [73] GlueX Collaboration. Total Absorption Counter. https://halldweb1.jlab.org/wiki/index.php/Total_Absorption_Counter, last access 3/6/2020.

- [74] Alexander Austregesilo. Orientations of the Photon Beam Polarization for Spring 2017 from ρ (770) Decay Asymmetries. Technical Report GlueX-doc-3977-v3, 2019.
- [75] C. D. Keith. Hall D LH2 Cryotarget. https://halldweb1.jlab.org/wiki/images/b/b8/HallD_Target_Table.pdf, last access 3/6/2020, 2014.
- [76] E. Pooser, et al. The GlueX Start Counter Detector. *Nuclear Instruments and Methods in Physics Research Section A: Accelerators, Spectrometers, Detectors and Associated Equipment*, 927:330–342, 2019. doi:10.1016/J.NIMA.2019.02.029.
- [77] E. Pooser. *The GlueX Start Counter & Beam Asymmetry Σ in Single π^0 Photoproduction*. PhD thesis, Florida International University, 2016.
- [78] N.S. Jarvis, et al. The Central Drift Chamber for GlueX. *Nuclear Instruments and Methods in Physics Research Section A: Accelerators, Spectrometers, Detectors and Associated Equipment*, 962:163727, 2020. doi:10.1016/j.nima.2020.163727.
- [79] M. J. Staib. *Calibrations for charged particle tracking and measurements of ω photoproduction with the GlueX detector*. PhD thesis, Carnegie Mellon University, sep 2017.
- [80] L. Pentchev, et al. Studies with cathode drift chambers for the GlueX experiment at Jefferson Lab. *Nuclear Instruments and Methods in Physics Research Section A: Accelerators, Spectrometers, Detectors and Associated Equipment*, 845:281–284, 2017. doi:<https://doi.org/10.1016/j.nima.2016.04.076>.
- [81] T. D. Beattie, et al. Construction and performance of the barrel electromagnetic calorimeter for the GlueX experiment. *Nuclear Instruments and Methods in Physics Research Section A: Accelerators, Spectrometers, Detectors and Associated Equipment*, 896(January):24–42, 2018. doi:10.1016/j.nima.2018.04.006.
- [82] GlueX collaboration. Technical Construction Report. Technical Report GlueX-doc-2511-v6, Jefferson Lab, 2017.
- [83] GlueX collaboration. Forward Calorimeter. <https://gluexweb.jlab.org/content/photo/fcal-front>, last access 3/6/2020.
- [84] A. Ostrovidov. TOF status. Technical Report GlueX-doc-3030, 2016.
- [85] GlueX collaboration. Spring 2017 Trigger Summary. https://halldweb.jlab.org/wiki/index.php/Spring_2017_Trigger_Summary, last access 3/6/2020.
- [86] GlueX collaboration. hdgeant4. <https://github.com/JeffersonLab/HDGeant4>, last access 3/6/2020.

- [87] S. Agostinelli, et al. Geant4 - a simulation toolkit. *Nuclear Instruments and Methods in Physics Research Section A: Accelerators, Spectrometers, Detectors and Associated Equipment*, 506(3):250–303, 2003. doi:10.1016/S0168-9002(03)01368-8.
- [88] GlueX collaboration. Spring 2017 Trigger Configuration. https://halldweb.jlab.org/wiki-private/index.php/Spring_2017_Dataset_Summary#Trigger_configuration_changes, last access 3/6/2020.
- [89] Jefferson Lab. EVIO. <https://data.jlab.org/drupal/evio>, last access 3/6/2020.
- [90] Jefferson Lab. CODA. <https://coda.jlab.org/drupal/>, last access 3/6/2020.
- [91] T. Britton. Calibration Browser. https://halldweb.jlab.org/data_monitoring/CalibBrowser.html, last access 3/6/2020.
- [92] B. Zihlmann. GlueX Time of Flight Calibration. Technical Report GlueX-Doc-2767, 2017.
- [93] T. Britton and K. Mizutani. Plot Browser. https://halldweb.jlab.org/data_monitoring/Plot_Browser.html, last access 3/6/2020.
- [94] R. E. Kalman. A new approach to linear filtering and prediction problems. *Journal of Fluids Engineering, Transactions of the ASME*, 82(1):35–45, 1960. doi:10.1115/1.3662552.
- [95] R. E. Kalman and R. S. Bucy. New results in linear filtering and prediction theory. *Journal of Fluids Engineering, Transactions of the ASME*, 83(1):95–108, 1961. doi:10.1115/1.3658902.
- [96] R. Brun and F. Rademakers. ROOT: An object oriented data analysis framework. *Nucl. Instrum. Meth.*, A389:81–86, 1997. doi:10.1016/S0168-9002(97)00048-X.
- [97] GlueX collaboration. Analysis Launch Cuts. https://halldweb.jlab.org/wiki/index.php/Spring_2017_Analysis_Launch_Cuts, last access 3/6/2020.
- [98] P. Mattione. Least Squares Kinematic Fitting of Physics Reactions. Technical Report GlueX-doc-2112-v5, Jefferson Lab, 2016.
- [99] GlueX collaboration. DSelector framework. https://github.com/JeffersonLab/gluex_root_analysis, last access 3/6/2020.
- [100] M. Pivk and F. R. Le Diberder. sPlot: a statistical tool to unfold data distributions. *Nucl. Instrum. Meth.*, A555:356–369, 2005. doi:10.1016/j.nima.2005.08.106.

- [101] R. Aaij, et al. Observation of $J/\psi p$ Resonances Consistent with Pentaquark States in $\Lambda_b^0 \rightarrow J/\psi K^- p$ Decays. *Physical Review Letters*, 115(7):072001, 2015. doi:10.1103/PhysRevLett.115.072001.
- [102] S. Gardner, et al. Photon asymmetry measurements of $\vec{\gamma} p \rightarrow \pi^0 p$ for $E_\gamma = 320\text{--}650$ MeV. *The European Physical Journal A*, 52(11), 2016. doi:10.1140/epja/i2016-16333-5.
- [103] J. M. Blatt and V. F. Weisskopf. *Theoretical Nuclear Physics*. Dover books on physics. Springer, New York, NY, 1979. doi:10.1007/978-1-4612-9959-2.
- [104] D. I. Glazier. brufit. <https://github.com/dglazier/brufit>, last access 3/6/2020.
- [105] W. Verkerke and D. P. Kirkby. The RooFit toolkit for data modeling. *eConf*, C0303241:MOLT007, 2003, arXiv:physics/0306116 [physics].
- [106] T. Sjöstrand, L. Lönnblad, and S. Mrenna. PYTHIA 6.2 Physics and Manual. aug 2001. url <http://arxiv.org/abs/hep-ph/0108264>.
- [107] GlueX Collaboration. bggen. https://github.com/JeffersonLab/halld_sim/tree/master/src/programs/Simulation/bggen, last access 3/6/2020.
- [108] K. Livingston. Binned fitting techniques for measuring photon beam asymmetry. Technical Report, priv. communication, University of Glasgow, 2012.
- [109] F. James and M. Roos. Minuit: A System for Function Minimization and Analysis of the Parameter Errors and Correlations. *Computer Physics Communication*, 10:343–367, 1975. doi:10.1016/0010-4655(75)90039-9.
- [110] R. Barlow. Extended maximum likelihood. *Nuclear Instruments and Methods in Physics Research A*, 297:496–506, 1990. doi:10.1016/0168-9002(90)91334-8.
- [111] M. Hatlo, et al. Developments of mathematical software libraries for the LHC experiments. *IEEE Transactions on Nuclear Science*, 52:2818–2822, 2005. doi:10.1109/TNS.2005.860152.
- [112] R. Barlow. Systematic Errors: Facts and Fictions. Technical report, 2002. url <https://arxiv.org/pdf/hep-ex/0207026.pdf>.
- [113] M. Bonamente. *Statistics and Analysis of Scientific Data*. Springer, New York, 2017. doi:10.1007/978-1-4939-6572-4.

- [114] N. Metropolis, A. W. Rosenbluth, M. N. Rosenbluth, A. H. Teller, and E. Teller. Equation of state calculations by fast computing machines. *The Journal of Chemical Physics*, 21:1087–1092, 1953. doi:10.1063/1.1699114.
- [115] W. K. Hastings. Monte Carlo sampling methods using Markov chains and their applications. *Biometrika*, 57(1):97–109, 1970. doi:10.1093/biomet/57.1.97.
- [116] J. Lee, W. Sung, and J. H. Choi. Metamodel for efficient estimation of capacity-fade uncertainty in Li-Ion batteries for electric vehicles. *Energies*, 8(6):5538–5554, 2015. doi:10.3390/en8065538.
- [117] L. Moneta, et al. The RooStats project. In *Proceedings of Science*, volume 93, page 057. Sissa Medialab Srl, 2010. doi:10.22323/1.093.0057.
- [118] D. Foreman-Mackey. corner.py: Scatterplot matrices in Python. *The Journal of Open Source Software*, 1(2):24, 2016. doi:10.21105/joss.00024.
- [119] H. Matevosyan, R. Mitchell, and M. Shepherd. AmpTools. <https://github.com/mashephe/AmpTools/wiki>, last access 3/6/2020.
- [120] E. W. Lemmon, M. O. McLinden, and D. G. Friend. Thermophysical Properties of Fluid Systems. *NIST Chemistry WebBook, NIST Standard Reference Database Number 69*, Eds. P.J. Linstrom and W.G. Mallard, National Institute of Standards and Technology, Gaithersburg MD, 20899, <https://doi.org/10.18434/T4D303>, (retrieved April 27, 2020).
- [121] P. Pauli, et al. Mass-dependent cuts in longitudinal phase space. *Physical Review C*, 98(6), 2018. doi:10.1103/PhysRevC.98.065201.
- [122] M. Shi, et al. Double-Regge Exchange Limit for the $\gamma p \rightarrow K^+ K^- p$ Reaction. *Physical Review D*, 91(3):34007, 2015. doi:10.1103/PhysRevD.91.034007.
- [123] L. Van Hove. Longitudinal Phase-Space Plots of Multiparticle Hadron Collisions at High Energy. *Nuclear Physics B*, 9(3):331–348, 1969. doi:http://dx.doi.org/10.1016/0550-3213(69)90133-3.
- [124] A. Białas, et al. Longitudinal phase space analysis of three-body final states in meson-nucleon collisions. *Nuclear Physics B*, 11(2):479–494, 1969. doi:10.1016/0550-3213(69)90096-0.
- [125] L. Van Hove. Final state classification and new phase space plot for many-body hadron collisions. *Physics Letters B*, 28(6):429–431, 1969. doi:10.1016/0370-2693(69)90343-8.

- [126] D. I. Glazier. HASPECT6. <https://github.com/dglazier/HASPECT6>, last access 3/6/2020.